Coventry University

DOCTOR OF PHILOSOPHY

A theoretical and experimental study of automotive catalytic converters

Clarkson, Rory J

Award date:
1995

Awarding institution:
Coventry University

Link to publication

General rights
Copyright and moral rights for the publications made accessible in the public portal are retained by the authors and/or other copyright owners and it is a condition of accessing publications that users recognise and abide by the legal requirements associated with these rights.

- Users may download and print one copy of this thesis for personal non-commercial research or study
- This thesis cannot be reproduced or quoted extensively from without first obtaining permission from the copyright holder(s)
- You may not further distribute the material or use it for any profit-making activity or commercial gain
- You may freely distribute the URL identifying the publication in the public portal

Take down policy
If you believe that this document breaches copyright please contact us providing details, and we will remove access to the work immediately and investigate your claim.

Download date: 07. May. 2023

A THEORETICAL AND EXPERIMENTAL STUDY OF AUTOMOTIVE CATALYTIC CONVERTERS

Rory John Clarkson, B.Eng

A thesis submitted in partial fulfilment of the University's requirement for the Degree of Doctor of Philosophy

May 1995

Coventry University

ABSTRACT

In response to the increasingly widespread use of catalytic converters for meeting automotive exhaust emission regulations considerable attention is currently being directed towards improving their performance. Experimental analysis is costly and time consuming. A desirable alternative is computational modelling. This thesis describes the development of a fully integrated computational model for simulating monolith type automotive catalytic converters.

Two commercial CFD codes, PHOENICS and STAR-CD, were utilised to implement established techniques for modelling the flow field in catalyst assemblies. To appraise the accuracy of the flow field predictions an isothermal steady flow rig was designed and developed. A selection of axisymmetric inlet diffusers and 180° expansions were tested, with the velocity profile across the monolith, the wall static pressure distribution along the inlet section and the total pressure drop across the assembly being measured. These datum sets were compared with predictions using a variety of turbulence models and solution algorithms. The closest agreement was achieved with a two-layer near wall approach, coupled to the fully turbulent version of the RNG k-ε model, and a nominally second order differencing scheme. Even with these approaches the predicted velocity profiles were too flat, the maximum velocity being as much as 17.5% too low. Agreement on pressure drops was better, the error being consistently less than 10%. These results illustrate that present modelling techniques are insufficiently reliable for accurate predictions. It is suggested that the major reason for the relatively poor performance of these techniques is the neglecting of channel entrance effects in the monolith pressure drop term. Despite these weaknesses it was possible to show that the model reproduces the correct trends, and magnitude of change, in pressure drop and velocity distributions as the catalyst geometry changes.

The PHOENICS flow field model was extended to include the heat transfer, mass transfer and chemical reactions associated with catalysts. The methodology is based on an equivalent continuum approach. The result is a reacting model capable of simulating the three-dimensional distribution of solid and gas temperatures, species concentrations and flow field variables throughout the monolith and associated ductwork. Other features include external heat loss through the monolith mat and the effects that moisture has on the transient warm-up of the monolith. To assess the reacting model's accuracy use was made of published light-off data from a catalyst connected to a test bed engine. Comparison with predicted results showed that the model was capable of reproducing the correct type, and time scales, of temperature and conversion efficiency behaviour during the warm-up cycle. From these predictions it was possible to show that the flow distribution across the monolith can significantly change during light-off.

Following the identification, and subsequent modelling, of the condensation and evaporation of water during the warm-up process it was possible to show that, under the catalyst conditions tested, these moisture effects do not affect light-off times. Conditions under which moisture might affect light-off have been suggested.

Although the general level of model accuracy may be acceptable for studying many catalyst phenomena, known deficiencies in the reaction kinetics used, errors in the flow field predictions, uncertainty over many of the physical constants and necessary model simplifications mean that accurate quantitative predictions are still lacking. Improving the level of accuracy will require a systematic experimental approach followed by model refinements.

ACKNOWLEDGEMENTS

There are a number people and organisations, without whom this project would not have been completed. They are, in no particular order:

My supervisors Dr S.F. Benjamin, Mr S. Richardson (of Jaguar Cars) and Professor N.S. Girgis who all offered considerable advice and encouragement throughout the project,

Mr B.K. Hoverd and Mr G. Ireland, who made, and helped design, the steady flow rig,

Johnson Matthey for supplying the monoliths,

Mr N. Will and Dr C. Bennett (of Johnson Matthey) for their invaluable advice,

Jaguar Cars and the Science and Engineering Research Council, for putting up the money,

Miss C.M. Sanders, who made sure I was well fed and watered,

and everyone else who helped me along the way.

CONTENTS

NOMENCLATURE

1 Symbols

a_c	- catalyst area per unit reactor volume	m^2NM/m^3
a_v	- ratio of reactor surface to reactor volume	m^2/m^3
c_{gw}	- mass fraction of water in exhaust gas	kg/kg
c_p	- specific heat capacity	J/kg K
C	- coefficient in PHOENICS source term	
C_{gi}	- concentration of gas species i	mol/mol
C_{si}	- concentration of species i on monolith surface	mol/mol
C_{pw}	- wall static pressure coefficient	
C'_{sw}	- concentration of water in washcoat	kg/m^3
d	- hydraulic diameter of monolith channels	m
D_i	- diffusivity of species i	m^2/s
f	- phase volume fraction	
F_i	- body force per unit volume	kg/m^2s^2
G	- monolith orthotropic conductivity factor	
h	- heat transfer coefficient	W/m^2 K
h_{ext}	- external surface heat transfer coefficient	W/m^2 K
h_{fg}	- latent heat of vaporisation	J/kg
h_g	- enthalpy of exhaust gas	J/kg
ΔH_i	- heat of reaction of species i	J/mol
k	- turbulent kinetic energy	m^2/s^2
k_e	- empirical constant in Equation 7.1	N/m^2
k_{eff}	- effective thermal conductivity of monolith in radial direction	W/m K
k_g	- thermal conductivity of exhaust gas	W/m K
k_r	- constant that is a function of channel cross sectional shape	
k_s	- thermal conductivity of monolith	W/m K
K	- porous media permeability in STAR-CD	kg/s m^3
K_{mi}	- mass transfer coefficient for species i	m/s
l	- turbulent length scale	m
L	- length of monolith	m
$\dot{m}$	- mass flow rate	kg/s
M_{Rg}	- molar mass of exhaust gas	kg/kmol
P	- pressure	N/m^2
ΔP_e	- pressure drop in monolith due to entrance effects	N/m^2

ΔP_s^*	- non-dimensional static pressure drop	
r_i	- intrinsic reaction rate of species i	$mol/m^2NM\ s$
$\bar{r}_i$	- apparent reaction rate	$mol/m^2NM\ s$
R_g	- exhaust gas specific gas constant	J/kg K
R_i	- reaction rate per unit volume of reactor, for species i	$mol/m^3\ s$
t	- time	s
T	- temperature	K
	- (Section 4.4.1) PHOENICS source term type	
u_i	- fluctuating velocity components	m/s
U	- monolith channel mean velocity	m/s
U'	- monolith channel velocity when $\alpha = 0$	m/s
U	- velocity of exhaust gas	m/s
U_i	- time averaged velocity component	m/s
$\hat{U}_i$	- instantaneous velocity component	m/s
v	- turbulent velocity scale	m/s
v_w	- volume available to store chemical species per unit reactor volume	
v'_{sw}	- specific volume of saturated water vapour	m^3/kg
V	- value in PHOENICS source term	
x,y,z	- co-ordinate axes	
x_i	- co-ordinate direction	
α	- (Sections 2.1 and 6.5) kinetic energy coefficient	
	- monolith porosity	
ε	- turbulent kinetic energy dissipation rate	m^2/s^3
ϕ	- dependent variable	
Φ	- ΔH augmentation factor	
Γ	- kinematic diffusivity	m^2/s
Λ	- washcoat thickness	m
η_s	- reaction rate effectiveness factor	
μ	- dynamic viscosity	kg/m s
μ_t	- turbulent dynamic viscosity	kg/m s
ν	- kinematic viscosity	m^2/s
ρ	- density	kg/m^3
σ_p	- turbulent Prandtl number	
σ_s	- turbulent Schmidt number	
Θ	- temperature	°C

2 Subscripts

g - gas
s - solid
w - water

3 Abbreviations

cpsi - cells per square inch
CeO_2 - ceria
CFD - computational fluid dynamics
CO - carbon monoxide
ESDU - Engineering Sciences Data Unit
H_2O - water
HC - hydrocarbon
NM - noble metals
NO_x - oxides of nitrogen
Nu - Nusselt number
Pd - palladium
PIL - PHOENICS input language
Pt - platinum
Re - Reynolds number
Rh - rhodium
RNG - renormalization group
Sc - Schmidt number
SFCD - self filtering central differencing
Sh - Sherwood number

1 INTRODUCTION

Air pollution caused by motor vehicle exhaust emissions was first recognised as a problem in the 1950's. The first legislation requiring the control of automotive emissions was introduced in California in 1966. Since then awareness of the emissions problem has spread, with many countries now adopting ever more stringent emissions regulations. In addition, it is increasingly being acknowledged that motor vehicles make a major contribution to atmospheric carbon dioxide levels, one of the main "green house" effect gases. This, and the economic need to conserve energy, has led to some countries introducing fuel consumption regulations.

The undesirable chemical species that constitute the main exhaust emissions produced by spark ignition engines are hydrocarbons (HC's), carbon monoxide (CO) and nitrogen oxides (NO_x). CO results from incomplete combustion of fuel. The HC's are thought to originate from incomplete combustion, desorbtion of fuel from lubricating oil following combustion and fuel trapped and subsequently released from crevices. NO_x result from high temperature, high pressure combustion. When oxidised in the atmosphere HC's and NO_x produce peroxy-acetyl-nitrate (PAN) and ozone, both of which lead to smog formation. CO is toxic to animal life, reducing oxygen levels in blood by causing the formation of carboxyhaemoglobin in preference to normal oxyhaemoglobin. The relative proportions of emissions species discharged from an engine is a function of the engine design, its control system, the engine load, the fuel being used and the ratio of air to fuel in the combustion charge. Figure 1.1 illustrates how these relative proportions typically vary with air-fuel ratio.

A number of solutions to the emissions problem have been tried, including lean air-fuel ratios ("lean-burn"), exhaust gas recirculation (EGR) and stratified charge combustion. One of the most successful has been the use of a catalytic converter situated in the exhaust system. Catalytic converters, for brevity referred to simply as catalysts, are chemical reactors that act as afterburners. They contain chemical compounds, typically the noble metals platinum, palladium and rhodium, that promote the complete combustion of emission species without forming part of the reactions.

The first generation of catalysts used for automotive applications were only designed to convert HC's and CO to carbon dioxide (CO_2) and water (H_2O). Both of these processes consist of exothermic oxidation reactions, hence their generic name "oxidation catalysts". Engines run at the stoichiometric air-fuel ratio should have sufficient oxygen atoms available in the exhaust for complete conversion of the HC's and CO, however many of these atoms are combined as NO_x and are therefore not readily available for reaction. To overcome the resulting shortfall in available oxygen, secondary air has to be injected into the exhaust gas, upstream of the catalyst. The inability of these catalysts to reduce NO_x, to harmless nitrogen, represented a major weakness. It can be

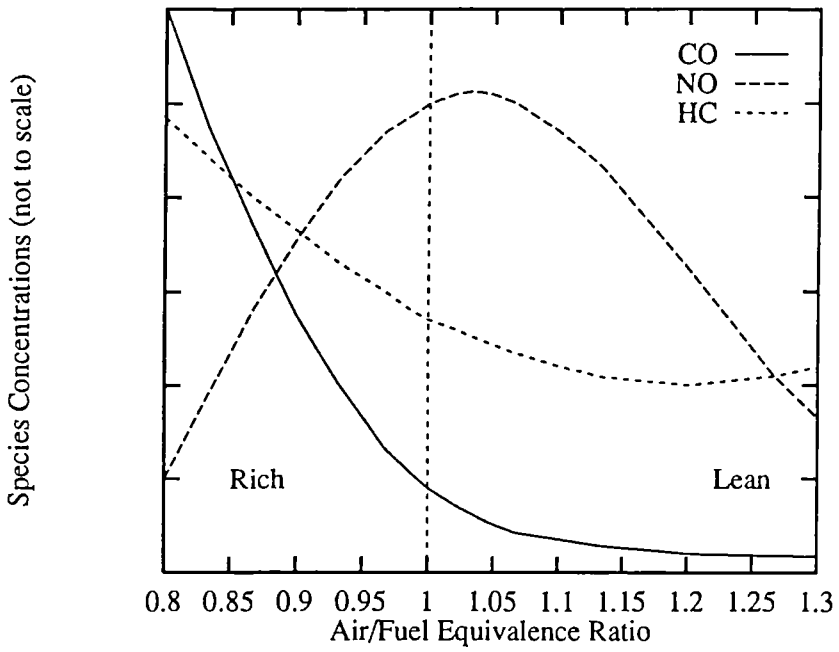

Figure 1.1 - Variation in concentration of emissions discharged by a typical spark ignition engine as a function of air-fuel ratio.

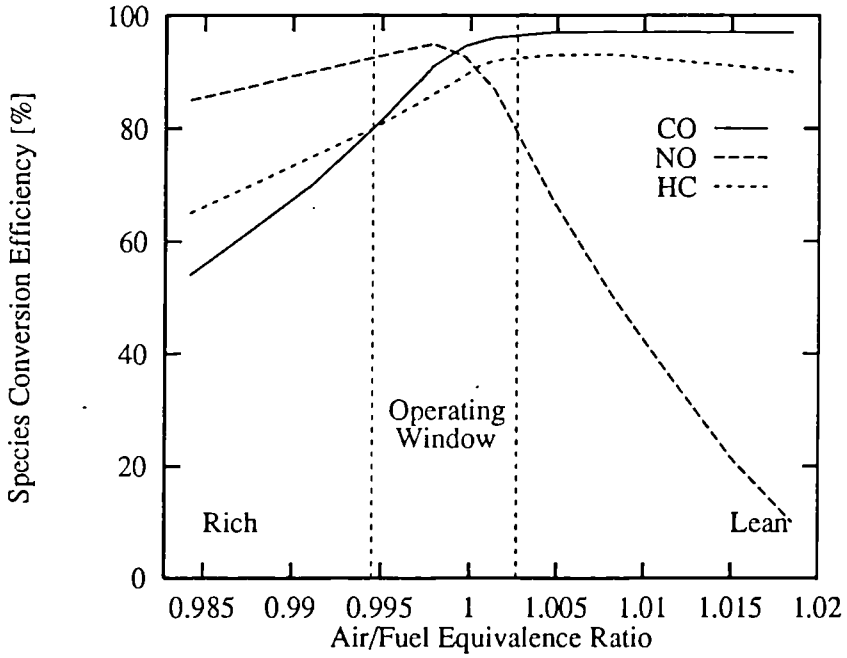

Figure 1.2 - Emission species conversion efficiency for a three-way catalyst as a function of engine air-fuel ratio

partially overcome by either running the engine with a rich air-fuel ratio, which naturally reduces the engine NO_x emissions (see Figure 1.1) and injecting additional secondary air to oxidise the subsequently increased levels of HC's and CO in the exhaust, or run the engine slightly lean, which again can reduce NO_x levels and also removes the need to inject additional oxygen. Unfortunately the first strategy has a detrimental effect on fuel consumption and CO_2 emissions, and the achievable reductions in NO_x levels with both approaches is limited.

A superior strategy is to use a catalyst that can reduce NO_x to nitrogen, another exothermic reaction, as well as oxidise HC's and CO. Reduction of NO_x liberates oxygen which can then be used in oxidation reactions, removing the need for secondary air injection. Because of the chemical kinetics involved, to operate properly these "three-way" catalysts require engines to be run within a narrow band either side of the stoichiometric air-fuel ratio (see Figure 1.2).

Most of the emissions regulations currently being adopted dictate that, at present, three-way catalysts are the only practical solution to the problem. Their inability to operate at lean air-fuel ratios handicaps combustion efficiency. Catalysts also cause elevated exhaust back pressures, which reduces engine performance. Both effects handicap low fuel consumption. To meet the tightening emissions regulations considerable research is being undertaken to find ways of improving catalyst performance. Additional stimuli are being provided by the desire to reduce their impact on engine performance and limit component cost, both of which are proportional to catalyst size. Improvements in catalyst performance should lead to reduced catalyst size.

Catalysts can be split into two broad categories, packed beds and monoliths. Packed beds consist of alumina pellets upon which the catalytically active noble metals are supported. The term monolith implies a single structure, the substrate, which is coated with an alumina washcoat that supports the noble metals. The substrate can be made of either a ceramic, usually cordierite, or a metal, and normally consists of a series of small capillary passages running parallel to each other. Both types have their strengths and weaknesses. The present trend in the automotive industry is to use monolith type catalysts with either ceramic or metallic substrates. Figure 1.3 shows the layout of a typical monolith type catalyst.

Like many systems catalysts have a number of performance criteria. The areas of particular interest with regard to emissions regulations are the cold start characteristics, the "steady state" conversion efficiencies and component durability. Catalysts can only convert significant quantities of emission species if their temperature is raised several hundred degrees above ambient. The process by which the catalyst goes from virtually negligible species conversion to considerable conversion is known as light-off, and can occur over a very narrow temperature range. The time taken to reach this process, usually following a cold start, is known as the light-off time, the temperature at which it

occurs the light-off temperature. Prior to light-off a considerable proportion of the allowable total emissions are discharged. Thus particular attention is being directed towards shortening the light-off time.

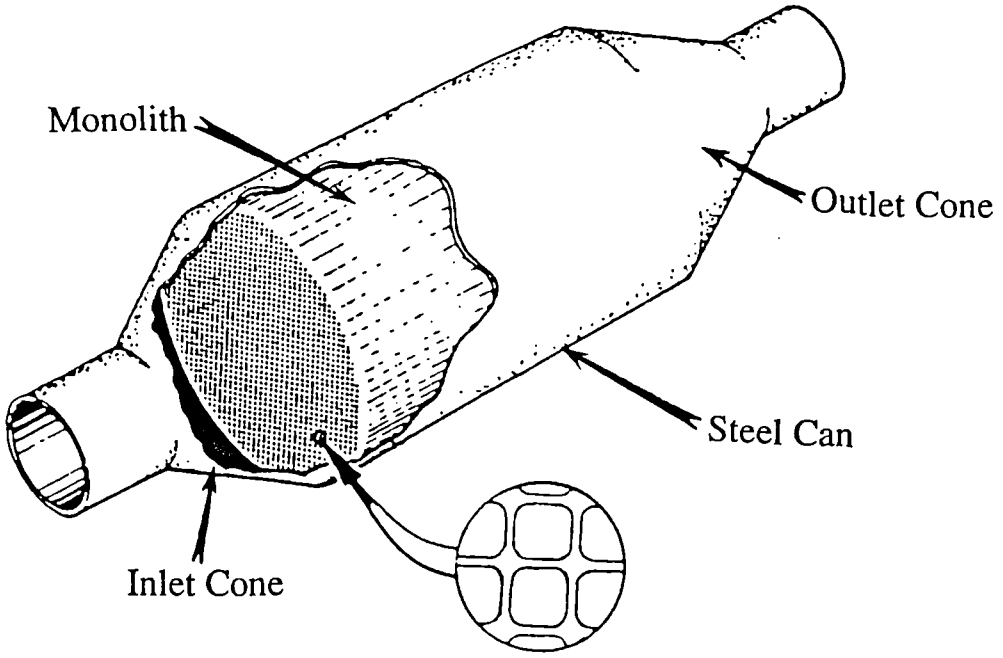

Figure 1.3 - Typical monolith type catalyst assembly

The "steady state" conversion efficiencies refer to the emissions conversion performance after light-off. It should be recognised however that even after light-off catalysts are still operating under transient conditions, due to the variation in engine load. Therefore a more appropriate name for this set of performance criteria is post-light-off, or fully warm, conversion efficiencies. Durability is reduced by either deterioration in activity (the ability to promote chemical reactions) or by mechanical failure. The former results from thermal degradation and poisoning (by contaminants in the exhaust gases), the latter from vibrational or thermal stresses. Component longevity is important because catalysts are now required to last in excess of 100 000 miles and performance levels need to be maintained throughout the full life cycle.

1.1 Investigative Approaches

Before new improved catalyst designs can be built, an understanding of the factors and parameters that affect performance must be obtained. There are two approaches to this; experimental analysis and mathematical modelling. Experimental analysis is time consuming and costly. To assess the influence different parameters have requires the testing of many different configurations. Collecting

data may require the use of intrusive measuring techniques, with limited access being another potential problem. Transient analysis is also necessary for assessing catalyst light-off behaviour. By contrast mathematical modelling is potentially fast and inexpensive. No intrusive measuring techniques are required, data can be collected from inaccessible locations and rapidly changing phenomena can be studied relatively easily.

Although mathematical modelling is attractive a pre-requisite is that acceptably accurate solutions can be obtained comparatively quickly. To develop such a model it is necessary to be able to represent the fundamental physics governing catalyst behaviour as mathematical functions. Fortunately the majority of catalyst phenomena are governed by established transport and conservation equations that take the form of non-linear, partial differential equations. To solve these equations, without making gross simplifications, requires a numerical approach. A purpose built computer code would require considerable development time and testing. An alternative approach, and the one adopted for this research project, is to utilise the solution algorithms of a commercially available computational fluid dynamics (CFD) code.

Although the transport and conservation equations can be solved, there still remains some doubt over the values of many of the coefficients and constants that appear in them. Additionally there is uncertainty over the details of the expressions that dictate the reaction chemistry. Thus there is a need to validate any mathematical models against experimental data. Consequently both the experimental and mathematical approaches need to be carried out in parallel, until sufficient generality and accuracy can be achieved with a computational model such that extensive experimental analysis is unnecessary.

1.2 The Present Study - Aims and Objectives

The main objective of the work presented here was to develop a mathematical model that allows investigation of parameters that affect the performance of catalysts, and to demonstrate, using experimental data, under which conditions the model gives acceptable answers. Because of present trends attention has been directed towards modelling monolith type catalysts, however the techniques employed could be adapted to other types of catalyst. The project originated from the desire within the automotive industry to have a design tool, based on a commercially available CFD code, capable of predicting the behaviour of catalytic converters.

The next two sections of this thesis review the present state of knowledge on catalyst behaviour and the attempts to model them mathematically. Section 4 describes how two commercial CFD codes, PHOENICS and STAR-CD, have been used to develop isothermal computational models of catalyst flow fields, followed in Section 7 by an assessment of their predictive performance against

experimental data. Section 5 describes how the isothermal experimental data was collected, with an analysis of the data being carried out in Section 6. Section 8 discusses how the isothermal model developed using PHOENICS was extended to include the heat transfer, mass transfer and the chemical reactions that take place within the catalyst. Section 9 compares results from this reacting catalyst model with data taken from work carried out on engine test beds. A summary of the projects major contributions and conclusions is included as Section 10. Finally, recommendations for future work are discussed in Section 11.

2 CATALYST PERFORMANCE

Since the introduction of catalysts as emission control devices in the USA during the early 1970's a substantial amount of research into the parameters that affect their performance has been carried out. All areas of catalyst performance have attracted interest, most notably the light-off behaviour, post-light-off conversion efficiency, component mechanical integrity, durability and effect on engine performance. All can be influenced by a number of different factors, the more important of which are discussed below.

2.1 Influence of Catalyst Housing

Originally catalysts where used retrospectively as add on solutions to the emissions problem and as such had to be fitted into confined spaces on existing automobile models. It was recognised that one way of reducing back pressure is to use short catalysts, pressure drop being proportional to catalyst length. However, to ensure sufficient catalyst volume is available for satisfactory conversion of emissions the catalyst cross-sectional area has to be made larger than that of the inlet exhaust pipe. Thus an expansion cone or diffuser is used upstream of the catalyst inlet face. Because of the limited space available these inlet diffusers had to be short and wide angled. Such diffusers are inefficient at spreading the exhaust gas uniformly across the catalyst, the resulting flow distributions frequently having a pronounced peak or maximum.

Early workers soon established that these non-uniform velocity profiles have a detrimental effect on the conversion efficiency and durability of monolith catalysts. Comfort (1974) [1] studied the effect various velocity distributions have on conversion efficiency using a simplified mathematical model which assumed mass transfer controlled reaction rates. It was concluded that the flatter, more uniform the velocity profile the better the conversion efficiency. Howitt and Sekella (1974) [2] experimentally studied the effect of velocity distribution on an oxidation catalyst. A selection of flow tailoring devices, placed in the throat of the diffuser, were used to try and flatten the velocity profile. These included several "pinwheel" vortex generators designed to produced swirling flow fields in the diffuser, which cause exhaust gas to be distributed towards the monolith perimeter. Discs and cones were also used to deflect the flow towards the perimeter. In addition they found that a relatively narrow angled diffuser of 24° produced a flatter velocity profile. The results of the study showed that a flatter profile reduced ageing effects, improved conversion efficiency but lengthened light-off times. The flow tailoring devices, however, tended to increase the pressure drop through the system.

Lemme and Givens (1974) [3] undertook a theoretical analysis of the effect flow maldistribution has on catalyst life. Taking the basic assumption that conversion efficiency decreases linearly with

the accumulated mass of gas passing through a given segment of catalyst, it was shown that a non-uniform flow distribution reduces durability. However, it was suggested that there is a maldistribution beyond which additional flattening of the profile ceases to produce improvements in durability. They also studied some of the factors that affect flow distribution. Three different types of inlet expansion were investigated, a conical diffuser, a 180° expansion and a spherical expansion. When all the same, relatively short, length each type produced essentially the same monolith velocity profiles. Increasing the length of the 180° expansion tended to flatted the profile, a trend that was also produced by increasing the diameter of the inlet pipe (reducing the expansion ratio) and lengthening the monolith. A conical flow deflector successfully flattened the velocity profile of the conical diffuser, but with an associated pressure drop penalty.

An experimental study by Germidis et al. [4] of metallic substrate catalysts illustrates the effect inlet diffuser geometry can have on catalyst thermal behaviour. The monolith radial temperature distributions, produced by a 90°, a 36° and a trumpet shaped diffuser, where taken at high and low flow rates. At the low flow rate all three geometries produced essentially the same temperature distributions, but at the high flow rate the larger cone angle resulted in a central temperature approximately 100 K higher than the other two cones. Although warm-up characteristics were tested, no comments were made as to the relative light-off performance of each cone.

Most of the attempts to improve velocity profiles included in the work reviewed in the preceding paragraphs were somewhat crude in nature. As many authors have pointed out, velocity profiles are strongly dependent on diffuser performance. Diffusers have been used within fluid dynamic applications for a substantial length of time, and their performance has been studied likewise. The normal criterion for good diffuser performance is its ability to convert dynamic head into static head; its pressure recovery capabilities. Although good pressure recovery has not been considered of primary importance with catalysts applications, it is usually associated with more uniform velocity profiles. Poor pressure recovery results from frictional losses in separated flow and high levels of flow non-uniformity at the exit plane of the diffuser. The more non-uniform, or maldistributed, the velocity profile the more kinetic energy the fluid has for a given flow rate (the kinetic energy coefficient, α, is greater). Thus a poor exit velocity profile represents poor conversion of dynamic head to static head.

Since the 1950's considerable research has been carried out on the flow fields that exist in diffusers and the ways in which their pressure recovery can be improved. Two concise reviews of this work, one on flow phenomena in diffusers [5] and one on methods of improving diffuser performance [6], have been published by the Engineering Sciences Data Unit (ESDU). Despite the usefulness of much of this work, the presence of a large flow resistance, the monolith, at the exit of catalyst diffusers will make their flow fields significantly different from those found in conventional

diffusers. Although, as a result, it is likely that quantitative data on conventional diffuser performance will not be directly applicable to catalyst diffusers, it would be reasonable to assume that qualitative trends will still be the same.

All the techniques used for improving pressure recovery work by eliminating separation and flattening velocity profiles. As a result they should be doubly beneficial to catalysts. Many of them however are only effective if used with relatively narrow angled diffusers (i.e. less than 15° wall angle). Two techniques that have been successfully used for wide angled diffusers are concentric vanes and perforated screens in combination with wall curvature. Both techniques work by deflecting flow into low momentum boundary layers. One of the most effective ways of achieving optimum diffuser performance is to use long, narrow angled diffusers that have an innate aerodynamic efficiency. Despite the fact that modern catalysts have become more integrated within automobile designs lack of space is still a problem prohibiting the use of efficient diffusers.

Despite the conclusions of the early studies on catalyst velocity profiles little attention was directed towards them until the mid 1980's. In 1986 Wendland and Matthes [7] studied the steady flow fields that occur in the inlet diffuser and exit cone of dual-bed, race-track catalysts (race track catalysts have an elliptical type of cross section). To allow visualisation of the flow the catalyst housing was made out of transparent acrylic. Water, with small opaque particles suspended in it, was passed through the system and illuminated with a laser sheet. Photographs could then be taken of the particle streaks. The study showed that the flow separated from the diffuser walls at its throat, producing a central jet surrounded by recirculating fluid. It should be noted that the diffuser used was short and wide angled. The flow in the exit cone showed no separation. Data for the pressure drop across the whole catalyst assembly indicated good agreement with an expression based on laminar flow within the monolith channels.

A study by Wendland et al. [8] attempted to quantify the effect various diffuser and exit cone geometries have on the pressure drop across a catalyst assembly. They took a relatively long and a relatively short diffuser, plus a truncated 180° expansion, and tested them with an outlet cone and a 180° sudden contraction under varying inlet Reynolds numbers (Re). Both outlet types were produced with centrally located and offset exit pipes. To correlate their results they extended the pressure drop expression developed by Wendland and Matthes [7] to include empirical terms for the losses in the diffuser and exit cone. They found that the non-dimensional pressure drop caused by the diffuser and exit cone was independent of the Re, contributing about a third of the total pressure loss at moderate flow rates, increasing to about half at high flow rates. The data also suggested that the truncated 180° expansion produced no significant increase in pressure drop compared with the long diffuser. Note that dimensions were not given for either assembly; it is possible that the relatively long diffuser was quite short.

In a later paper Wendland et al. [9] took the same catalyst geometries used by Wendland et al. [8] and tested their relative light-off performance and post-light-off conversion efficiency. It was found that shortening the inlet diffuser/expansion had very little effect on the time to light-off or post-light-off conversion efficiency, although there was some evidence that with a sudden expansion at inlet and a sudden contraction at outlet warm-up times might be lengthened. The observation made at the end of the previous paragraph about relative lengths of the inlet assemblies can again be made.

The introduction of tighter emissions regulations in Europe and the USA at the beginning of the 1990's stimulated more interest in velocity profiles. Lai et al. (1991) [10] undertook a theoretical study, using a commercial CFD code, of the steady isothermal flow in a catalyst assembly. They looked at the effect of inlet Re, monolith resistance and upstream pipe geometry, concluding that the smaller the Re, the straighter and shorter the inlet pipe and the larger the monolith resistance the flatter the velocity profile. A further study, again using a commercial CFD code, was carried out by Kim et al. [11] on the flow fields that exist in axisymmetric catalysts. They came to essentially the same conclusions as Lai et al. [10], finding that smaller diffuser angles reduced both the pressure drop across the system and the flow maldistribution. They also found that increased monolith resistance, through increasing either cell density (see Section 2.2) or monolith length, would reduce flow maldistribution but increase the pressure drop. Finally they found that increasing the inlet pipe Reynolds number increased the flow maldistribution. Although these findings are entirely plausible, no detailed experimental validation of the results was offered. The work does imply, however, that CFD technology is capable of making at least qualitatively reliable predictions.

Following the work of Lai et al. [10], CFD has increasingly been used to study catalyst flow fields. For example Bella et al. [12] used a commercial CFD code to predict the steady flow field in a race track catalyst assembly. The monolith velocity profile was then flattened by inserting concentric flow deflection vanes within the diffuser. As an extension to the study the predicted velocity profiles were used as boundary conditions for a catalyst reaction model, which confirmed the detrimental effect that poor flow distribution has on post-light-off conversion efficiency.

2.2 Substrate Materials and Geometry

The choice of monolith substrate material lies between ceramics and metals. Currently the majority of catalysts have ceramic substrates, however many authors have propounded the strengths of metallic substrates. In an early paper Delieu et al. [13] outlined two advantages that metallic substrates have over ceramic ones; increased flexibility of design and the potential for thinner cell

walls. Thinner cell walls allow the number of cells per monolith cross-sectional area, the cell density, to be increased without significantly reducing the monolith free, or open, volume. Increased cell densities mean increased surface area per unit reactor volume. Thus total catalyst volume could be reduced without reducing the total reactor surface area. Conversely, for a fixed cell density thinner walls would increase the monolith free volume, which leads to lower pressure drops. Thinner walls can also mean lower masses. Later papers by Nonnenmann [14], Oser [15], Kaiser and Pelters [16] and Nishizawa et al. [17] have reiterated these strengths and added that metallic substrates have a greater thermal and mechanical shock resistance, and a higher thermal conductivity than ceramic substrates. The latter point allows heat generated at local hot spots to be quickly dissipated to cooler areas.

An additional advantage that metallic substrates offer is their ability to be resistively heated using electricity. Whittenberger and Kubsh [18] are only two out of numerous authors that have undertaken studies of this technology. The benefit from being able to electrically heat a catalyst is a greatly reduced light-off time.

Nishizawa et al. [17] pointed out that most of the metallic monoliths presently being produced are used as small starter catalysts situated close to the engine exhaust manifold, so called "close coupled" catalysts. The small size of starter catalysts means the gases passing through them will have high velocities, a situation where the lower pressure drop offered by metallic substrates is particularly beneficial. Their lower mass, allied with a lower specific heat, compared to ceramic substrates, gives them lower thermal masses which should result in shorter warm-up times. Nishizawa et al. [17] also commented on some of the weaknesses of metallic catalysts. These included their large thermal expansion coefficients, their tendency to suffer permanent deformation when exposed to excessive thermal or mechanical stresses, their high cost and the poor adhesion between the substrate and washcoat. The latter point arises from the non-porous nature of the metal substrate, something that is not a problem with ceramic substrates. Stroom et al. [19] have also suggested that metallic monoliths require greater thermal and acoustic insulation compared with ceramic monoliths, and at temperatures above 900 °C can experience monotonic softening and embrittlement. Gulati et al. [20] tested the mechanical strength of both types of monolith and found that ceramic monoliths have superior mechanical strength at high temperatures.

Many of the points discussed in the previous paragraph relate to durability. A study by Jasper et al. [21] compared the light-off performance of three metallic catalysts, with different cell densities, against a similarly sized ceramic catalyst. They found that under maldistributed flow conditions ceramic monoliths light-off faster than metallic monoliths, however the converse may be the case if the flow field is uniform, and that lower cell densities (lower thermal mass) hasten light-off. In addition they studied the effect of aspect ratio (constant volume, different length) and of using split

bricks (two monoliths occupying essentially the same volume as one) on ceramic catalyst light-off. Longer, narrower monoliths and split bricks both accelerate light-off. It should be noted that the conclusions on the effect of monolith aspect ratio are complicated by variations in velocity profiles caused by differences in the expansion ratio of the inlet diffusers.

The main rationale behind the use of split bricks is that gas to solid heat and mass transfer rates are significantly enhanced in the entrance region of monolith channels. Split bricks provide two such entrance regions, which should thus improve conversion efficiencies and reduce light-off times. In addition to Jasper et al. [21], the influence of split bricks has also been studied by Wendland et al [8] and Wendland et al [9]. Wendland et al [8] found that split bricks can increase pressure drops from between 0.7% to 4.1%. Wendland et al [9] compared the relative light-off performance and post-light-off conversion efficiency of a group of single brick catalysts with a similar group of split brick catalysts. Unfortunately the combined volume of the two split bricks was 57% larger than the single bricks. Bearing this complicating factor in mind, their results indicated that the single bricks light-off consistently faster than the split bricks, possibly because the smaller length of the single bricks produced a more maldistributed velocity profile. No firm conclusion can be drawn from their post-light-off conversion efficiency data, neither group of catalysts performing significantly better than the other.

Further evidence on the significance of cell density was obtained by Kaiser and Pelters [16] who tested the performance of a selection of different metallic substrate geometries; a 200, a 300 and a 400 cell per square inch (cpsi) format, a 400 cpsi format with repeated transverse ridges running across each cell, and a novel, corrugated, 200 cpsi substrate with slots, allowing radial and circumferential flow (Nonnenmann [22]). They found that pressure drop increased as cell density and complexity increased and that at lower cell densities light-off was more rapid, but that post-light-off conversion efficiencies were poorer (lower reactor surface area). An interesting finding was that the geometry with transverse ridges had a similar light-off performance to the standard 200 cpsi geometry.

Yamamoto et al. [23] undertook an experimental investigation of the effect various cell densities, wall thicknesses and cordierite densities have on ceramic monolith light-off. Their results on the influence of increased cell density were mostly inconclusive. With fresh catalysts it appeared to quicken light-off, with aged catalysts it appeared to have no effect. Other evidence indicated that lower cordierite densities reduce light-off times. They also showed that the greater reactor surface area given by higher cell densities resulted in improved post-light-off conversion efficiency. An experimental study of ceramic monoliths by Day and Socha [24] also examined the effect of varying cordierite density and cell density (with a fixed total reactor surface area, achieved by varying the monolith length). They concluded that increasing cell density under their fixed surface

area constraint had little effect on light-off times, but increased the post-light-off conversion efficiencies and pressure drop. Variations in the cordierite density, which alters the thermal mass, also had little effect on light-off times. In addition they found that increasing the substrate length, with a fixed cell density, reduced the light-off temperature, improved post-light-off conversion efficiencies, but increased pressure drops.

A theoretical analysis of the effect substrate length, cell density, wall thickness and overall diameter have on pressure drop was carried out by Day and Socha [25]. Taking the assumption that the pressure drop through a channel is given by the Hagen-Poiseuille equation and that the exhaust gas is uniformly distributed across the monolith, they derived a set of relationships relating the above mentioned variables. These indicated that at constant substrate volume the pressure drop is inversely proportional to the overall diameter to the fourth power and proportional to the length squared. At constant length the pressure drop is inversely proportional to the diameter squared and at constant diameter it is proportional to the length. Their analysis showed that cell density and wall thickness are of minor importance to pressure drop. The value of such a study however is limited by the assumption that the inlet diffuser works perfectly to produce a uniform velocity profile.

A paper by Day [26] illustrates some of the potential improvements in catalyst performance that can be obtained from developments in substrate technology. Using an analytical approach he showed that doubling the substrate strength could lead to thinner cell walls, which could be used directly to reduce flow resistance or indirectly to improve conversion efficiency through greater cell density.

2.3 Noble Metal and Washcoat Formulations

Considerable advances have been made in catalyst performance by developments in the noble metal and washcoat formulations. Although not the only catalytically active agents, the platinum group noble metals, platinum (Pt), palladium (Pd) and rhodium (Rh), have been found to be the most effective for automotive applications. The primary purpose of the washcoat is to provide a porous medium with a greatly enlarged surface area upon which the noble metals are dispersed. The greater the surface area available for reactions to take place on, the better the activity of the system. An additional role for the washcoat is to promote the activity and thermal stability of the noble metals. Improving activity improves conversion efficiencies and reduces light-off temperatures, which will reduce light-off times. Improving thermal stability improves durability.

A review by Church et al. [27] explains the role of some of the more important components involved in washcoat and noble metal formulations. Pt and Pd are effective at promoting the

oxidation of CO and HC's, whereas Rh promotes the reduction of NO_x, particularly at stoichiometric exhaust compositions. Three-way catalysts usually contain Rh and one of, or both, Pt and Pd. Additional agents can be incorporated to promote the effectiveness of these metals, for example base metals. Ceria (CeO_2) is usually added to the washcoat to inhibit sintering of the noble metals, but can also promote activity and improve oxygen storage. This latter feature is particularly useful when engine air-fuel ratios oscillate either side of stoichiometric.

Many authors have assessed the merits of various combinations of noble metals in three-way catalysts. Monroe and Krueger [28] studied how the proportions of Pt and Rh in a Pt/Rh three-way catalyst effected conversion performance. They found that increasing the proportion of Rh improved the NO_x light-off and conversion efficiencies. Increasing the proportion of Pt had little effect on NO_x emissions but improved CO conversion efficiencies. HC conversion efficiencies were improved by increases in either component. Lui and Dettling [29] assessed the relative merits of Pt/Rh and Pd/Rh three-way catalysts for CO-NO_x reactions. They reported that Pd/Rh formulations perform less well than Pt/Rh formulations, that Pd is susceptible to poisoning and can inhibit Rh activity. Yamada et al. [30] found that a Pd/Rh three-way catalyst gave better HC conversions than a comparable Pt/Rh three-way catalyst, even though the Pt/Rh formulation had a 40 K lower light-off temperature. Another study of Pt/Rh and Pd/Rh three-way formulations, by Summers et al. [31], compared their relative durability and light-off performance as a function of several ageing cycles (different air-fuel ratio oscillations, temperature histories and flow rates). The findings indicated that ageing history can be as important an influence on performance as formulation.

Examples of how other agents may affect performance can be found in the literature. Tauster [32] has shown how the addition of base metal oxides can reduce the tendency of Rh to deactivate in high temperature lean conditions. An illustration of how high levels of ceria can improve performance and durability has been given by Cooper and Truex [33], who also indicated that nickel can be used to enhance performance. Bartley et al. [34] showed how a new proprietary stabiliser and an improved method for incorporating ceria into catalyst formulations had a beneficial effect on three-way catalyst thermal stability.

2.4 Variations in Air-Fuel Ratio

As already stated, for three-way catalysts to operate effectively the exhaust gas composition has to be kept close to that produced by engines running with a stoichiometric air-fuel ratio. To achieve such an air-fuel ratio closed loop fuel metering systems must be used. These normally consist of an electronic fuel injection system with an oxygen sensor in the exhaust, which gives an indication of the engine air-fuel ratio. Because of the dynamics of these systems they cannot provide a truly

constant air-fuel ratio, but produce a mixture that oscillates between lean and rich. Although the average air-fuel ratio will still remain near stoichiometric, the oscillations significantly alter catalyst performance. The amplitude, frequency and shape of the oscillations vary as a function of the control system characteristics and driving conditions (Ribbens [35]).

Figure 2.1, taken from Kaneko et al. [36], illustrates how oscillations affect conversion efficiencies over a range of air-fuel ratios. Note that the air-fuel ratio quoted for the oscillating case is the cycle mean. Under steady state conditions the range of air-fuel ratios at which conversion of all the emission species is above 80% is very narrow. Under oscillating conditions the range over which conversion remains above 80% is widened but the conversion efficiencies near the stoichiometric point are lowered. Shulman et al. [37] showed that the changes in conversion efficiencies are a function of the amplitude, frequency and shape of the oscillations.

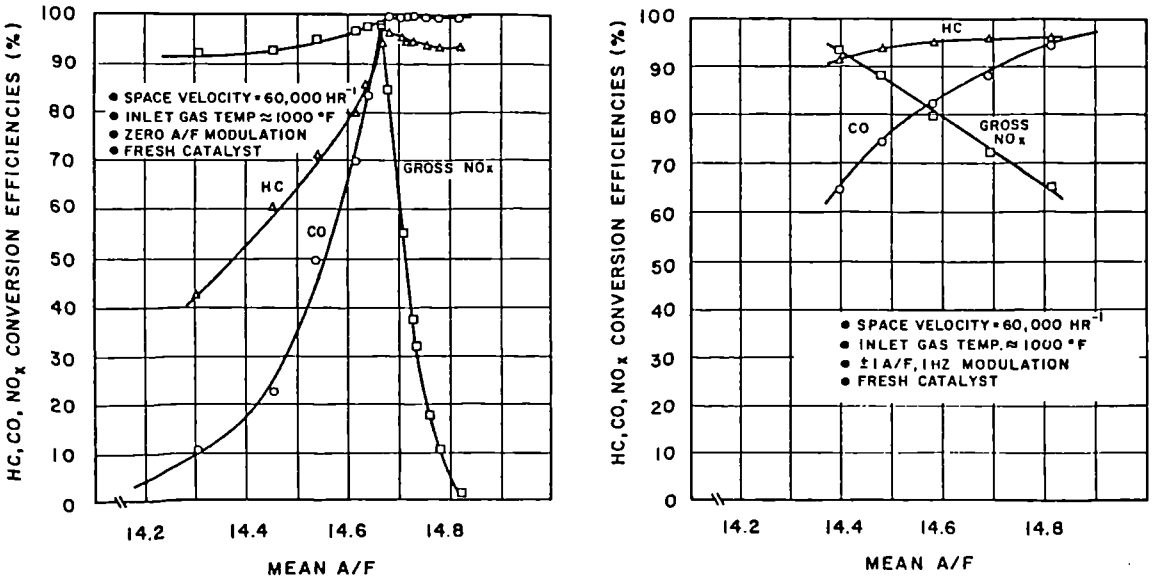

Figure 2.1 - Effect of oscillations in air-fuel ratio (A/F) on conversion efficiency of three-way catalysts: (a) Steady state (amplitude = 0, frequency = 0); (b) Oscillating A/F (amplitude = 1.0 A/F, frequency = 1 Hz)

During acceleration air-fuel ratios can become rich for relatively long time periods. Hertz and Shinouskis [38] showed that these rich excursions may seriously reduce conversion efficiencies of three-way catalysts. O'Sullivan and Will [39] undertook an experimental and theoretical study of the effect increased HC concentrations have on peak catalyst temperatures. Two scenarios for producing high exhaust HC levels were investigated; engine misfire and the air-fuel ratio excursion

following deceleration. They found that at low and moderate exhaust flow rates the peak catalyst temperature was proportional to the misfire rate, catalyst melting being anticipated at a rate of 51%. At high flow rates, increases in the misfire rate, above a threshold level, tended to reduce the peak catalyst temperature. The spike in HC concentrations following a throttle shut deceleration, although producing a temporary spike in the peak catalyst temperature, did not result in substrate melting.

2.5 Chemical Poisoning

Chemical poisoning refers to the process by which catalysts loose their activity through absorption of foreign impurities. For automotive applications there are essentially three agents that cause chemical poisoning; lead, phosphorus and sulphur. A review by Taylor [40] outlines the sources of these poisons and their effect on catalyst performance. Lead is introduced via the engine fuel. It has a tendency to narrow the operating window of three-way catalysts and can rapidly reduce conversion efficiencies if introduced in relatively large amounts. For this reason unleaded fuel, which still contains trace amounts a lead, should be used with vehicles fitted with catalysts. There is some evidence that high Rh levels reduces the effects of lead. There are two sources of phosphorus in exhaust gas, from the fuel and from lubricating oils. Evidence suggests that the phosphorus from lubricating oils has a more detrimental effect than that from fuel. The addition of alkaline earth metals to lubricants seems to reduce the harmful effects. Sulphur present in fuel finds its way into exhaust gases as sulphur dioxide. Sulphur dioxide has been shown to reduce the activity of three-way catalysts and selectively suppresses the oxidation of some HC's. It has been suggested that short term poisoning by sulphur is reversible.

2.6 Miscellaneous Factors

There are a number of additional factors that affect catalyst performance which have already been alluded to in the preceding sections. For completeness they have been grouped together as miscellaneous factors. They include the thermal history of the catalyst, its proximity to the engine and the design of the upstream exhaust system. Koberstein et al. [41] pointed out that the higher vehicle speed limits encountered in Europe may result in catalysts operating at higher temperatures than in North America. Similarly a system will experience a different thermal history if it is operated under predominantly urban conditions as opposed to high speed motorway driving. As already stated, Summers et al. [31] pointed out the importance of ageing cycles on catalyst performance. A paper by Moore and Mondt [42] highlighted the importance of a catalyst's position relative to the engine and the design of the exhaust system between the catalyst and engine on the light-off time. By placing the catalyst close to the engine and designing an exhaust system that

conserves the thermal energy of the exhaust gas, the temperature of the gas entering the catalyst will by high, which in turn leads to shorter light-off times.

2.7 Discussion

As the preceding text has shown, an extensive amount of research has been carried out on catalyst performance. Despite this there are several areas where knowledge and understanding is still lacking. Even in those areas that have received considerable attention some of the findings have been inconclusive, the reasons for which vary. In some cases the parameters that affect performance have been varied over too small a range, in some too many parameters have been varied.

An area where some uncertainty remains is the influence monolith flow distribution has on light-off performance. Much of the evidence, although by no means all, suggests that increased flow maldistribution quickens light-off. Even where the benefits of a uniform velocity profile have been established (i.e. durability and post-light-off conversion efficiencies) attempts to achieve such profiles have been somewhat crude and of limited success. Although a qualitative understanding of the factors that affect velocity profiles has been established, no systematic experimental studies have been undertaken to quantify the influence of the important parameters.

As with flow distributions, certain trends have been established in the way substrate design influences performance. Increasing the monolith length reduces light-off temperature but increases pressure drops. Similarly, increasing cell density improves conversion efficiencies but again increases pressure drops. An increased cell density will shorten light-off times for metallic substrates, however with ceramic substrates the picture is unclear. The influence of cordierite densities on light-off is also uncertain. Some evidence suggests that lower densities quicken light-off, other evidence suggests that it has no influence. A similar story is found with split bricks. The improvements achieved in washcoat and noble metal formulations have benefited all aspects of catalyst performance and further improvements can be anticipated. Greater control over air-fuel ratio oscillations, resulting from developments in engine management systems, will also enhance catalyst performance.

One of the problems facing catalyst designers is that improving one performance criterion may impair another. Thus compromises have to be reached. To reach a compromise a quantitative assessment of the trends in behaviour is required. Attempts have been made to derive relationships that quantify the effect of substrate design, however, these relationships are of limited value unless some account is made of the influence different catalyst housing designs have on flow distributions, as well as the feedback effects changes in substrate design have. A way around this problem would

be to use a mathematical model that could simulate the interrelation between velocity profiles, catalyst housing design and substrate design. It would also be advantageous if such a model could be used to predict the effect changes in these parameters have on light-off, post-light-off conversion efficiencies and pressure drop. Finally, additional benefits would be available if the model could incorporate improvements in washcoat and noble metal formulations.

3 MATHEMATICAL MODELLING

Even before the widespread introduction of catalysts the benefits of being able to mathematically model them had been recognised. Although the fundamental transport and conservation equations governing catalyst behaviour are straightforward to derive, a number of different simplifications can be made to facilitate ease of solution. These simplifications have lead to a small group of slightly different modelling approaches. Increasing the degree of simplification reduces the amount of computational effort needed to solve the equations. Balanced against this must be the loss of model generality and accuracy of predictions.

3.1 One-Dimensional Thin Film Single Channel Models

The earliest computational model that simulated the main catalyst phenomena, developed by Kuo et al. (1971) [43], was a one-dimensional model applied to a packed bed type catalyst, however, the authors did point out that the method could be applied to a monolith type catalyst. In 1973 Hawthorn [44] developed a one-dimensional monolith single channel model, the assumption being made that each channel could be treated as an adiabatic system. Nusselt (Nu) and Sherwood (Sh) number correlations were used to calculate the heat and mass transfer between the exhaust gas and the substrate. It was also assumed that the chemical reactions take place on the washcoat surface, within a thin film, a simplification to the fundamental governing equations that combines the interaction of mass diffusion, heat transfer and reactions within the washcoat into an apparent reaction rate term. The apparent reaction rate ($\bar{r}$), or mean intrinsic reaction rate, is given by the integral of the intrinsic reaction rate (see Section 3.5) through the washcoat, divided by the washcoat thickness (Λ).

$$\bar{r} = \frac{\int_L r(C_s, T_s)dx}{\Lambda} \qquad 3.1$$

Note that the intrinsic reaction rate is a function of species concentrations (C_s) and washcoat temperature (T_s).

It is often assumed that the species concentrations and temperature through the washcoat are uniform, which allows the intrinsic surface reaction rate to be taken as the apparent reaction rate. Schweich and Leclerc [45] showed that this assumption is not always valid. They indicated that the temperature distribution through the washcoat can be taken as constant. However, if the reaction rates are fast and the diffusional resistance of the washcoat is high, the distribution of the species concentration through the washcoat will not be uniform. Under these conditions an effectiveness factor can be used to obtain the apparent reaction rate. The effectiveness factor (η_s) is defined as the ratio between the mean intrinsic reaction rate and the intrinsic surface reaction rate.

$$\eta_s = \bar{r}/r(C_{s0}, T_{s0}) \qquad 3.2$$

(C_{s0} and T_{s0} are the species concentrations and temperature at the washcoat surface.) Unfortunately the effectiveness factor is itself a function of surface species concentrations and temperature.

Other one-dimensional models have been developed, variations between them arising from the use of different Nu and Sh relationships, different chemical kinetics rate expressions and minor differences over the simplifications made to the governing equations. One of the commonest simplifications made to the governing equations is to ignore the effect of radiative heat transfer along a channel. Oh and Cavendish [46] and Fueyo [47] both used transient one-dimensional models that do not include the effect of radiative heat transfer to model catalyst light-off. One-dimensional models that include the effect of radiative heat transfer were proposed by Lee and Aris [48], who analysed catalyst steady state behaviour, and Psyllos and Philippopoulos [49], who analysed catalyst transient behaviour. Both concluded that the inclusion of radiative heat transfer tended to flatten out axial temperature gradients, by increasing heat transfer from hot regions to cool regions, there by making a significant difference to their results. To avoid the computational effort required to model radiative heat transfer in full, Lee and Aris [48] suggested that its effects could be represented with a radiative conductivity term.

The above models assumed that the flow within a channel is steady, however, the pulsed nature of engine exhaust flow means that in reality the flow is unsteady. Baruah et al. [50] developed a one-dimensional model of the unsteady flow through a four cylinder engine and its exhaust system, which included a catalyst. The catalyst was modelled using the same Nu and Sh relationships that Hawthorn [44] used, and a simple Arrhenius equation for the reaction scheme. In essence the model imposed fluctuating temperature and velocity fields on a one-dimensional catalyst model. The predicted species concentrations entering the catalyst varied little with time compared with the gas temperature. Very good agreement was found with experimental data.

3.2 Multi-Dimensional Single Channel Models

During the mid-1970's a number of authors developed multi-dimensional single channel models that calculate the conjugate heat and mass transfer between the gas and substrate. As a result they do not require heat and mass transfer coefficient relationships. These models, however, still used the thin reacting film assumption. Such models were proposed by Sinha et al. [51], Heck et al. [52] and Young and Finlayson [53]. Heck et al. [52] and Young and Finlayson [53] both compared the results from one-dimensional and multi-dimensional single channel thin film models. Both noted

differences between local Nu and Sh values derived from the multi-dimensional models compared with typical values used for the one-dimensional models. In particular both found that at the channel reaction front the multi-dimensional models predicted spikes in the Nu and Sh distributions. Noting that, again, there were slight differences between the respective models, Heck et al. [52] concluded that the errors introduced into their one-dimensional model by using predetermined Nu and Sh relationships were acceptable, particularly when compared to other uncertainties within the model. Young and Finlayson's [53] results also indicated that, providing an erroneous steady state solution is avoided, the differences in predictions between the two approaches are relatively small.

Multiple steady states are known to exist in catalysts. It can be shown, Schweich and Leclerc [45], that they arise from the specific form of the reaction rate expressions and the mass transfer behaviour of the washcoat. The phenomenon was experimentally observed in an isothermal reactor by Hegedus et al. [54], who also showed that increases in the diffusional resistance of the washcoat, through poisoning and pore plugging, makes its occurrence more likely. It is very unlikely to occur if the diffusional resistance of the washcoat is low, which is the case if the effectiveness factor used with the thin film assumption is one, a procedure that is usually adopted. Unfortunately the use of fixed Nu's and Sh's reduces the governing equations to a form where multiple steady states can mathematically arise when the properties of the washcoat preclude the possibility. However, even when the equations are in this form, transient simulations starting from cold generally give predictions that correspond to the true steady state solution, problems only arising when models simulate the cooling down of a warm catalyst.

To overcome some of the problems associated with using apparent reaction rates, Oh et al. [55], for a single pellet, and Zygourakis and Aris [56], for a monolith channel, developed models that simulated the diffusion of species through the washcoat. Oh et al. [55] were primarily concerned with the effect the depth of Pt impregnation had on poison-resistance and rapid light-off. Zygourakis and Aris [56] studied the effect that temperature and species concentrations have on effectiveness factors.

Ryan et al. [57] developed an axisymmetric single channel model that included the transfer of heat and species concentrations through both the washcoat and the gas phase. The effect of radiative heat transfer was also included. A comparison was made between the results from the two-dimensional model and a one-dimensional thin film model that used constant Nu and Sh values. They noted that for circular channels the one-dimensional model tended to predict slightly higher solid temperatures and faster light-off. Unfortunately no comment was made as to the reaction rates used for the one-dimensional model, thus it is unclear whether the differences, particularly with light-off, arose from the use of fixed Nu and Sh or from reaction rate assumptions.

3.3 Multi-Dimensional Monolith Models

Although single channel models can be used to study many catalyst phenomena, they are of limited use for comparing the performance of different catalyst assembly geometries. As has been discussed, the velocity fields that exist in catalyst assemblies are three-dimensional in nature, the degree of flow non-uniformity having a significant effect on catalyst performance. On their own, single channel models imply a uniform velocity profile, and are thus unable to predict changes in catalyst performance caused by changes in flow distribution. Because the velocity profile is a function of the catalyst assembly geometry, it follows that single channel models cannot quantify the effect of changes in geometry. To overcome this weakness a three-dimensional representation of the whole monolith is required.

It is conceivable that a complete three-dimensional computational model of a monolith, with every channel represented in full, could be developed. However, Jasper et al. [58] showed that to adequately solve such a model would require a computational grid of the order of 10^7 cells. Present hardware capabilities make such a model prohibitive. Two alternative approaches have been proposed; the equivalent continuum approach and that of modelling a limited number of representative channels. An equivalent continuum method treats the monolith as a porous medium, calculating the average distribution of properties through the catalyst. To model heat and mass transfer Nu and Sh relationships are required, in a similar way to one-dimensional single channel models. It is also necessary to use the thin film assumption. The principle of the multiple channel approach is to model a limited number of representative channels, using a single channel model, situated in different parts of the velocity profile.

Flytzani-Stephanopoulos et al. [59] used an equivalent continuum method to model the transient heat conduction in a metallic monolith as it warmed up. Using the same Nu relationship that Heck et al. [52] used, predictions were within 10% of experimental data. Chen et al. [60] and Zygourakis [61] developed their own transient equivalent continuum models, that included reactions, for cylindrical ceramic monoliths. Zygourakis [60] used Nu and Sh relationships derived for developing laminar flow, whereas Chen et al. [60] used constant values. Neither group made comparisons with experimental data. Chen and Cole [62] extended Chen et al.'s [59] model to a metallic monolith and found reasonable agreement with experimental data. All these models assume that the flow distribution across the monolith remains constant with time, the inlet velocity profile being given as a boundary condition. As such they are unable to simulate the feedback effect the changes occurring in the monolith have on the flow distribution. As heat is absorbed by the solid and released by chemical reactions the temperature of the gas changes. This changes the pressure drop through the monolith, which affects the incoming velocity profile.

Will and Bennett [63] and Bella et al. [12] both developed steady state models of the multiple channel type. Both took their monolith inlet velocity profiles from separate CFD codes that predicted the velocity field upstream of the monolith. However, only Will and Bennett [63] provided a feedback loop to the velocity field via the pressure drop term in the momentum equations for the monolith. Bella et al. used the predicted velocity field as a fixed boundary condition for the single channel calculations. Note that both groups used one-dimensional single channel models, Will and Bennett [63] linking each channel by radial heat conduction, Bella et al. [12] assumed each channel to be adiabatic.

3.4 Isothermal Catalyst Assembly Models

Most of the catalyst models discussed above involve complex solution algorithms, and as such require a considerable amount of time and expertise in numerical techniques to develop. This, plus some remaining uncertainties in the fundamental physics, has meant that very few of them have been adopted as design tools. As has already been indicated, one area of mathematical modelling that is being increasingly used as a design tool by engineers is computational fluid dynamics, a situation that has been greatly helped by the development of commercially available software. Because it is known that the performance of catalysts is a function of the flow field in the whole catalyst assembly, designers have started using CFD to optimise the monolith inlet velocity profile under isothermal conditions. Examples include the work of Weltens et al. [64] and Baxendale [65].

Again, because of hardware limitations, modelling the detailed fluid flow in every monolith channel is at present impractical. As an alternative, most authors, including Will and Bennett [63], Bella et al. [12], Lai et al. [10], Weltens et al. [64] and Baxendale [65], have adopted the equivalent continuum approach to represent the gas flow through the monolith. Of these studies only Will and Bennett [63] and Weltens et al. [64] offered experimental validation of their results. Will and Bennett's [63] predicted peak monolith velocities were approximately 25% below their experimental values at high flow rates and approximately 14% too low at low flow rates. Weltens et al. [64] claimed very good agreement on monolith velocity profiles for a limited number of catalyst geometries. Unfortunately no comparison was offered between pressure drops. It is possible to obtain the correct velocity profile by reducing monolith resistances, but unfortunately the pressure drop across the system is then seriously in error. Both sets of results indicate that the modelling approach needs further development before it can be relied upon to give accurate predictions.

3.5 Chemical Kinetics Data

Before accurate predictions of catalyst behaviour can be achieved, mathematical expressions describing the rate of reaction of the emission species are required. The procedures for gaining such data are complex and need specialised expertise. This and other factors, such as commercial sensitivity, means that limited reaction rate data are generally available. What data have been published can be divided into three sets. One set consists of intrinsic reaction rates given as the rate per unit surface area of noble metal; Voltz et al. [66]. These are derived from simplified laboratory reactors and noble metal single crystal studies. The second and third sets consist of apparent reaction rates given, respectively, as the rate per unit reactor volume (Montreuil et al. [67]) and the rate per unit reactor surface area (Will and Bennett [63] and Boehman et al. [68]). The first of these sets are derived from actual monolith catalysts and are specific to the particular substrate geometry, washcoat and noble metal formulation being tested. The last set are derived from simplified catalyst structures, are specific to a given washcoat and noble metal formulation, but can be applied to different substrate geometries.

The weakness with the first set is that when applied to a full catalyst geometry allowance has to be made for noble metal loadings and dispersion, as well as washcoat properties. If a thin film approach is being used allowance also has to be made for variations in the effectiveness factor. The weakness with the other two sets is that the rates can only be relied upon for accurate predictions for that specific generic group of catalysts. As noble metal formulations and catalyst geometries develop the reaction rate data become obsolete.

Another complicating factor that can introduce significant errors when using catalyst reaction rates is that most of them have been derived under steady state conditions. By steady state conditions it is meant that not only is the flow rate and inlet temperature kept constant but the gas composition is held constant. There is evidence that under transient air-fuel ratio, thermal and flow rate conditions the chemical kinetics are different from those at steady state. As has been indicated in section 2.4 above, oscillations in the air-fuel ratio, which cause oscillations in the exhaust gas composition, reduces conversion efficiencies. Kaneko et al. [36] and Shulman et al. [37] both showed that predicting these reductions in conversion efficiency by applying steady state derived kinetics to oscillating conditions gives different answers to the experimental data.

3.6 Discussion

As has been seen, numerous attempts have been made at developing mathematical models of automotive catalytic converters. Although some predictive success has been achieved with computational modelling it has been suggested (Germidis et al. [4]) that existing models are still

insufficiently accurate for design purposes. The reason for this lack of accuracy arises from uncertainties in the relationships that govern the heat transfer, mass transfer, chemical kinetics and fluid dynamics that occur in catalysts

All the above models, except Baruah et al [50], have assumed that the exhaust gas flow is non-pulsating. Although no rigorous analysis has been carried out, it is likely that the presence of pulsations has a significant affect on catalyst transient and steady state behaviour, particularly with catalysts situated close to the engine exhaust manifold. Again, because of hardware limitations, at present the time required to model three-dimensional pulsating flow during transient operation of catalysts is of the order of weeks rather than days or hours. For this reason most authors have simplified the velocity field to be that of steady flow. A further simplification common to most models is the neglecting of the effect of radiative heat transfer along a monolith channel, the exceptions including those by Lee and Aris [48], Psyllos and Philippopoulos [49], Sinha et al. [51] and Ryan et al. [57].

Another criticism that could be levelled at existing models is that they are not generally available and cannot predict the full range of catalyst behaviour. Specifically, as yet no transient, three-dimensional model has been developed that can predict the effects that the fluid dynamics entering the monolith have on the emissions conversion process, in addition to the simultaneous feedback effect the conversion process has on the fluid dynamics. The development of such a model would be an aid to the process of achieving a better understanding of catalyst heat transfer, mass transfer, chemical kinetics and fluid dynamics, and ultimately it could be used as a design tool. Also, if such a model is to become more accessible, and attractive, to design engineers the predictive software needs to be widely available, flexible and easy to use. An obvious route to this objective would be to utilise the solution algorithms of a commercial CFD code to predict the thermodynamics and chemistry, as well as the fluid dynamics, that occur in catalysts. The development of such a fully integrated model is included in the following work.

4 ISOTHERMAL FLUID DYNAMICS MODEL

The first step in developing a fully integrated computational model of a catalyst is to develop a model of the complete flow field that exists in the monolith and associated assembly. These flow fields are very complex. In addition to the pulsed nature of the exhaust gas, turbulent regimes exist in the inlet and outlet cones, whilst laminar regimes exist in the capillary channels of the monolith. It is also possible that the mean flow field changes as the catalyst passes through light-off and experiences varying driving conditions. As already indicated (Section 3.3), although considerable advances have been made in hardware technology, to model all the flow phenomena in detail would still require computer resources beyond the scope of most organisations. Until such resources become available simplified mathematical models have to be employed.

4.1 Fundamental Equations

The fundamental relationships that govern the fluid dynamics within catalyst assemblies are the Navier-Stokes equations. Expressed in tensor notation they are,

Continuity

$$\frac{\partial \hat{\rho}}{\partial t}+\frac{\partial \hat{\rho}\hat{U}_i}{\partial x_i}=0 \qquad 4.1$$

Momentum

$$\frac{\partial \hat{\rho}\hat{U}_i}{\partial t}+\frac{\partial \hat{\rho}\hat{U}_j\hat{U}_i}{\partial x_j}=-\frac{\partial \hat{P}}{\partial x_i}+\frac{\partial}{\partial x_i}\left\{\mu\left(\frac{\partial \hat{U}_i}{\partial x_j}+\frac{\partial \hat{U}_j}{\partial x_i}\right)\right\}-\frac{2}{3}\frac{\partial}{\partial x_i}\left\{\mu\frac{\partial \hat{U}_j}{\partial x_j}\right\}+F_i \qquad 4.2$$

where ρ is the density, μ the dynamic viscosity, $\hat{U}_i$ the velocity components, x_i the co-ordinate directions, t time, P the pressure and F_i any body forces. Note that the "hat" symbol signifies an instantaneous value. The solution of such non-linear partial differential equations requires a numerical approach, several of which are available. Numerical solutions to the above equations have been obtained for low Reynolds number turbulent flows in simple geometries. However, the size of the smallest length and time scales of such flows means that considerable processing time, even on very large computers, is required. Therefore, at present it is impractical to undertake such direct simulations of complex turbulent flows. An alternative is to solve the Reynolds averaged Navier-Stokes equations (Hinze [69]):

Continuity

$$\frac{\partial \rho}{\partial t}+\frac{\partial}{\partial x_i}\left(\rho U_i+\overline{\tilde{\rho} u_i}\right)=0 \qquad 4.3$$

Momentum

$$\frac{\partial \rho U_i}{\partial t}+\frac{\partial \rho U_j U_i}{\partial x_j}=-\frac{\partial P}{\partial x_i}+\frac{\partial}{\partial x_i}\left\{\mu\left(\frac{\partial U_i}{\partial x_j}+\frac{\partial U_j}{\partial x_i}\right)\right\}-\frac{2}{3}\frac{\partial}{\partial x_i}\left\{\mu\frac{\partial U_j}{\partial x_j}\right\}+F_i$$
$$-\left(\frac{\partial}{\partial x_j}\overline{\rho u_i u_j}+\frac{\partial}{\partial t}\overline{\tilde{\rho} u_i}+\overline{\tilde{\rho} u_j}\frac{\partial U_i}{\partial x_j}+\frac{\partial}{\partial x_j}\overline{\tilde{\rho} u_i}U_j+\frac{\partial}{\partial x_j}\overline{\tilde{\rho} u_i u_j}\right) \qquad 4.4$$

Where

$$\hat{U}_i = U_i + u_i,\ \hat{P} = P + p,\ \hat{\rho} = \rho + \tilde{\rho}$$

Note that the upper case symbols are the mean values and the lower case symbols the fluctuations. It should be noted that the effect of fluctuations in the viscosity, resulting from fluctuations in the fluid temperature, have been neglected. The length and time scales of the mean quantities that appear in these equations are sufficiently large to make numerical solution practical. Unfortunately the appearance of the additional turbulence terms on the right hand side of Equation 4.4 means that there are now more unknowns than equations. The only way of forming a closed set of equations is to equate these terms to known or calculable quantities.

The next simplification that is commonly made when modelling catalyst flows is to assume that the flow field is steady [10,11,12,63,64,65]. The arguments against modelling pulsed flow are the extra computational effort and time required, and that sufficient information about how a catalyst assembly affects the flow distribution can be gained from studying their steady flow fields. Whether such a simplification is justified is debatable. It is possible that pulsations make the flow fields significantly different from those that exist under steady flow conditions. However, any debate over whether to simulate pulsations or not is irrelevant if it cannot be demonstrated that other modelling simplifications give satisfactory predictions for steady flow. A suitable way of demonstrating whether the modelling techniques work is to compare experimental results from simplified catalyst geometries under steady isothermal flow conditions against steady isothermal flow predictions.

Under steady isothermal flow conditions at low Mach numbers the fluid can be taken to be incompressible (ρ = constant). If the flow is incompressible Equations 4.3 and 4.4 reduce to:

Continuity

$$\frac{\partial U_i}{\partial x_i} = 0 \qquad 4.5$$

Momentum

$$\rho\frac{\partial U_i}{\partial t} + \rho U_j\frac{\partial U_i}{\partial x_j} = -\frac{\partial P}{\partial x_i} + \frac{\partial}{\partial x_j}\left(\mu\frac{\partial U_i}{\partial x_j} - \rho\overline{u_i u_j}\right) + F_i \qquad 4.6$$

As has been stated, it is impractical to model the full details of the flow through every monolith channel. If an equivalent continuum approach is to be used the equations governing the behaviour of the flow through the porous media must be known. The hydraulic diameter of a monolith channel is typically of the order of 1 mm. The catalyst inlet pipe Re can range from between 3 000 to 100 000. The corresponding channel Re for a typical catalyst geometry will then be between 10 and 1000. These values indicate that the channel flow is essentially laminar, however it should be recognised that additional flow phenomena will also be present. These include entrance effects, such as the sudden contraction and change in direction of the flow (which both cause locally separated flow), decay of turbulence and boundary layer development. Exit effects will also exist, being caused by the sudden expansion of the flow. If these effects are significant they should be included in the equivalent continuum governing equations.

An approach used by several authors [12,63,64,65] is to neglect entrance and exit effects so that the flow can be taken to behave as fully developed laminar flow. The pressure gradient expression for such flow, which also represents the governing equation for momentum, is given by the Hagen-Poiseuille equation,

$$\frac{\partial P}{\partial x} = -\frac{k_r \mu U}{d^2} \qquad 4.7$$

where k_r is a constant that is a function of the channel cross-sectional shape, x is the flow direction, U is the channel mean velocity and d the hydraulic diameter of the channels.

Entrance and exit effects will tend to cause larger pressure gradients than those produced by fully developed laminar flow. The justification for neglecting these effects is based on the assumption that they contribute little to the overall channel pressure drop. This is only true if they exist over short distances and if the monolith is relatively long. Kim et al. [11] and Lai et al. [10] both attempted to include the effect of boundary layer development by introducing a coefficient, D_l, into the Hagen-Poiseuille equation that augments the overall pressure drop;

$$\Delta P = -\frac{D_l k_r \mu U L}{d^2} \qquad 4.8$$

where L is the overall channel length and D_l, which was taken from Wendland and Matthes [7], is given by,

$$D_l = \left[1 + 0.0445 \frac{\rho U d^2}{\mu L}\right]^{0.5} \qquad 4.9$$

An assessment of the relative magnitude of the pressure losses caused by the sudden contraction and expansion of the flow as it enters and leaves the monolith was carried out by Wendland et al. [8]. The relationships used to estimate these losses, taken from Benedict et al. [70], are,

Contraction Losses

$$\Delta P = \left\{(0.975 C_c)^{-2} - \frac{2}{C_c} + 1\right\} \frac{\rho U^2}{2} \qquad 4.10$$

$$C_c = 0.6137 + 0.1332\alpha - 0.2609\alpha^2 + 0.51146\alpha^3$$

Expansion Losses

$$\Delta P = (1-\alpha)^2 \frac{\rho U^2}{2} \qquad 4.11$$

where α is the ratio of free volume to total volume within the monolith. Unfortunately the relationship used for the expansion losses is only applicable when the Re is greater than 4 000. However, in the absence of a more appropriate expression Equation 4.11 will be used. Taking values of α = 0.65, d = 1 mm and a channel Re = 1000 (the worst case) it can be shown that for a 4 inch monolith the approximate contraction and expansion losses, compared to losses from purely fully developed laminar flow, are 4.0% and 2.1% respectively. The corresponding figures for a 6 inch monolith are 2.7% and 1.4% respectively. These relative losses are proportional to the Re, the contraction loss for the 4 inch monolith diminishing to 1% at a Re = 250.

It should be noted that in conventional monoliths the channel walls prevent any radial or circumferential transfer of momentum, producing unidirectional flow in the axial direction. This condition has to be included within the model.

4.2 Turbulence Models

As has been stated above, Reynolds averaging introduces additional terms into the Navier-Stokes equations. The evaluation of these terms, so as to create a closed set of equations, requires a mathematical model that must be based on theoretical considerations and empirical relationships. The resulting turbulence models are by there nature simplifications of the full mathematical representation of the flow problem. The additional terms that appear in Equation 4.6 $\left(\rho\overline{u_i u_j}\right)$ are known as Reynolds stresses. There are essentially two approaches that can be used for calculating the Reynolds stresses; either solve some form of stress transport equation or assume that the stresses act like ordinary viscous stresses, making them proportional to mean velocity gradients.

4.2.1 Eddy Viscosity Methods

The assumption that the Reynolds stresses behave in a similar way to ordinary viscous stresses leads to the adoption of a turbulent (or eddy) viscosity, μ_t, where,

$$\overline{u_i u_j} = \frac{2}{3}k\delta_{ij} - \frac{\mu_t}{\rho}\left(\frac{\partial U_i}{\partial x_j} + \frac{\partial U_j}{\partial x_i}\right) \qquad 4.12$$

k being the turbulent kinetic energy. Under these assumptions μ_t effectively acts to augment the molecular viscosity. Variations in the turbulence models that use this approach arise form the different ways in which μ_t is arrived at. They are collectively called eddy viscosity models. The simplest such models equate μ_t to a characteristic turbulence length scale, l, (also known as the mixing length) and a turbulence velocity scale, v;

$$\mu_t = \rho v l \qquad 4.13$$

A well known example is the Prandtl mixing length model. They are commonly referred to as zero-equation models and rely heavily on application specific empirical data. Thus they lack generality. Slightly more sophisticated eddy viscosity models solve the transport equation of a turbulence quantity, which is then used to calculate either the turbulence length or velocity scale. Most of these models, collectively known as one-equation models, solve the transport equation of k, the square root of k being assumed proportional to the turbulence velocity scale. Although more general than zero-equation models they still rely heavily on empirical relationships for the length scale.

The most complex eddy viscosity models developed to date solve the transport equations of two turbulence quantities, the most popular being k and its dissipation rate, ε. Instead of using these quantities to calculate length and velocity scales, μ_t can be obtained directly from,

$$\mu_t \propto \rho \frac{k^2}{\varepsilon} \qquad 4.14$$

The exact transport equations for k and ε can be derived from the Navier-Stokes equations, however certain terms within them contain quantities that are neither known nor calculable. Consequently these terms have to be approximated using calculable variables and empirical constants to form a closed set of equations. A number of variations to these approximate expressions have been proposed. The most commonly used variation is the one proposed by Harlow and Nakayama [71], accordingly referred to as the "standard" k-ε model. A more recent set of k and ε equations have been derived using renormalisation group theory (Yakhot and Orszag [72]), the so called RNG k-ε model. The mathematical representations of both the standard and RNG k-ε models are included as Appendix A. The inclusion of a second transport equation increases the generality of these two-equation models, however some of the assumptions used in their formulation mean that they are still incapable of representing certain features of turbulence. As a result when applied to some flow situations they can give inaccurate predictions.

4.2.2 Stress Transport Models

In common with k and ε, differential transport equations for Reynolds stresses can be derived from the Navier-Stokes equations. These equations also contain terms with unknown and uncalculated quantities which have to be equated to calculable variables and empirical constants. Despite the empirical content of these differential stress models (DSM's) they are able to represent many of the detailed features of turbulence that eddy viscosity models fail to characterise. As a result they tend to give more reliable predictions for complicated flows. Unfortunately the added complexity of these models makes extracting solutions from them computationally expensive. For three-dimensional simulations seven turbulence quantity transport equations have to be solved. An alternative approach that attempts to overcome this weakness, without sacrificing too much predictive performance, involves simplifying the stress transport equations by replacing the diffusion and convection terms with algebraic expressions. The resulting algebraic stress models (ASM's) tend, however, to produce stiff equation sets that can be less amenable to solution than those from DSM's. Also, as yet, no generally applicable model has been developed.

4.2.3 Near Wall Effects

Many of the assumptions used to derive the turbulence models mensioned above are based on the premise that the flow is fully turbulent. Thus it is inappropriate to use them to model low Re flows such as those occurring near walls. To overcome these problems special treatments have been adopted which provide a means of modelling the near wall regions. One of the simplest, and hence commonest approaches is to describe the behaviour of the flow from the wall to the fully turbulent region using an algebraic expression, or wall function. For a large number of cases it has been found that the behaviour of turbulent flow adjacent to walls can be characterised by the same relationship, known as the law of the wall (Launder and Spalding [73]). Although attractive, these wall functions usually only apply when local equilibrium (production and dissipation of turbulence are equal) exists all the way to the wall, a condition that is departed from when the flow separates or experiences adverse pressure gradients.

Alternative treatments have relied upon extensions to existing high Re turbulence models to allow them to properly predict near wall effects. For example, several authors (see Wilcox [74]) have introduced damping factors into the μ_t expression (Equation 4.14) and ε equation of the standard k-ε model in an attempt to mimic the suppression of turbulence, by viscous effects, in the near wall region. Such models have become known as "low Reynolds number" k-ε models. Another way of approaching the problem is to use a modified low order turbulence model to describe the low Re region and a higher order, usually two-equation, model in the fully turbulent region. The benefit of using a zero- or one-equation model near the wall is their relative computational simplicity, which can be important where gradients are steep. In addition their high empirical content can produce more reliable predictions in areas where a specific type of wall effect is known to exist (e.g. adverse pressure gradients and separation). The difficulty with these "two-layer" approaches lies in the coupling of the two models.

The need for special wall procedures within stress transport models is no less important. A variety of effects have to be included that do not occur in fully turbulent flow. For example, the individual normal stresses experience different influences, those normal to the wall being strongly damped, while those in the streamwise direction become enhanced. Dissipation of turbulence also becomes increasingly anisotropic towards the wall. Several attempts have been made at modifying the high Re versions of the stress transport equations to take account of the near wall effects, however there is still considerable uncertainty over the appropriate formulations [75].

4.2.4 Effect of Compressibility

Comparison of Equations 4.4 and 4.6 shows that for compressible flow there are four additional turbulence terms, involving fluctuations in the density, that are absent when the density is constant. Developing a mathematical model for each additional term in the equations for compressible flow represents a particularly challenging task. An approach that can be adopted which simplifies this task is to introduce density-weighted mean velocities into the Navier-Stokes equations, known as Favre averaging (Hinze [69]). This process produces a single turbulence term that is similar to the Reynolds stresses in the equations for incompressible flow. Although Favre averaging reduces the number of turbulence terms in the momentum equations, it is still necessary to modify the turbulence models for incompressible flow to account for compressibility effects.

Fortunately, however, it can be demonstrated [69] that the ratio of the density fluctuation to the mean density is proportional to the square of the turbulence Mach number (defined as the ratio of the fluctuating velocity to the speed of sound). This ratio only becomes significantly large during very high speed flows and turbulent combustion, neither of which are encountered within the present work.

4.3 Solving the Equations

The basic aim behind most strategies for solving partial differential equations is to obtain algebraic expressions that give the value of the dependent variables at a finite number of locations within the solution domain. The differences between such discretized forms of the partial differential equations lies in the way they are obtained. The two most commonly used approaches for discretizing the Navier-Stokes equations are the finite volume and finite element methods. Whichever approach is used to generate the discretized equations, their form dictates that an iterative numerical method is required to extract the desired dependent variable values. The only practical way of carrying out these numerical iterations is with a computer. As has been indicated in Section 1.1, to develop a computer code capable of performing both the derivation of the algebraic expressions and the numerical iterations requires considerable development time, and not a little expertise in numerical techniques. For these reasons a number of organisations have developed commercially available, general purpose codes that solve the Navier-Stokes equations. These commercial CFD codes are increasingly being used by industrial companies to carry out fluid flow simulations. Because of their cost, such companies have a desire to utilise these codes for solving as many flow problems as possible. For this reason, and to avoid spending time developing a specific catalyst code, it was decided that a commercial CFD code would be used to model catalyst flow fields.

Most of the original commercial CFD codes were based on the finite volume approach, however an increasing number based on the finite element approach have become available. A review of the pros and cons of either approach is included in a book by Shaw [76]. The two codes used for the work presented here are both based on the finite volume method. The reasons for choosing them came from the fact that Jaguar Cars had an existing licence for STAR-CD and Coventry University had an existing licence for PHOENICS. An introduction to the basic principles of the finite volume method can be found in a book by Patankar [77]. An outline of the methods salient points are discussed in Appendix B. A full description of the structure, and use, of PHOENICS and STAR-CD can be found in their respective documentation [78,79].

A feature of most commercial CFD codes is the provision of a variety of "built-in" modelling and solution options. These can include choices of convection term differencing scheme, turbulence models, boundary conditions and algebraic equation solvers. The availability of such choices can be seen as a strength, because the user is liberated from the task of having to code a particular option into the program themselves. Conversely, it can lead to a weakness, particularly if the "built-in" options are limited and there is no provision made for the user to include new or novel modelling approaches. Both PHOENICS and STAR-CD have extensive modelling options available as standard, and both provide facilities for users to include their own modelling approaches. However, of the two PHOENICS provides far greater flexibility for including additional modelling, and solution, approaches. Discussion of the available options will be limited to those used in the present work.

4.3.1 PHOENICS

The PHOENICS software package consists on a number of distinct elements; a pre-processor (SATELLITE), a main processor (EARTH), two post-processors (PHOTON and AUTOPLOT) and some auxiliary programs. They are all separate programs that are run independently. The fundamental solution algorithms that PHOENICS uses are all included within EARTH. The solution strategy is based on a structured staggered grid with a variant of the SIMPLE scheme, known as SIMPLEST, as the velocity-pressure coupling algorithm.

The purpose of SATELLITE is to interpret instructions given to it by the user that specify the problem to be solved. Having interpreted the instructions it then generates a data file (EARDAT) that contains the detailed information which EARTH needs to solve the problem. The SATELLITE instructions can be provided in four ways; interactively using either the package command language (PIL) or a menu system, a command file (Q1), written in PIL, or through FORTRAN coding.

To allow the user to implement their own modelling approaches access is provided to an EARTH subroutine, called GROUND, that shadows the main solution procedures. The user can interrupt these procedures at virtually any point and, by inserting their own coding, can get the program to perform whatever calculations may be needed. Access to almost every program variable is provided, and the user can even incorporate their own algebraic equation solver if desired.

4.3.2 STAR-CD

Like PHOENICS, STAR-CD has a pre- processor (PROSTAR) that is used to specify the flow problem, and a main processor (STAR) that sets up and solves the appropriate algebraic equations. PROSTAR also acts as a post-processor. Again, both elements of the package are run independently. The solution strategy of the package is based on an unstructured collocated variable mesh, consisting of hexahedral, tetrahedral, triangular prism and pyramid shaped cells. Three velocity-pressure coupling algorithms are available, SIMPLE, PISO and SIMPISO. PISO is normally only used for transient simulations.

PROSTAR is in essence run interactively, either by commands or by a menu system. So that a history of the problem specification can be obtained an echo file of the interactive commands is automatically generated. PROSTAR provides the main STAR processor with the boundary condition, solution procedure and geometric data that it requires to solve the problem.

There are a number of subroutines within STAR that are provided for the user to incorporating their own modelling approaches. These subroutines allow modifications to existing features, for example by the addition of source terms in transport equations or making material properties a function of time, space or temperature. Adjustments can also be made to boundary conditions, turbulence length scale calculations, initial conditions etcetera, etcetera. The main weakness of the facilities provided is that within each subroutine the number of program variables that can be accessed is limited.

4.4 Model Implementation

Although it has been established that PHOENICS and STAR-CD have the capabilities for solving the equations that govern the fluid dynamics within catalysts, implementation of the monolith equivalent continuum modelling approach requires special treatments to be carried out within the codes. With both codes there is more than one method of implementing the approach, however, detailed descriptions of the methods will be restricted to those actually used. The choice of method was based on ease of implementation and numerical stability.

4.4.1 Implementation Within PHOENICS

One of the aims of the equivalent continuum approach is to reproduce the unidirectional nature of the bulk flow within the monolith, the direction of the flow being parallel to the axial direction of the monolith channels. There are two ways of achieving this within PHOENICS. Whichever method is adopted a computational grid is required that consists of a series of parallel "computational channels" (see Figure 4.1), the directions of which are the same as the actual monolith channels (i.e. one of the grid directions should be aligned in the axial direction of the monolith channels). Preventing momentum transfer between adjacent computational channels means that flow can only travel along them. Differences in the two methods arises from the way the momentum transfer is suppressed.

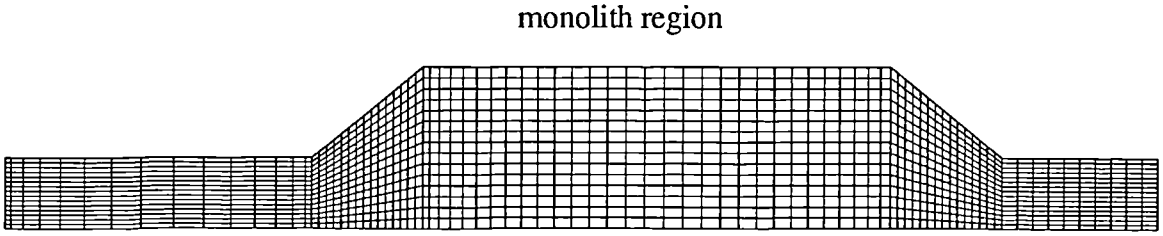

Figure 4.1 - computational grid of an axisymmetric catalyst assembly

The easiest way of preventing momentum transfer is to use the cell face porosity feature within PHOENICS. The equations in PHOENICS were set up so that wherever the cell face areas appear they are multiplied by a coefficient, their porosity. The feature allows access to these coefficients on a grid direction basis. They can be set to any non-negative value over a specified region of the grid. If the cell porosities are set to zero in the monolith radial and circumferential directions, transport of all variables by any means is prevented in those directions.

A second method suppresses transport of momentum by preventing convection and diffusion separately. To prevent convective transport the velocity components perpendicular to the desired flow direction are set to zero, which is achieved using a procedure that fixes variable values. To prevent transport by diffusion use is made of a facility that allows the diffusion terms of a particular transport equation, in a particular direction, to be multiplied by a constant. When the constant is equal to zero diffusion of that variable, in that direction, is cancelled. This second method is more involved than the first, because it requires the setting up of more features, however it has its uses because it selectively prevents transport of dependent variables perpendicular to the flow field, a facet that will be used when modelling heat transfer effects within catalysts. Finally, there is a third method that is essentially a variation on the second method. An alternative way of preventing

convective transport can be achieved by using a facility, similar to the one used for preventing diffusive transport, whereby a coefficient of the convective terms is set to zero.

When each computational channel is isolated from its neighbours, which is what prevention of all but axial momentum transfer achieves, the local flow field behaves as if the individual monolith channels have uniform velocity profiles. In addition there will be no friction at their walls. Such flow is ideal and will not produce a pressure drop. The user is thus free to impose any desired pressure drop by introducing momentum sinks into the momentum equations. A momentum sink is an additional source term and can be introduced using the standard source term facilities within PHOENICS. These are set up as linearised terms of the form,

$$S = TC(V - \phi_p) \qquad 4.15$$

where T is a coefficient that is a function of how the source term is introduced (referred to as the source type; examples include by per unit volume, by per unit area, etc.), ϕ_p is the value of the solved for variable at the point where the source is being applied and C and V are values specified by the user.

If the desired pressure drop is to be given by Equation 4.7, the obvious way of arranging the source term is to set,

$$C = \frac{k_r \mu}{d^2} \qquad 4.16$$

and,

$$V = 0 \qquad 4.17$$

with the appropriate source type being by per unit volume. Unfortunately μ is not directly accessible within PHOENICS and has to be obtained from the product of ρ and ν. In PHOENICS, when a source term is multiplied by ρ, particularly when ρ is not constant, it is more convenient to introduce the source term using a source type that automatically multiplies by ρ. Wherever possible this source type has been used. If more complex pressure drop expressions are to be incorporated into the monolith model, such as that given by Equation 4.8, use has to be made of the user coding facilities in the GROUND subroutine.

Although a method has been described by which unidirectional flow, with a prescribed pressure gradient, can be generated, a further feature of monolith flow fields has to be accounted for. The reduction in the monolith free volume, caused by the presence of the substrate, means that to satisfy continuity the velocities through the monolith have to be greater that those produced when

there is no reduction in free volume (i.e. when $\alpha = 1$). These increased velocities are the channel velocities that appear in Equation 4.7. There are two ways in which such velocities can be represented within PHOENICS. Either reduce the computational flow volume to correspond to the actual flow volume, or adjust Equation 4.7 so that the velocity that appears in it is that produced when $\alpha = 1$. The first method is achieved by setting the porosity of the cell faces perpendicular to the flow direction to α, the second by substituting,

$$U = \frac{U'}{\alpha} \qquad 4.18$$

into Equation 4.7, where U' is the channel velocity when $\alpha = 1$. Thus Equation 4.7 becomes,

$$\frac{\partial P}{\partial x} = -\frac{k_r \nu \rho U'}{\alpha d^2} \qquad 4.19$$

One remaining aspect of catalyst flow fields that should be considered is the effect the monolith has on turbulence levels. As has been stated, the flow in the monolith channels is predominantly laminar, with the suppression of turbulence probably taking place within the channels. Because an equivalent continuum approach is being used, any significant impact this suppression of turbulence has on the channel flow must be included in the monolith pressure drop expression. If the laminarisation process takes place upstream from the channel entrances, providing it occurs in close proximity to the entrances, its effects can still be entirely accounted for by the monolith pressure drop expression. Across the monolith front face the axial velocity component should be entirely positive, such that any reduced turbulence levels in this region will not be transported to the rest of the inlet diffuser. Thus there will be no need to represent the laminarisation phenomenon within any turbulence modelling approach. If no adjustment is made to the turbulence model it will predict the existence of turbulence within the monolith. Although spurious its presence will have negligible influence on the predicted channel fluid dynamics, which, as has been shown above, is dominated by the monolith pressure drop expression.

The other region of the flow domain where the monolith affects turbulence levels is immediately downstream of the monolith itself. As the fluid emerges from the rear face of the monolith it forms a series of jets separated by small wakes, each jet being associated with a single channel. Although the flow leaving the channels will be laminar, the interaction of the emerging jets will set up shear layers, which will lead to the generation of turbulence. The level of the turbulence will be a function of the Re and the shape and dimensions of the channels, and must be known if the behaviour of the flow in the catalyst outlet assembly is to be studied in detail. The appropriate

treatment within the computational model is to set the exit plane turbulence level as a boundary condition.

4.4.2 Implementation Within STAR-CD

STAR-CD has a built-in feature for modelling flow through porous media whereby the local momentum equations become,

$$\frac{\partial P}{\partial x} = -KU' \qquad 4.20$$

where x is one of the local co-ordinate directions, U' is the superficial velocity in the direction of x (essentially the same as U' in Equation 4.18) and K is the permeability in the direction of x. K is assumed to be a quasilinear function of the superficial velocity magnitude, given by,

$$K = \gamma U' + \beta \qquad 4.21$$

where γ and β are user specified coefficients that are by default constants. They can, however, be made functions of the velocity and fluid properties etcetera, by making use of the user coding facilities.

Suppression of momentum transfer perpendicular to the direction of the monolith channels can be achieved by setting both γ and β to large values in these directions. A suitable value, and the one used in the present work, is to set both coefficients to 1 000 000. Such a value effectively makes the flow resistance perpendicular to the monolith channels infinite. The flow is then forced to travel in the direction of the channels, giving it a unidirectional nature. If the desired pressure drop is to be given by Equation 4.7, the permeability in the direction of the flow should be set up such that,

$$\gamma = 0 \qquad 4.22$$

and

$$\beta = \frac{k_r \mu}{\alpha d^2} \qquad 4.23$$

Comments made in the previous section about the effect of turbulence suppression at the front of the monolith are just as applicable to STAR-CD as they are to PHOENICS.

5 ISOTHERMAL STEADY FLOW RIG

Although great advances have been made in the field of CFD over the last 20 years there are still many flow situations where predictions are known to be relatively unreliable. Amongst these are simulations involving turbulent flow in complex geometries, particularly those where severe streamline curvature, flow separation and adverse pressure gradients exist. As a result of these weaknesses experimental validation of predictions of flows exhibiting such phenomena is still necessary. The flow through most catalyst assemblies contains all of these phenomena. In addition there is a need to test the validity of the assumptions made within the simplified catalyst model described in Section 4.

To provide suitable experimental data an isothermal steady air flow rig was designed and built. The primary aim of the exercise was to produce a rig where the major flow phenomena known to exist in catalyst assemblies could be studied, yet the geometric detail could be kept as simple as possible. Geometric simplicity was required to avoid complicating the flow field with features of secondary importance, such as small scale local separations and flow asymmetry. Such features can result from welds, poorly matched joints, pipe curvature, etcetera. An added bonus is that the complexity of the computational grid would be limited. For these reasons an axisymmetric geometry was selected. A schematic diagram of the rig is included as Figure 5.1. The only part of the flow field that is directly relevant for validation purposes is that existing in the inlet pipe and the catalyst assembly. For convenience these parts of the rig are referred to as the working section. The remainder of the rig, for convenience referred to as the upstream section, was designed to provide a steady flow of air at a known flow rate.

5.1 Description of Working Section

One of the main design specifications for the working section was that boundary conditions would be known and could be set up within the mathematical model using standard CFD techniques. For this reason the roughness of the internal surfaces was kept as smooth as possible, so that hydraulically smooth boundary walls could be taken. To limit the disruption to flow caused by joints between component parts, the number of components in the working section were kept to a minimum. These consisted of the inlet pipe, the inlet expansion, the monolith and an outlet sleeve. Where possible the inlet expansion was machined as one piece. As a result, in most cases, the only joint that could influence the flow field was the one between the inlet pipe and the inlet expansion. To minimise the effect of this joint it was placed 30 mm upstream from the inlet expansion throat, and was made to be as smooth as possible by matching the internal diameter of both parts. All parts in the working section were held together by friction fits and sealed, where necessary, with Plasticine.

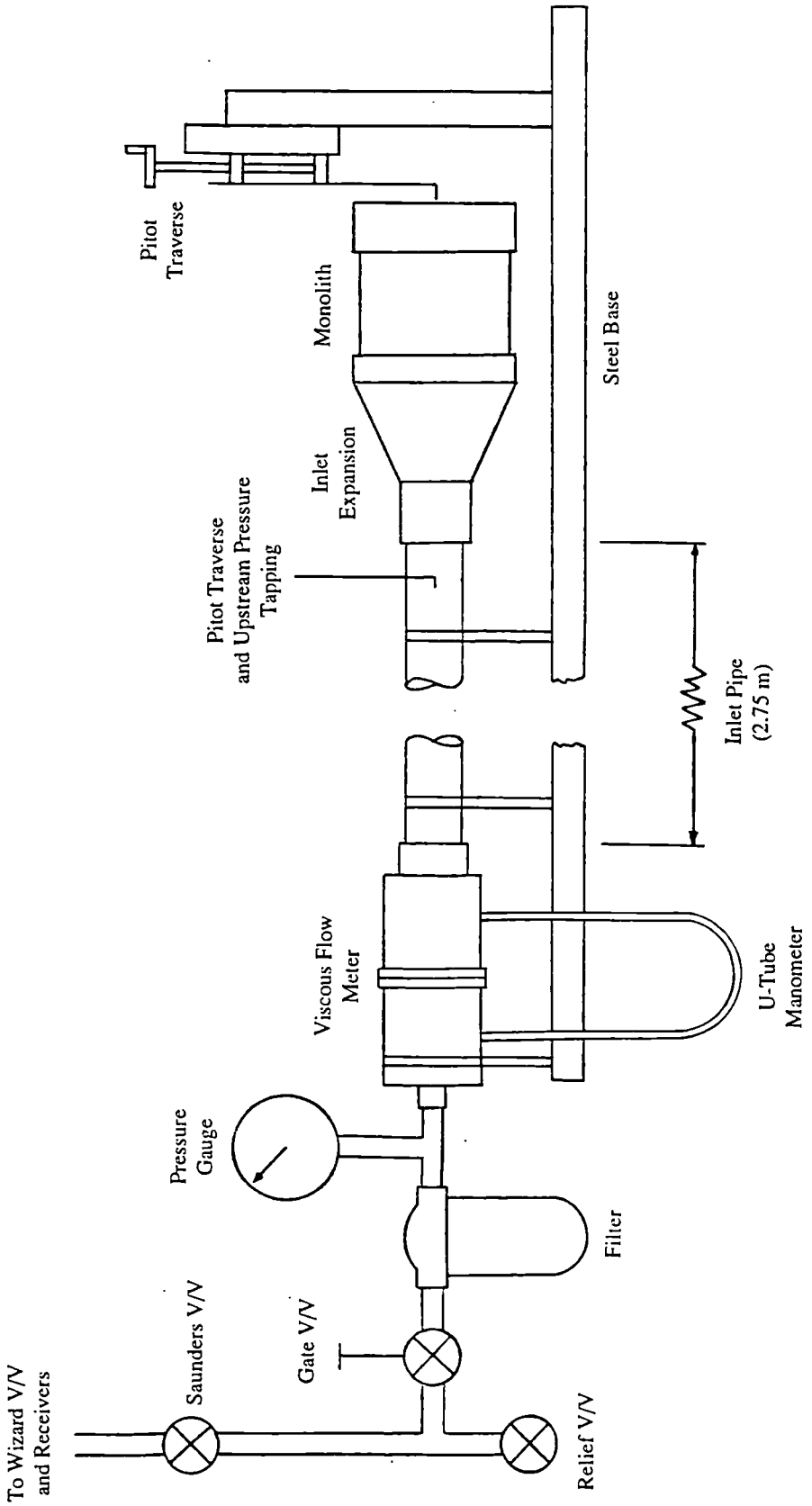

Figure 5.1 - Schematic of isothermal steady flow rig

It is generally accepted that the performance of conventional diffusers deteriorates as the boundary layer of the inlet velocity profile increases in thickness. Thus it is reasonable to assume that for axisymmetric flow conditions the worst case scenario for the monolith flow distribution would be a fully developed velocity profile at the exit of the inlet pipe. For this reason sufficient length of straight upstream pipe was provided (50 diameters) to produce a fully developed velocity profile. An additional consequence of using such an inlet pipe is that the inlet expansion inlet boundary conditions, which include turbulence levels, should be known and should be independent of the working section inlet conditions. A proprietary make of extruded PVC pipe was used for the inlet pipe. It had a designated size (diameter) of 2 inches, a typical exhaust pipe diameter. The actual internal diameter of the pipe varied circumferentially, being between 54.5 mm and 55.0 mm, indicating that it was slightly out of round. Consequently an exact match on diameters could not be achieved with the inlet expansion. As a compromise the internal diameter of the expansion was set at 55.0 mm.

The monoliths used in the project were all provided by Johnson Matthey plc. So that the influence of monolith length could be studied three monoliths, one 6 inches long, one 5 inches long and one 4 inches long, were selected for testing. With the exception of two tests, these three monoliths were used throughout the study. The cell density and diameter of these monoliths were nominally the same, being 400 cells per square inch (cpsi) and 4.66 inches respectively. Using a fixed monolith diameter means that the area ratio of the inlet expansion becomes fixed. Originally it was intended that washcoated monoliths would be used, however because of variations in, and uncertainty over, their channel dimensions and shape, unwashcoated monoliths were used. It cannot be guaranteed that the washcoat is distributed uniformly. Unwashcoated monoliths should have regular, square section channels, with controlled tolerances on their dimensions.

Table 5.1 - Dimensions of monoliths used on rig.

Monolith (Length)	Channel Breadth [mm]	Cell Density [cpsi]	Void Fraction [%]
4 inch	1.09	380	70.0
5 inch	1.10	387	72.5
6 inch	1.10	387	72.5

The manufacturers drawings specified that the breadth of unwashcoated monolith channels should have been 1.12 mm. With a cell density of 400 cpsi, and assuming the channels have a square cross-section, it can be shown that the monolith void fraction will be 77.8%. As a result of some discrepancies in the experimental results, the channel dimensions and cell densities of the monoliths in use were measured, the former using a projection micrometer. These measurements revealed that both the channel breadths and cell densities were less than the design specifications. Table 5.1

details the dimensions of the monoliths used and the resulting void fractions. Note that the breadth of the channels varied slightly across the monoliths, the figures quoted in Table 5.1 being averages.

The obvious, and most commonly used, design for the inlet expansion is a conical diffuser. So that the effect of different divergence angles could be studied, a selection of conical diffusers with total angles (twice the wall angles) of 80°, 60°, 40°, 30°, 20° and 10° were produced. For cost reasons and ease of manufacture all but one of these diffusers were machined from wood (Jelutong). After machining, their surfaces were sanded with fine grade paper, varnished and waxed to produce a smooth finish. A sectioned drawing of the 60° diffuser is included as Figure 5.2. The other diffusers are similar in design, the only differences being their length and wall angle.

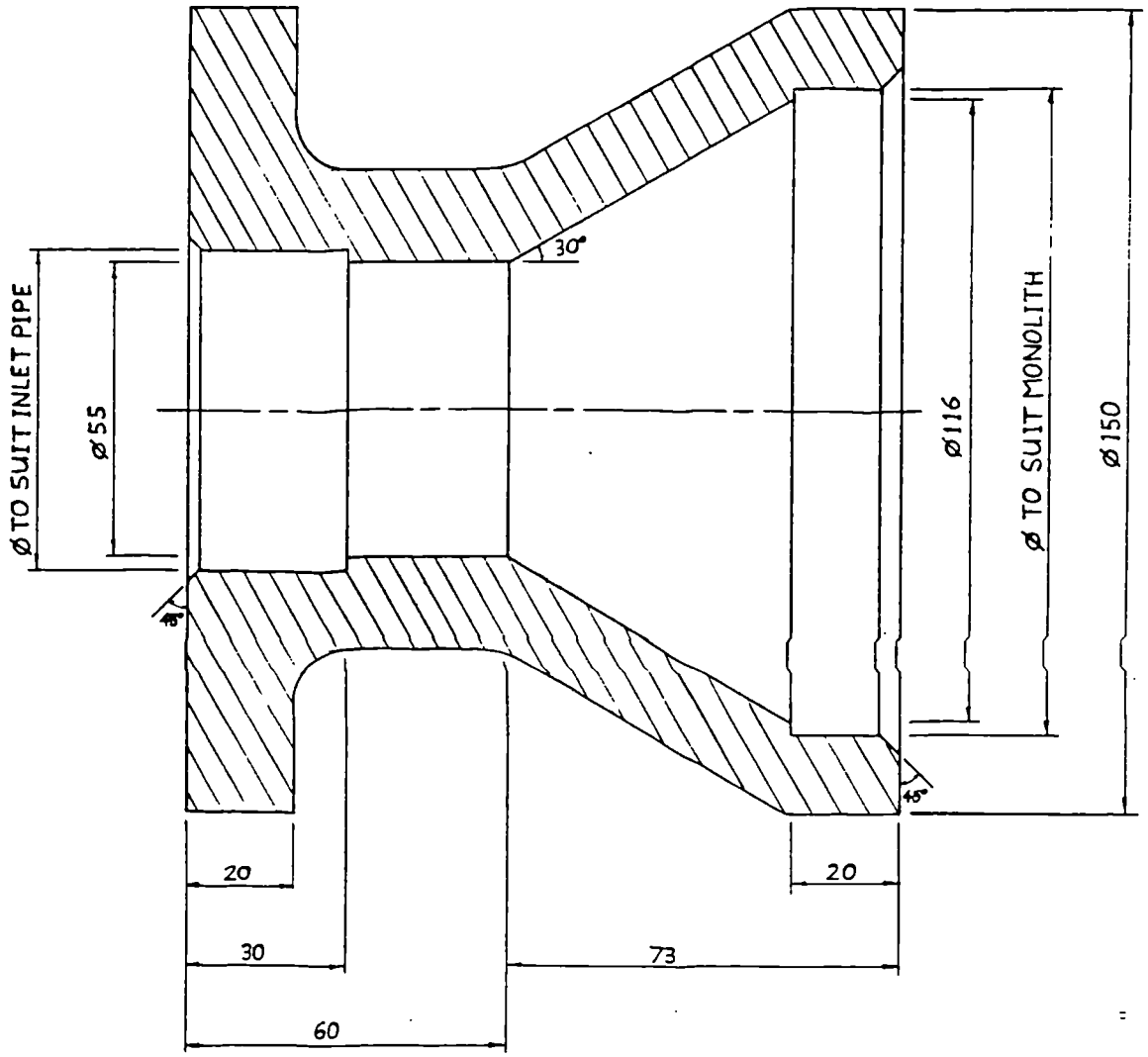

Figure 5.2 - Sectioned drawing of 60° diffuser (dimensions in mm)

In addition to the diffusers, three 180° expansions where made with lengths corresponding to the 80°, 40° and 20° diffusers. Although the rationale for including 180° expansions in the study was

primarily driven by modelling considerations (orthogonal grid and certainty over point of flow separation), their presence allows model performance to be tested for two significantly different types of inlet geometry. Again, to limit cost and make manufacture easier, these 180° expansions were made in sections. There were common inlet and outlet sections, with each expansion being formed by inserting different mid-sections. Sectioned drawings of these components are included as Figure 5.3. Although saving on wood, this approach meant that more joints were introduced that could disturb the flow. It was felt, however, that the flow fields in these expansions would be minimally affected by the presence of the extra joints.

Like the inlet pipe, the diameter of each monolith varies circumferentially. There is also a tendency for the outer most monolith channels to be distorted. To eliminate both problems the outlet diameter of the inlet expansions was set at 116 mm, which is slightly smaller than the actual monolith diameter. To allow the monoliths to be placed adjacent to this smaller diameter a sleeve, the same diameter as the monoliths, was machined into the inlet expansions (see Figures 5.2 and 5.3(b)). The monoliths could then be slid into the sleeve and held in position.

To make the measurement of monolith velocity profiles easier no outlet cone was attached to the catalyst assembly, which consequently exhausts, almost, directly to atmosphere. Although the presence of an outlet cone will influence the monolith flow distribution, Lemme and Givens [3] showed that the effects are small. They found that the absence of an outlet cone might reduce the peak monolith velocity by 4%. Thus it is reasonable to assume that the general characteristics of the flow field existing in the inlet cone are unaffected by the presence, or otherwise, of an outlet cone. An added advantage of this approach is that uncertainties over modelling flow in converging sections are avoided. Any discrepancies between predictions and experimental results will only be caused by the inlet geometry and monolith.

The jets that emerge from each monolith channel create a velocity profile across the exit plane of the monolith that consists of a series of peaks and troughs. 30 mm away from the monolith the jets have mixed to such an extent the velocity profile appears smooth. Thus it was decided to measure the monolith velocity profile 30 mm from its rear face, the assumption being made that the bulk distribution of flow will change little over this distance. It was also assumed that the direction of the flow would not change, remaining parallel to the monolith channels, i.e. entirely axial. To prevent entrainment of surrounding air by the jets emerging from the peripheral channels, giving rise to errors, a 30 mm long outlet sleeve was provided (see Figure 5.4). It should be noted that the internal diameter of the outlet sleeve was 116 mm, thus matching the outlet diameter of the inlet expansion.

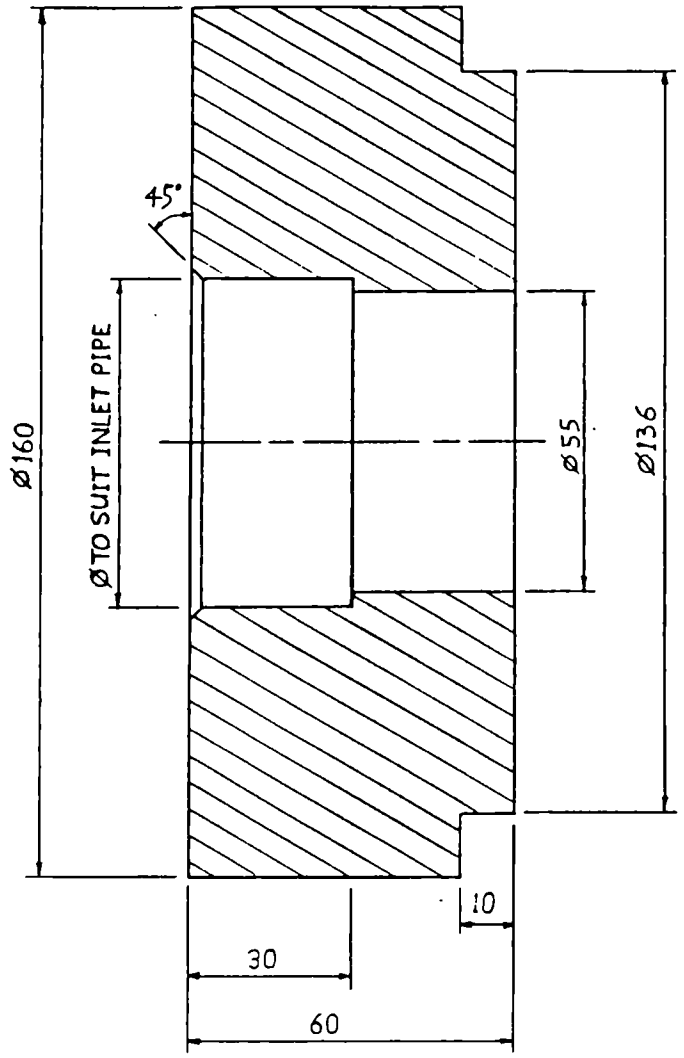

Figure 5.3(a) - Inlet section of 180° expansion

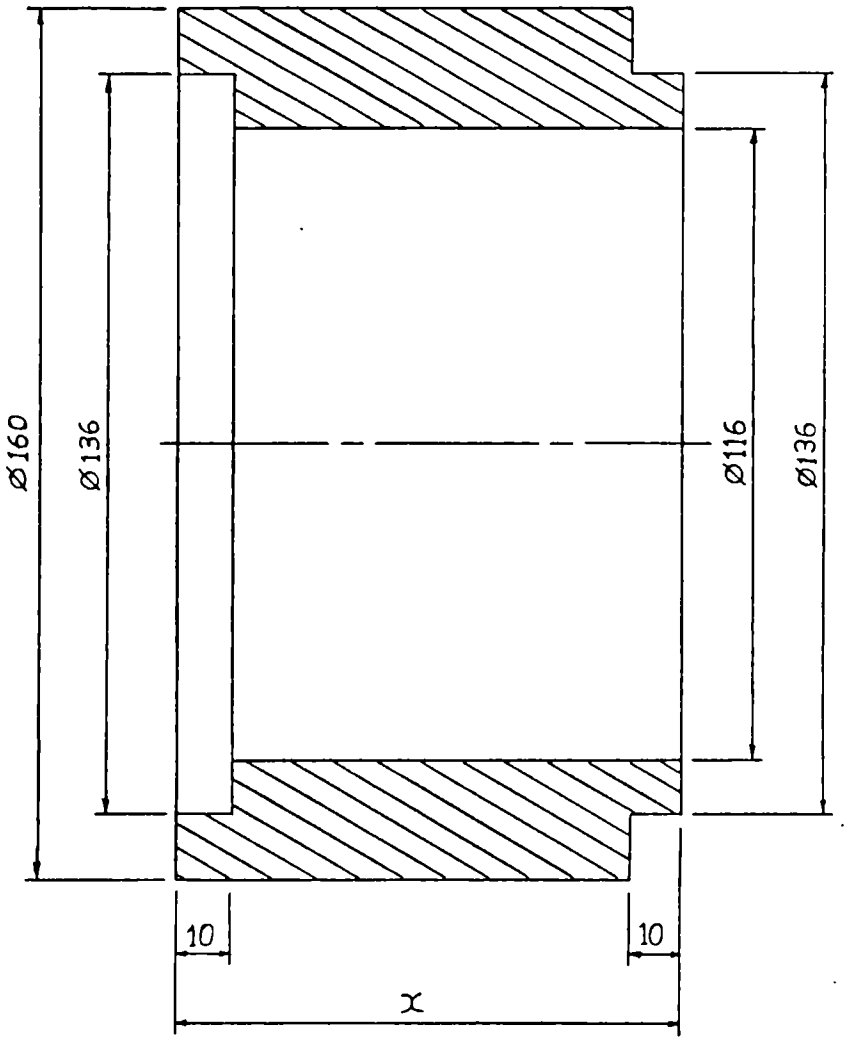

Figure 5.3(b) - Mid-section of 180° expansion

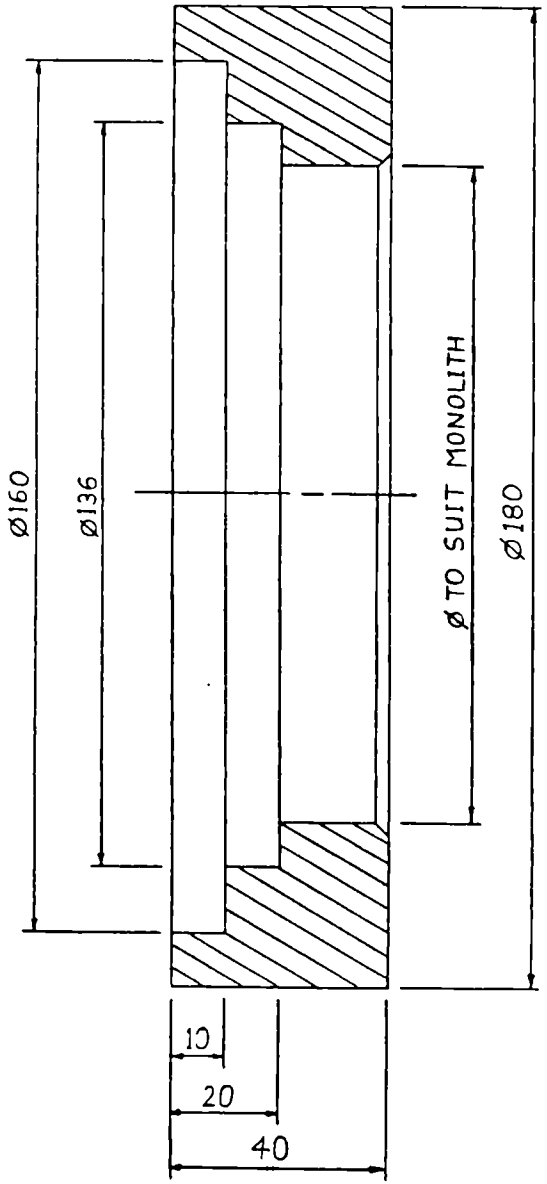

Figure 5.3(c) - Outlet section of 180° expansion

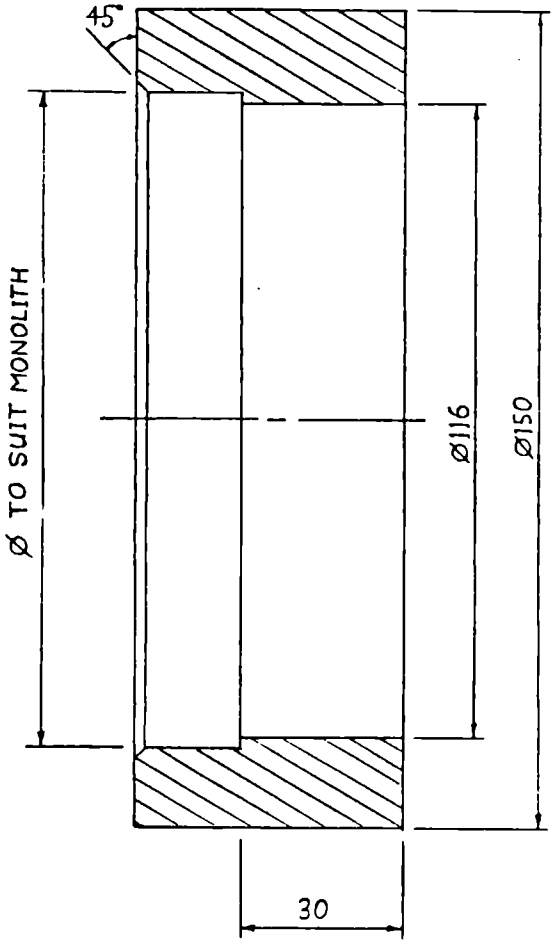

Figure 5.4 - Monolith outlet sleeve

The whole working section was rigidly clamped to a steel base, made from 1.5 inch box section, running the full length of the rig. A summary of the relevant working section dimensions is included in Table 5.2. Plates 5.1(a) and 5.1(b) show the outlet end of the working section.

Table 5.2 - Nominal dimensions of working section components

Component	Dimension	Nominal Size
Inlet Pipe	Length I/D	2.75 m 55 mm
Inlet Expansion	Inlet I/D Outlet I/D Area Ratio	55 mm 116 mm 4.448
Monolith	"Wetted" Diameter	116 mm
Outlet Sleeve	I/D Length	116 mm 30 mm

Conical Diffusers	
Total Angle	Nominal Length
80°	37 mm
60°	53 mm
40°	84 mm
30°	114 mm
20°	173 mm
10°	349 mm

180° Expansions Nominal Length
37 mm
84 mm
173 mm

5.2 Description of Upstream Section

The rig air supply was taken from an existing compressed air system. The system is fed from two large receiver tanks that are rated up to pressures of 30 bar. The particular limb of the system to which the rig was attached has a "Wizard" control valve between it and the receiver tanks, the purpose of which is to provide a constant downstream pressure from varying upstream pressures. However, a combination of age and design means that for the low pressures and high flow rates required by the rig, the valve does not quite give constant downstream pressures. Despite this, the resulting rate of change of pressure is small enough to allow periodic adjustment to the

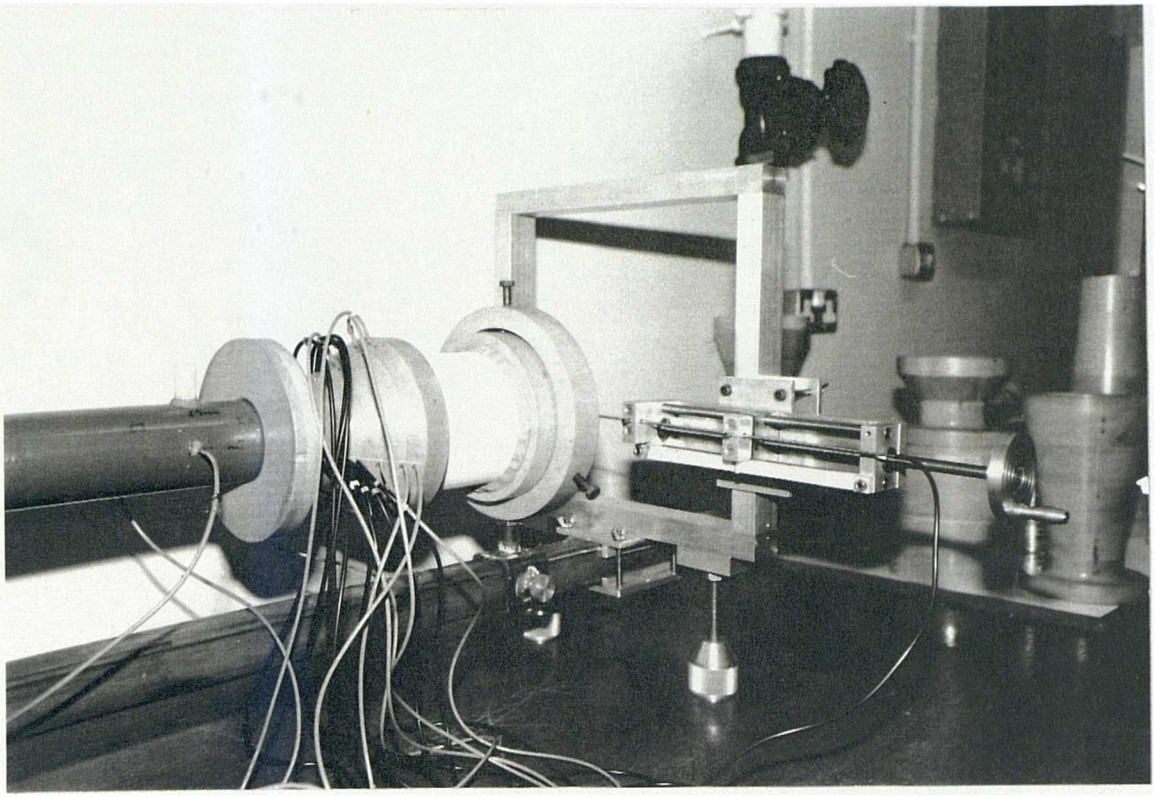

Plate 5.1 (a) - General arrangement of outlet end of working section

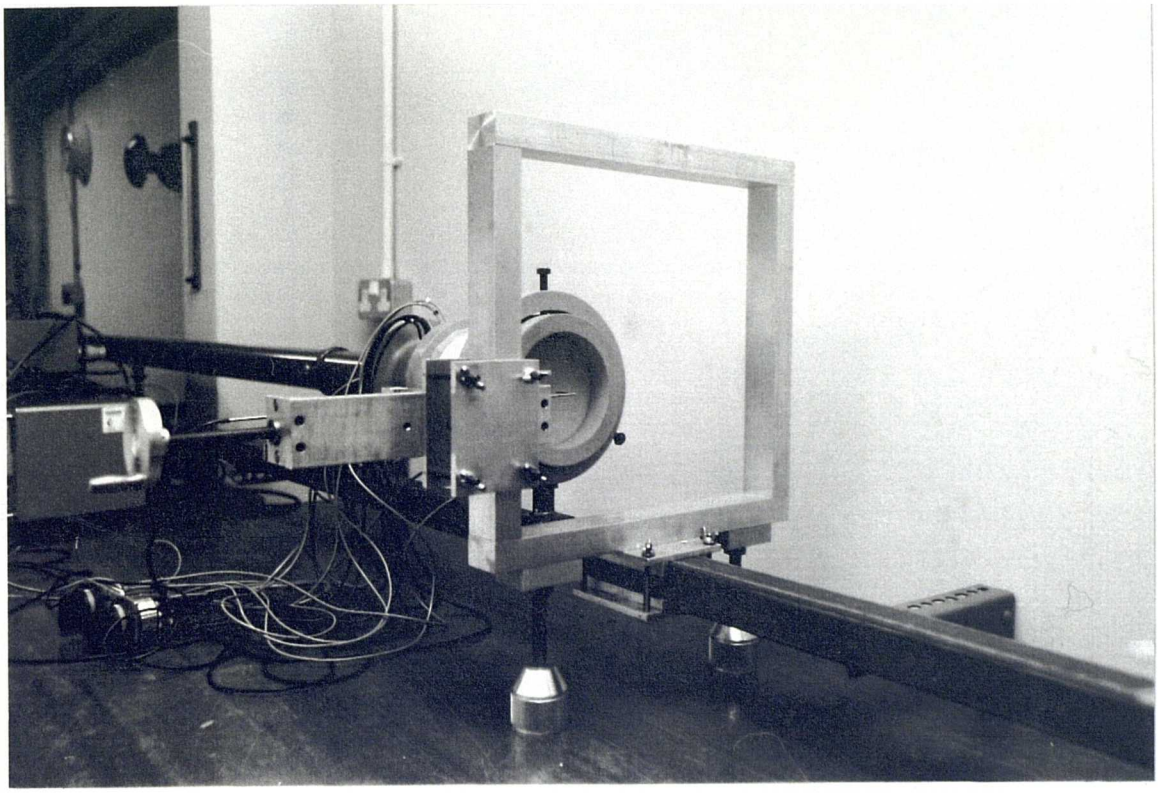

Plate 5.1 (b) - General arrangement of outlet end of working section

downstream resistance to keep the flow rate essentially constant. Without adjustment the maximum relative rate of change of flow is 0.3% per minute. A gate valve was thus provided to allow fine adjustment of the flow rate.

During normal operation the limb of the air system used for the rig would not have its line pressure set above 4 bar. However it is conceivable that the line pressure could be set to 30 bar. Thus for safety reasons an 8 bar relief valve was provided to protect the downstream components, which are only rated to 10 bar. The presence of oil and moisture in the system meant that a filter had to be placed upstream of the viscous flow meter. Contamination of the flow meter would cause its pressure drop/flow rate characteristics to change. The Saunders diaphragm valve was provided as an isolating valve, and the pressure gauge as a check on the line pressure.

5.3 Instrumentation and Data Collection

Two data sets were selected for comparison with CFD predictions; the monolith velocity profile and the inlet expansion wall static pressure profile. Included in the latter set is the static pressure drop across the catalyst assembly. The main reasons for selecting these sets were ease of collection, that relatively unsophisticated equipment would be needed and because both sets are the most pertinent to catalyst performance. In addition, it is considered that for the model validation to be meaningful acceptable agreement with predicted results should be achieved between both the assembly pressure drop and the flow distribution. It is possible to force good agreement with one but not the other.

Data supplied by Jaguar Cars Ltd, for a 4 litre AJ6 engine, fitted with a twin exhaust system, indicated that catalyst inlet pipe Re's range from 3 000 to 100 000. Will and Bennett [63] have shown that the degree of flow maldistribution increases with Re, thus the higher Re's represent the worst case scenario for the flow field. However, the driving conditions needed to produce the higher Re's are relatively rare, equating to high engine speeds and very high power outputs. A more normally encountered high exhaust Re would be 60 000, which equates to a high speed cruise driving condition. Consequently it was decided to study the flow field under these conditions. To check that the computational model would work over a range of flow rates, a second Re was selected for inclusion in the study, the choice being dictated by the technique used to measure velocities. Because of their simplicity and ease of use, a decision was made to use pitot tubes. Under atmospheric conditions a Re of 30 000 equates to a monolith mean dynamic pressure of 2 Pa, with a minimum in the 1.4 Pa to 1.8 Pa range. The manometer used to measure dynamic pressure had a resolution of 0.05 Pa. Thus at Re's below 30 000 it would be difficult to accurately resolve the details of the monolith velocity profile using the equipment available. Thus the second Re was taken as 30 000.

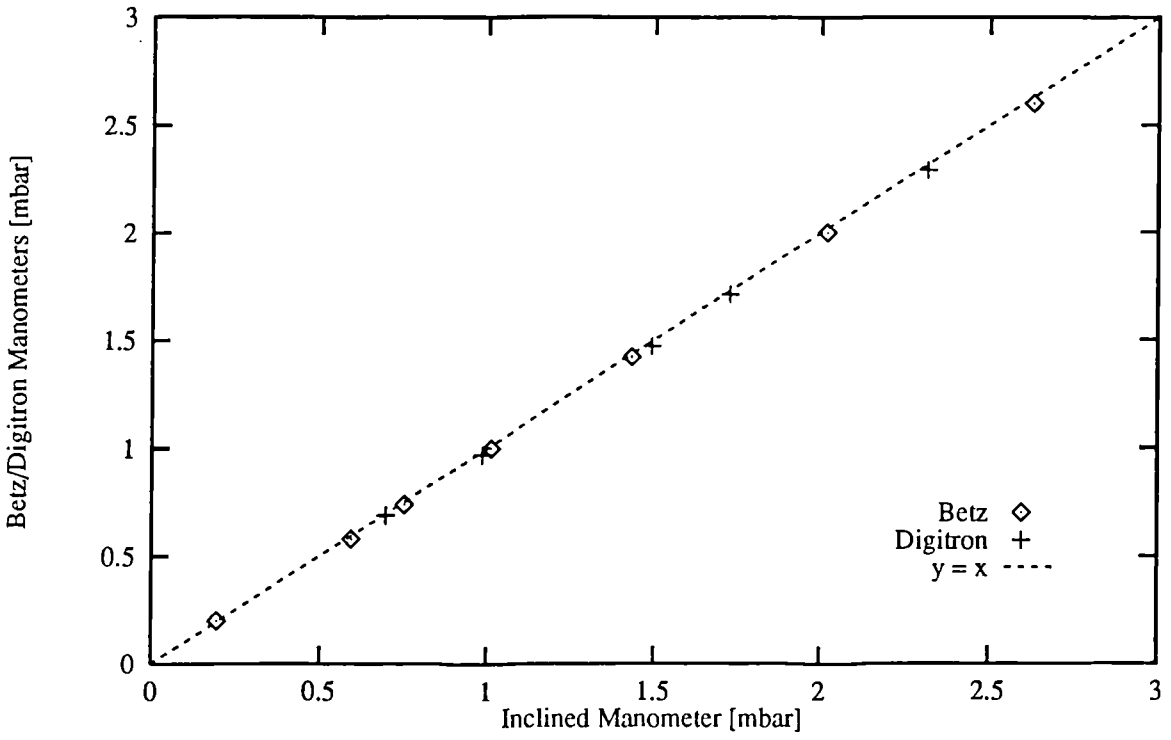

Figure 5.5 - Calibration of inclined (Combustion Instruments Ltd) manometer against Betz and Digitron manometers (when y = x agreement is perfect)

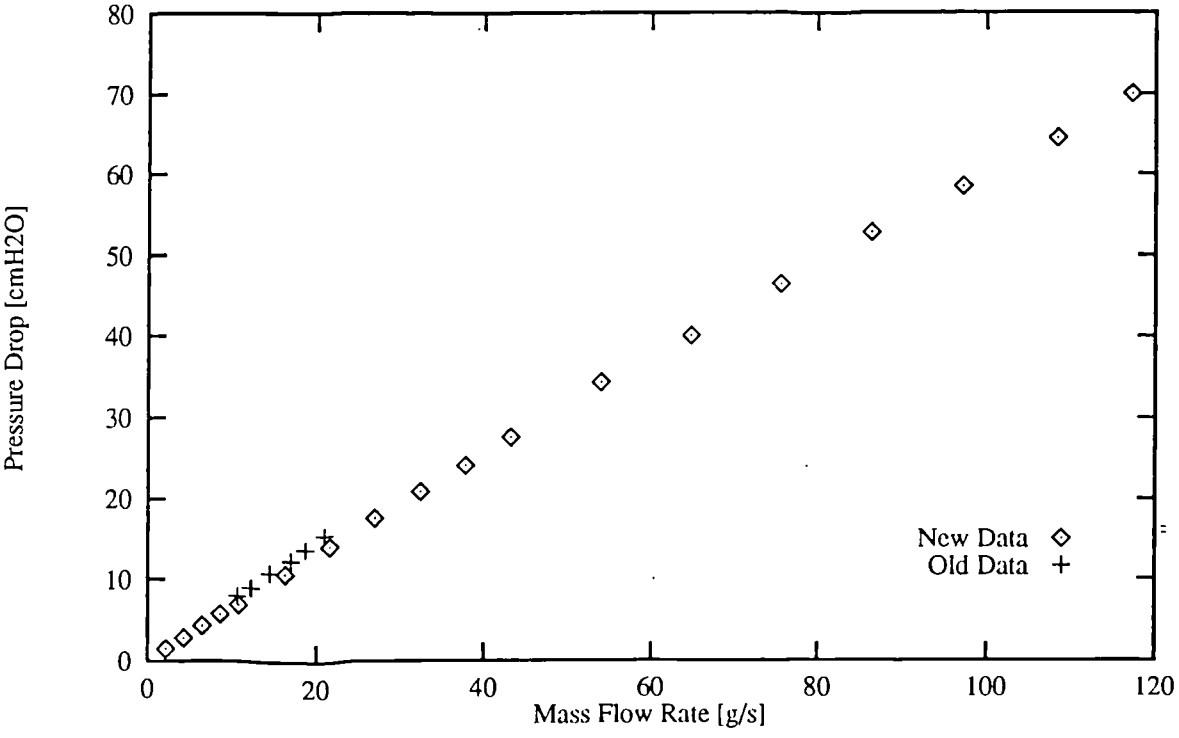

Figure 5.6 - Viscous flow meter pressure drop/flow rate characteristic

The monolith velocity profile pitot tube was supported on a lead screw based traversing mechanism (see Plates 5.1(a) and (b)). Although limited to traversing in only one direction, the capability for performing two perpendicular traverses was incorporated into the design by allowing the mechanism to be clamped, either vertically or horizontally, on a square frame. The square frame was in turn clamped to the box section base.

The wall static pressure tappings were formed by fitting 1 mm diameter capillary tubes into the wall of the inlet expansions. Although distributed along their full length, a higher concentration of tappings were fitted near the throat, where the wall pressure gradient was expected to be high. To check the symmetry of the flow, tappings were also placed at different circumferential positions. So that there would be no interference from pressure variations at the throat, the upstream pressure reading for the overall pressure drop was taken 110 mm upstream from the inlet expansion throat. At this location three evenly distributed tappings were provided on the same circumference. To facilitate the collection of data each wall pressure tapping was connected to a manifold system that allowed individual pressures to be measured in turn.

To check that the inlet velocity profile to the catalyst assembly was fully developed, a pitot traverse was inserted 110 mm upstream from the inlet expansion throat. The assumption was made that the static pressure across the traverse would be constant, and could be taken from the wall static pressure tappings at the same point. A simple sliding traverse mechanism was employed at this location.

All wall static pressures and flow field dynamic pressures were measured using the same inclined differential manometer. Its working fluid is a light oil (relative density = 0.84). It has a range of 0 to 300 Pa, with, as mentioned above, a resolution of 0.05 Pa, and was made by Combustion Instruments Ltd (*circa* 1980). Its calibration was checked against a Digitron electronic manometer and a Betz manometer, the results of which are included as Figure 5.5. Note that neither the Betz nor the Digitron instruments could be reliably used to measure pressures of less than 10 Pa.

The viscous flow meter was included so that a known flow rate could be passed through the rig and it could be established that the flow rate was not changing. Its presence also meant that a comparison could be made between it and the flow rate given by integrating the velocity profiles. The flow meter was taken from an existing engine rig, however it required some alteration to its housing before it could be incorporated into the present rig. It was calibrated against a similar flow meter owned by Jaguar Cars Ltd. The temperature of the air used for this exercise was approximately 30 °C, whereas the air supplied to the experimental rig was usually 17 °C (plus or minus 2 °C). To correct for this difference in temperature it was assumed that laminar flow exists within the flow meter core, giving a pressure drop relationship of the form,

$$\Delta p = k\nu\dot{m} \qquad 5.1$$

where k is a constant, ν the kinematic viscosity and $\dot{m}$ the mass flow rate. Providing k remains constant with changes in temperature, the pressure drop can be corrected for changes in the kinematic viscosity. The resulting pressure drop/flow rate characteristic was compared with data collected prior to the modifications to its housing. Good agreement was found (see Figure 5.6).

The pitot tubes used for measuring dynamic pressures were made in house from stainless steel capillary tube, having an internal diameter of approximately 0.5 mm (see Plate 5.2). Although the length of the right angled arm differed, preliminary tests indicated that this did not influence velocity profile measurements. In most cases the one with the longer arm was used, essentially because it was easier to ensure it remained parallel to the flow. To check their accuracy the pitot tubes were calibrated against a hot wire calibration nozzle. This consists of a plenum chamber and a high contraction ratio nozzle. It is assumed that the gas in the plenum chamber is virtually stationary, such that its has negligible dynamic pressure, and that frictional losses are also negligible. Thus the dynamic pressure of the gas leaving the nozzle is the same as the static pressure in the plenum chamber. When the pressure tapping on the plenum chamber was connected to one limb of the differential manometer and the pitot tube, positioned at the exit to the nozzle, to the other no perceivable difference in the pressures was detectable. Consequently the pitot tubes were taken to be reliable.

So that an indication of the air density and viscosity could be obtained the atmospheric pressure was measured using a mercury barometer, and the temperature of the air leaving the rig was measured using a mercury in glass thermometer. The air density was then calculated using the equation of state for an ideal gas, the kinematic viscosity being taken from thermodynamic property tables for dry air.

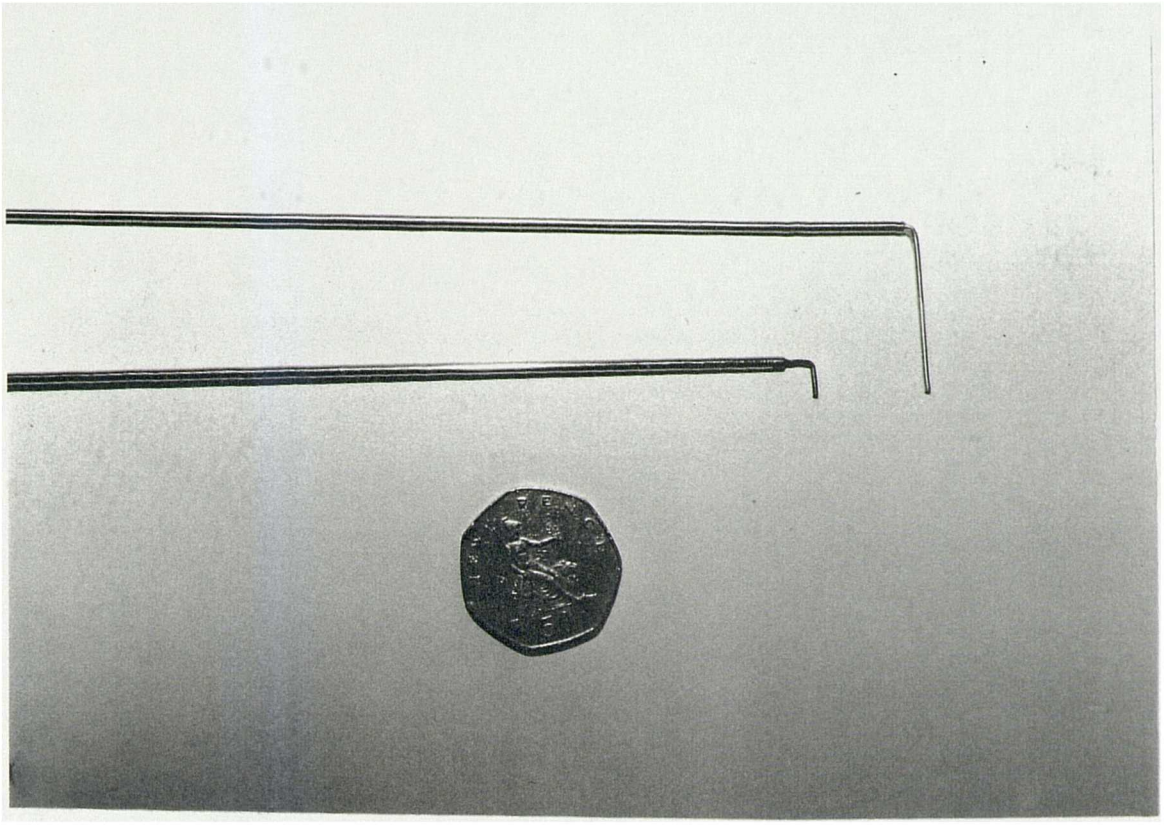

Plate 5.2 - Pitot tubes

6 ISOTHERMAL RIG RESULTS

A listing of the geometric configurations tested at the two Re's is included as Table 6.1. Conical diffusers normally require two parameters from a possible three, the inlet to outlet area ratio, the inlet to outlet length and the total (or wall) angle, for their geometric shape to be fully described; 180° expansions require the area ratio and the length to be defined. Because the area ratio is fixed at 4.448, it is only necessary to specify one parameter to fully describe any of the inlet expansions used in this work. For convenience the diffusers will be identified by their total angles, and, through lack of a sensible alternative, the 180° expansions will be identified by their lengths.

Each geometric configuration and Re combination was assigned a case number. Note that only two of the inlet expansions were tested with the 5 inch monolith, the 80° and 20° diffusers. Although it was originally intended to test all the inlet expansions with the 5 inch monolith it became apparent that this would be unnecessary, as no significant additional information would be obtained. The two diffusers tested indicated that the flow parameters of interest are equidistant between those for the 4 inch and 6 inch monolith cases. In some cases more than one velocity profile measurement was taken, the reasons for which varied from repeatability tests to investigating why relatively poor results were obtained. To differentiate between two sets of results from the same designated case a letter has been added to the case name (e.g. Case 3a).

Table 6.1 - Listing of catalyst geometric configurations tested and their case numbers.

Monolith Length	6"		5"		4"	
Re	$6x10^4$	$3x10^4$	$6x10^4$	$3x10^4$	$6x10^4$	$3x10^4$
Total Diffuser Angle (Length mm)	Case Numbers					
80° (37.0)	1	7	13	19	25	31
60° (53.0)	2,2a	8,8a	-	-	26	32
40° (84.0)	3,3a	9,9a	-	-	27	33
30° (114.0)	4	10	-	-	28,28a	34
20° (173.0)	5,5a	11	17	23	29	35
10° (349.0)	6	12	-	-	30	36
180° Expansions, Length mm						
37.0	37	42	-	-	57	62
84.0	39	44	-	-	59	64
174.0	41	46	-	-	61,61a,61b	66

6.1 Inlet Velocity Profiles

To establish that the inlet pipe did produce fully developed flow, velocity profiles across its exit were measured, at both test Re's, with the catalyst assemblies removed. The mass flow rates were

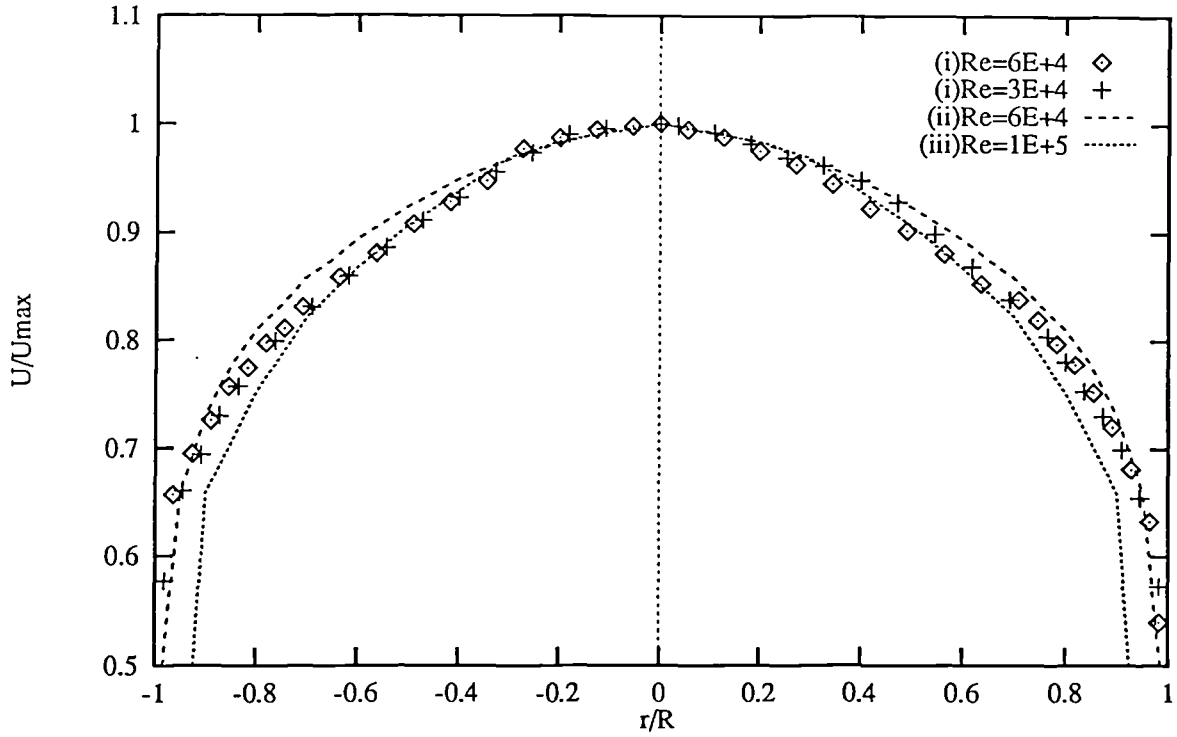

Figure 6.1 - Velocity profiles at the exit to the inlet pipe; (i) Experimental data, (ii) From Schlichting [80], (iii) From Heitor and Rodrigues [81].

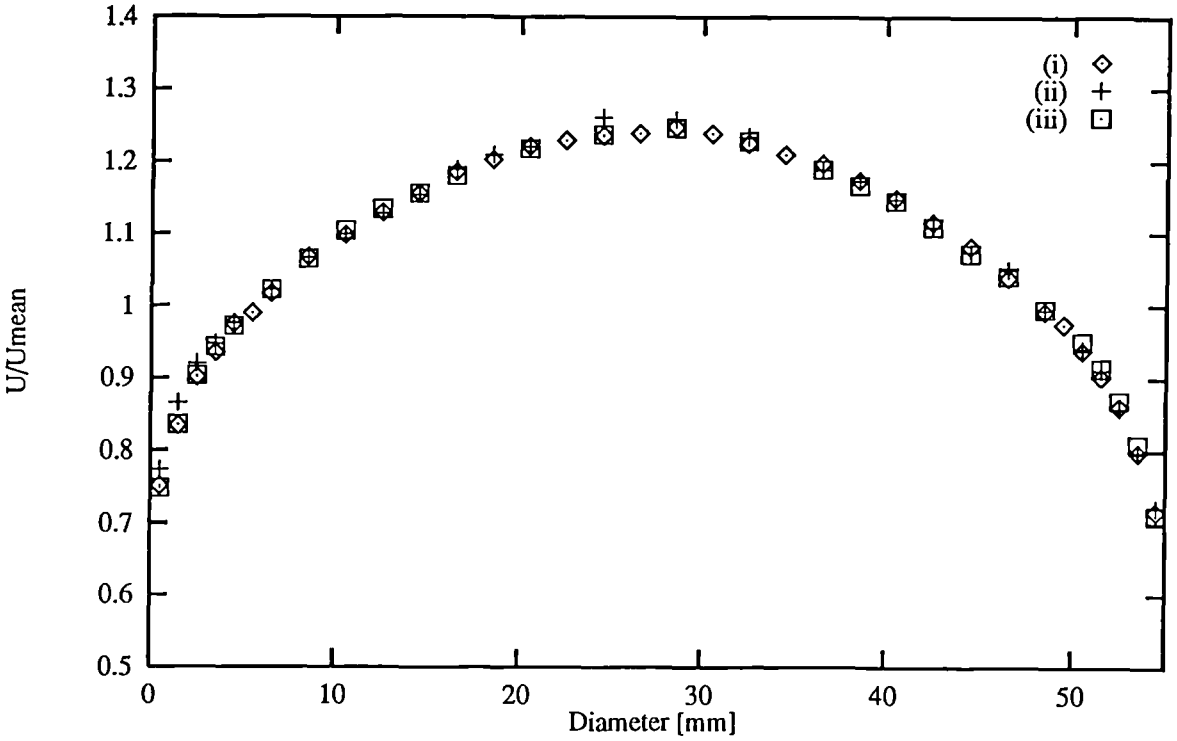

Figure 6.2 - Inlet pipe velocity profiles at upstream pitot traverse, with Re = 60 000; (i) No catalyst assembly attached, (ii) 20° diffuser and 6" monolith attached, (iii) 80° diffuser and 4" monolith atteched

calculated using a numerical method based on the trapezium rule and linear interpolation (the calculations were carried out using a FORTRAN program, a listing of which is included as Appendix C). Consideration of the general nature of the experimental data lead to the conclusion that a more sophisticated method was unnecessary. Because the velocity profiles were measured across a diameter, it was possible to carry out a separate integration on each radius, the flow rate for the whole velocity profile being taken as the mean of the two integrated values. When the mean values were compared with the viscous flow meter readings the errors were less than 1.5% for both Re's.

The velocity profiles were then compared against two sources of experimental data, Schlichting [80] and Heitor and Rodrigues [81] (see Figure 6.1). Note that the Re's at which the data apply are not consistent. The data from Schlichting [80], appropriate for flow at a Re = 60 000, has been interpolated from data taken at Re's of 23 000 and 110 000. Heitor and Rodrigues [81] only presented data at a Re = 100 000, however Schlichting [80] indicates that profiles become peakier as the Re decreases; the ratio of the maximum to mean velocity increases. Thus it would be expected that the profile at a Re = 60 000 would be more peaky. Note also that the profiles are non-dimensionalised against the maximum velocity (from Schlichting). Figure 6.1 shows that the velocity profiles from the rig inlet pipe are peakier than Schlichting's data but flatter than Heitor and Rodrigues's data. The differences in the profiles may arise from errors in the various measuring techniques or from an erroneous assumption about the fully developed nature of one or more of the flows. However, although the comparison is not totally satisfactory, the relative similarity in the profile shapes does suggest that the inlet pipe produces at least something very close to fully developed flow.

To test whether the presence of a catalyst assembly modifies the inlet pipe velocity profile, measurements were taken, using the upstream pitot traverse, with the 20° diffuser/6 inch monolith and 80° diffuser/4 inch monolith assemblies fitted. Because such a method introduces a blockage to the flow, as the pitot tube is progressively inserted into the pipe, the velocity profiles are lopsided. So that a more coherent "before and after" comparison can be made a similar velocity profile was taken, using the same equipment, with no catalyst assembly fitted. Note that the tests were only carried out at a Re = 60 000. Figure 6.2 compares the results, which show excellent agreement, indicating that the presence of a catalyst housing does not affect the flow 110 mm upstream from the diffuser throats.

6.2 Monolith Velocity Profiles

As part of the rig commissioning process a brief assessment of the axisymmetric nature of the flow was made by measuring the monolith velocity profiles across two perpendicular diameters (see

Cases 5 and 5a). A comparison of these profiles can be seen in Figure 6.3, and shows acceptable agreement indicating that the flow was axisymmetric. At a later stage a further comparison was undertaken with Cases 61 and 61b (Figure 6.4), which again confirms the axisymmetric nature of the flow. Consequently, unless suspicions were raised, in the majority of cases the velocity profile was measured across only one diameter.

It was originally felt that to ensure the full detail of the velocity profiles were captured velocity measurements near the monolith periphery, where the greatest velocity gradients occur, would be required every millimetre and away from the periphery every 2 mm. Subsequent results indicated that such a measuring frequency away from the periphery is not necessarily required, however, a decision was made to complete the experimental programme using a consistent experimental procedure. Such a measuring frequency also improves the accuracy of the integration of the velocity profiles at points where velocity gradients change rapidly.

The integration of the velocity profiles was undertaken using the same numerical method discussed in Section 6.1 and Appendix C. By carrying out two separate integrations, one for each radius, an indication of the flow symmetry could be obtained. A symmetry error was defined as the difference between the two integrated flow rates, $\dot{m}_1$ and $\dot{m}_2$, divided by the mean of the two, $\dot{m}_{mean}$. The symmetry error for each case is included in Table 6.2. In only three cases does the error rise above 5%. Also included in Table 6.2 is the difference between the mass flow rate given by the viscous flow meter, $\dot{m}_{fm}$, and the mean integrated value, expressed as a percentage of the viscous flow meter value. In only five cases does the difference become greater than 5%, the largest being 8.33%. Both these sets of figures provide confidence in the reliability of the experimental data. (Note that Case 28 was repeated to investigate why the high symmetry error had occurred, and Case 61 was repeated to investigate why the high flow rate error had occurred.)

The velocity profiles for each case are presented, in graphical form, in Figures 6.13 to 6.22. Note that the velocities have been non-dimensionalised against the mean outlet velocity derived from the integrated velocity profiles. It was found that using this value, as opposed to using the mean velocity based on the viscous flow meter reading, made the results more consistent and easier to compare. As can be seen the velocity profiles are all similarly shaped, having their maximum velocities in the centre region and local maxima near the periphery. The occurrence of the maximum near the centre line is to be expected. The occurrence of the local maxima at the periphery is caused by a combination of factors. At the front face of the monolith, the large downstream resistance causes the fluid to have a significant radial velocity component. This component becomes more predominant towards the periphery, such that most of the fluid is flowing parallel to the monolith front face. However, the presence of the inlet expansion wall

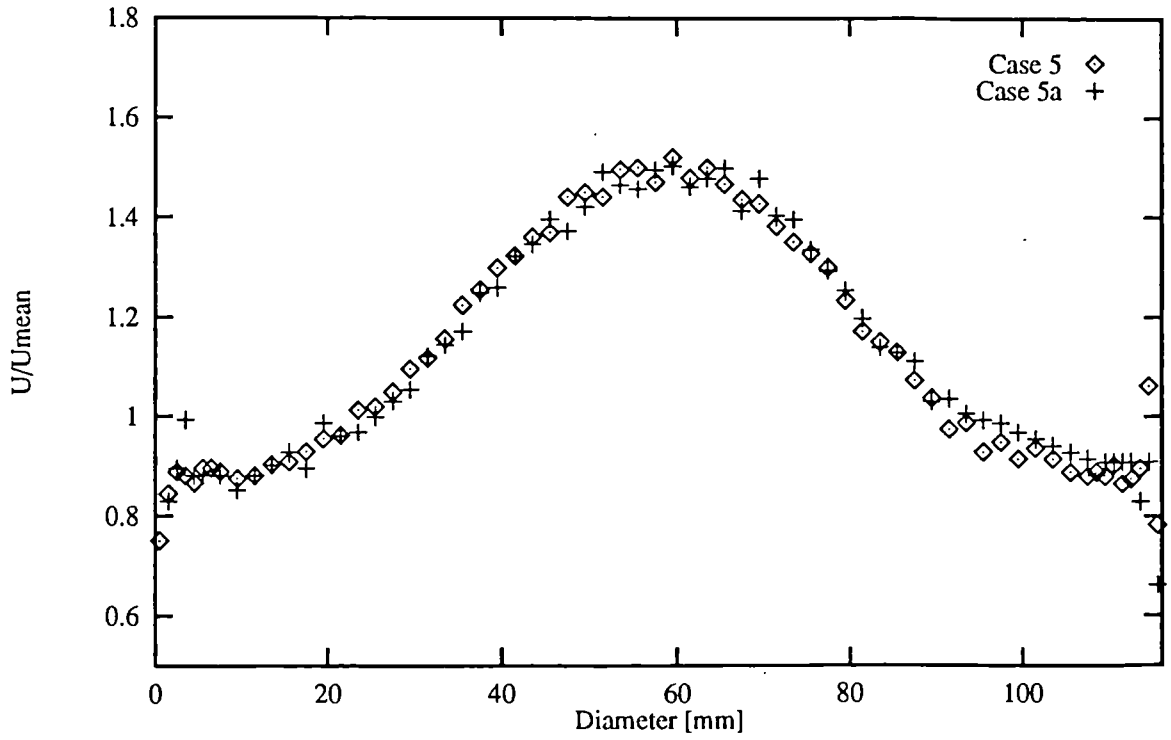

Figure 6.3 - Monolith velocity profile from 20° diffuser with 6" monolith at Re = 60 000; vertical traverse (Case 5) and horizontal traverse (Case 5a)

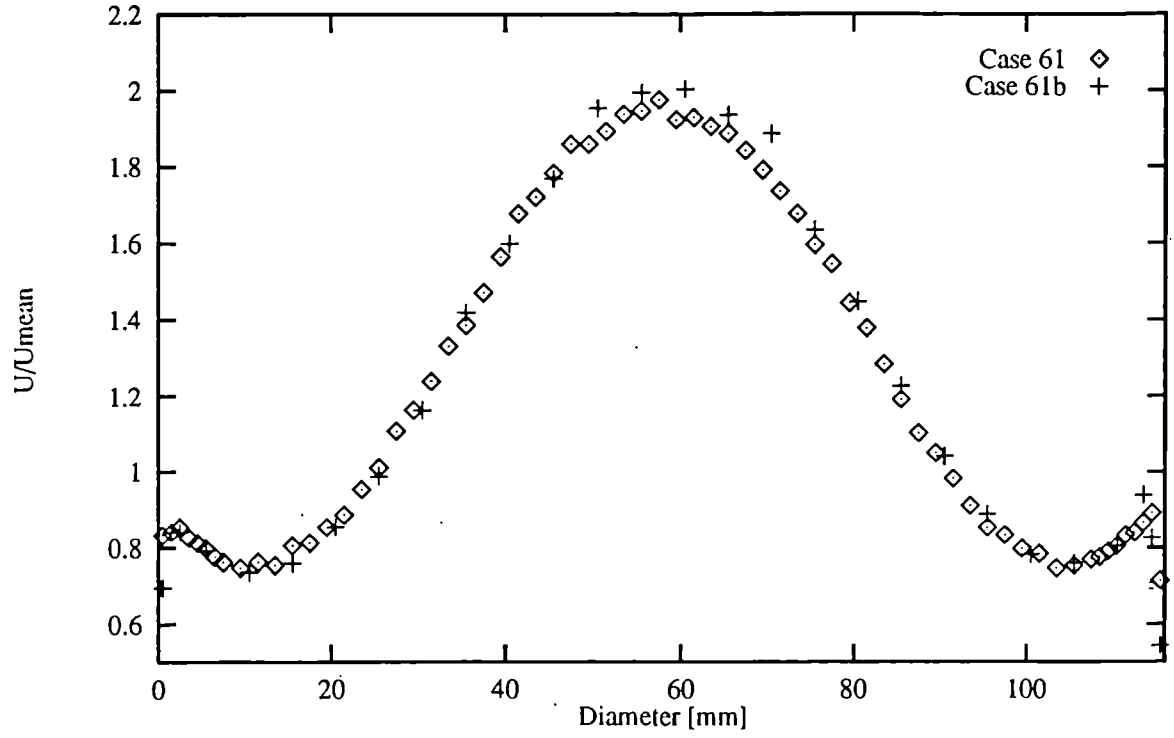

Figure 6.4 - Monolith velocity profile from 174mm 180° expansion with 6" monolith at Re = 60 000; vertical traverse (Case 61) and horizontal traverse (Case 61b)

Table 6.2 - Experimental data from isothermal steady flow rig

Cone Angle	Case No.	Δh Flow Meter [cmH_2O]	$\dot{m}_{fm}$ [g/s]	$\dot{m}_1$ [g/s]	$\dot{m}_2$ [g/s]	$\dot{m}_{mean}$ [g/s]	ρ [kg/m^3]	T [°C]	Flow Rate Error	Symm-etry Error
				6" Monolith; Re ~ 60 000						
80°	1	29.0	45.4	46.426	47.785	47.106	1.2246	16.0	3.76	2.88
60°	2	29.0	45.4	45.838	47.947	46.893	1.2071	15.0	3.29	4.50
	2a	29.1	45.6	47.379	47.817	47.598	1.2125	16.0	4.38	0.92
40°	3	28.8	45.0	46.000	46.594	46.297	1.1991	16.5	2.88	1.28
	3a	28.8	45.0	46.091	45.554	45.823	1.1901	17.0	1.83	-1.17
30°	4	28.9	45.2	46.049	45.172	45.611	1.1896	16.5	0.91	-1.92
20°	5	28.9	45.2	46.206	46.739	46.473	1.2091	16.0	2.82	1.15
	5a	28.9	45.2	45.593	47.426	46.510	1.2090	16.5	2.90	3.94
10°	6	28.9	45.2	46.581	46.632	46.607	1.2060	16.0	3.11	0.11
				6" Monolith; Re ~ 30 000						
80°	7	16.1	24.7	24.745	24.929	24.837	1.2091	17.5	0.55	0.74
60°	8	16.0	24.5	24.599	24.922	24.761	1.2002	16.5	1.07	1.30
	8a	16.0	24.5	25.040	24.610	24.825	1.2093	17.0	1.33	-1.73
40°	9	16.0	24.5	24.440	24.596	24.518	1.1906	18.0	0.07	0.64
	9a	16.0	24.5	24.439	24.328	24.384	1.1894	17.5	-0.51	-0.46
30°	10	16.0	24.5	23.197	23.139	23.168	1.1609	18.0	-5.44	-0.25
20°	11	16.0	24.5	23.856	23.942	23.899	1.2039	17.5	-2.45	0.36
10°	12	16.1	24.7	24.695	25.109	24.902	1.1986	17.5	0.82	1.66
				4" Monolith; Re ~ 60 000						
80°	25	28.9	45.2	45.679	46.676	46.178	1.2155	16.0	2.16	2.16
60°	26	29.0	45.4	47.152	47.060	47.106	1.2117	15.5	3.76	-0.20
40°	27	28.9	45.2	46.133	45.028	45.581	1.1863	15.5	0.84	-2.42
30°	28	28.8	45.0	45.228	49.137	47.183	1.1990	17.0	4.85	8.28
	28a	28.6	44.6	46.122	42.850	44.486	1.1691	16.5	-0.25	7.36
20°	29	28.9	45.2	48.229	50.134	49.182	1.2396	15.0	8.33	3.87
10°	30	28.8	45.0	44.431	43.662	44.047	1.1609	18.0	-2.55	-1.74
				4" Monolith; Re ~ 30 000						
80°	31	16.0	24.5	24.414	24.710	24.562	1.2099	17.5	0.25	1.21
60°	32	16.0	24.5	24.726	24.834	24.780	1.1970	17.5	1.14	0.44
40°	33	16.0	24.5	24.954	24.531	24.743	1.1836	17.0	0.99	-1.71
30°	34	16.0	24.5	24.000	25.189	24.595	1.1862	18.0	0.39	4.83
20°	35	16.0	24.5	25.605	25.239	25.422	1.2048	16.5	3.76	-1.44
10°	36	15.9	24.3	23.530	23.540	23.535	1.1644	18.0	-3.15	0.04
				5" Monolith; Re ~ 60 000						
80°	13	29.0	45.4	46.147	48.573	47.360	1.2307	16.0	4.32	5.12
20°	17	28.9	45.2	46.100	47.120	46.610	1.2030	16.0	3.12	2.19
				5" Monolith; Re ~ 30 000						
80°	19	16.0	24.5	24.273	25.389	24.831	1.2278	16.5	1.35	4.49
20°	23	16.0	24.5	23.760	23.780	23.770	1.1989	17.5	-2.98	0.08

Table 6.2 (Continued)

180° Expan. Length	Case No.	Δh Flow Meter [cmH_2O]	$\dot{m}_{fm}$ [g/s]	$\dot{m}_1$ [g/s]	$\dot{m}_2$ [g/s]	$\dot{m}_{mean}$ [g/s]	ρ [kg/m^3]	T [°C]	Flow Rate Error	Symm-etry Error
				6" Monolith; Re ~ 60 000						
37mm	37	28.8	45.0	45.921	46.279	46.100	1.2130	17.5	2.44	0.78
84mm	39	28.9	45.2	45.285	46.359	45.822	1.2055	20.5	1.38	2.34
174mm	41	28.9	45.2	47.148	46.869	47.009	1.1879	16.5	4.00	-0.59
				6" Monolith; Re ~ 30 000						
37mm	42	15.9	24.3	24.934	25.205	25.070	1.2208	16.5	3.17	1.08
84mm	44	15.9	24.3	24.627	25.313	24.970	1.2039	19.5	2.76	2.75
174mm	46	16.0	24.5	25.460	25.446	25.453	1.1930	17.5	3.89	-0.06
				4" Monolith; Re ~ 60 000						
37mm	57	28.9	45.2	47.009	47.939	47.474	1.2265	16.0	5.03	1.96
84mm	59	28.9	45.2	45.727	47.096	46.412	1.2220	18.0	2.68	2.95
174mm	61	28.8	45.0	48.615	48.593	48.604	1.2015	16.0	8.01	-0.05
	61a	29.0	45.4	44.937	45.496	45.217	1.1962	17.5	-0.40	1.24
	61b	28.9	45.2	47.300	48.821	48.061	1.2168	16.0	6.33	3.16
				4" Monolith; Re ~ 30 000						
37mm	62	15.9	24.3	24.896	24.524	24.710	1.2188	17.5	1.69	-1.51
84mm	64	15.9	24.3	23.983	24.184	24.084	1.1839	22.0	-0.89	0.83
174mm	66	16.0	24.5	25.083	24.800	24.942	1.1987	17.5	1.80	1.13

prevents the fluid from continuing to flow in the radial direction, causing a stagnation point at the edge of the monolith. The relatively high pressure of the stagnation point forces a locally increased volume of fluid through the peripheral channels. Hence the local maximum in velocity.

Inspection of the results from the cases where a high symmetry error occurred indicates that, in most of them, the error appears to arise from a shift in the whole velocity profile, by up to 4.5 mm, to one side of the monolith (Cases 2, 5a, 28, 29 and 34). A possible explanation for these shifts would be the displacement, away from the centreline, of the jet emerging from the inlet expansion throat. Such shifting of the jet might be caused by a slight defect in the inlet expansion, a slight asymmetry in the monolith, or slight changes in geometry resulting from variations in the way the rig was assembled. Although in most cases the same monoliths and inlet expansions were used, no control was exercised over their rotational position, so it is conceivable, if unlikely, that any asymmetry might not be detected along a particular diameter. If the flow was displaced and a symmetric velocity profile was obtained, the traverse cannot have passed through the flow maximum, which by necessity must have been some way from the traverse centre. A consequence of this situation would be an integrated flow rate that was too low. However, the high frequency with which relatively symmetric velocity profiles were obtained, that did not have appreciable flow rate errors, suggests that neither inlet expansion defects nor asymmetry in the monoliths is a

significant cause of flow shifting, and that in the majority of cases the flow can be taken to be virtually axisymmetric. Even in those cases where the flow appears asymmetric the reasonable agreement between the integrated flow rates and the viscous flow meter suggests that the level of asymmetry is slight and the measured velocity profiles are acceptably representative of a truly axisymmetric flow field.

It would be convenient if a single parameter was available that reflects the impact a velocity profile has on catalyst performance. A number of relatively simple parameters can be derived, such as the one proposed by Lemme and Givens [3], called the flow distribution efficiency, η_{flow}, given by,

$$\eta_{flow} = \frac{\int_A UdA}{U_{max}A} \qquad 6.1$$

and the maldistribution index, M', proposed by Wendland and Matthes [7], given by,

$$M' = \frac{U_{max} - U_{mean}}{U_{mean}} \qquad 6.2$$

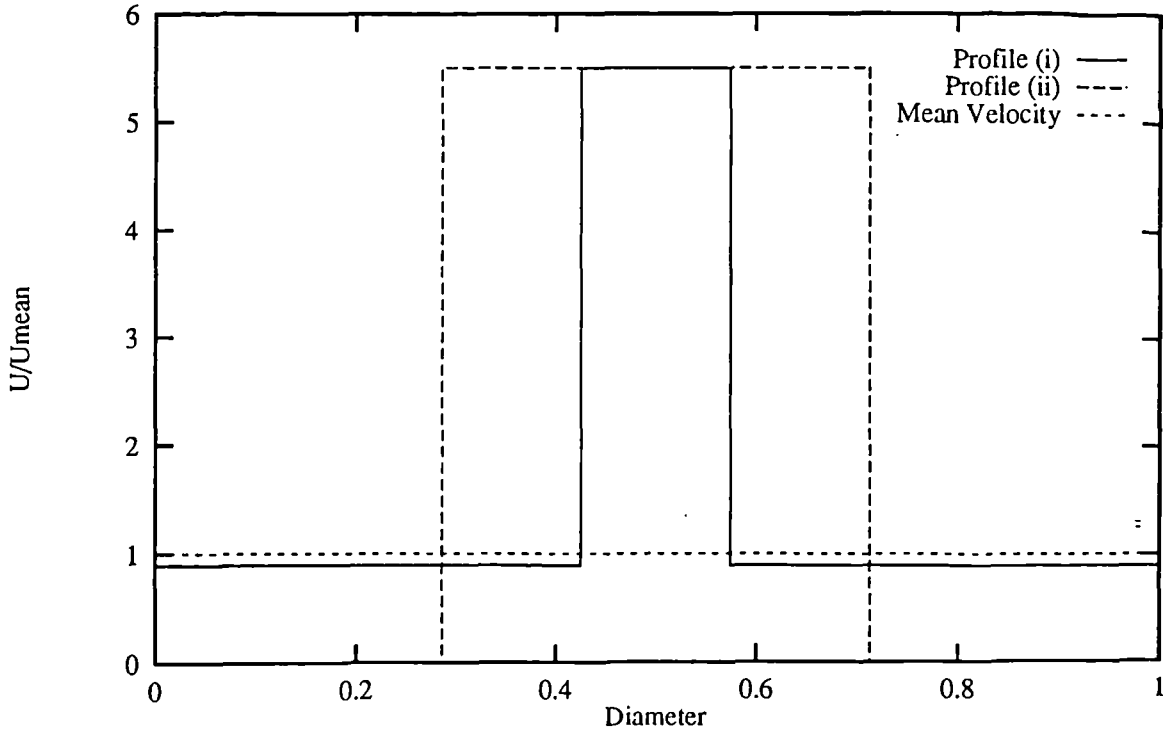

Figure 6.5 - Different velocity profiles with the same maximum to mean velocity ratio

The main weakness of these flow maldistribution indices is that much of the detail of the velocity profile is lost. It is possible for a profile with a large area of high velocity flow (see Profile (ii), Figure 6.5) to have the same maldistribution index as another profile with a smaller area of high velocity flow (Profile (i)). Despite this, it is probable that Profile (i) has a less detrimental effect on post-light-off conversion efficiency and durability than Profile (ii). Several authors have proposed more complex indices that attempt to quantify the differences between such profiles (Lai et al. [10] and Weltens et al. [64]). However, the similarity of shape of the profiles presented here means that one of the simpler indices should adequately quantify their relative impact on catalyst performance. Such an index, and one commonly used within industry, is the ratio of the maximum velocity to the mean velocity, for convenience referred to as the maldistribution ratio, M.

The scattered nature of the experimental points, particularly in the central region, means that taking the measured maximum velocity may give a misleadingly high value to the maldistribution ratio. This would be particularly true when attempting to compare predicted profiles, which are inherently smooth, with the experimental data. The predicted profile might lie as a best fit line through the experimental data, showing excellent agreement, however the maldistribution ratios of the two sets of data would be different. Even though the flow fields are taken to be axisymmetric, the scatter means that the centreline velocity also need not necessarily be representative of the maximum velocity, as might be expected. To overcome these shortcomings it was decided to make use of the relatively flat nature of the velocity profiles in the central region and take the maximum velocity from an estimated best fit line. Although inevitably arbitrary such a method is still considered preferable to the alternatives.

There should only be three variables affecting the velocity distribution; the monolith length, the dimensions of the inlet expansion and the inlet pipe Re. The effect on maldistribution ratio as each parameter varies, while the other two are held constant, can be seen from Table 6.3. The velocity profiles become flatter as,

i) the monolith length increases,

ii) the diffuser angles become smaller,

iii) the Re is reduced.

These findings confirm the trends found by previous workers. Although not very strong, there is some suggestion in the results that the profiles become flatter as the 180° expansion length increases.

Table 6.3 - Maldistribution ratio (M) as a function of geometry and Re.

Monolith Length	6"		5"		4"	
Approx. Re	$6x10^4$	$3x10^4$	$6x10^4$	$3x10^4$	$6x10^4$	$3x10^4$
Total Diffuser Angle (Length mm)	Maldistibution Ratio (Case)					
80° (37.0)	1.78 (1)	1.39 (7)	1.88 (13)	1.51 (19)	1.98 (25)	1.57 (31)
60° (53.0)	1.70 (2) 1.70 (2a)	1.36 (8) 1.36 (8a)	-	-	1.94 (26)	1.54 (32)
40° (84.0)	1.65 (3) 1.65 (3a)	1.36 (9) 1.36 (9a)	-	-	1.88 (27)	1.48 (33)
30° (114.0)	1.57 (4)	1.32 (10)	-	-	1.73 (28) 1.74 (28a)	1.42 (34)
20° (173.0)	1.50 (5) 1.50(5a)	1.26 (11)	1.54 (17)	1.29 (23)	1.63 (29)	1.34 (35)
10° (349.0)	1.37 (6)	1.20 (12)	-	-	1.47 (30)	1.25 (36)
180° Expansions, Length mm						
37.0	1.78 (37)	1.42 (42)	-	-	2.07 (57)	1.61 (62)
84.0	1.74 (39)	1.36 (44)	-	-	2.02 (59)	1.50 (64)
174.0	1.75 (41)	1.39 (46)	-	-	1.96 (61) 1.98 (61a) 2.00 (61b)	1.51 (66)

Any non-uniform velocity profile entering a monolith will generate a non-uniform pressure distribution across the monolith front face, the pressure peaks being associated with the higher velocities. Such pressure distributions will tend to force fluid away from the high velocity areas towards the low velocity areas, consequently causing a flattening of the velocity, and pressure, profile. Increasing monolith length increases its flow resistance, which means that for a given velocity distribution the difference between the maximum and minimum pressures at the monolith front face increases. Increasing this differential causes a greater flattening tendency.

The flattening of the velocity profiles as diffuser angle decreases results from the improved performance of the diffusers. The narrower the diffuser angle the less severe the adverse pressure gradient, which makes separation less likely. Once the flow has separated it behaves in a similar fashion to a jet, which expands into the larger flow area at a slower rate than attached flow. This point is illustrated by the similarity of the velocity profiles from Cases 1 and 37, 7 and 42, 25 and 57 and 31 and 62 (the 80° diffuser and 37 mm 180° expansion; see Figures 6.6 and 6.7). In these cases the adverse pressure gradient of the 80° diffuser is so severe it behaves in virtually the same way as a sudden expansion. Contrast these results with those from the 20° diffuser and the 174 mm 180° expansion (Table 6.3). The flow in this diffuser is probably attached over more of its length than the sudden expansion. Consequently the diffuser, which expands the flow more efficiently, produces a flatter velocity profile than the sudden expansion.

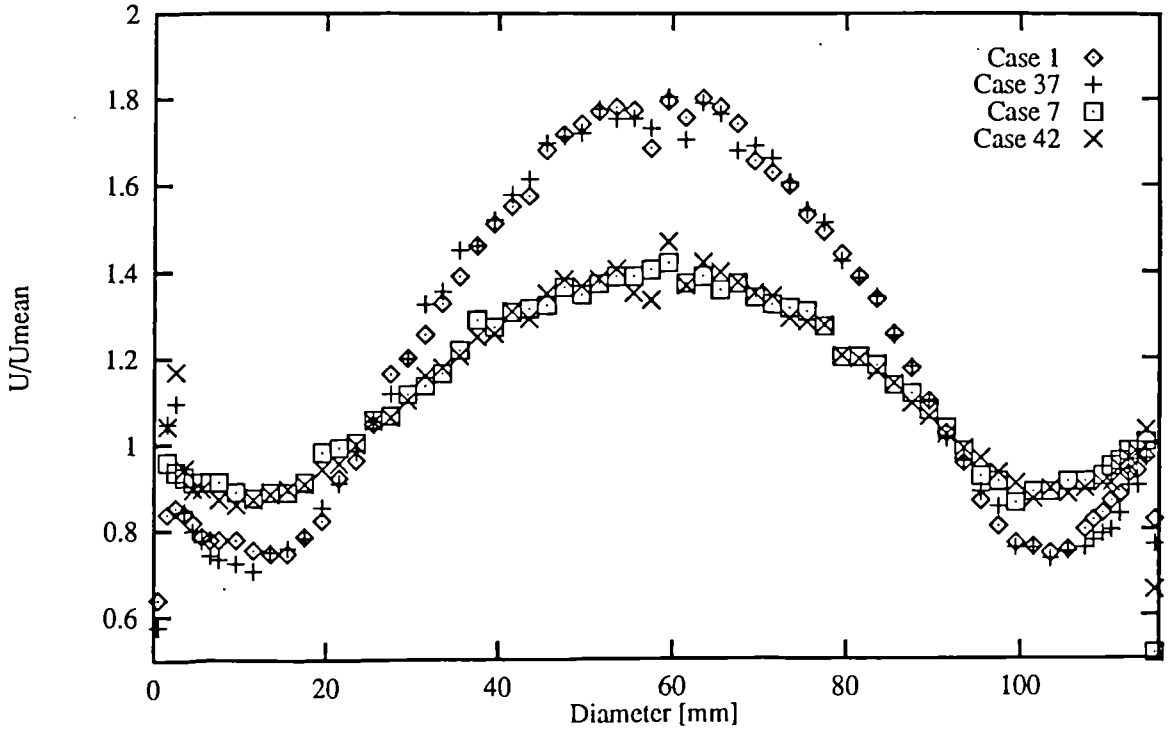

Figure 6.6 - Monolith velocity profiles from 80° diffuser (Cases 1 and 7) and 37 mm 180° expansion (Cases 37 and 42) with a 6" monolith; for Cases 1 and 37 Re = 60 000, for Cases 7 and 42 Re = 30 000

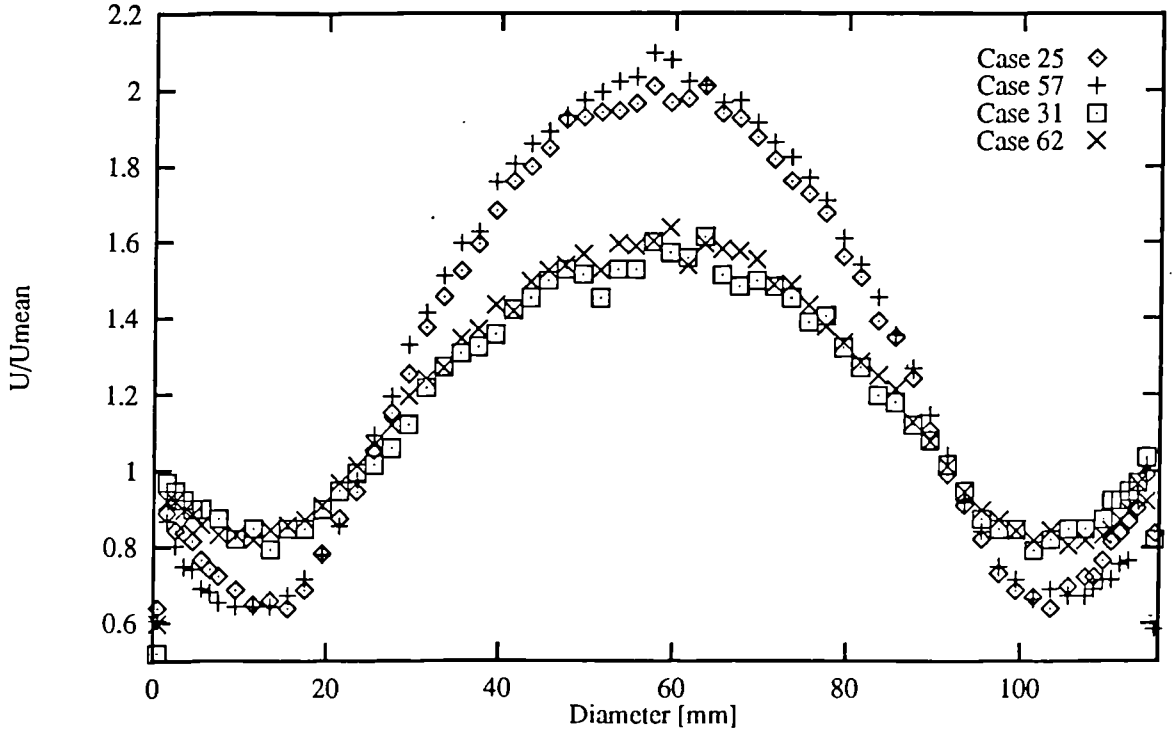

Figure 6.7 - Monolith velocity profiles from 80° diffuser (Cases 25 and 31) and 37 mm 180° expansion (Cases 57 and 62) with a 4" monolith; for Cases 25 and 57 Re = 60 000, for Cases 31 and 62 Re = 30 000

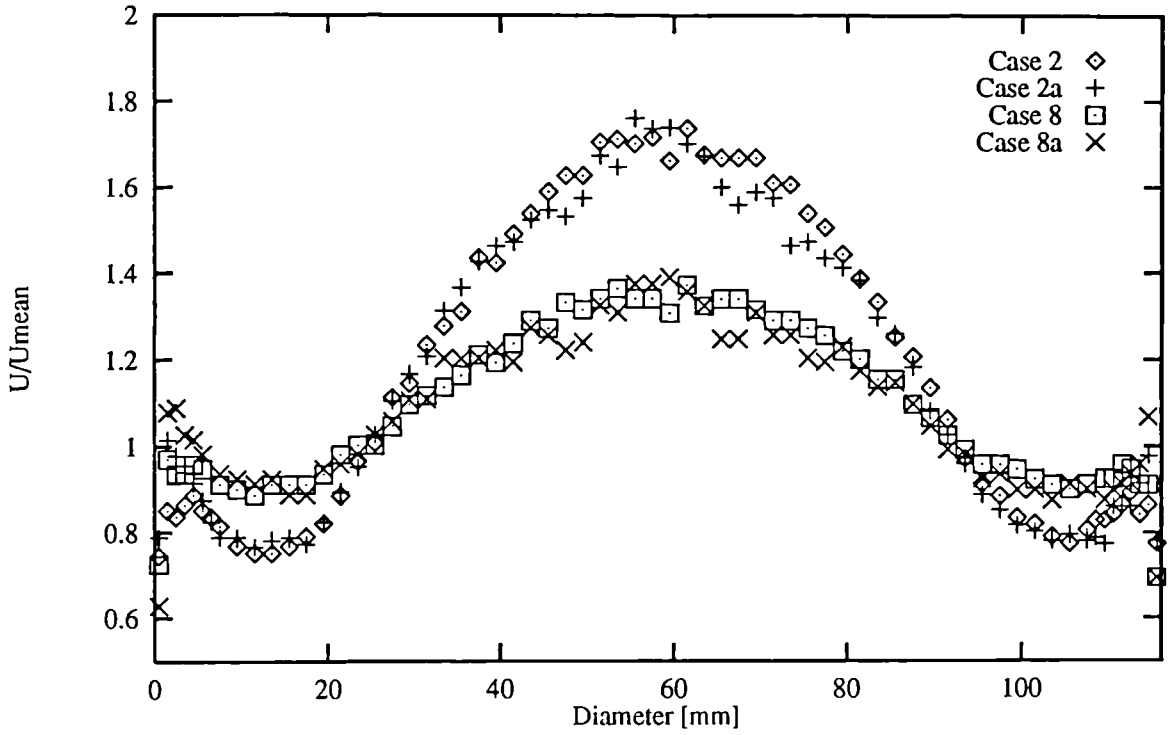

Figure 6.8 - Monolith velocity profiles from two different 60° diffusers with different 6" monoliths; (Cases 2 and 2a at Re = 60 000, Cases 8 and 8a at Re = 30 000)

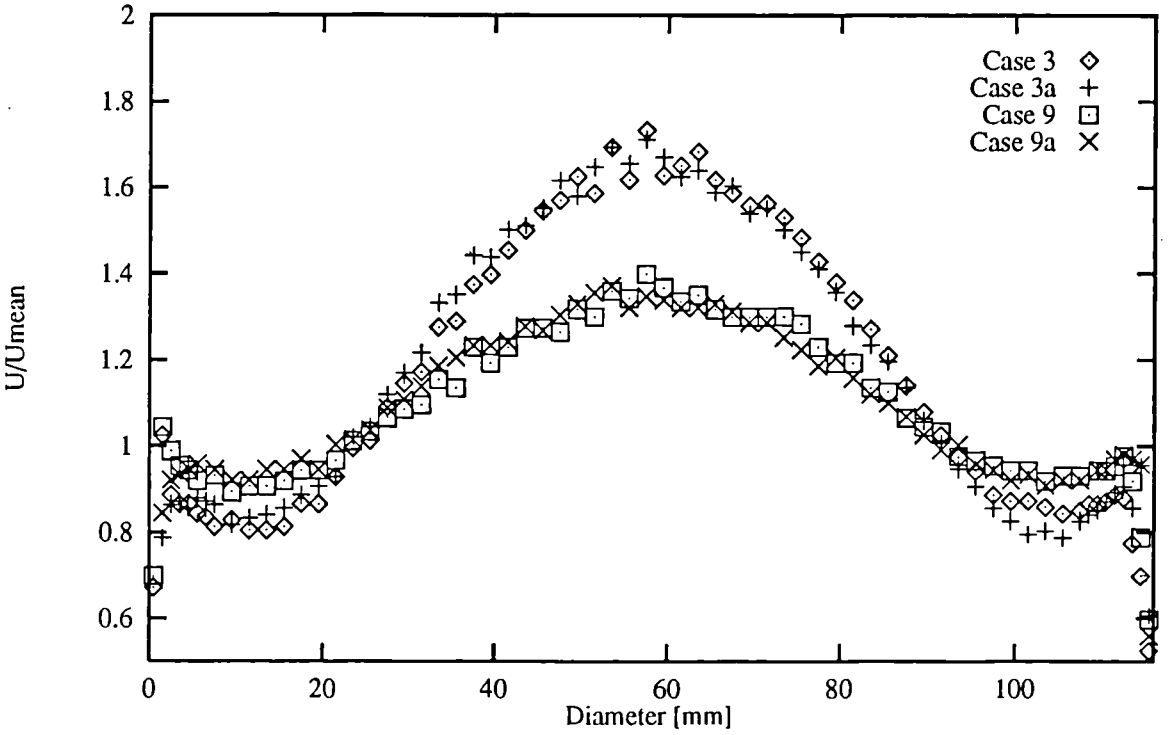

Figure 6.9 - Monolith velocity profiles from two different 40° diffusers using the same 6" monolith; (Cases 3a and 9a had an aluminium diffuser)

The reason for flatter velocity profiles at lower Re's is assumed to arise from the change in the ratio of inertia forces to viscous forces within the inlet expansion.

Although dependent on all three parameters, the velocity profiles are influenced the most by the inlet pipe Re. For example, reducing the Re from approximately 60 000 to 30 000 has a greater flattening effect than reducing the diffuser angle from 80° to 20°. Similarly, the same reduction in Re has a more pronounced effect than increasing the monolith length from 4 inches to 6 inches (These points can be easily seen from Figure 6.11). It is also worth noting that the effect of monolith length and Re is stronger with larger diffuser angles than with narrow angles. In addition, as implied above, the flattening effect caused by the lengthening of the 180° expansions is less marked than the flattening effect caused by the corresponding increases in diffuser length.

6.3 Repeatability Tests

Throughout the experimental programme a number of features of the catalyst assemblies were identified that might have caused inconsistencies between the modelling approach and reality. For example, because the diffusers were made from wood their throats had a slight radius on them, in contrast to the computational models which assumed the throats had perfectly sharp corners. In addition it was found that the dimensions of the diffusers varied slightly, by 1 or 2 mm, from those specified in the drawings, and that the "wetted" surfaces were not perfectly smooth. Variations in the internal dimensions of the monoliths can also be expected.

To assess how sensitive results were to these slight variations in assembly geometry two repeatability tests were set up. In the first a duplicate 60° diffuser was made from wood, which, almost inevitably, differed in length from the original diffuser by 1.5 mm. No wall pressure tappings were machined and a different 6 inch (unwashcoated) monolith was fitted. It was tested at Re's of 60 000 and 30 000. A comparison of the velocity profiles from these tests, Cases 2a and 8a, and Cases 2 and 8 (see Figure 6.8) shows good agreement, the differences between the profiles being similar to the differences between profiles from two perpendicular diameters on the same assembly. In the second set of tests a duplicate 40° diffuser was machined from aluminium, the aim being to produce a sharp corner at the throat and a uniform, good quality, surface finish on the internal walls. Again no pressure tappings were machined, but the original 6 inch monolith was fitted. The velocity profiles at Re's of 60 000 and 30 000, Cases 3a and 9a, are presented in Figures 6.9, where a comparison is made with the corresponding cases, Cases 3 and 9. Again agreement is good.

These results show that a slight radius on the throats of diffusers with total angles greater than 40° does not significantly affect their flow fields. Although not tested, it is also likely that the flow fields of diffusers with total angles of less than 40° are likewise unaffected by a slight radius on

their throats. A similar conclusion is reached with respect to the effect of slight variations in diffuser and monolith dimensions, and surface roughness.

6.4 Wall Static Pressures

To make comparison of the wall static pressure distributions easier the pressure readings have been normalised by subtracting the static pressure taken 110 mm upstream from the inlet expansion throats (P_0), and non-dimensionalised by dividing by the inlet pipe "mean" dynamic pressure, $\rho\overline{U_0^2}/2$, i.e. a pressure coefficient (C_{pw}) has been defined as,

$$C_{pw} = \frac{P_i - P_0}{\rho\overline{U_0^2}/2} \qquad 6.3$$

The resulting C_{pw} distributions are included as Figures 6.23 to 6.31. Note that the axial distance datum point has been taken at the throat of the inlet expansion, and that for the 180° expansions no pressure measurements where taken immediately upstream of this datum.

Upstream from the throat, all the diffuser cases follow a similar trend. The pressure decreases, at an increasing rate, towards the throat, where a suction peak forms. With virtually every case a relatively high level of scatter is present in these readings, compared with the downstream readings, suggesting perhaps that circumferential variations in wall pressure existed and/or the pressure tapping capillary tubes protruded slightly.

Downstream from the throat the level of scatter in the readings is low, and a series of distinct patterns can be seen in the C_{pw} distributions. The most striking feature of these distributions is the similarity between cases with the same inlet expansion geometry, i.e. it is not clear whether their shape and numerical values are a function of monolith length and Re. The distributions from the diffusers can be broadly split into three groups; those produced by the 80° and 60° diffusers, those produced by the 30°, 20° and 10° diffusers and those produced by the 40° diffuser. With the first group there is a modest initial recovery in pressure immediately downstream from the throat. After this initial recovery, the pressures decrease slightly, reaching a minimum 10 to 15 mm in front of the monolith, then increases rapidly to a maximum at the monolith. With the second group there is initially a rapid rise in pressure, the rate of which gradually decreases until just before the monolith, where, with the 30° and 20° diffusers the gradient increases again, but with the 10° diffuser the pressure actually falls slightly. The third group of distributions falls between the other two groups, consisting of an extended initial, if slow, rise in pressure until about 15 mm before the monolith, where upon it rises rapidly towards the monolith.

It should be noted that, because of difficulty of access, pressure tappings could not be fitted to the last 12 mm of the 180° expansions. Over the axial positions where readings have been taken on the 37 mm 180° expansion the shape of the C_{pw} distributions resembles those from the 80° diffuser, over the corresponding axial positions, however their numerical values are lower by approximately 0.05. From this similarity of shape, allied with the similarity in velocity profiles, it would be reasonable to assume that, as with the 80° diffuser, there is a sharp rise in pressure over the last 12 mm of the 37 mm 180° expansion. This assumption could also be made about the pressure in the 84 mm 180° expansion, its C_{pw} distribution having a similar shape to the 60° diffuser, over the corresponding axial positions. The C_{pw} distributions from the 174 mm 180° expansion are virtually flat, with only a very small drop in pressure, until approximately 30 mm before the monolith, where upon the pressure starts to increase, at a progressively increasing rate. In light of the general similarities in the measured pressure distributions between the 180° expansions and the diffusers, it would seem reasonable to assume that the pressure distributions upstream of the 180° expansion throats are much the same as those upstream from the diffusers throats.

As stated above, it appears that the only factor affecting the shape, and numerical value, of the C_{pw} distributions is the inlet expansion geometry. Closer examination indicates that, apart from the 20° diffuser, there is no distinct pattern in the change in C_{pw} numerical values, above that expected from normal experimental variations, as the monolith length varies. An absence of a relationship between monolith length and C_{pw} values would suggest that the inlet expansion flow fields are unaffected by monolith length, a contradiction of the trends found in the behaviour of the monolith velocity profiles. The results from the 20° diffuser do show that, at both Re's, as the monolith becomes shorter the C_{pw} numerical values decrease, a trend that is consistent with the findings from the velocity distributions; as the velocity profiles become more maldistributed the efficiency of the diffuser reduces. It is quite possible, however, that the 20° diffuser results arise from a systematic fault with data collection, and that the lack of a trend in C_{pw} values displayed by the other geometries is real.

The effect of Re is more complex. Results from the 80°, 60°, 40° and 30° diffusers and the 174 mm 180° expansion suggest that as the Re decreases the C_{pw} values decrease, however with the remaining diffusers and 180° expansions the C_{pw} values either increase as the Re decreases, or remain the same. ESDU Item Number 76027 [5] reports that, in conventional diffusers, at Re's of less than 10 000 C_{pw} values decrease with decreasing Re, but above a Re = 50 000 the values are independent of Re.

It would be acceptable to assume that the flow in the 180° expansions separates at the throat, and that a flat or decreasing C_{pw} distribution starting at the throat is indicative of such flow. A logical

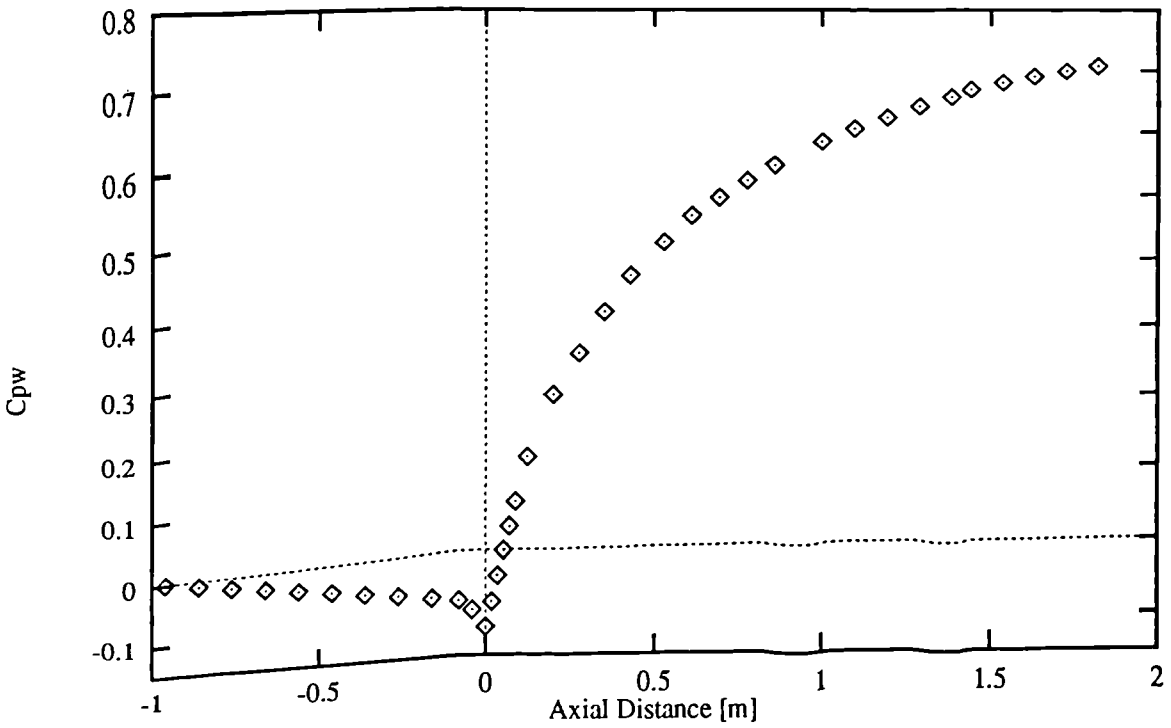

Figure 6.10 - Wall static pressure coefficient for a conventional 6° conical diffuser, of area ratio 4.

extension to this reasoning would be to assume that when a diffuser exhibits such a flat or decreasing C_{pw} distribution the flow over that region is separated. Such an assumption would lead to the conclusion that in the 80° and 60° diffusers separated flow exists over most of their length, only reattaching in the last 10 mm or so before the monolith. These deductions are confirmed by flow visualisation results taken by Girgis and Benjamin [82] from a water flow rig consisting of transparent axisymmetric catalyst assemblies. The findings of this study show that with a 45° diffuser, at a Re = 32 000, the flow separates at the throat and remains separated until a centimetre or so from the monolith. The occurrence of such a flow regime in a 45° diffuser suggests that one may also occur in a 40° diffuser. If so the pressure distributions given by the 40° diffuser will also be indicative of flow fields with large separated regions.

Performance data for conventional conical diffusers (i.e. no outlet resistance) indicates that a 10° diffuser, of area ratio 4.45, will have a flow field that is predominantly attached (ESDU Item Number 73024 [83]), the only departure being transitory "bubbles" of separated flow near the exit. The presence of a large resistance tends to suppress separation and stabilise the flow (ESDU Item Number 87015 [6]). Therefore the flow in the catalyst assembly with the 10° diffuser should be entirely attached, and it can be inferred that the associated C_{pw} distribution is representative of such flow. Results from Pozzorini [84] (Figure 6.10) provide supporting evidence that fully attached diffusers have the same kind of C_{pw} distributions as that displayed by the 10° diffuser. (Pozzorini

studied the flow field of a 6° diffuser, of area ratio 4, which again should contain predominantly attached flow.)

6.5 Assembly Pressure Losses

Although the static pressure distributions along the wall of the inlet expansions are useful for comparison with model predictions, the total static pressure loss across the whole catalyst assembly is of greater relevance to catalyst performance. With most production catalyst assemblies the dimensions of the inlet and outlet pipes are the same, thus, providing the velocity profiles in each pipe are similar, the drop in static pressure from inlet to outlet represents the total losses across the system. The absence of an outlet cone on the rig assemblies means that the total losses have to be found from the change in total pressure across the system. At any section, assuming that the static pressure profile is uniform, the total pressure, P_t, is given by,

$$P_t = P_s + \frac{\int_A (\rho U^2/2) d\dot{m}}{\dot{m}} \qquad 6.4$$

Where $\dot{m}$ is the mass flow rate and P_s the static pressure.

For each case the dynamic pressure at the monolith outlet was obtained from the experimental velocity profiles, calculated using a numerical integration procedure similar to the one used to calculate flow rates (Appendix C). The dynamic pressure across the inlet section was obtained by using a kinetic energy coefficient, α, derived from the pipe velocity profiles measured with the catalyst assemblies removed (again obtained using the code listed in Appendix C). It was found that at a Re = 30 000, α = 1.095, and at a Re = 60 000, α = 1.060. Consequently the inlet dynamic pressure, P_{d0}, for each case was calculated from,

$$P_{d0} = \alpha_0 \frac{\rho \overline{U_0}^2}{2} \qquad 6.5$$

where $\overline{U}_0$ is the mean inlet velocity.

A listing of the drop in total pressure and static pressure for each case is included as Table 6.4. Note that both changes in pressure have been non-dimensionalised against the respective inlet "mean" dynamic pressures ($\rho \overline{U_0}^2/2$), calculated using the integrated flow rates. A brief inspection of the data from the diffusers reveals that both pressure drops become smaller as the diffuser angles become smaller and the monoliths become shorter. Both these trends are consistent with the

findings of previous investigators. It should be noted that because the Re is proportional to velocity and the dynamic pressure is proportional to the velocity squared the non-dimensional pressure drops increase as the Re decreases, whereas the actual pressure drops decrease. It is also interesting to note that the difference between both sets of pressures is approximately one inlet dynamic pressure, a point that reflects the relatively small value of the outlet dynamic pressure compared to the inlet dynamic pressure.

Table 6.4 - Drop in static and total pressure across catalyst assemblies.

		Diffusers			
Case	$Re/10^4$	$\Delta P_s/(\rho\overline{U}_0^2/2)$	$\Delta P_t/(\rho\overline{U}_0^2/2)$	K_{t-lam}	$K_{t-lamDl}$
		6" Monolith; Re ~ 60 000			
1	6.1	1.655	2.648	0.4502	0.3372
2	6.2	1.619	2.616	0.4794	0.3703
3	6.1	1.569	2.568	0.4249	0.3199
3a	6.1	1.639	2.637	0.4813	0.3749
4	6.1	1.488	2.490	0.3784	0.2797
5	6.1	1.330	2.334	0.2545	0.1587
6	6.1	1.221	2.228	0.1926	0.1014
		6" Monolith; Re ~ 30 000			
7	3.2	3.317	4.355	0.4273	0.3310
8	3.3	3.260	4.300	0.4495	0.3555
9	3.2	3.291	4.345	0.4425	0.3487
9a	3.2	3.320	4.360	0.4501	0.3557
10	3.1	2.989	4.030	0.0378	-0.0542
11	3.1	3.177	4.218	0.2632	0.1717
12	3.3	2.867	3.910	0.1173	0.0274
		4" Monolith; Re ~ 60 000			
25	6.0	1.077	2.060	0.4019	0.2674
26	6.2	1.002	1.987	0.3859	0.2548
27	6.1	0.973	1.963	0.3832	0.2605
28	6.2	0.804	1.801	0.2904	0.1780
29	6.3	0.651	1.651	0.2100	0.1056
30	5.9	0.694	1.700	0.2089	0.1133
		4" Monolith; Re ~ 30 000			
31	3.2	2.183	3.219	0.3635	0.2584
32	3.2	2.097	3.134	0.3454	0.2416
33	3.3	2.045	3.083	0.3516	0.2501
34	3.2	1.966	3.006	0.2555	0.1565
35	3.3	1.730	2.772	0.1269	0.0314
36	3.2	1.862	2.906	0.1400	0.0467
		5" Monolith; Re ~ 60 000			
13	6.1	1.326	2.316	0.4456	0.3273
17	6.1	1.002	2.005	0.2661	0.1683
		5" Monolith; Re ~ 30 000			
19	3.2	2.765	3.802	0.4468	0.3469
23	3.1	2.582	3.624	0.2707	0.1785

Table 6.4 (Continued)

180° Expansions

Case	$Re/10^4$	$\Delta P_s/(\rho\overline{U}_0^2/2)$	$\Delta P_t/(\rho\overline{U}_0^2/2)$	K_{t-lam}	$K_{t-lamDl}$
		6" Monolith; Re ~ 60 000			
37	6.0	1.752	2.745	0.4852	0.3705
39	5.8	1.731	2.727	0.4644	0.3551
41	6.2	1.623	2.621	0.5402	0.4362
		6" Monolith; Re ~ 30 000			
42	3.2	3.298	4.337	0.4289	0.3323
44	3.2	3.272	4.327	0.4017	0.3075
46	3.3	3.181	4.221	0.4872	0.3942
		4" Monolith; Re ~ 60 000			
57	6.1	1.073	2.051	0.3907	0.2492
59	5.9	1.087	2.070	0.3922	0.2583
61	6.4	0.982	1.973	0.4775	0.3566
61a	5.9	1.110	2.102	0.4836	0.3621
61b	6.3	1.025	2.014	0.4687	0.3446
		4" Monolith; Re ~ 30 000			
62	3.2	2.208	3.243	0.3574	0.2495
64	3.1	2.254	3.291	0.3831	0.2805
66	3.1	2.132	3.170	0.4310	0.3308

The total losses can be split into two groups; those caused by the monolith and those caused by the inlet expansion, the last 110 mm of inlet pipe and the outlet sleeve. The second group will be dominated by the losses in the inlet expansion, thus for convenience are collectively referred to simply as the expansion losses. An indication of the magnitude of the first group of losses, referred to as the monolith losses, can be gained by calculating them using either Equation 4.7 or Equation 4.8. The calculation procedure is again based on the numerical integration method discussed in Section 6.1 (and Appendix C), and uses the experimentally derived monolith velocity profiles and monolith dimensions listed in Table 5.1. By inference, because the expansion losses are the difference between the monolith losses and the total losses, an indication of the magnitude of the expansion losses is also gained. When the expansion losses are non-dimensionalised against the inlet "mean" dynamic pressure they become analogous to the total pressure loss coefficient, K_t, of conventional diffusers.

The K_t values of the experimental data have been included in Table 6.4. Note that the subscripts "lam" and "lamDl" have been used to indicate whether Equation 4.7 or Equation 4.8, respectively, were taken to calculate the monolith losses. Examination of these K_t values shows that, although a relatively high level of scatter exists, apparent trends can be seen. The expansion losses appear not to vary with diffuser angle for angles of 40° and greater. Below an angle of 40° the losses decrease as the angle decreases. Such behaviour is consistent with conventional diffuser performance, the K_t values of which have been included, for comparison, as Table 6.5 (Data taken from [83]). With the

180° expansions the expansion losses remain independent of expansion length up to lengths of 84 mm, however they start to increase with length somewhere between 84 mm and 174 mm. Conventional 180° expansion theory only applies if sufficient length is provided for full pressure recovery, where upon the expansion losses are only a function of expansion ratio (With an expansion ratio of 4.45, $K_t = 0.60$; ESDU Data Item 72011 [85]).

A somewhat surprising trend in the K_t values is that for a given inlet expansion they become smaller as the monolith length and the Re decrease. As mentioned above, with reference to C_{pw} values, for conventional diffusers K_t values increase with decreasing Re, for Re's below 10 000, and are independent of Re above Re = 50 000. The reduction in K_t implies that the opposite is occurring with catalyst diffusers. The flattening of monolith velocity profiles as monolith length increases suggests that the performance of the inlet expansions improves as monoliths become longer. Again this contradicts the trend in K_t values. A possible explanation for these inconsistencies would be that neither Equation 4.7 nor Equation 4.8 completely describe the monolith losses, and that an additional pressure drop term exists. Such a term would need to increase as the monolith length and Re increase. Because of these considerations, it is not possible to comment on the suitability of using Equation 4.8 to account for the development of boundary layers in monolith channels. It would be reasonable to assume that the presence of a monolith will reduce the expansion losses compared to those from corresponding conventional diffusers and 180° expansions. Comparison of the K_t values in Tables 6.4 and 6.5 indicates that this is the case for both calculation methods, except when Equation 4.7 is applied to Cases 6, 30 and 36. The existence of an additional monolith pressure drop term will reduce all catalyst K_t values.

Table 6.5 - Conventional conical diffuser K_t values.
(Fully developed inlet velocity profile; Expansion ratio = 4.45)

Total Diffuser Angle	K_t
80	0.72
60	0.72
40	0.63
30	0.54
20	0.35
10	0.14

An instructive way of illustrating the trends in the monolith velocity profiles and the total pressure losses, together, is to plot the flow maldistribution ratio against the non-dimensional total losses. Such a plot for the diffuser assemblies has been included as Figure 6.11. Note that tentative contours of constant monolith length and diffuser angle have been drawn at the two Re's tested. Because the tests were only carried out at two Re's, the high dependency of both performance

parameters on the Re prohibits the use of statistical techniques for finding regression curves. Before such techniques can be used tests at several other Re's would need to be taken.

The 180° expansion data have not been included in Figure 6.11 because they would clutter the diagram and would only be bunched around the 80° diffuser points. However, they have been included as a separate diagram, Figure 7.23, where a comparison with the predicted results is carried out.

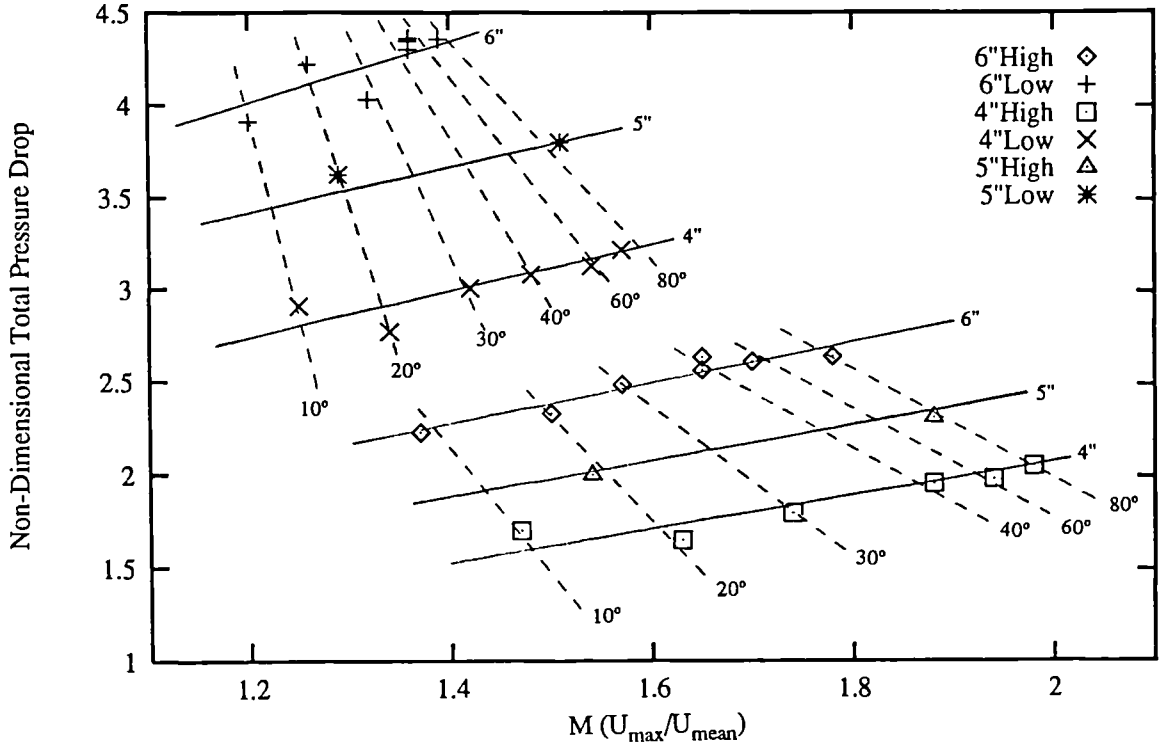

Figure 6.11 - Maldistribution ratio versus total pressure drop for various diffuser angles, monolith lengths and Re's (in key number of inches refers to monolith length, "High" refers to Re = *60 000*, "Low" refers to Re = 30 000)

6.6 Monolith Resistance Tests

If the monoliths could be provided with a uniform upstream flow field a clearer indication of the appropriate equation to use for monolith pressure drops ought to be obtained. A uniform upstream flow field would eliminate the entrance effects caused by fluid entering channels at acute angles. These effects are present when there is a significant radial velocity component at the monolith front face, and neither Equation 4.7 nor 4.8 attempt to model them. If they can be eliminated the only entrance effects that will then remain will result from the sudden reduction in flow volume, decay of turbulence and boundary layer development.

To produce a truly uniform flow field would require a plenum chamber and a contracting nozzle; a lengthy design and manufacturing exercise. As a compromise it was realised that a simple modification to the existing rig would effectively allow a section of monolith to be place within, and at the end of, the inlet pipe. The monolith would then be provided with an inlet velocity profile given by fully developed pipe flow, which although not uniform, is more uniform than the inlet expansions could provide. The slight non-uniformity of the pipe velocity profile will cause it to be modified by the monolith resistance, producing a modest radial velocity component at the front face. These radial velocity components should be small compared to those generated in the inlet expansions, and neglecting their effect should introduce only minor errors.

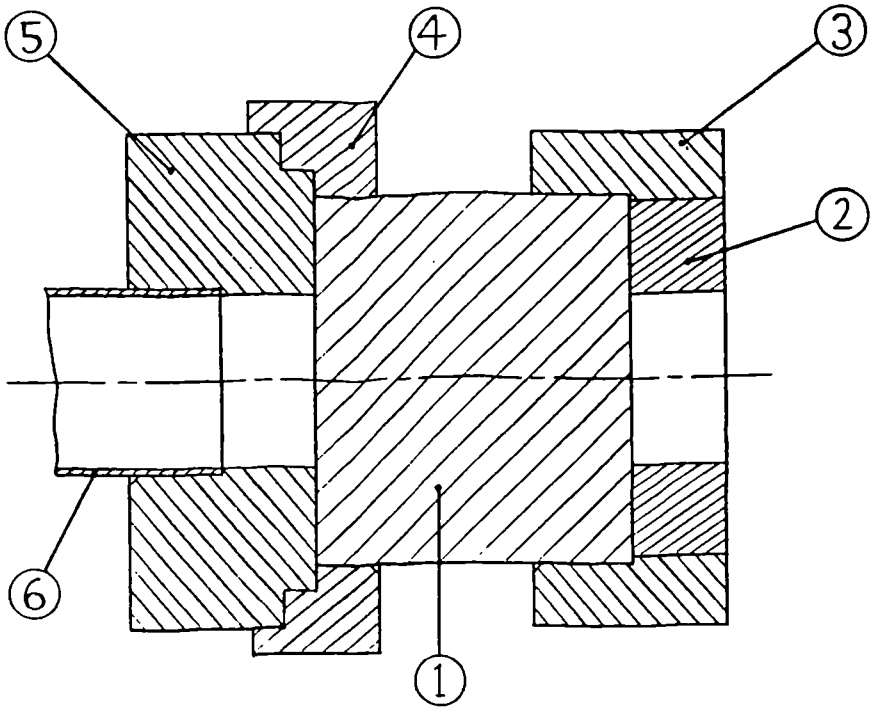

Figure 6.12 - Sectioned drawing of modified catalyst assembly for resistance tests; (1) monolith, (2) outlet sleeve insert, (3) outlet sleeve, (4) outlet section of 180° expansion, (5) inlet section of 180° expansion and (6) inlet pipe

The rig modification was achieved by fitting the 180° expansion inlet and end sections (Figures 5.3(a) and 5.3(c)) together, so that the monoliths could be placed directly against the inlet pipe (see Figure 6.12). Note that although the whole monolith is positioned in the rig, only the central 55 mm diameter section has flow passing through it. An insert was also made that fitted into the monolith outlet sleeve which allowed the velocity profile 30 mm downstream of the monolith rear face to be measured (Figure 6.12). Six tests were carried out, all using the 4 inch monolith, at mean

monolith channel velocities equivalent to a full axisymmetric assembly inlet pipe Re of between 26 000 and 76 000. The results from the tests are presented in Table 6.6, along with the predicted pressure drops using Equations 4.7 and 4.8.

The integrated flow rates were calculated from the measured velocity profiles. At the higher flow rates these profiles displayed significant scatter, a major reason for the poor agreement between the flow meter and integration results. As a consequence the flow meter flow rates were taken to be the most accurate, and were used, along with the monolith dimensions given in Table 5.1, to calculate the predicted pressure drops.

Table 6.6 - Monolith resistance measurement results

	Flow Rate [g/s]			ΔP [Pa]		
Test	Flow Meter	Integrated	Equivalent $Re/10^4$	Measured	Predicted lam	Predicted lamDl
1	11.4	12.3	6.6	231.7	247.4	264.2
2	13.1	14.4	7.6	273.0	284.3	306.3
3	8.2	8.9	4.8	163.0	178.0	186.7
4	12.4	12.2	7.2	252.9	269.1	288.8
5	4.5	4.37	2.6	87.0	98.6	101.2
6	6.3	6.34	3.6	128.0	138.0	143.2

Note: lam denotes that ΔP calculated using Equation 4.7; lamDl signifies Equation 4.8 used.
Equivalent Re is the inlet pipe Re's from the full catalyst geometries, with diffusers, that would cause the same mean channel velocities .

Comparison between the predicted and measured results shows that both Equation 4.7 and 4.8 give pressure drops that are too large. The level of agreement between the results is made worse when it is considered that the measured pressure drops were taken between a pressure tapping 110 mm upstream of the monolith and the rig exit plane; the pressure drop across the monolith would be slightly smaller than the values quoted. The reason for the predicted pressure drops being higher than the measured pressure drops is unclear. The pressure drop given by fully developed laminar flow (Equation 4.7) is, under the experimental conditions, the lowest that is theoretically possible. Thus the discrepancies must arise from unreliable flow and pressure measurements or remaining uncertainties over the monolith dimensions. It is also possible that the slight non-uniformity of the inlet velocity field is affecting the results. It was obvious that further investigations, including modifications to the rig, would be needed, and that insufficient time and resources were available to carry out these investigations as part of the present project.

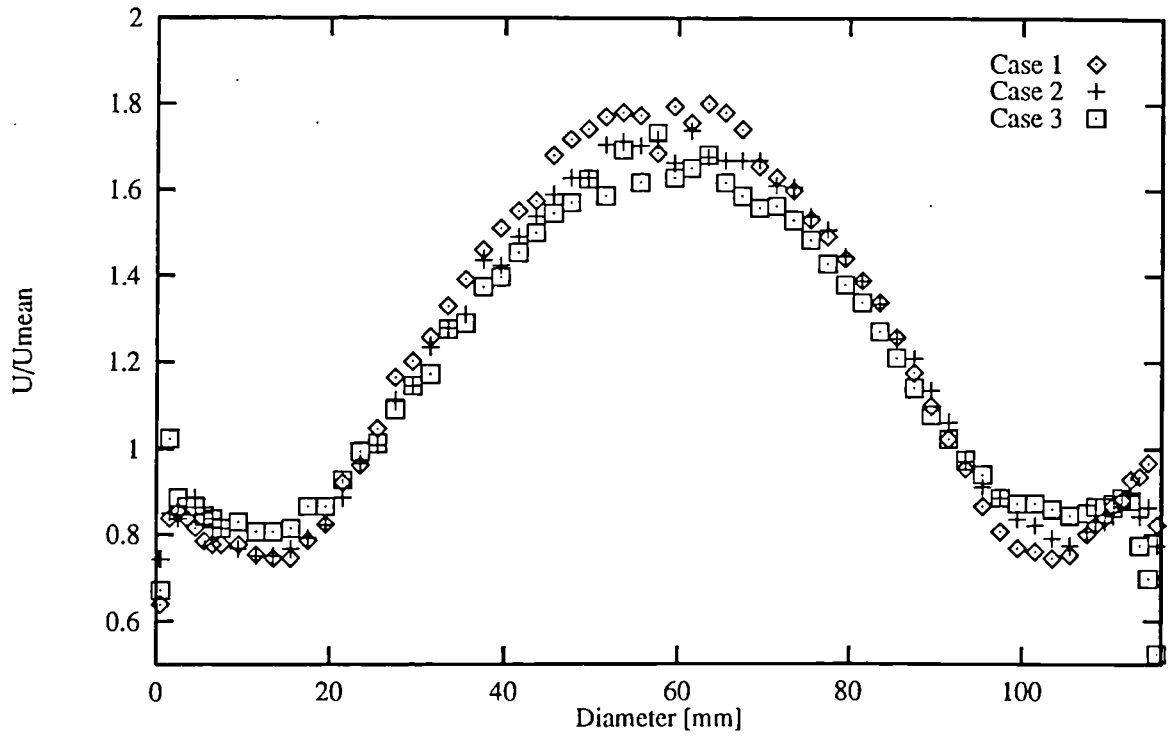

Figure 6.13(a) - Monolith velocity profiles; 6 " monolith , Re = 60 000, diffusers: Case 1 - 80°, Case 2 - 60°, Case 3 - 40°

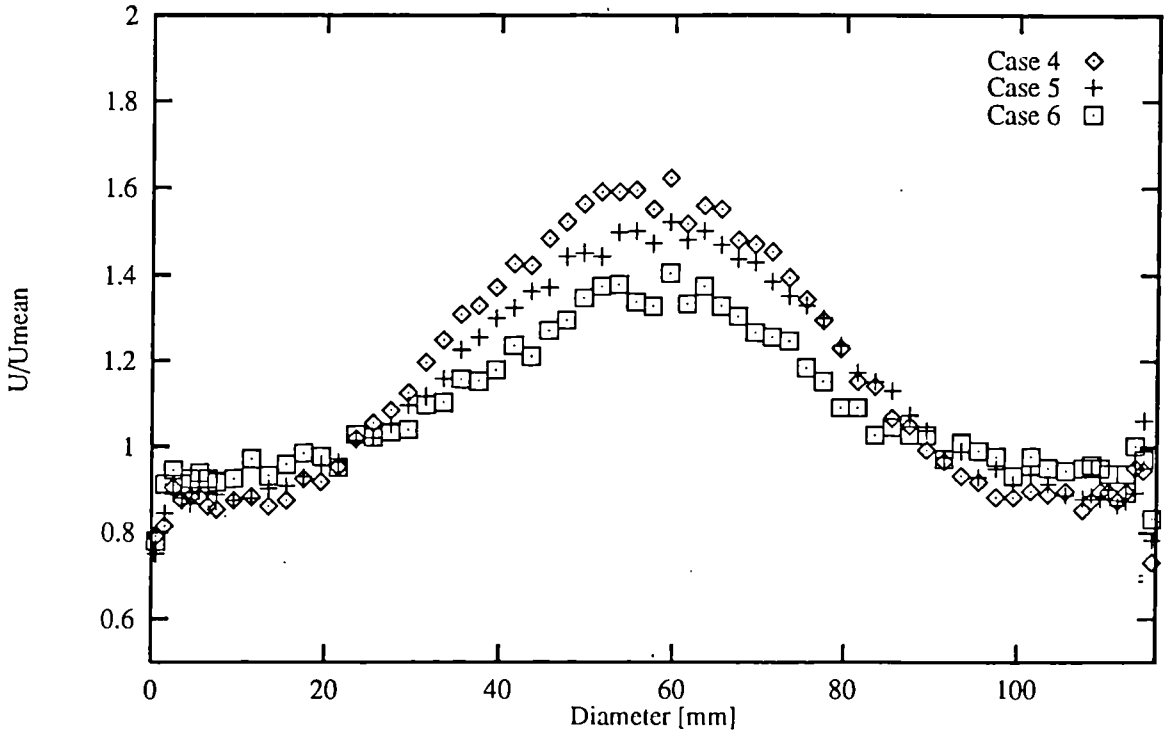

Figure 6.13(b) - Monolith velocity profiles; 6 " monolith , Re = 60 000, diffusers: Case 4 - 30°, Case 5 - 20°, Case 6 - 10°

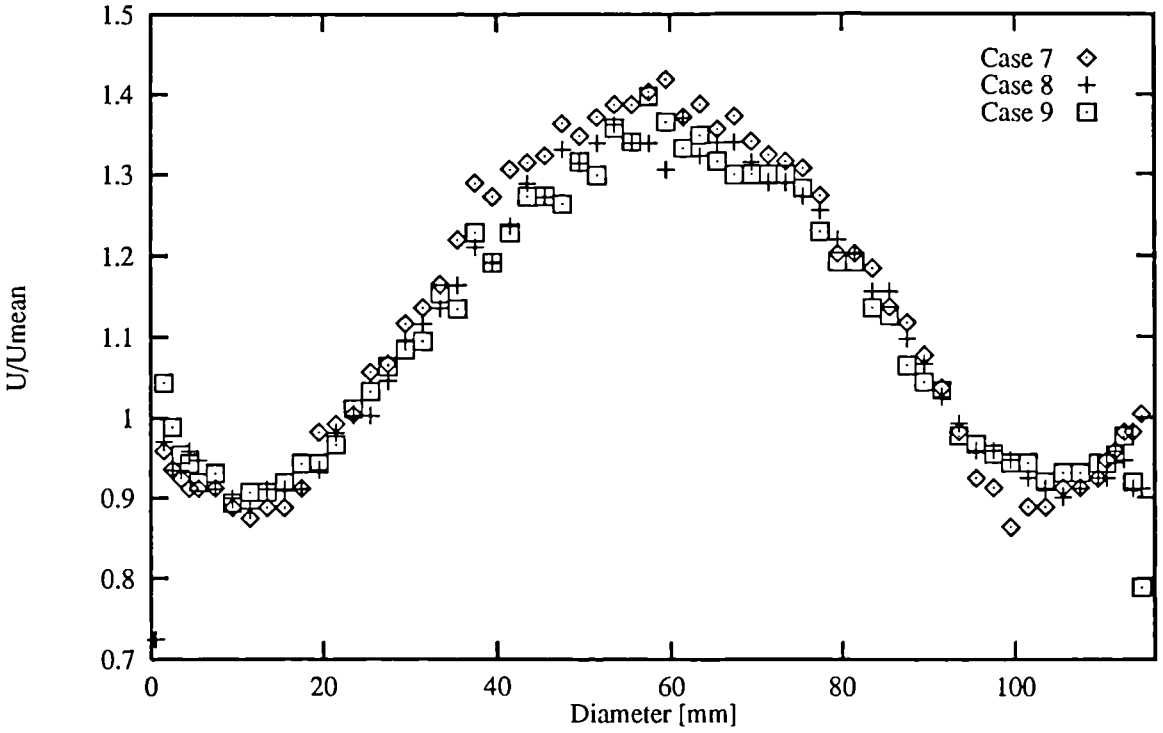

Figure 6.14(a) - Monolith velocity profiles; 6 " monolith , Re = 30 000, diffusers: Case 7 - 80°, Case 8 - 60°, Case 9 - 40°

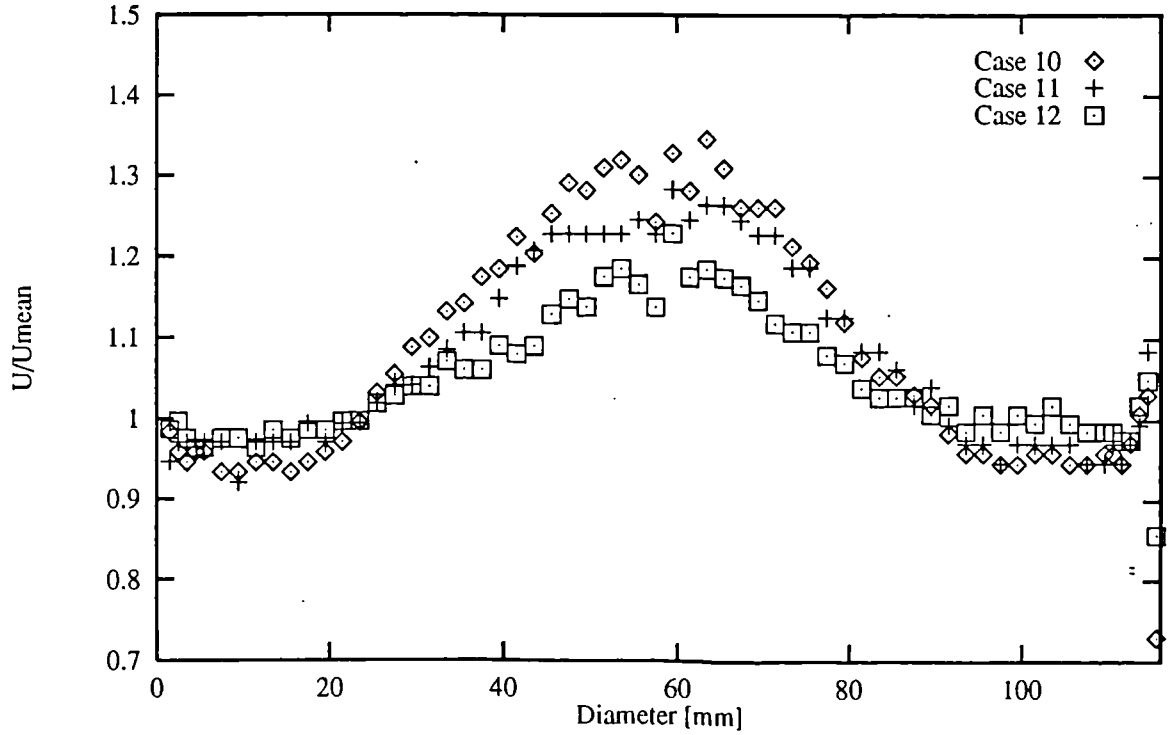

Figure 6.14(b) - Monolith velocity profiles; 6 " monolith , Re = 30 000, diffusers: Case 10 - 30°, Case 11 - 20°, Case 12 - 10°

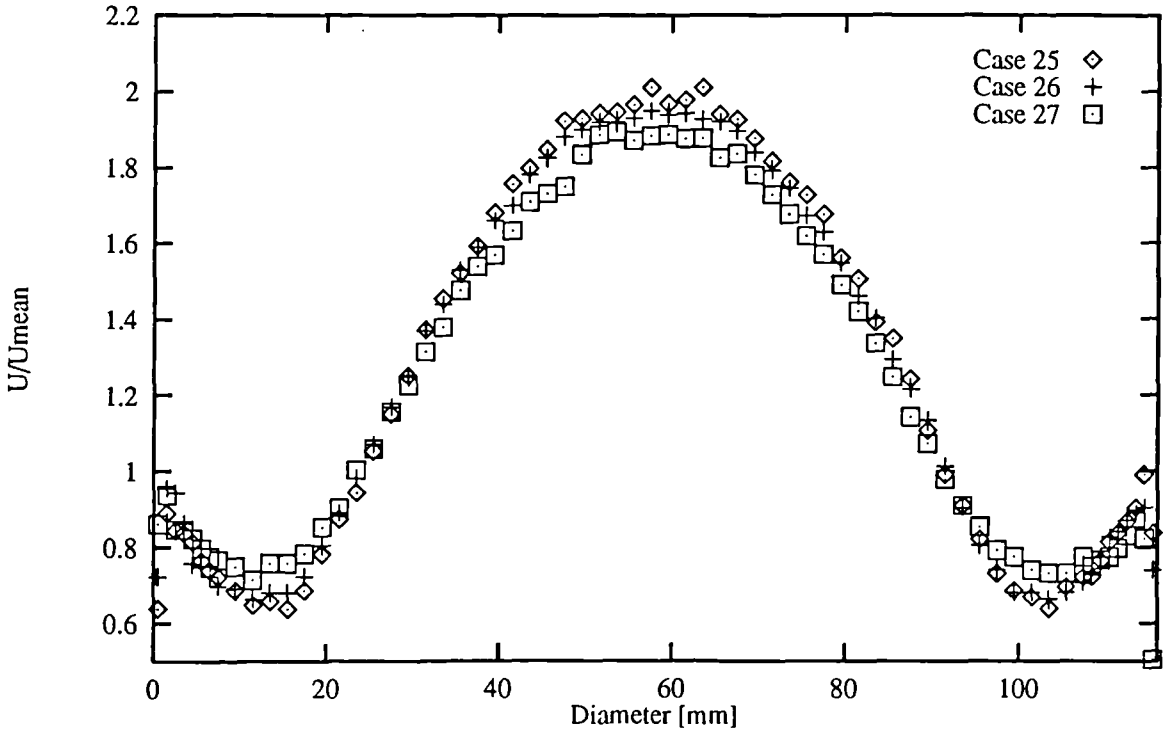

Figure 6.15(a) - Monolith velocity profiles; 4 " monolith , Re = 60 000, diffusers: Case 25 - 80°, Case 26 - 60°, Case 27 - 40°

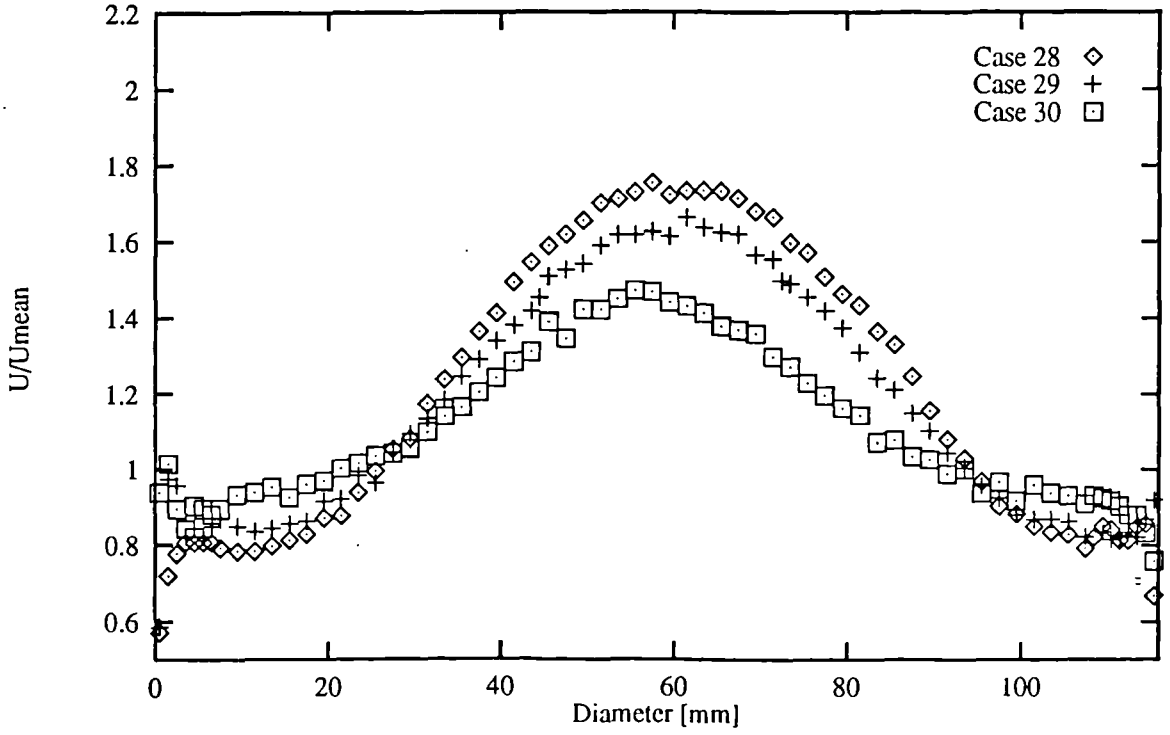

Figure 6.15(b) - Monolith velocity profiles; 4 " monolith , Re = 60 000, diffusers: Case 28 - 30°, Case 29 - 20°, Case 30 - 10°

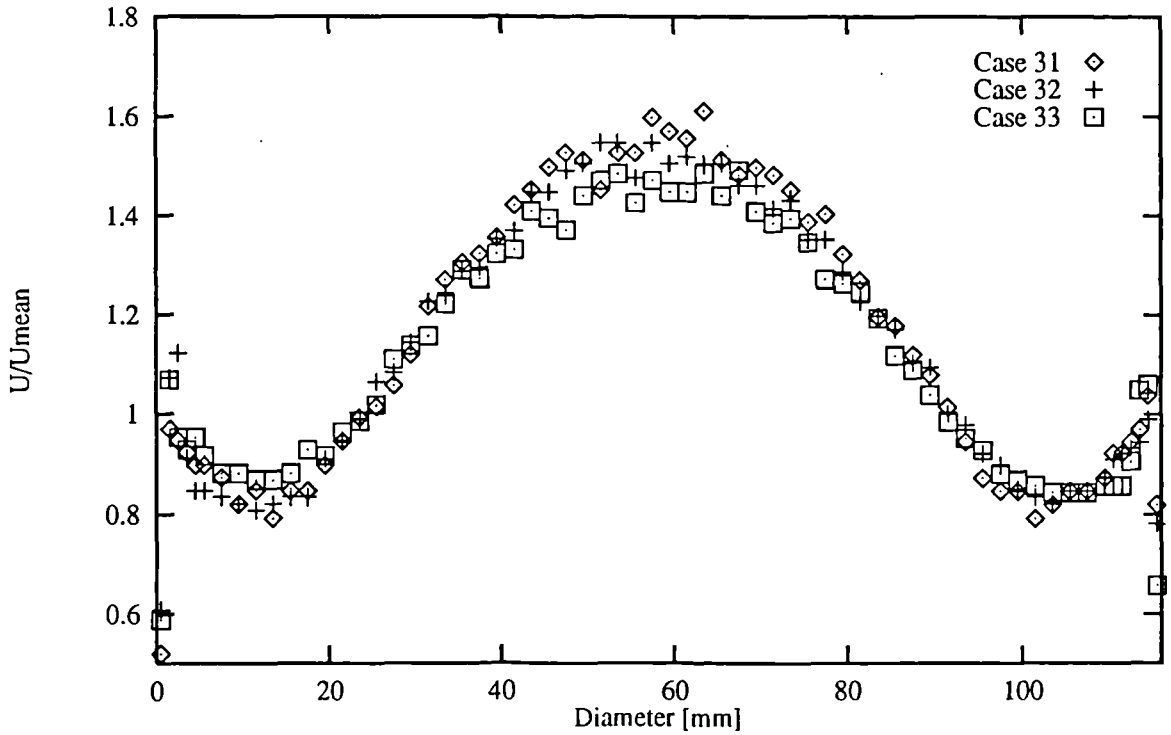

Figure 6.16(a) - Monolith velocity profiles; 4 " monolith , Re = 30 000, diffusers: Case 31 - 80°, Case 32 - 60°, Case 33 - 40°

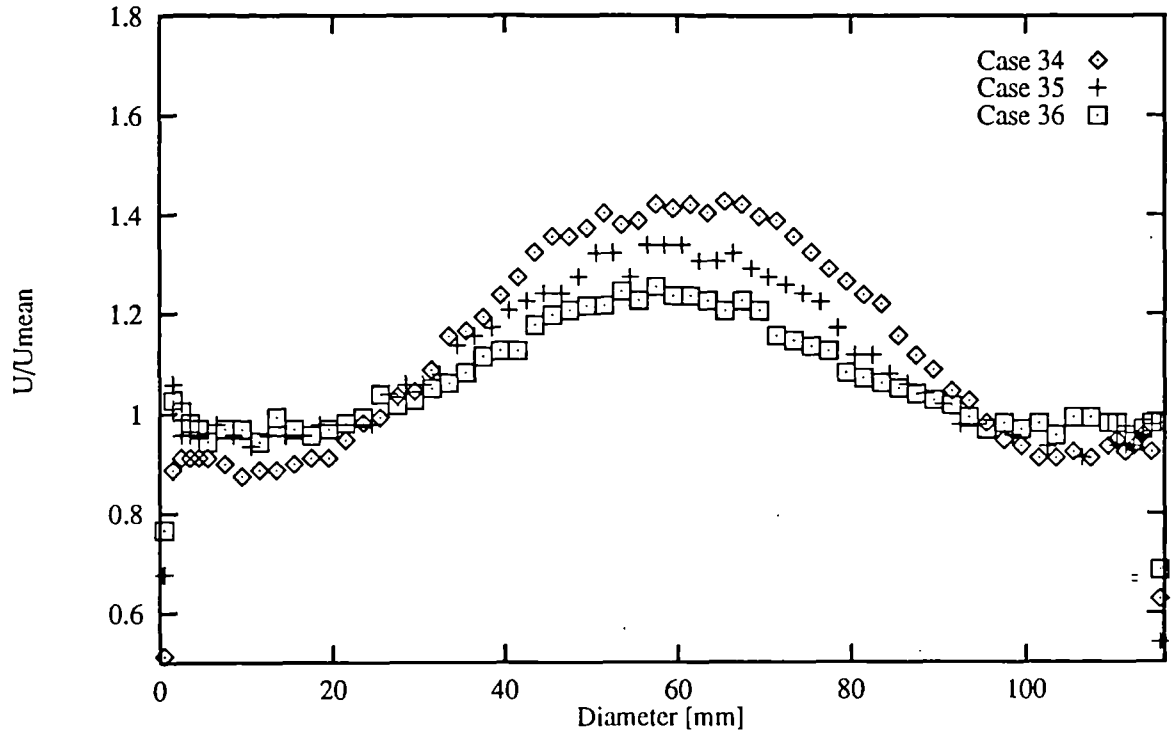

Figure 6.16(b) - Monolith velocity profiles; 4 " monolith , Re = 30 000, diffusers: Case 34 - 30°, Case 35 - 20°, Case 36 - 10°

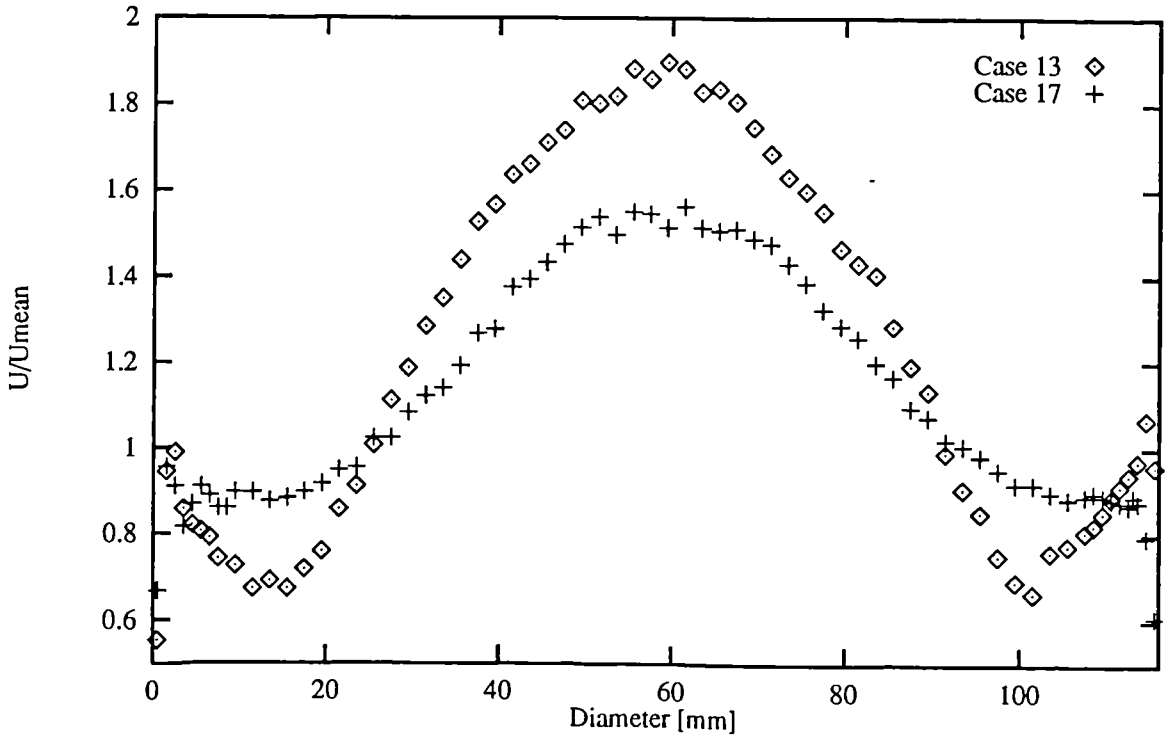

Figure 6.17 - Monolith velocity profiles; 5 " monolith , Re = 60 000, diffusers: Case 13 - 80°, Case 17 - 20°

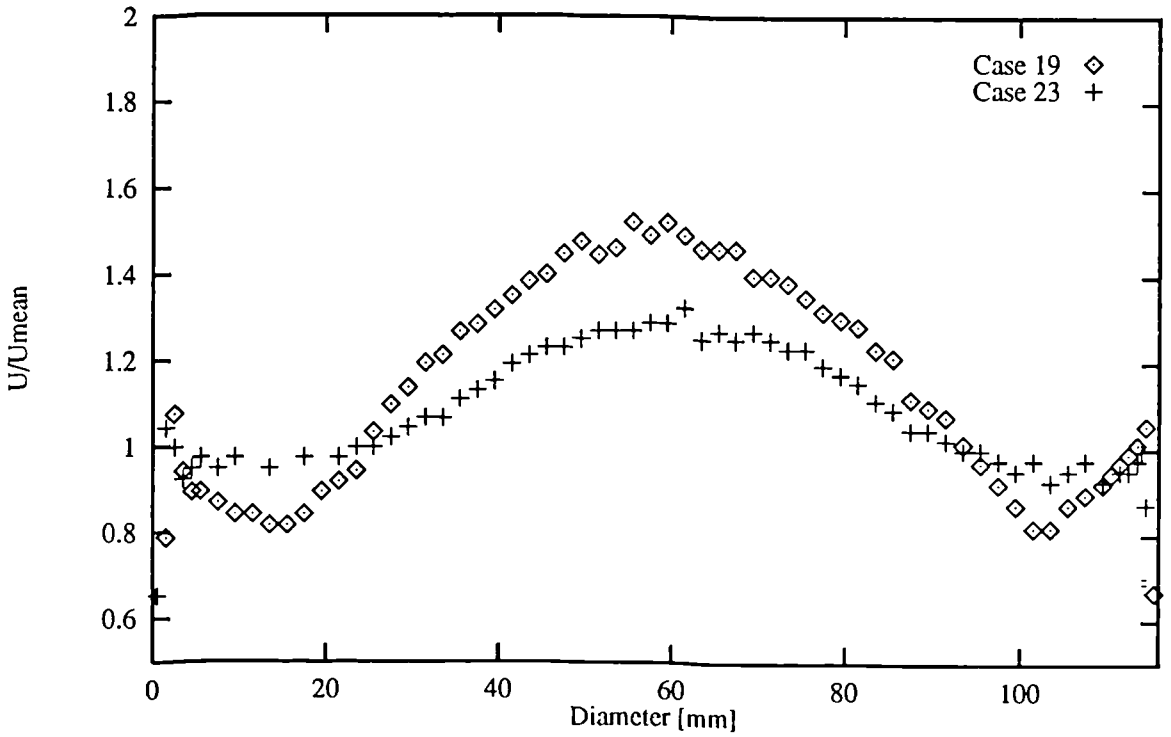

Figure 6.18 - Monolith velocity profiles; 5 " monolith , Re = 30 000, diffusers: Case 19 - 80°, Case 23 - 20°

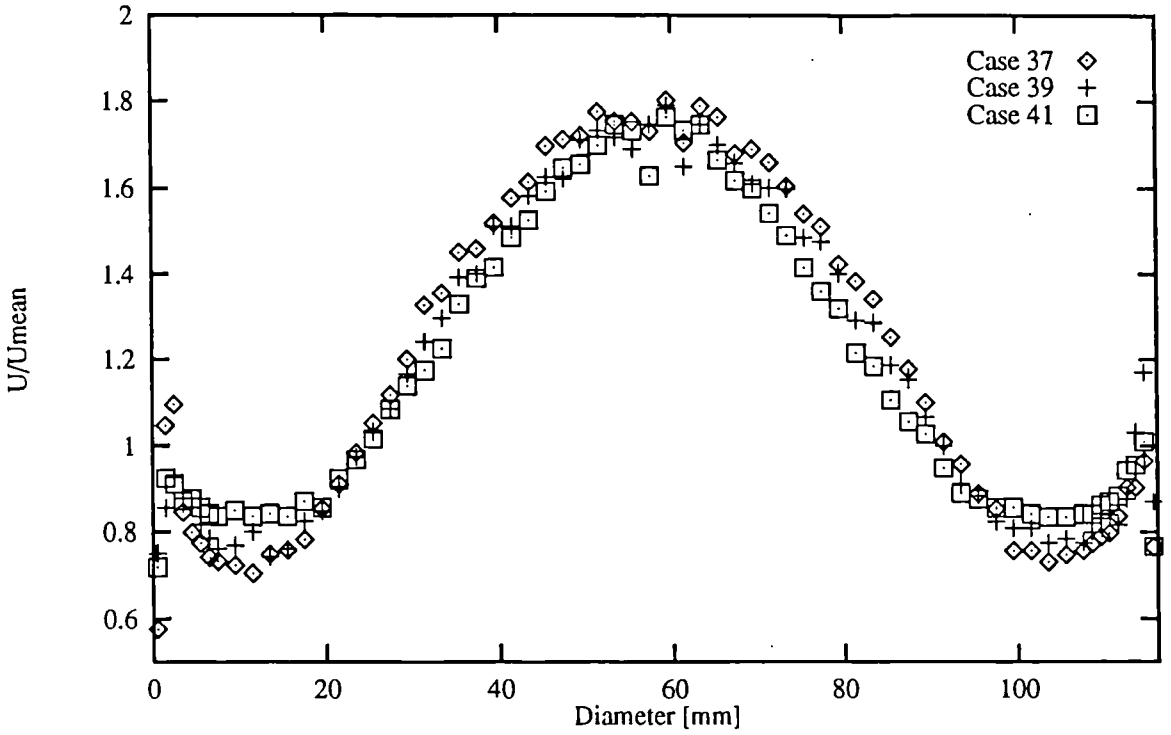

Figure 6.19 - Monolith velocity profiles; 6 " monolith , Re = 60 000, 180° expansions: Case 37 - 37 mm, Case 39 - 84 mm, Case 41 - 174 mm

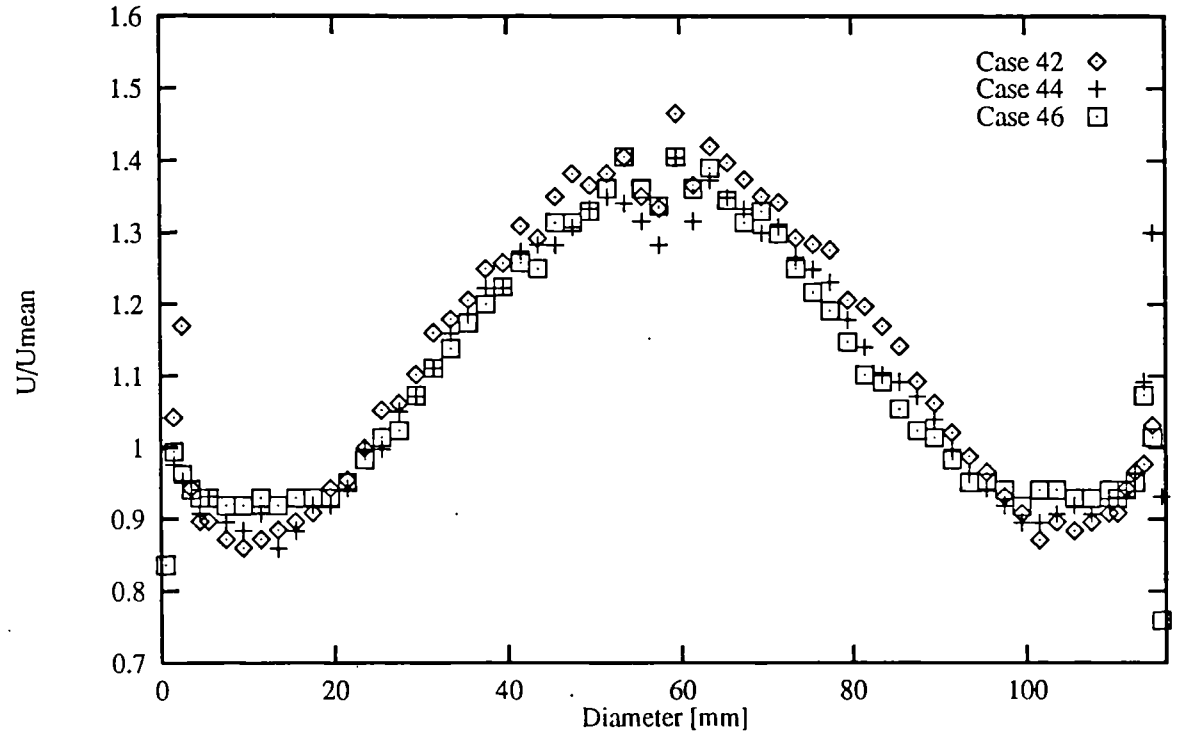

Figure 6.20 - Monolith velocity profiles; 6 " monolith , Re = 30 000, 180° expansions: Case 42 - 37 mm, Case 44 - 84 mm, Case 46 - 174 mm

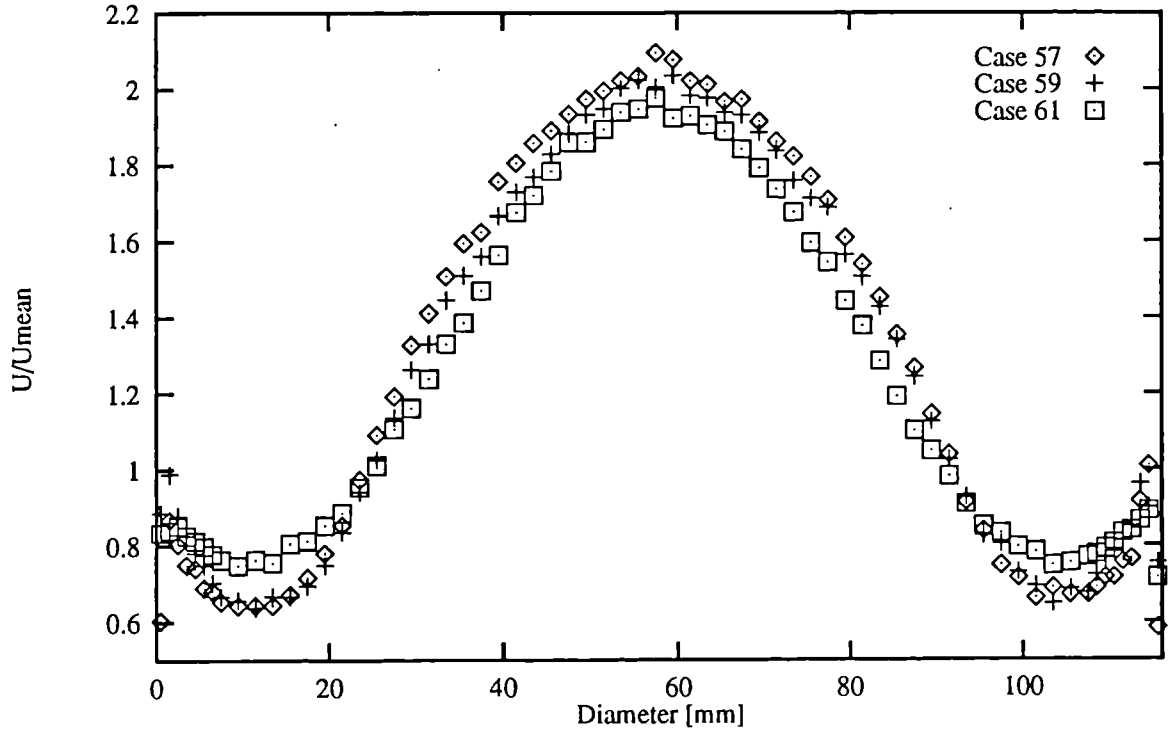

Figure 6.21 - Monolith velocity profiles; 4 " monolith , Re = 60 000, 180° expansions: Case 57 - 37 mm, Case 59 - 84 mm, Case 61 - 174 mm

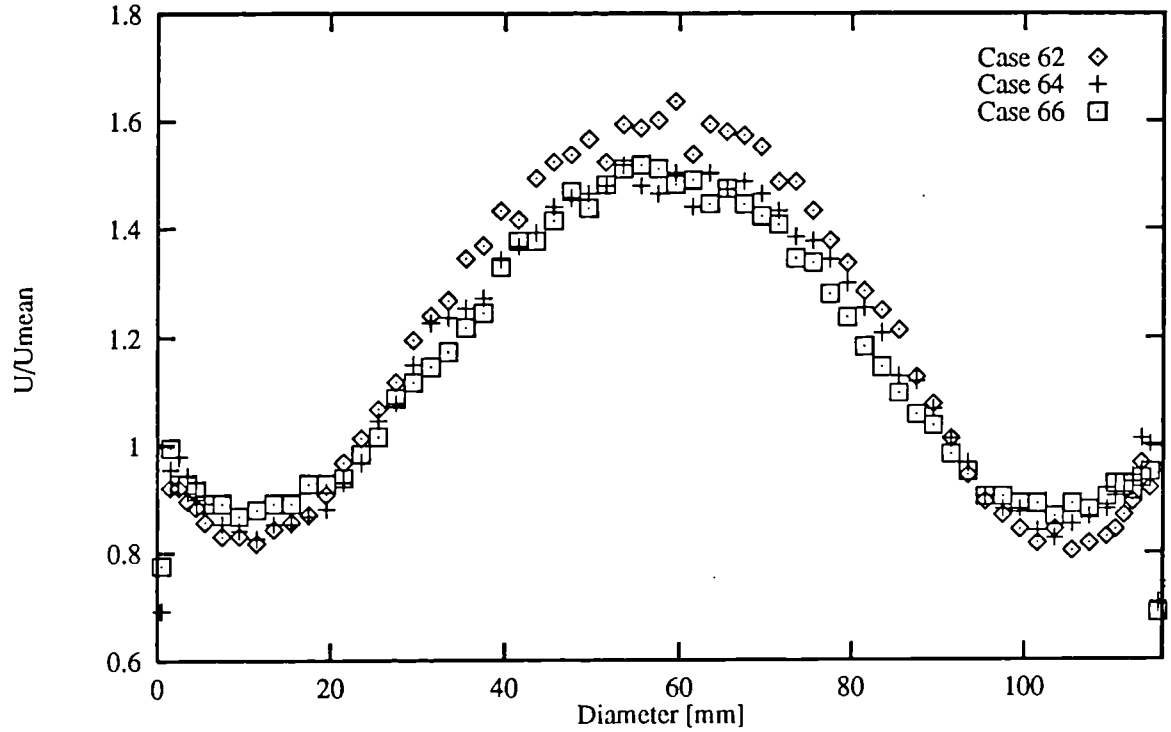

Figure 6.22 - Monolith velocity profiles; 4 " monolith , Re = 30 000, 180° expansions: Case 62 - 37 mm, Case 64 - 84 mm, Case 66 - 174 mm

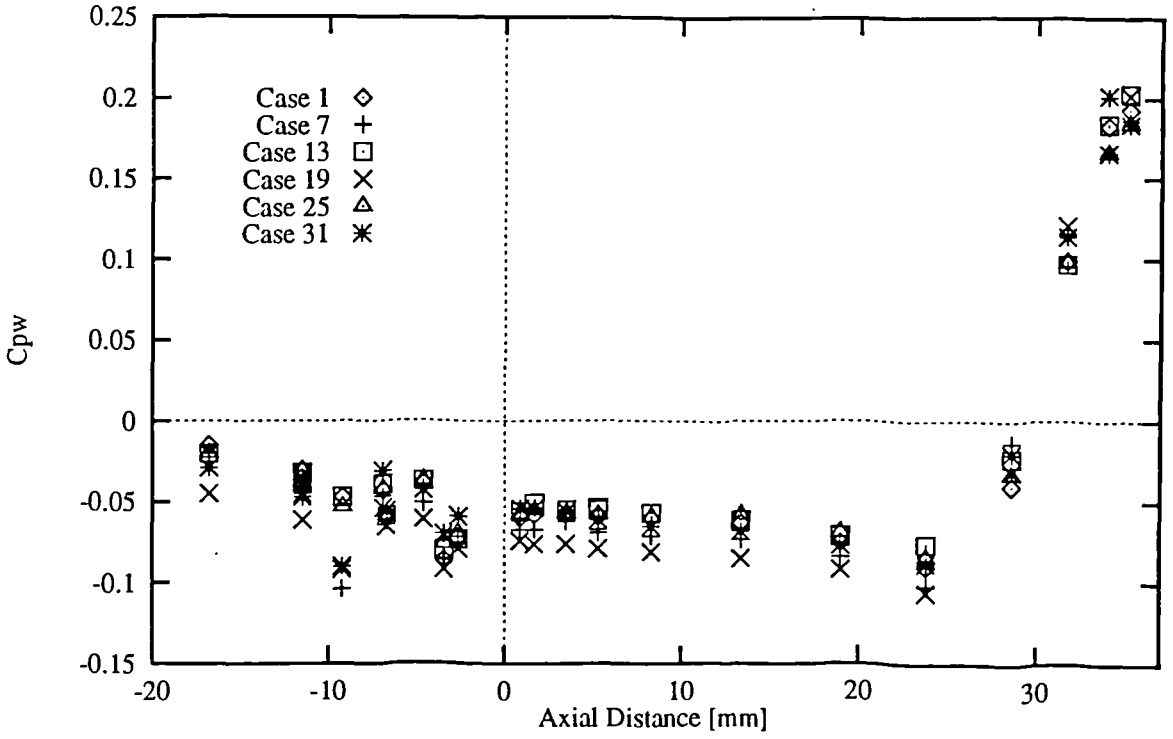

Figure 6.23 - Wall static pressure coefficients for the 80° diffusers: Re = 60 000 (Cases 1, 13, 25), Re = 30 000 (Cases 7, 19, 31); monoliths - 6" (Cases 1 & 7), 5" (Cases 13 & 19), 4" (Cases 25 & 31)

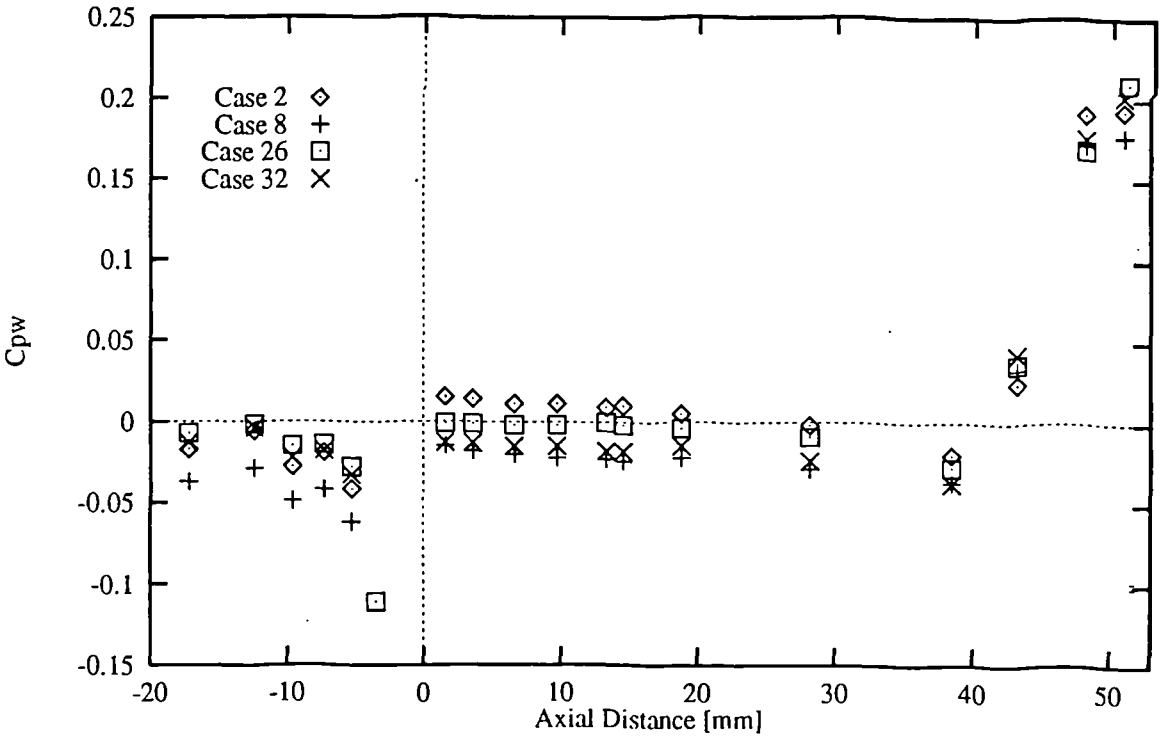

Figure 6.24 - Wall static pressure coefficients for the 60° diffusers: Re = 60 000 (Cases 2 & 26), Re = 30 000 (Cases 8 & 32); monoliths - 6" (Cases 2 & 8), 4" (Cases 26 & 32)

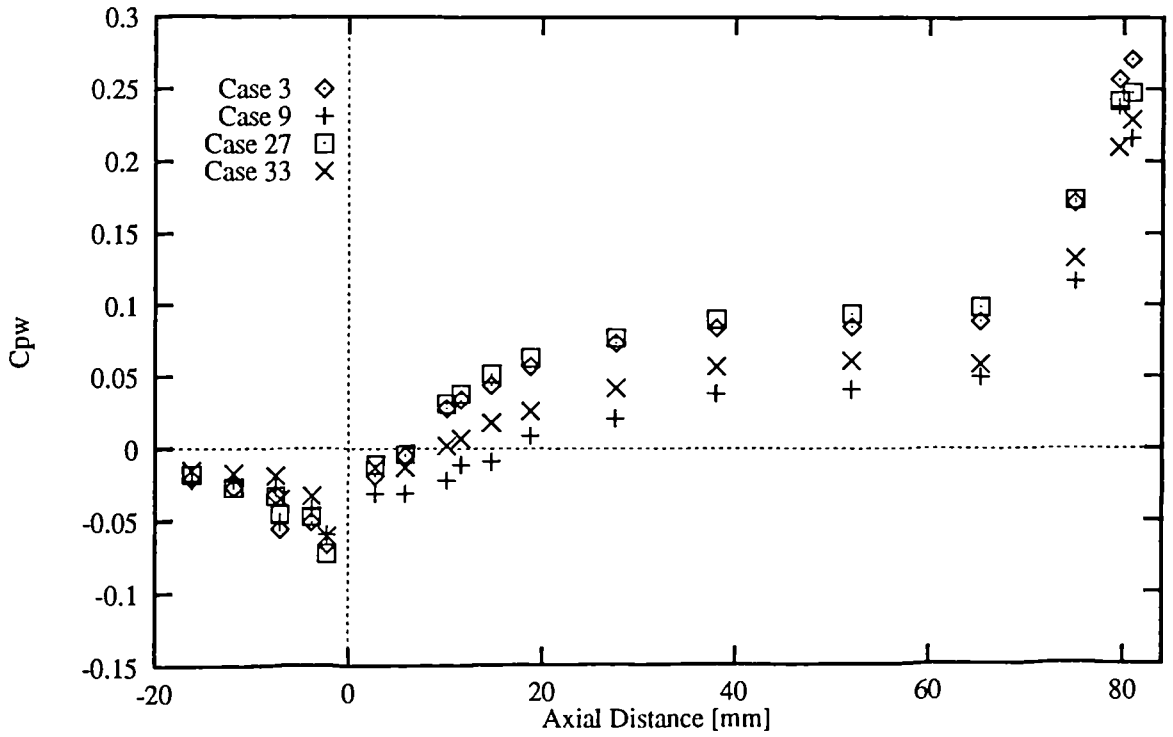

Figure 6.25 - Wall static pressure coefficients for the 40° diffusers: Re = 60 000 (Cases 3 & 27), Re = 30 000 (Cases 9 & 33); monoliths - 6" (Cases 3 & 9), 4" (Cases 27 & 33)

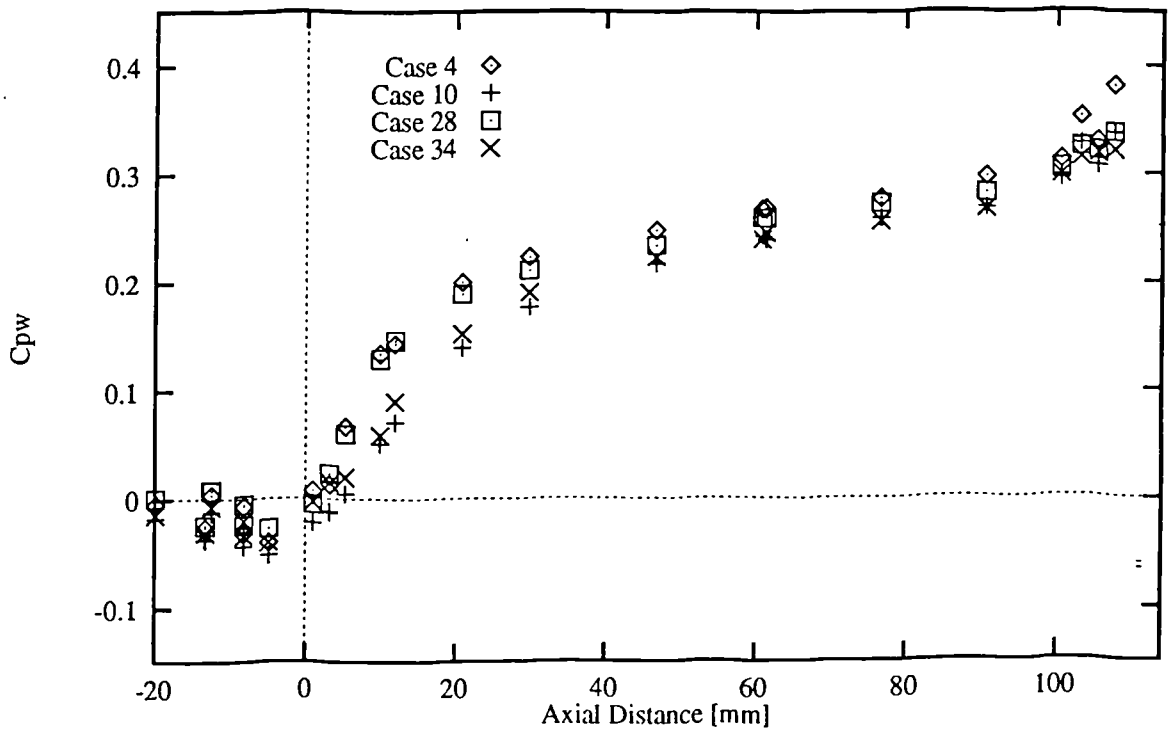

Figure 6.26 - Wall static pressure coefficients for the 30° diffusers: Re = 60 000 (Cases 4 & 28), Re = 30 000 (Cases 10 & 34); monoliths - 6" (Cases 4 & 10), 4" (Cases 28 & 34)

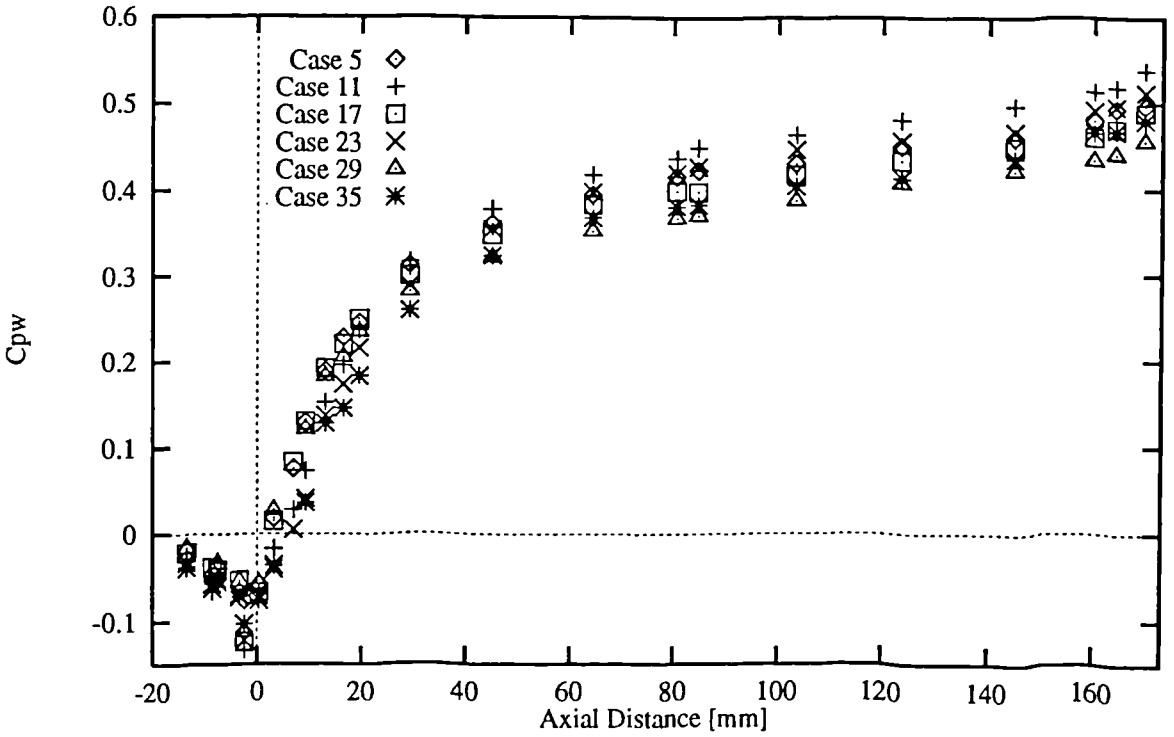

Figure 6.27 - Wall static pressure coefficients for the 20° diffusers: Re = 60 000 (Cases 5, 17, 29), Re = 30 000 (Cases 11, 23, 35); monoliths - 6" (Cases 5 & 11), 5" (Cases 17 & 23), 4" (Cases 29 & 35)

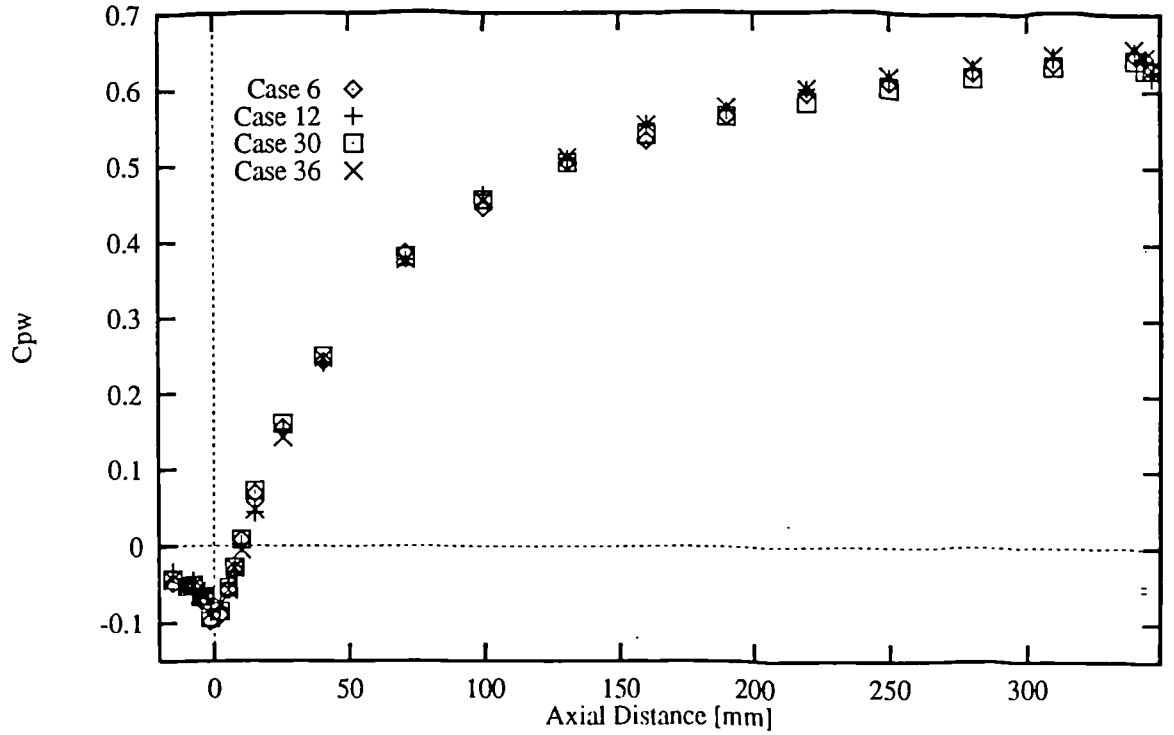

Figure 6.28 - Wall static pressure coefficients for the 10° diffusers: Re = 60 000 (Cases 6 & 30), Re = 30 000 (Cases 12 & 36); monoliths - 6" (Cases 6 & 12), 4" (Cases 30 & 36)

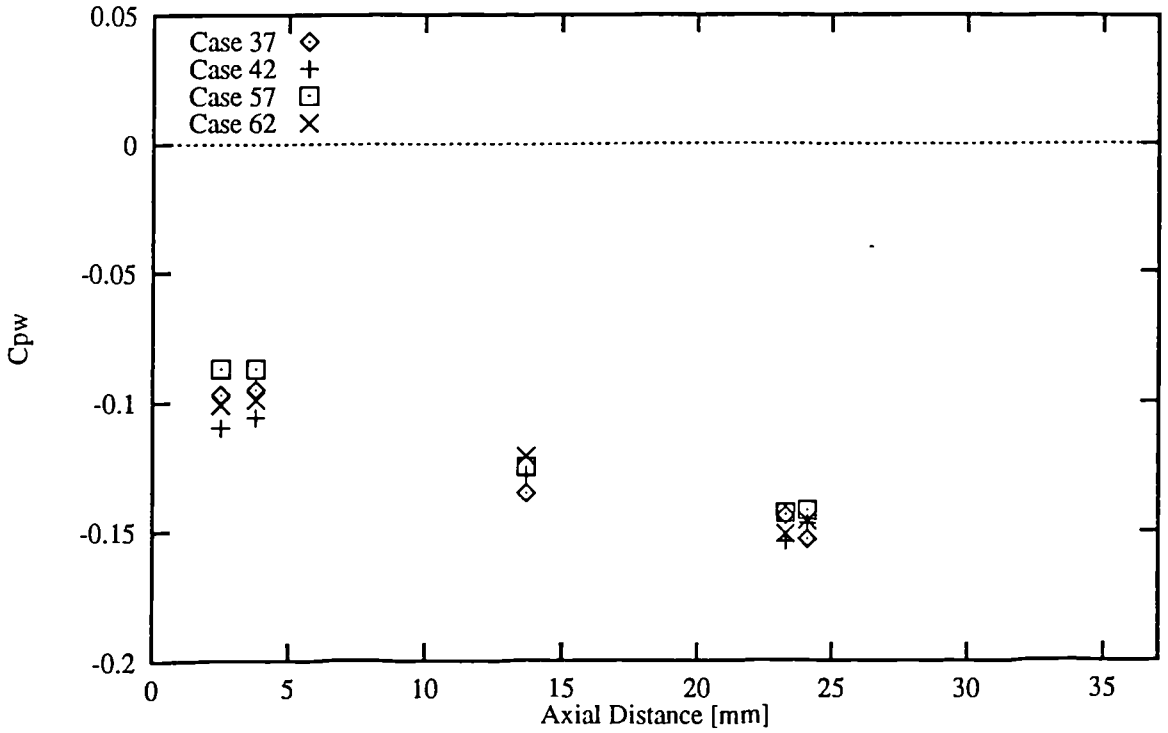

Figure 6.29 - Wall static pressure coefficients for the 37 mm 180° expansion: Re = 60 000 (Cases 37 & 57), Re = 30 000 (Cases 42 & 62); monoliths - 6" (Cases 37 & 42), 4" (Cases 57 & 62)

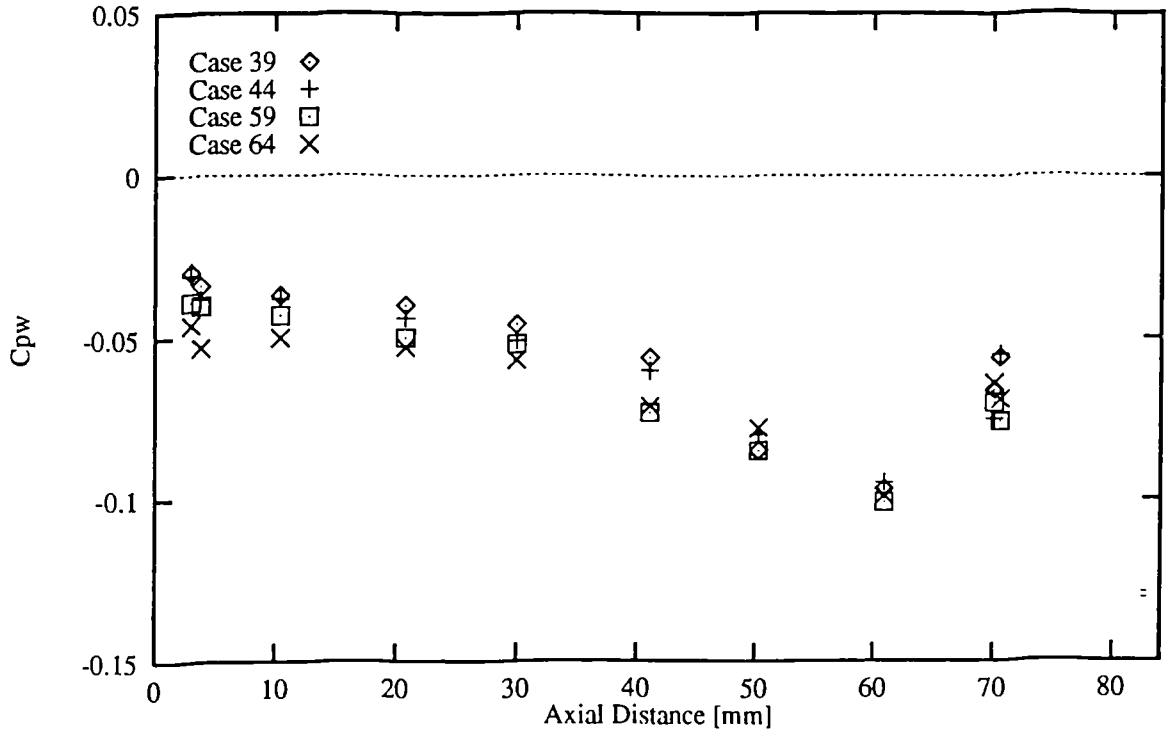

Figure 6.30 - Wall static pressure coefficients for the 84 mm 180° expansion: Re = 60 000 (Cases 39 & 59), Re = 30 000 (Cases 44 & 64); monoliths - 6" (Cases 39 & 44), 4" (Cases 59 & 64)

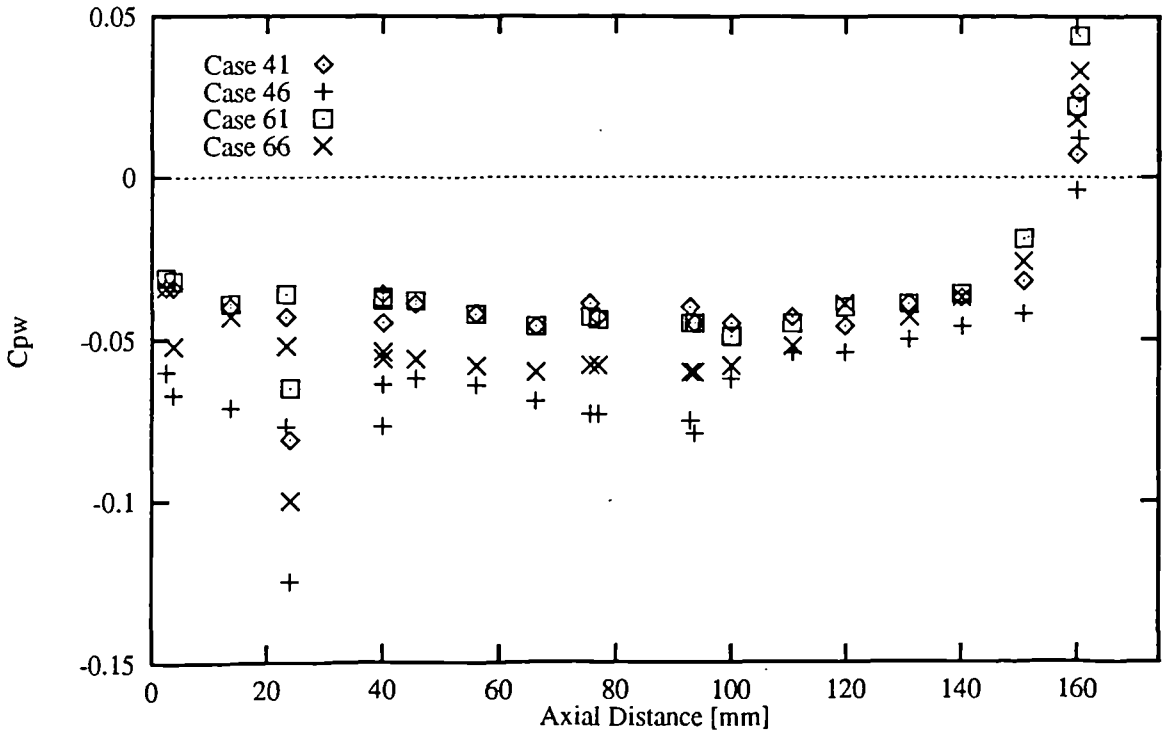

Figure 6.31 - Wall static pressure coefficients for the 174 mm 180° expansion: Re = 60 000 (Cases 41 & 61), Re = 30 000 (Cases 46 & 66); monoliths - 6" (Cases 41 & 46), 4" (Cases 61 & 66)

7 ISOTHERMAL STEADY FLOW PREDICTIONS

The first modelling decision that had to be made was which formulation to use for the monolith pressure drop term. Numerical analysis of laminar flow in a square duct shows that the axial pressure drop produced by boundary layers developing from a plug profile is predicted with acceptable accuracy by Equation 4.8. However, the flow field at the entrance to the monolith channels is likely to be significantly different from a plug profile. In most cases the entrance velocities will not be parallel to the channel direction, and because there is a sudden contraction in flow volume, a vena contracta will probably exist just downstream of the entrance. From these considerations, and the absence of any definite indications from the experimental results, it was felt that Equation 4.7 would be a more appropriate starting point for the pressure drop term.

As has been mentioned above, there are a variety of differencing schemes and turbulence models available within both PHOENICS and STAR-CD. To limit the number of computational cases and yet still test how accurately the various options can predict catalyst flow fields, it was decided that initially they would be applied to just one catalyst geometry, from which the most reliable combination of options could be found. The next stage of analysis would then involve testing this combination for mesh sensitivity on the chosen geometry. Once an appreciation of the level of mesh density required for mesh independent results was obtained, the analysis could be switched to applying the best modelling options to the remaining catalyst geometries. Consequently an assessment of how well the model predicted changes in the flow field, resulting from changes in geometry, would be obtained.

The choice of geometry for the initial studies was driven by the desire to provide the modelling approach with a taxing flow field and poor computational mesh, yet reduce the effect of any inaccuracies introduced by the assumptions made about the pressure drop relationship through the monolith. Originally it was felt that the influence of entrance effects would be smallest with a 6 inch monolith, the pressure drop being dominated by fully developed laminar flow. For these reasons the geometry selected for the initial stages of analysis was the 80° diffuser, with a 6 inch monolith, at a Re = 60 000.

When the work reported here began it was intended that the modelling would be carried out exclusively using the PHOENICS code. Unfortunately it became apparent that the original version of the code being used had several "bugs" within it that resulted in erroneous flow phenomena being predicted. In particular a spurious peak in the k and ε levels was predicted along the centre line of the geometry. Additionally, the number of "built-in" turbulence options was limited. Thus it was decided that, rather than wait for the suppliers of PHOENICS to correct the "bugs" and

introduce the scheduled turbulence models, flow simulations would be carried out using the STAR-CD code.

7.1 Preliminary Studies

The turbulence models available within STAR-CD are all based on the eddy-viscosity approach and consist of various two-equation models, a one-equation model and a zero equation model. Because of the absence of data on length scales within the inlet expansions it was felt that the greater generality of the two-equation models would be required for the analysis. It has also been shown (Habib and Whitelaw [86]) that the standard k-ε model, with wall functions, can produce reasonably accurate predictions of the flow fields within wide angled diffusers. Although all the two-equation models within STAR-CD are based on similar k and ε equations, it has been claimed that the slight differences between them can make a dramatic difference to the accuracy of predictions. For these reasons the following two-equation model variations were selected for the study;

(i) Standard k-ε model with wall functions, denoted "k-e+wall",

(ii) Renormalization group (RNG) k-ε model with wall functions, denoted "RNG+wall",

(iii) Standard k-ε model with the Norris-Reynolds [87] one-equation near wall model, denoted "k-e,NR",

(iv) RNG k-ε model with the Norris-Reynolds one-equation near wall model, denoted "RNG,NR".

The Norris-Reynolds one-equation model was chosen for the two-layer approach because it has been demonstrated (Rodi and Scheuerer [88]) to give reasonable results for diffuser flows.

To generate the fully developed velocity and turbulence profiles at the catalyst inlet the full 50 diameter length of upstream pipe was modelled using a mesh with between 20 to 45 cells in the radial direction and 200 to 300 cells in the axial direction. The pipe was given a uniform flow field at its entrance, with a turbulence intensity of 5% (Preliminary computational studies indicated that the velocity and turbulence profiles after 50 diameters are essentially independent of any reasonable pipe inlet conditions). With the air density and dynamic viscosity set, respectively, at 1.205 kg/m^3 and 1.81x10^{-5} kg/ms the corresponding mean inlet velocity at a Re = 60 000 is 16.5 m/s. Because the catalysts exhaust to atmosphere the static pressure across their exit planes will be uniform, and at atmospheric pressure. Consequently a fixed static pressure boundary was used as the outlet

boundary condition, the pressure being set at zero. As the flow is axisymmetric it is only necessary to model a thin sector running the length of the domain, each radial side being set as a symmetry plane. A sector angle of 0.05 radians was used throughout the study. The meshes used are of an essentially structured nature, an example being shown in Figure 4.1.

Unfortunately when this stage of the analysis was being carried out the internal dimensions of the monolith were believed to be those given by the manufacturers drawings, making the hydraulic diameter (d) 1.12 mm and the void fraction (α) 77.8%. It is acknowledged that these values are slightly greater than the measured values. However, they can still be used to evaluate the relative merit of the various modelling options provided it is remembered that their use will tend to give slightly more maldistributed velocity profiles and lower pressure drops. For square channels k_r in Equation 4.7 takes a value of 28.455. Thus β in Equation 4.21 was set at 527.7.

For all the isothermal flow simulations the part of the computational domain where the critical flow phenomena take place is the inlet expansion and the 20 mm of inlet pipe immediately upstream from the expansion. Thus variations in the computational meshes were concentrated within this region. For the initial studies two meshes were used in the critical section of the domain; a 80 x 45 (axial x radial) cell mesh (mesh 1) for the wall function models and a 60 x 30 cell mesh (mesh 2) for the two -layer models. The latter mesh had an additional 15 cells in the near wall region.

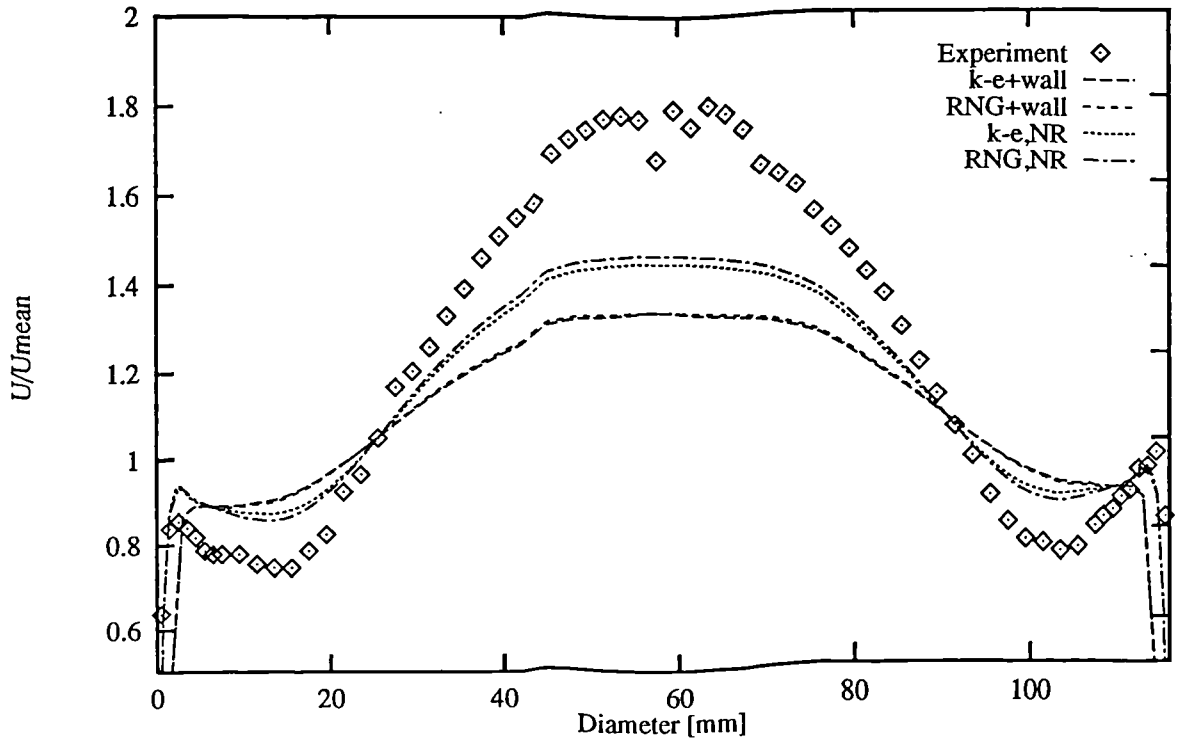

Figure 7.1 - Predicted monolith velocity profiles for the 80° diffuser, with 6" monolith, using the upwind differencing scheme and meshes 1 and 2

At first each turbulence model was tested with the upwind differencing scheme. The velocity profiles from these tests are presented in Figure 7.1, along with the experimental data. It can be seen that the predicted profiles are all similar in shape to the experimental profile, having their maximum velocity at the centre line and a local maximum adjacent to the monolith periphery. As with the experimental data the maximum to mean velocity ratio can be used as a one value index of predicted flow maldistribution. The maldistribution ratios from each profile, together with the non-dimensional drop in static pressure, are presented in Table 7.1. A comparison of the predicted and experimental wall C_{pw} distributions is made in Figure 7.2. All the results show that the two-layer approaches give predictions that are closer to the experimental data than the wall function approaches, the RNG version being marginally better than the standard k-ε version. Thus the RNG two-layer model was selected for the rest of the study.

Table 7.1 - Initial studies: Predictions for the 80° diffuser, with a 6" monolith at Re = 60 000.

Turbulence Model	Mesh	Differencing Scheme	ΔP_s*	Maldistribution Ratio (M)
k-e+wall	1	Upwind	1.206	1.340
RNG+wall	1	Upwind	1.196	1.341
k-e,NR	2	Upwind	1.411	1.450
RNG,NR	2	Upwind	1.423	1.478
RNG,NR	2	SFCD	1.482	1.503
RNG,NR	3	SFCD	1.469	1.503
RNG,NR	4	SFCD	1.472	1.503
RNG,NR	5	SFCD	1.467	1.504
Experimental	-	-	1.655	~1.78

~ indicates approximate nature of experimental M values.

ΔP_s*= static pressure drop non-dimensionalised against inlet dynamic pressure,

$$\text{i.e. } \Delta P_s^* = \Delta P_s / \left(\rho \overline{U}_0^2 / 2\right)$$

To test the potential for reducing numerical errors by using a higher order differencing scheme the most sophisticated second order scheme available within STAR-CD, designated the self filtering central difference (SFCD) scheme, was employed (see Appendix B). So that an assessment of its performance can be made it was applied to mesh 2 with the RNG two-layer model. As can be seen from Table 7.1 a slight improvement in both the velocity profile and pressure drop was achieved, thus it was retained for the rest of the study. Mesh sensitivity was investigated by using a 120 x 60 cell mesh with two levels of refinement in the near wall region, 15 cells (mesh 3) and 30 cells (mesh 4), and a 160 x 90 cell mesh with 30 cells in the near wall region (mesh 5). Comparison of the maldistribution ratio and pressure drop values, included in Table 7.1, and the wall C_{pw} values, presented in Figure 7.3, from these simulations indicates that meshes 3, 4 and 5 all give mesh independent solutions. Even mesh 2 gives solutions that are very close to the other meshes.

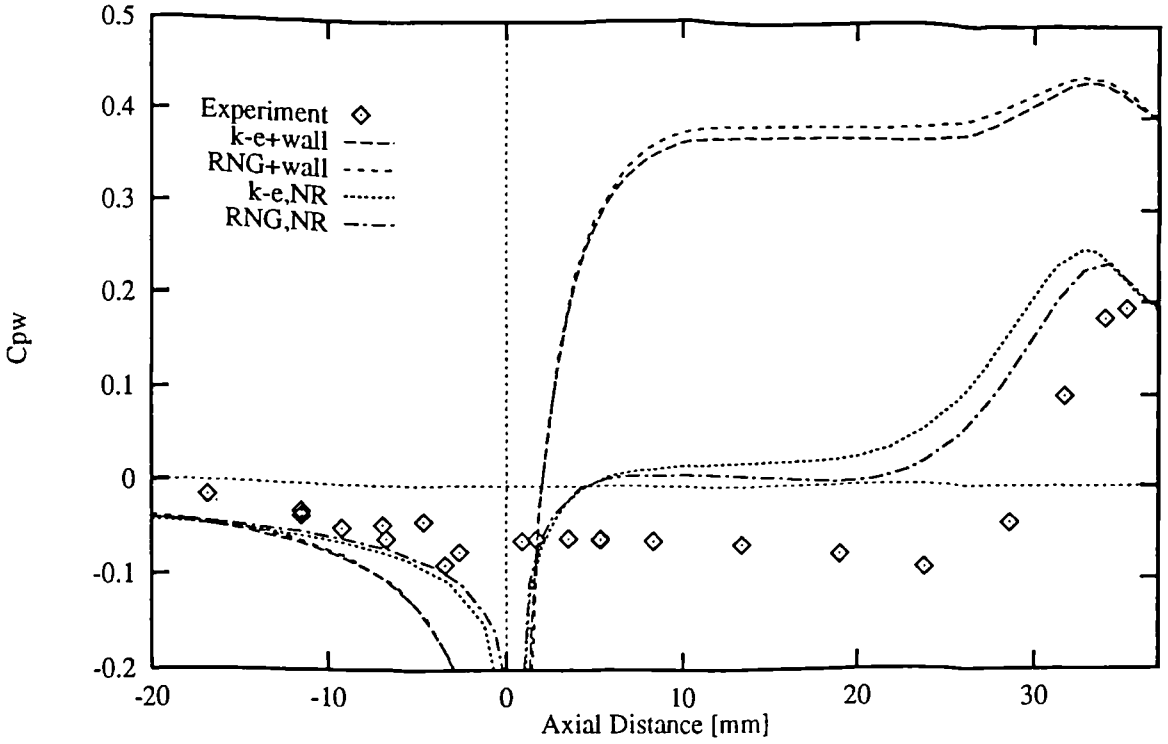

Figure 7.2 - Predicted wall static pressure coefficients for the 80° diffuser, with 6" monolith, using the upwind differencing scheme and meshes 1 and 2

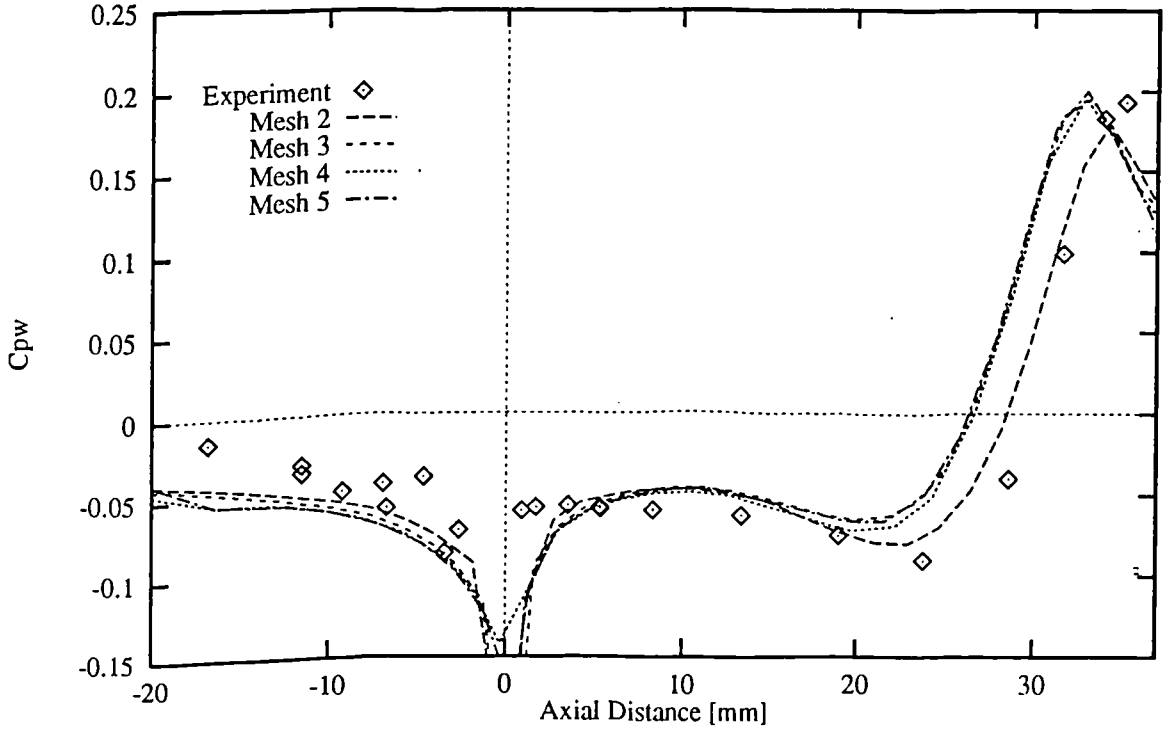

Figure 7.3 - Predicted wall static pressure coefficients for the 80° diffuser, with 6" monolith, using the SFCD differencing scheme and RNG,NR turbulence model

Thus the minimum level of mesh refinement required for mesh independent solutions is that corresponding to meshes 2 and 3.

7.2 Predictive Performance Under Geometric Variations

The next stage of the study combined the SFCD scheme with the RNG two-layer model to simulate a selection of the remaining catalyst geometries. Because analysis of the experimental data indicated that the flow fields are strongly influenced by the Re, and because most of the experimental results were taken at Re's slightly different from 60 000 and 30 000, it was felt that the predictions should be carried out at Re's that were more representative of the experimental values. Thus for the remaining predictions Re's of 62 000 and 33 000 were taken. The geometries chosen for simulation consisted of;

(i) the full range of diffusers with the 6 inch monolith,

(ii) the 80°, 40° and 20° diffusers with the 4 inch monolith,

(iii) the 80° diffuser with the 5 inch monolith,

(iv) all three 180° expansions with the 6 inch monolith,

(vi) the 37 mm 180° expansion with the 4 inch monolith,

each geometry being simulated at both Re's. The rationale for not including all the geometries was the considerable amount of processor time needed, and that no additional elucidation of the computational models performance would be gained.

Again when this stage of the analysis was started the monolith void fraction (α) and channel hydraulic diameters (d) were still believed to be 77.8% and 1.12 mm respectively. When it became apparent that these values were incorrect most of the simulations had already been carried out. Consequently it was decided that rather than discard all the simulations the programme would be completed using the same set of monolith parameters, so that trends resulting purely from variations in diffuser geometry and Re could be followed. The results from these predictions are presented in Table 7.2. (Note that mesh size does not include the 15 cells in the near wall region.)

Table 7.2 - Results from extended simulation programme, using RNG,NR and SFCD options with $\alpha = 0.778$ and $d = 1.12$ mm

		Predicted Results		Experimental Results		% Error in Predicted Results	
Case	Mesh	ΔP_s*	M	ΔP_s*	M	ΔP_s*	M
Diffusers							
6" Monolith; Re ~ 60 000							
1	90 x 60	1.427	1.514	1.665	1.78	14.3	14.9
2	120 x 60	1.366	1.481	1.619	1.70	15.6	12.9
3	110 x 50	1.229	1.396	1.569	1.65	21.7	15.4
3a	110 x 50	1.229	1.396	1.639	1.65	25.0	15.4
4	120 x 50	1.128	1.341	1.488	1.57	24.2	14.6
5	130 x 50	1.034	1.278	1.330	1.50	22.3	14.8
6	200 x 50	0.952	1.159	1.221	1.37	22.0	15.4
6" Monolith; Re ~ 30 000							
7	90 x 60	2.971	1.290	3.317	1.39	10.4	7.2
8	120 x 60	2.909	1.272	3.260	1.36	10.8	6.5
9	110 x 50	2.778	1.227	3.291	1.36	15.6	9.8
9a	110 x 50	2.778	1.227	3.320	1.36	16.3	9.8
10	120 x 50	2.678	1.195	2.989	1.32	10.4	9.5
11	130 x 50	2.594	1.160	3.177	1.26	18.4	7.9
12	200 x 50	2.510	1.093	2.867	1.20	12.5	8.9
4" Monolith; Re ~ 60 000							
25	90 x 60	0.839	1.741	1.077	1.98	22.0	12.1
27	110 x 50	0.641	1.573	0.973	1.88	34.1	16.3
29	130 x 50	0.452	1.398	0.651	1.63	30.6	14.2
4" Monolith; Re ~ 30 000							
31	90 x 60	1.859	1.423	2.183	1.57	14.8	9.4
33	110 x 50	1.659	1.330	2.045	1.48	18.9	10.1
35	130 x 50	1.491	1.236	1.730	1.34	13.8	7.8
5" Monolith; Re ~ 60 000							
13	90 x 60	1.131	1.609	1.326	1.88	14.7	14.4
5" Monolith; Re ~ 30 000							
19	90 x 60	2.414	1.344	2.765	1.51	12.7	11.0
180° Expansions							
6" Monolith; Re ~ 60 000							
37	64 x 64	1.530	1.566	1.752	1.78	12.7	12.0
39	104 x 64	1.474	1.526	1.731	1.74	14.8	12.3
41	184 x 64	1.464	1.508	1.623	1.75	9.8	13.8
6" Monolith; Re ~ 60 000							
42	64 x 64	3.082	1.326	3.298	1.42	6.5	6.6
44	104 x 64	3.028	1.301	3.272	1.36	7.5	4.3
46	184 x 64	3.014	1.288	3.181	1.39	5.2	7.3
6" Monolith; Re ~ 60 000							
57	64 x 64	0.940	1.813	1.073	2.07	12.4	12.4
6" Monolith; Re ~ 60 000							
62	64 x 64	1.989	1.482	2.208	1.61	9.9	8.0

ΔP_s*= static pressure drop non-dimensionalised against inlet dynamic pressure,

Discovery of the variance between the specified and measured internal dimensions of the monoliths late in the programme meant that there was only sufficient time to carry out repeat simulations, using the measured dimensions, of a selection of catalyst geometries. The geometries tested, and the results, are presented in Table 7.3. Note that meshes and simulation parameters are identical to those used for the corresponding cases in Table 7.2, except for the adjustments to α and d (see Table 5.1 for details).

Table 7.3 - Results from extended simulation programme, using RNG,NR and SFCD options with measured α and d values.

		Predicted Results		Experimental Results		% Error in Predicted Results	
Case	β	ΔP_s*	M	ΔP_s*	M	ΔP_s*	M
			Diffusers				
			6" Monolith; Re ~ 60 000				
1	587.1	1.625	1.468	1.665	1.78	2.4	17.5
3	587.1	1.428	1.362	1.569	1.65	9.0	17.5
5	587.1	1.237	1.252	1.330	1.50	7.0	16.5
			6" Monolith; Re ~ 30 000				
7	587.1	3.344	1.262	3.317	1.39	-0.8	9.2
9	587.1	3.145	1.205	3.291	1.36	4.4	11.4
11	587.1	2.967	1.148	3.177	1.26	6.6	8.9
			4" Monolith; Re ~ 60 000				
25	619.1	1.042	1.645	1.077	1.98	3.2	16.9
29	619.1	0.657	1.347	0.651	1.63	-0.9	17.4
			4" Monolith; Re ~ 30 000				
31	619.1	2.244	1.365	2.183	1.57	-2.8	13.1
35	619.1	1.875	1.205	1.730	1.34	-8.4	10.1
			5" Monolith; Re ~ 60 000				
13	587.1	1.297	1.554	1.326	1.88	2.2	17.3
			5" Monolith; Re ~ 30 000				
19	587.1	2.727	1.312	2.765	1.51	1.4	13.1
			180° Expansions				
			6" Monolith; Re ~ 60 000				
37	587.1	1.730	1.517	1.752	1.78	1.3	14.8
			6" Monolith; Re ~ 30 000				
42	587.1	3.458	1.296	3.298	1.42	-4.9	8.7

Note: negative error indicates that the model has over predicted the performance parameter.

β - monolith resistance set using Equation 4.21

Figures 7.7 to 7.14 have been included so that a comparison can be made between the experimental and predicted velocity profiles, produced using the measured monolith dimensions, of a selection of catalyst geometries. They show that, for the geometries selected, the computational model produces velocity profiles that are qualitatively the correct shape. The maximum velocity appears

at the centreline, and local velocity maxima appear at the monolith periphery. This pattern is repeated with the results from the remaining geometries and the simulations carried out using the design monolith dimensions. Predicted and experimental wall static pressure distributions are presented in Figures 7.15 to 7.23.

7.3 Sources of Error

A quick inspection of the results presented in Tables 7.2 and 7.3 indicates that, with both sets of monolith dimensions, the model always under predicts the maldistribution ratio and generally under predicts pressure drop. When the measured monolith dimensions are used the prediction of pressure drop is more accurate, being consistently within 5% of the experimental results and in some cases even being over predicted. Unfortunately, however, the measured monolith dimensions produce velocity profiles that are flatter than those given when the design dimensions are used, errors being as high as 17.5%. A number of possible causes for the discrepancies between the predictions and experimental data have been identified.

7.3.1 Numerical Errors

Numerical errors arise as a result of the discretization method used. Discretization is by its nature an approximation, the approximation becoming progressively better as the computational mesh becomes finer. As has been indicated in Appendix B, differencing schemes can be a major contributor to numerical errors, particularly if the predominant flow direction is at an oblique angle to the mesh, where upon numerical diffusion can become a problem. The smoothing out of steep gradients that numerical diffusion causes will lead to a greater rate of momentum transfer, in the radial direction, within the inlet expansion. Consequently the distribution of momentum across the monolith inlet face will be more uniform. By using the nominally second order SFCD differencing scheme, and by obtaining a mesh independent solution, it is believed that any numerical diffusion will be small. Increasingly finer meshes tend to reduce numerical diffusion.

Another source of numerical errors results from distortions in the computational mesh. If the computational cells are excessively non-orthogonal calculation of the mass fluxes at some cell faces requires the use of exaggerated approximations. One of the benefits from simulating 180° expansions is that a completely orthogonal mesh can be used. Although results from these simulations agree more closely with the experimental data than the results from the corresponding diffuser simulations, the velocity profiles are still too flat. Whether the closer agreement with experiment is due to a better quality mesh is uncertain. It could be due to generally more reliable predictions in the vicinity of the flow separation point or subtle changes in the appropriateness of

the near wall turbulence model. In addition, the errors from a non-orthogonal mesh should reduce as the mesh becomes finer, mesh independence indicating that the errors are small.

7.3.2 Turbulence Models

An indication of how turbulence models affect flow field predictions can be seen from the data given in Table 7.1 and Figures 7.1 and 7.2. Results obtained using Mesh 1 illustrate the known weaknesses of using wall functions; that the assumption of local equilibrium is not true for severe adverse pressure gradients and separated flows, and that they are unable to represent effects caused by large accelerations resulting from sharp bends (Launder [89]). These problems are exacerbated by the standard k-ε model's tendency to over predict eddy viscosities under adverse pressure gradients (Rodi and Scheuerer [88]) and during streamline curvature (Launder [89]). Both effects lead to the calculated flow remaining attached where experiments indicate otherwise. It is also probable that turbulent mixing in the jet emerging from the inlet pipe is over predicted. Rodi and Scheuerer [88] have shown that the Norris-Reynolds one-equation model can give superior results to the standard k-ε model under adverse pressure gradients. The reason for this probably comes from the prescription of ε using an empirically based algebraic expression. Therefore its use close to the wall not only avoids some of the weaknesses of wall functions but also tends to alleviate some of the problems associated with the standard k-ε model.

As has been seen from the initial flow simulations the RNG,NR model gives results that are closest to the experimental data. The originators of the RNG k-ε model claim that it overcomes many of the weaknesses of existing eddy viscosity methods, including those associated with near wall flows. Unfortunately the implementation of the RNG k-ε model available within STAR-CD is not the complete formulation derived using the RNG method, which allows for resolution of the flow into the laminar sub-layer. Thus this abbreviated version of the RNG model has to be coupled to alternative near wall approaches, which limits its potential benefits. (A comparison between the results obtained using wall functions and the two-layer approach shows that flow phenomena are strongly influenced by near wall effects.) Despite this it does appear to overcome some of the weaknesses the standard k-ε model has away from walls.

The fact that both pressure drop and flow maldistribution errors diminish as some of the known weaknesses in the turbulence models are removed implies that their continued improvement will ultimately lead to acceptably accurate predictions. To account for the prediction of velocity profiles that are too flat any weaknesses in the turbulence models will need to be producing excessive spreading of momentum in the radial direction. Such an effect is consistent with over prediction of the turbulent viscosity.

To test whether excessive turbulent viscosities are causing poor predictions two simulations were carried out with the turbulent viscosity set to zero i.e. a laminar flow simulation. The geometries tested were the 80° and 40° diffusers with 6 inch monoliths, and in both cases the inlet pipe Re was 62 000. To ensure that the diffuser inlet velocity profiles were appropriate the experimentally measure profiles where used to define the inlet boundary, which was positioned 110 mm upstream of the diffuser throat. In the vicinity of the diffuser, and immediate upstream pipe, both meshes had 40 cells in the radial direction. The 80° diffuser had 90 cells in the axial direction, the 40° diffuser 110 cells. The SFCD differencing scheme and measured monolith dimensions were also used for both simulations. The non-dimensional pressure drops and maldistribution ratios for each case are given in Table 7.4.

Table 7.4 - Results from laminar flow predictions

	Predicted Results		Experimental Results	
Diffuser	ΔP_s*	M	ΔP_s*	M
80°	1.693	1.536	1.665	1.78
40°	1.715	1.542	1.639	1.65

There are two striking features of these results. The one that is most pertinent to the present discussion is that the predicted maldistribution ratios are still lower than the experimental values, which suggests that over prediction of turbulent viscosity cannot be the major reason for the discrepancies between the predicted and experimental results. Despite the under prediction of the maldistribution ratio the predicted pressure drops are higher than the experimental values, a result that implies the prediction of the drop in total pressure in the diffuser is too great, which may be due to the simulation of unrealistic flow phenomena (i.e. laminar flow at such a high Re). The second striking feature is the prediction of a higher maldistribution ratio for the 40° diffuser than for the 80° diffuser. This is primarily caused by the existence of two large recirculation bubbles, as opposed to the usual one, existing in the 40° diffuser, which again is probably due to the simulation of unrealistic flow phenomena.

7.3.3 Monolith Pressure Drop Expression

As has been discussed in Section 4.1, the expression used to represent the pressure drop through the monolith, Equation 4.7, is an approximation. Analysis of the experimental results (Section 6.5) has highlighted effects that could be explained by the existence of additional pressure drop terms in either Equation 4.7 or Equation 4.8. The fact that Equation 4.8 is unable to resolve the apparent anomaly (effect of monolith length and Re) in the behaviour of the experimental K_t values indicates that the additional pressure drop terms are not caused by boundary layers developing from plug profiles. It is worth noting that the implementation of Equation 4.8 into the computational model would lead to the predicted velocity profiles being even flatter than when Equation 4.7 is used.

Equation 4.8 effectively makes the exponent of U in the pressure drop expression greater than 1. A fixed increase in the exponent applied across the whole of the monolith would make the pressure drop in the central region, where the velocities are greatest, proportionately higher, thus flattening the flow further.

To make the velocity profile more maldistributed the additional pressure drop term must increase in the radial direction. A physical phenomena that might cause such behaviour is the increased level of disturbance generated in the entrance region of the monolith channels as the angle at which the flow enters the monolith becomes more acute. The ratio of the radial to the axial velocity components at the monolith front face increases in the radial direction, and as it does so the flow enters the monolith at an increasingly acute angle. Increased disturbance and separation in a channel entrance region is likely to cause an increased pressure drop. These considerations suggest that the additional pressure drop term might be of the form,

$$\Delta P_e = k_e \frac{V_i}{U_i} \qquad 7.1$$

where V_i is the radial velocity component and U_i the axial component. k_e will be an empirically determined constant. Unfortunately, although the existence of a term like Equation 7.1 is plausible, it is difficult to see how it could explain the anomaly in the experimental K_t values.

Detailed inspection of the results presented in Tables 7.2 and 7.3 shows that, with both sets of monolith dimensions, the greatest errors in M are found to occur with the high Re cases, being approximately 3% - 8% greater than the errors from corresponding geometries at the low Re, a pattern that is independent of monolith length and inlet expansion geometry. The same pattern is also evident in the pressure drop errors. (The differences between the pressure drop errors, for corresponding assemblies at different Re's, show greater variation than the M errors, however the pattern is still evident.) These trends support the hypothesis that an additional pressure drop term similar in nature to Equation 7.1 exists. The generally flatter nature of the low Re velocity profiles will reduce the influence of such an expression, such that Equation 4.7 more closely describes the flow behaviour in the monolith.

There is some evidence in the error data that suggests that, for a set of cases at the same Re, Equation 4.7 gives better results for the 80° and 60° diffusers than the narrower angled diffusers. If such a trend was real it would contradict the existence of a term like Equation 7.1. However, most of the evidence for the trend comes from the simulations that used the design monolith dimension; it is not as apparent in the predictions that used the measured monolith dimensions. Thus in the absence of further supporting evidence the trend will not be accorded too much significance.

7.3.4 Miscellaneous

The reliability of the experimental data has been discussed in Section 6.2 and although inaccuracies will inevitably exist they are unlikely to be large enough to explain the discrepancies between the predicted and experimental results.

An additional factor that might contribute to the discrepancies in the results can be found when a comparison is made between predicted and measured inlet velocity profiles (see Figure 7.4). Here it can be seen that the most accurate turbulence modelling approach (RNG,NR) predicts a profile that is 2.0% too flat. Diffusers generally perform more efficiently if the inlet velocity profile is flattened. Thus the under prediction of the inlet profiles should lead to a flattening of the monolith velocity profile. An obvious way of eliminating the discrepancy in the inlet profile would be to use the experimentally measured profiles as the simulation inlet conditions. Unfortunately the necessary accompanying turbulence data is not available. An alternative would be to obtain experimental data from geometries that have a uniform inlet velocity profile and known turbulence intensities.

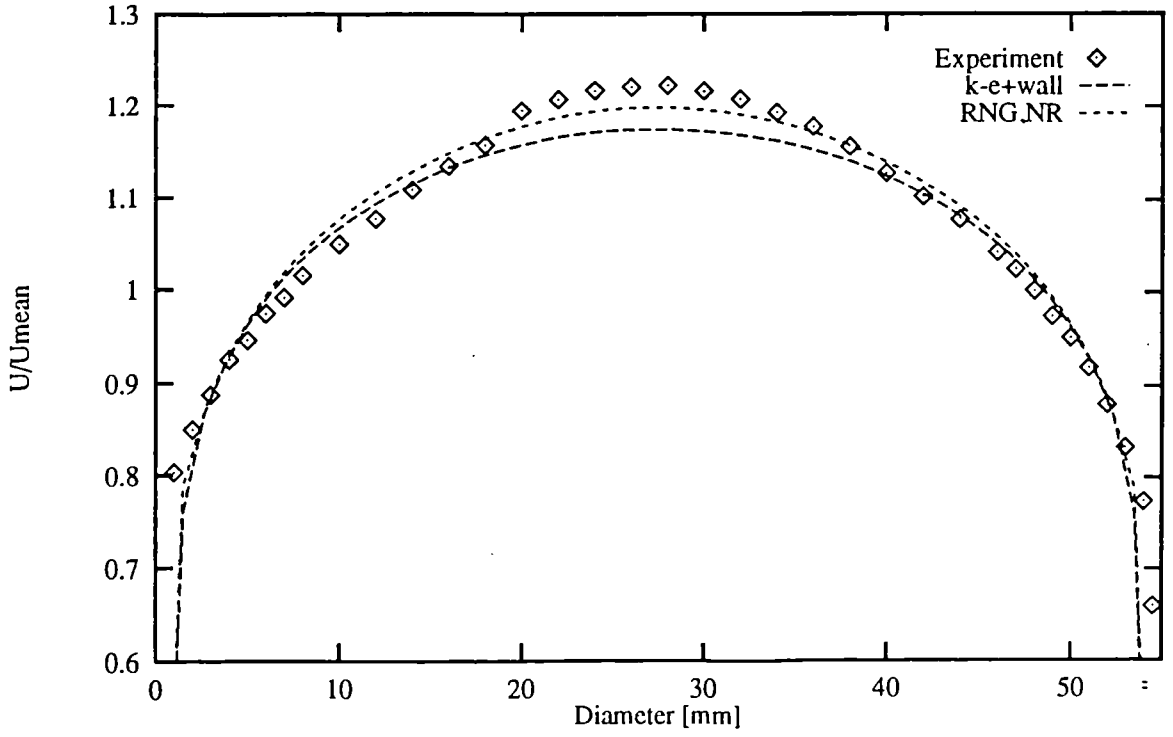

Figure 7.4 - Experimental and predicted velocity profiles 110 mm upstream of inlet expansion throat

7.4 Wall Static Pressure Profiles

The wall static pressure profiles shown in Figure 7.15 to 7.23 again illustrates that the model predicts the correct qualitative behaviour without achieving universally accurate quantitative results. Close inspection reveals that there are a number of points worth noting. The first is that with the diffusers most of the predicted C_{pw} values are greater than the corresponding experimental values, a feature that becomes more pronounced towards the monolith inlet face. Such a feature is consistent with the prediction of monolith velocity profiles that are too flat and overall static pressure drops that are too low, both of which suggest that the diffusers are working more effectively than they are in reality. Because of the lack of experimental values close to the monolith, it is unclear whether such a trend occurs with the 180° expansions. The second point is that where simulation of a geometry has been carried out using both sets of internal monolith dimensions there is virtually no difference between the predicted C_{pw} profiles, a feature that is in contrast to the predicted monolith velocity profiles and overall assembly pressure drops. As with the first point, one might expect the flatter velocity profiles given by the measured monolith dimensions to indicate more efficient diffuser performance, and that this might be displayed by the C_{pw} distributions.

The third point concerns the relative differences between the predicted and experimental C_{pw} distributions. The closest overall agreement is achieved with the 80° and 10° diffusers and the 180° expansions, the greatest discrepancies occurring with the 40° diffuser. The profiles from the diffusers with angles either side of 40° show discrepancies that lie between the two extremes. These trends seem to indicate that the predictions for the 40° diffuser are least accurate. However, there is no conclusive evidence to support such a suggestion from the maldistribution ratio and pressure drop data contained in Tables 7.2 and 7.3. In contrast, the generally more accurate C_{pw} distributions displayed by the 180° expansion predictions mirrors the trends shown in Tables 7.2 and 7.3, i.e. the maldistribution ratio and pressure drop values are generally closer to the experimental values.

7.5 Maldistribution Ratio - Pressure Drop Diagrams

To illustrate the trends in behaviour of the predicted results compared to the experimental results it would be useful to plot all three data sets, two predicted and one experimental, on the same maldistribution ratio - non-dimensional pressure drop diagram. Unfortunately the resulting diagram for the diffuser geometries would contain a confusingly high number of datum points, so it was decided to present each data set on a separate diagram (see Figure 7.5). For convenience the static pressure drop has been used, as opposed to the drop in total pressure. A comparison between Figures 6.30 and 7.5(a) shows that the relative position of the datum points is not affected by using

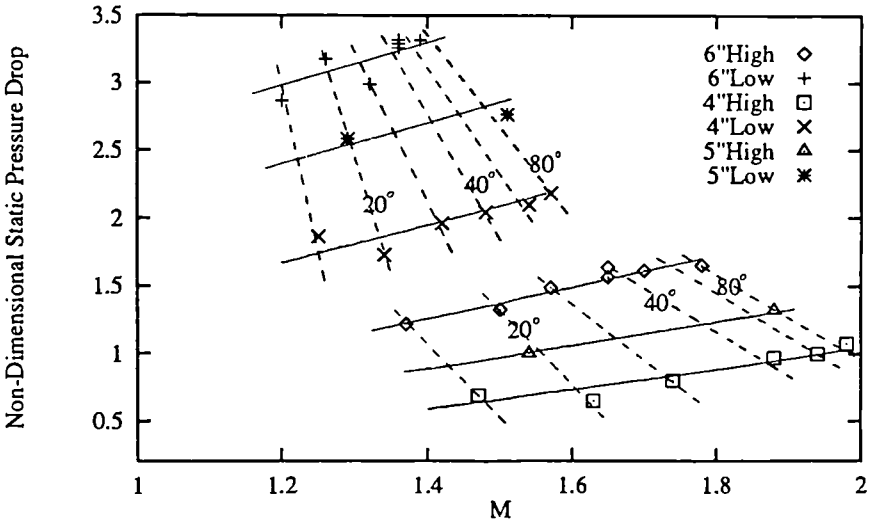

(a) - Experimental

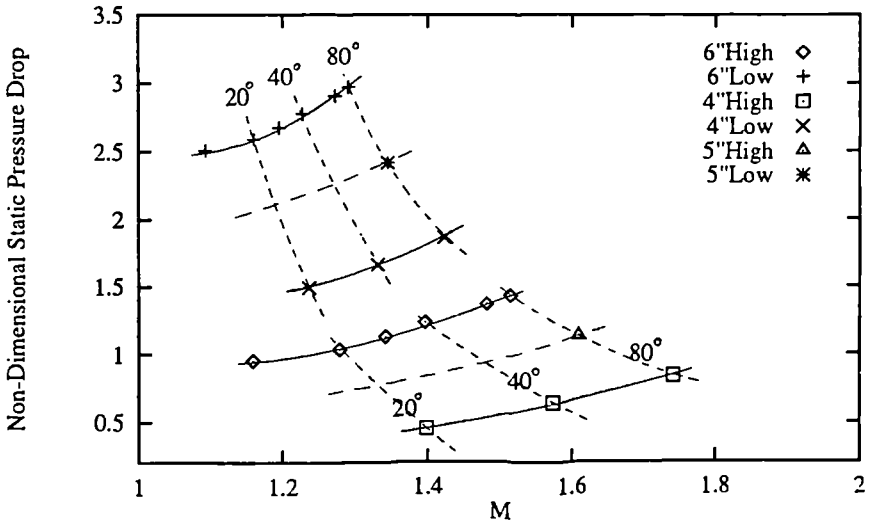

(b) - Design monolith dimensions

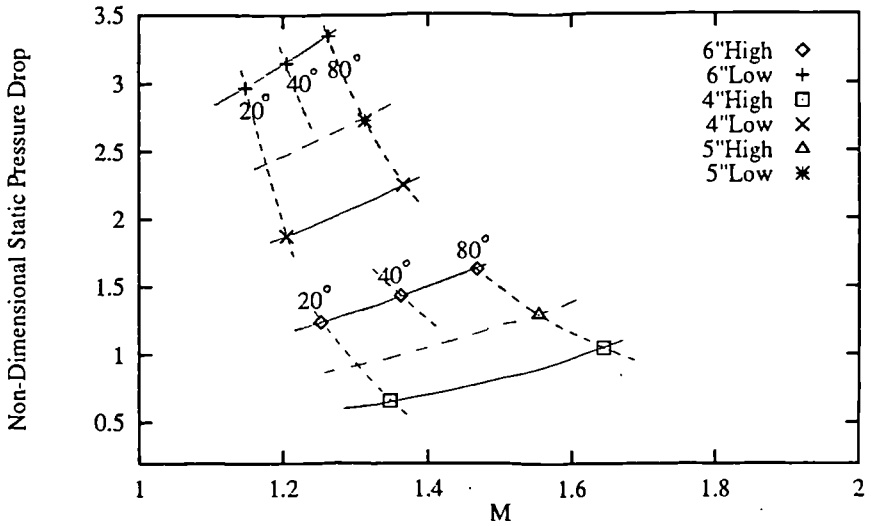

(c) - Measured monolith dimensions

Figure 7.5 - Maldistribution ratio versus static pressure drop diagrams for catalysts with conical diffusers (in key number of inches refers to monolith length, "High" and "Low" refer to Re's of 60 000 and 30 000 respectively, angles refer to diffuser angles)

the static pressure drop. The fewer number of datum points pertaining to the 180° expansions means that they can be accommodated on one diagram (Figure 7.6). From these diagrams it can be seen that the pattern of the predicted data points is very similar to that of the experimental points, although, not surprisingly, the points from both predicted data sets are displaced to the left (lower M), relative to the experimental data. In addition, the predicted points obtained using the design monolith dimensions (Figure 7.5(b)) are displaced slightly down (lower pressure drop), the other predicted set remaining at approximately the same level as the experimental data.

As mentioned in Section 6.5, the bunched nature of the experimental results from the 180° expansions means that displaying patterns is difficult. The patterns in the predicted data are more obvious, and follow the broad trends that are evident from the experimental data; i.e. as the expansion becomes longer the maldistribution ratio and pressure drop both decrease.

Although only a selection of predicted data points are available for comparison, and bearing in mind the observed differences, the general similarity between the distribution of the predicted and experimental data points indicates that the computational model is able to quantify the relative flow maldistribution and pressure drop of different axisymmetric catalyst geometries. It could even be suggested that, provided the correct monolith dimensions are used, such that acceptably accurate pressure drop predictions are achieved, the approximate maldistribution ratio can be obtained by multiplying the predicted value by a Re dependent correction factor. Suggested values at the two Re's used in this work are 1.2 at Re = 60 000 and 1.12 at Re = 30 000.

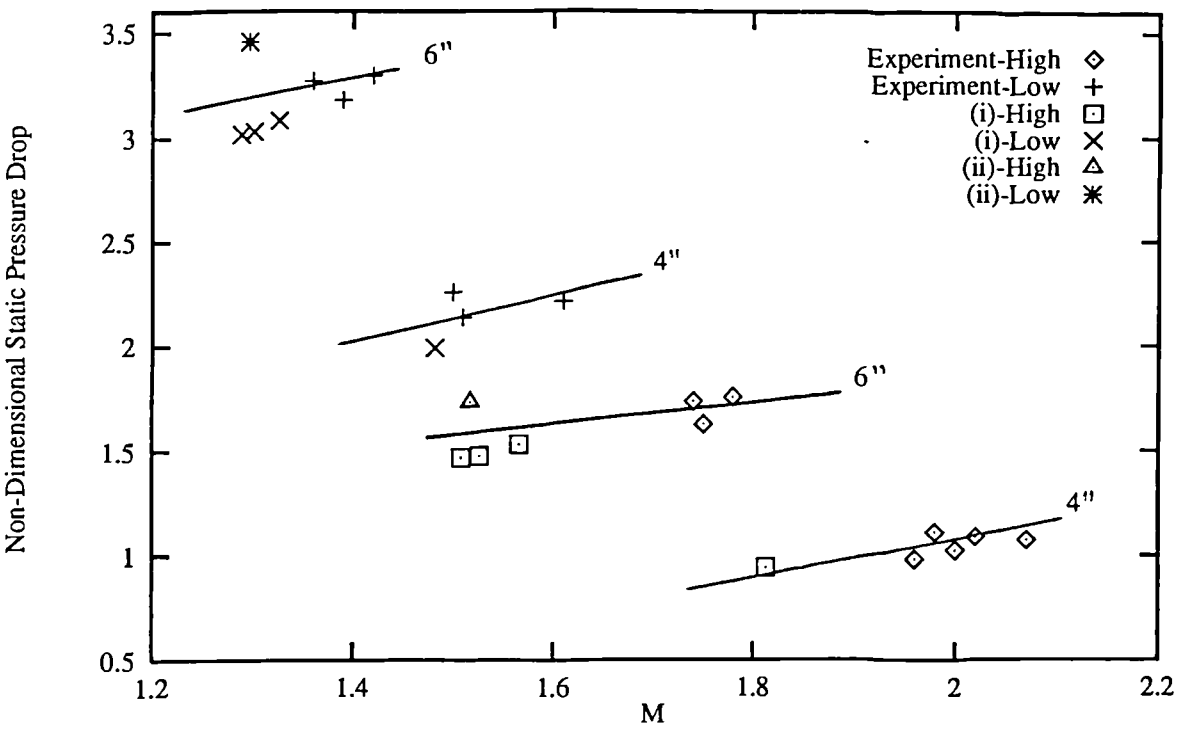

Figure 7.6 - Maldistribution ratio versus static pressure drop diagram for 180° expansions (number of inches refers to monolith length, "High" and "Low" refer to Re's of 60 000 and 30 000 respectively, (i) - predictions using design monolith dimension, (ii) - predictions using measured monolith dimensions)

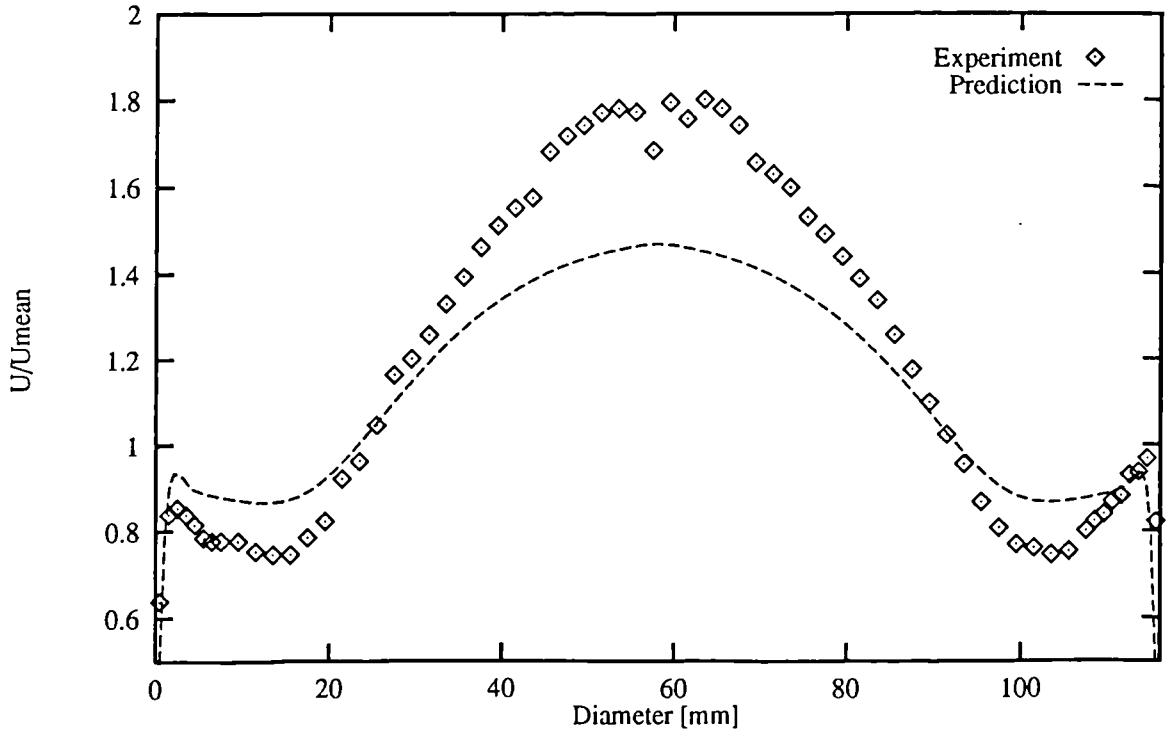

Figure 7.7 - Experimental and predicted (using RNG,NR and SFCD) monolith velocity profiles for the 80° diffuser, with 6" monolith and Re = 62 000

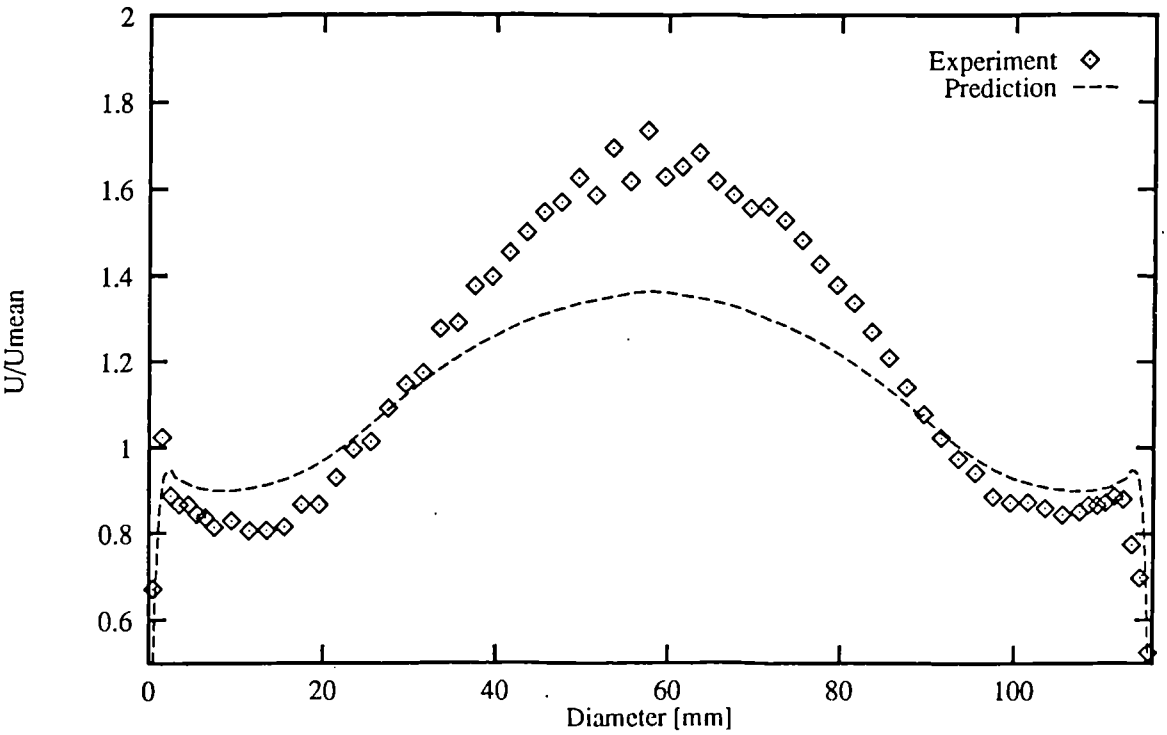

Figure 7.8 - Experimental and predicted (using RNG,NR and SFCD) monolith velocity profiles for the 40° diffuser, with 6" monolith and Re = 62 000

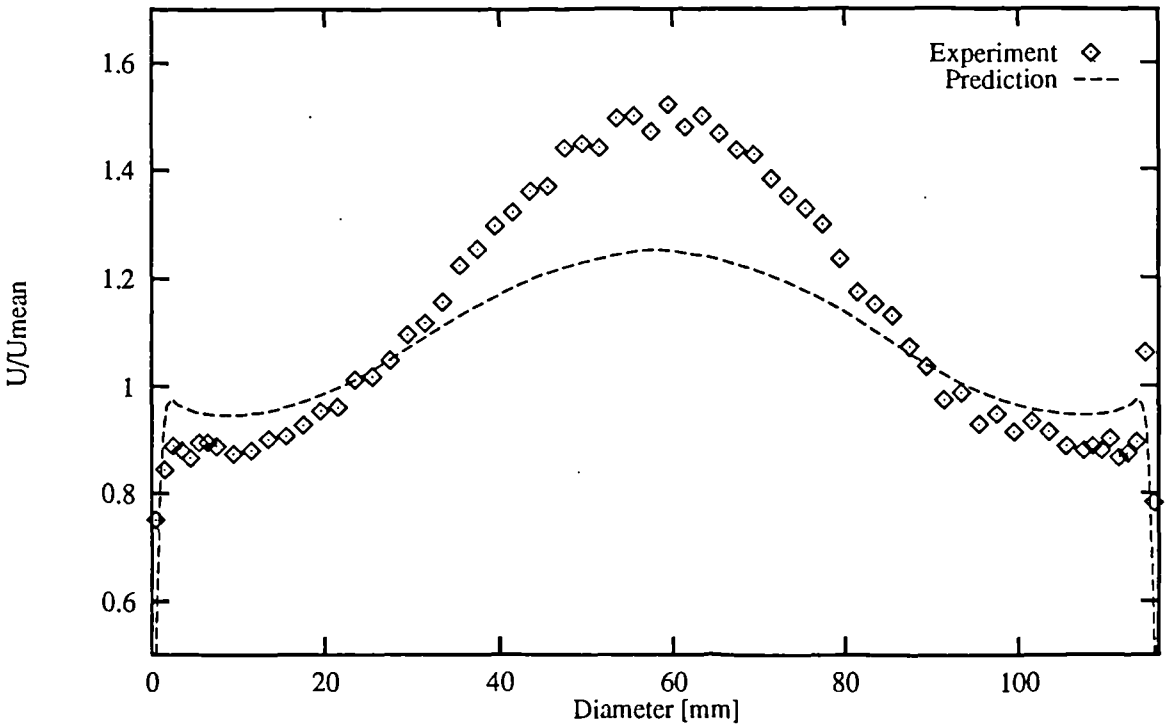

Figure 7.9 - Experimental and predicted (using RNG,NR and SFCD) monolith velocity profiles for the 20° diffuser, with 6" monolith and Re = 62 000

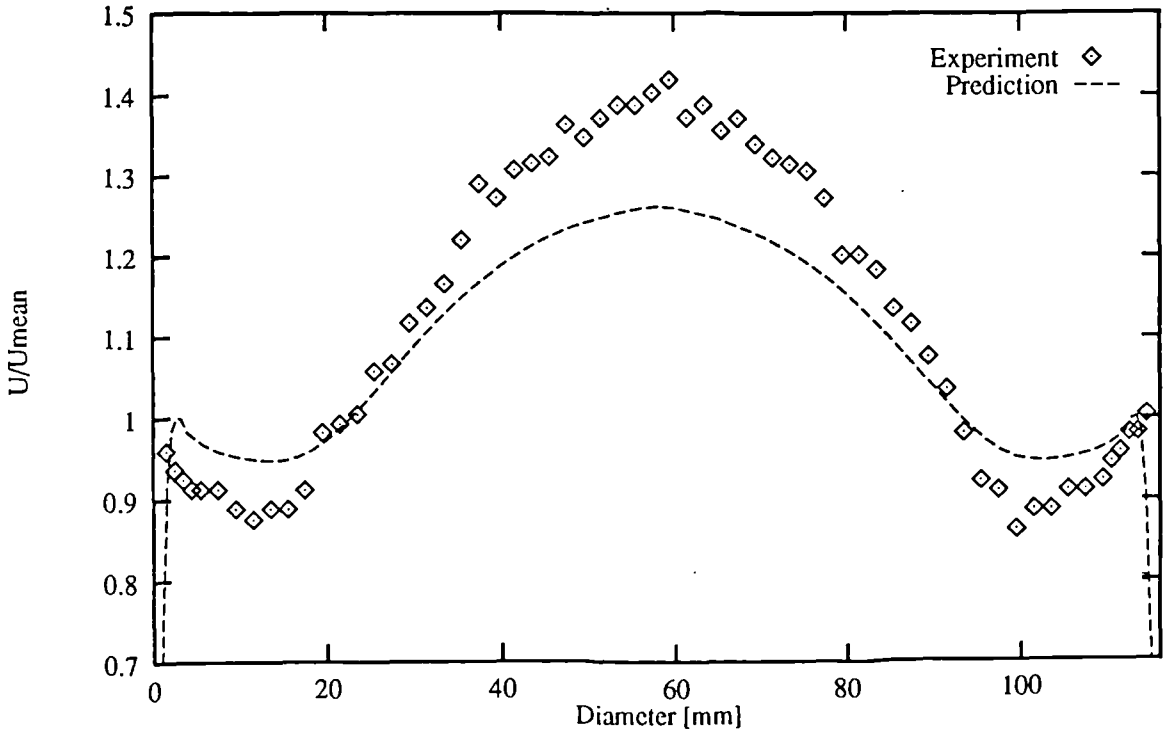

Figure 7.10 - Experimental and predicted (using RNG,NR and SFCD) monolith velocity profiles for the 80° diffuser, with 6" monolith and Re = 33 000

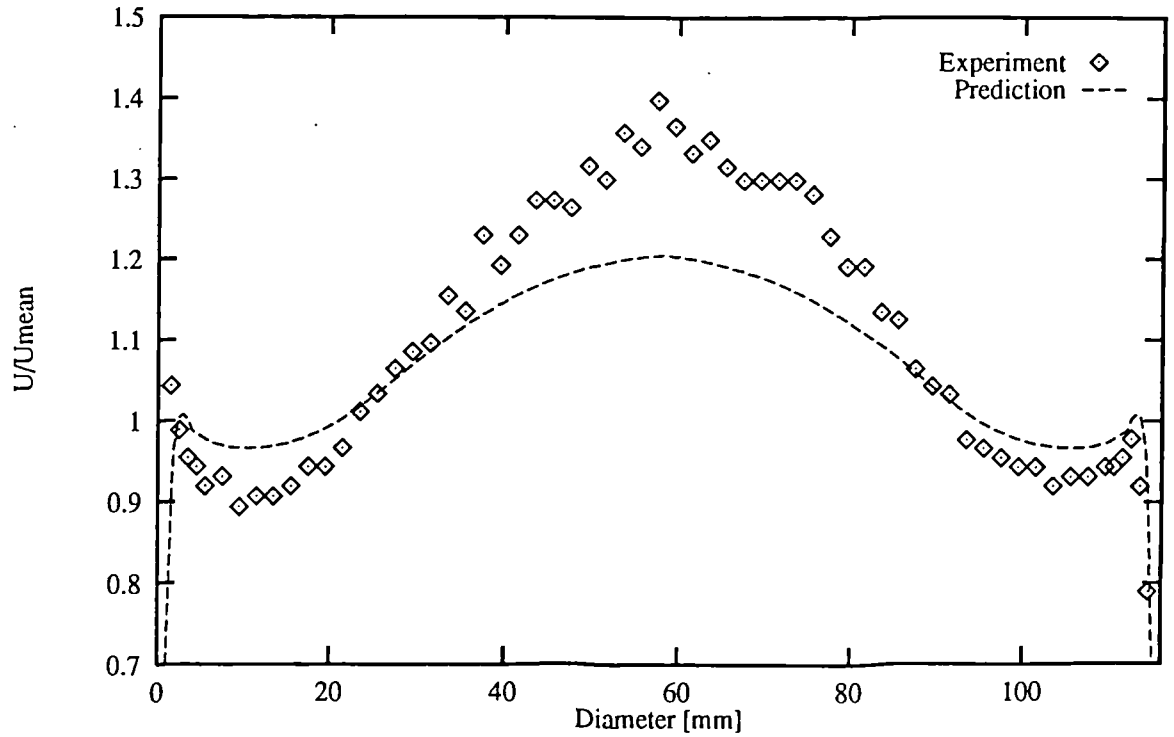

Figure 7.11 - Experimental and predicted (using RNG,NR and SFCD) monolith velocity profiles for the 40° diffuser, with 6" monolith and Re = 33 000

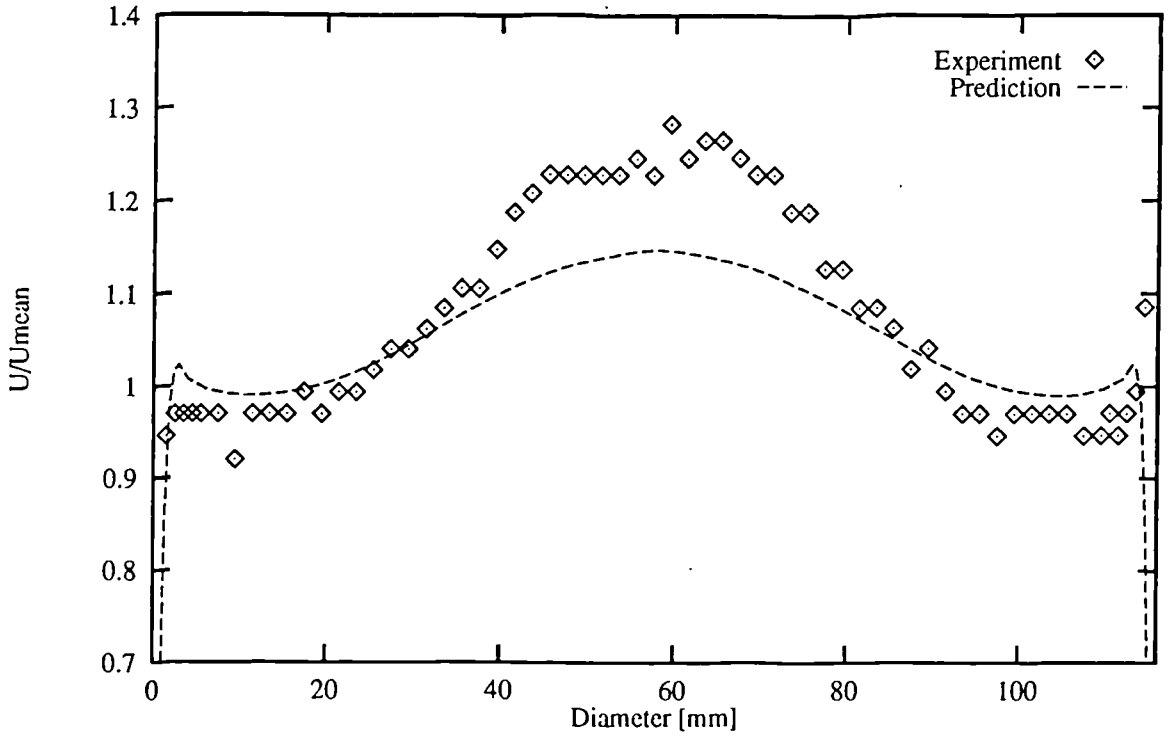

Figure 7.12 - Experimental and predicted (using RNG,NR and SFCD) monolith velocity profiles for the 20° diffuser, with 6" monolith and Re = 33 000

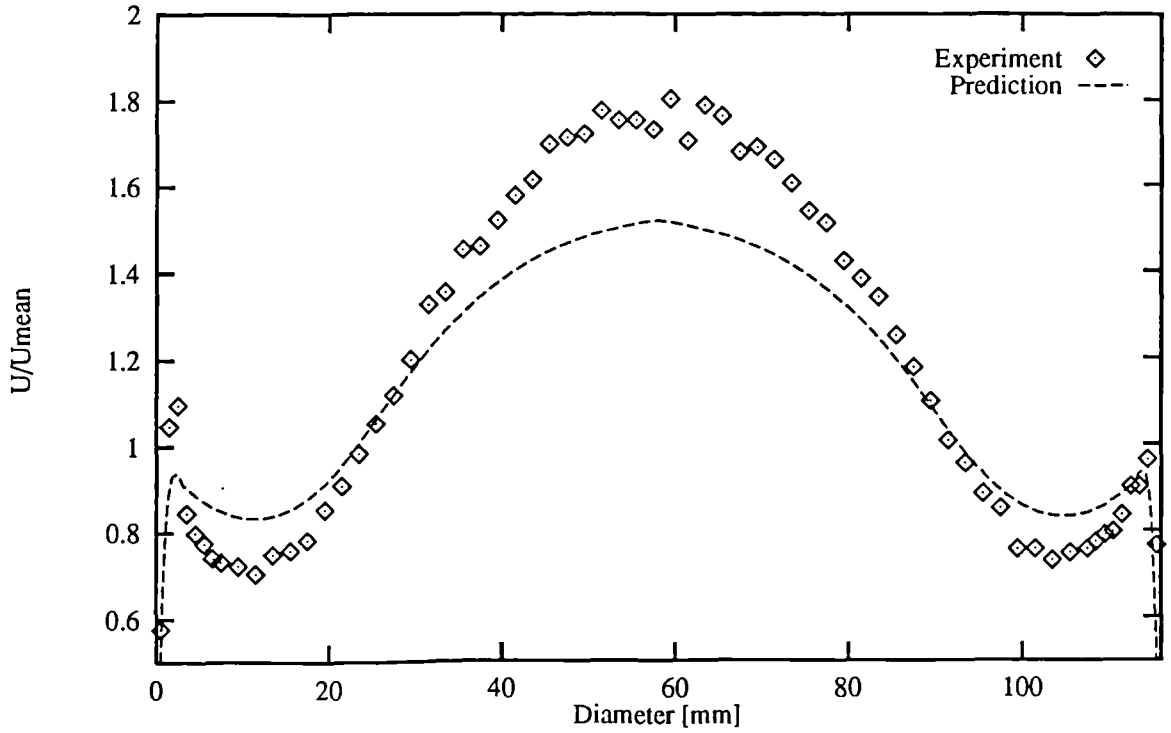

Figure 7.13 - Experimental and predicted (using RNG,NR and SFCD) monolith velocity profiles for the 37 mm 180° expansion, with 6" monolith and Re = 62 000

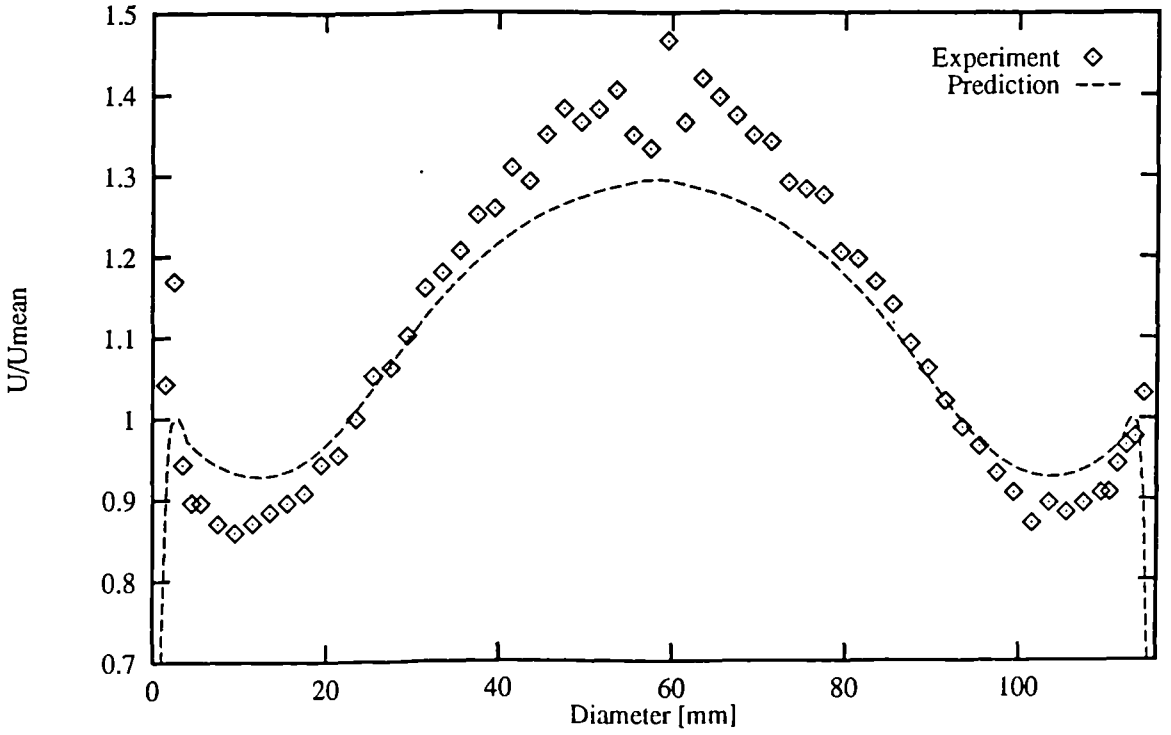

Figure 7.14 - Experimental and predicted (using RNG,NR and SFCD) monolith velocity profiles for the 37 mm 180° expansion, with 6" monolith and Re = 33 000

For Figures 7.15 to 7.23 all the predictions were carried out using the RNG,NR turbulence model and the SFCD differencing scheme. The design monolith dimensions were used with the predictions labelled (i), the measured monolith dimensions with the predictions labelled (ii).

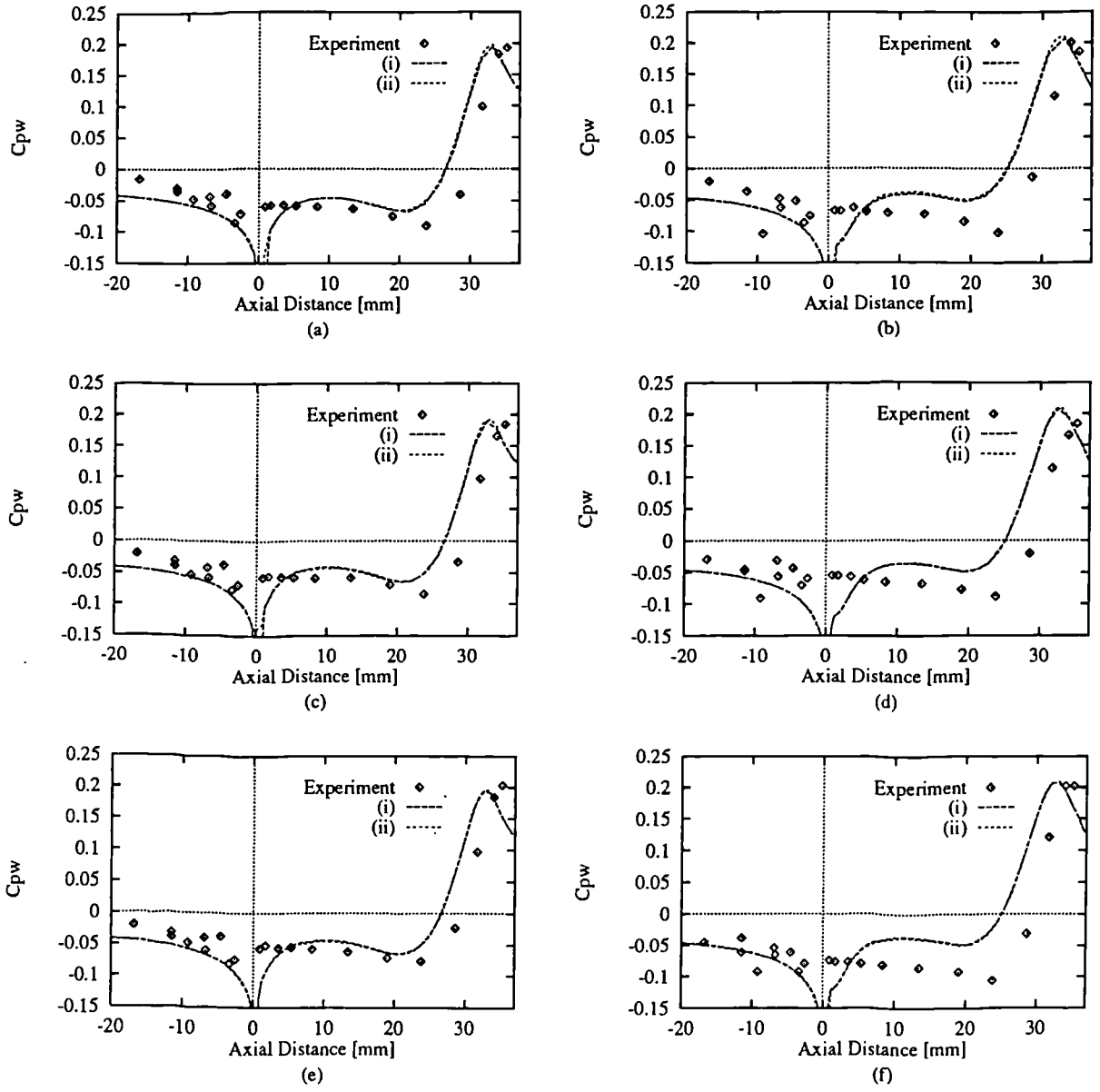

Figure 7.15 - Experimental and predicted wall static pressure coefficients for the 80° diffusers; (a) Case 1, (b) Case 7, (c) Case 13, (d) Case 19, (e) Case 25, (f) Case 31

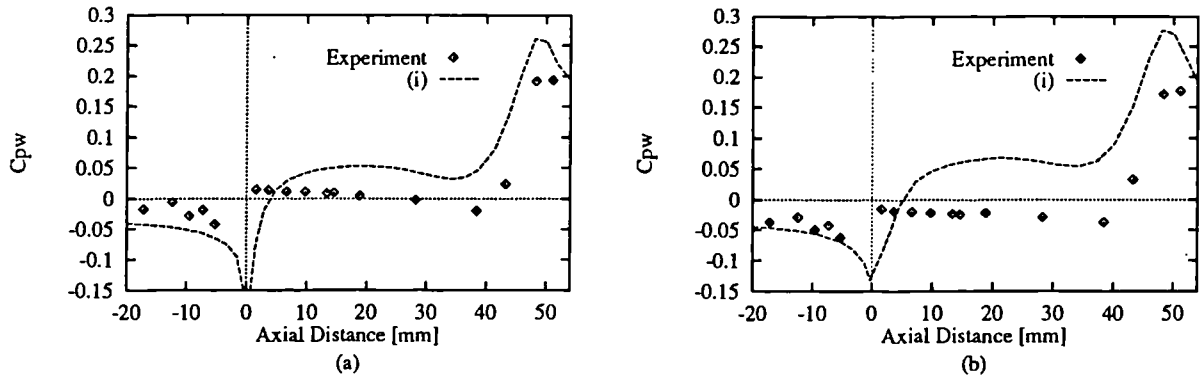

Figure 7.16 - Experimental and predicted wall static pressure coefficients for the 60° diffusers; (a) Case 2, (b) Case 8

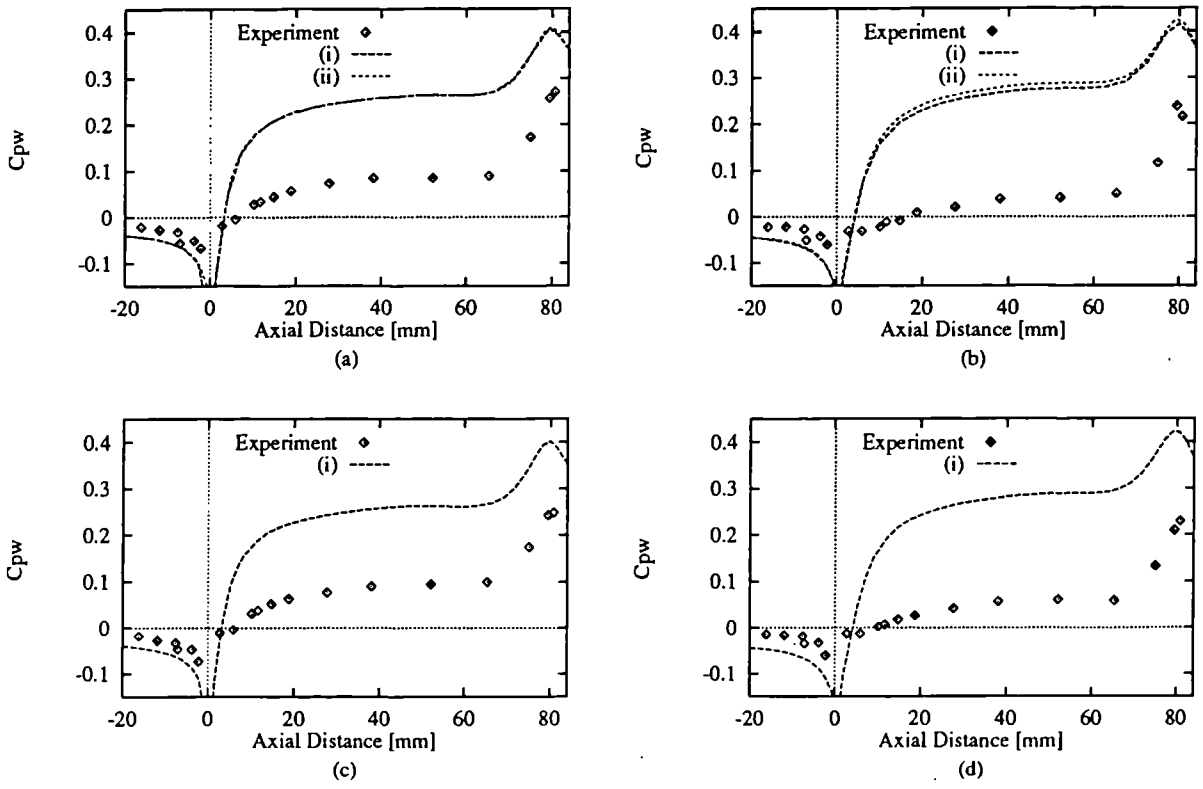

Figure 7.17 - Experimental and predicted wall static pressure coefficients for the 40° diffusers; (a) Case 3, (b) Case 9, (c) Case 27, (d) Case 32

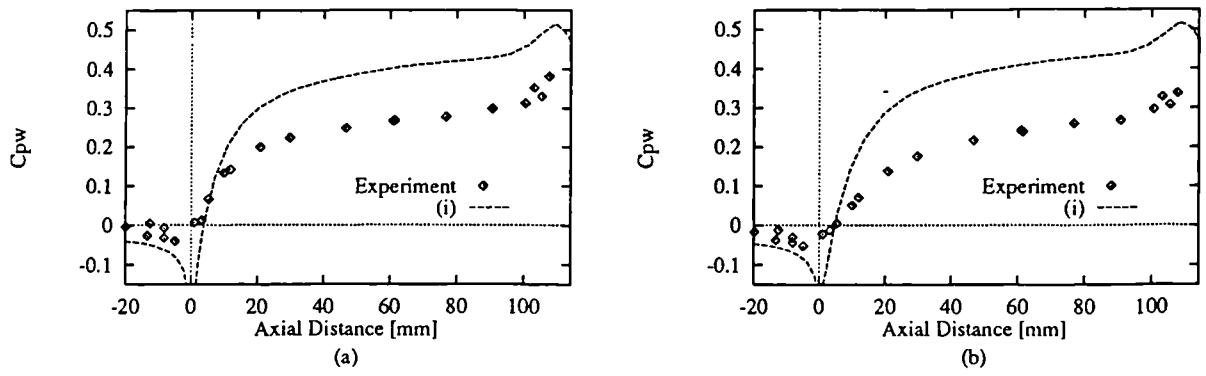

Figure 7.18 - Experimental and predicted wall static pressure coefficients for the 30° diffusers; (a) Case 4, (b) Case 10

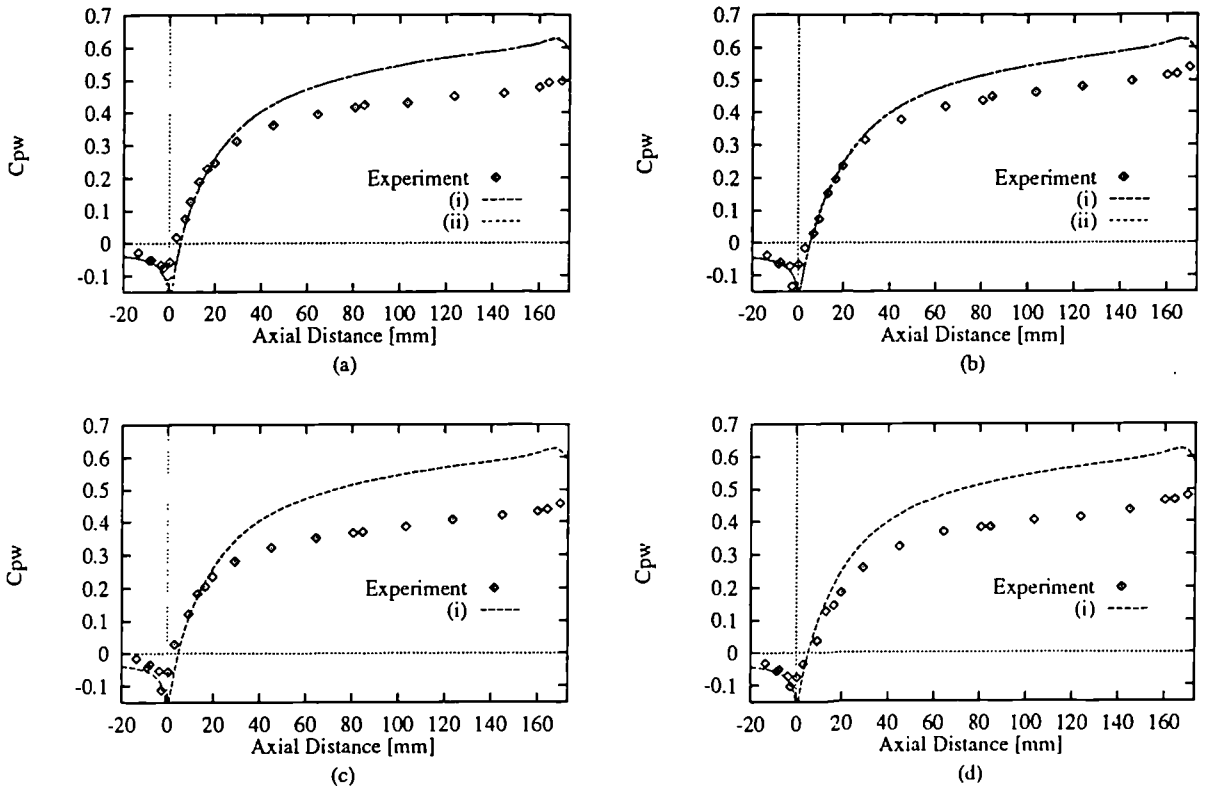

Figure 7.19 - Experimental and predicted wall static pressure coefficients for the 20° diffusers; (a) Case 5, (b) Case 11, (c) Case 29, (d) Case 35

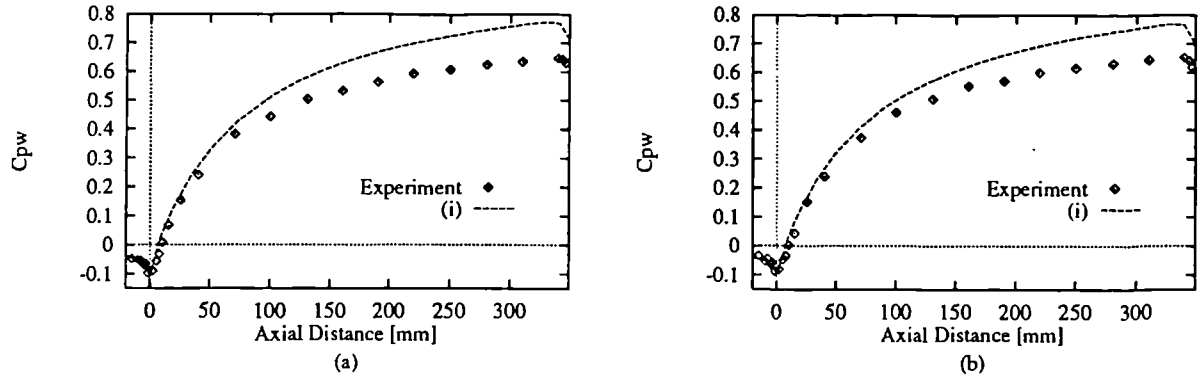

Figure 7.20 - Experimental and predicted wall static pressure coefficients for the 10° diffusers; (a) Case 6, (b) Case 12

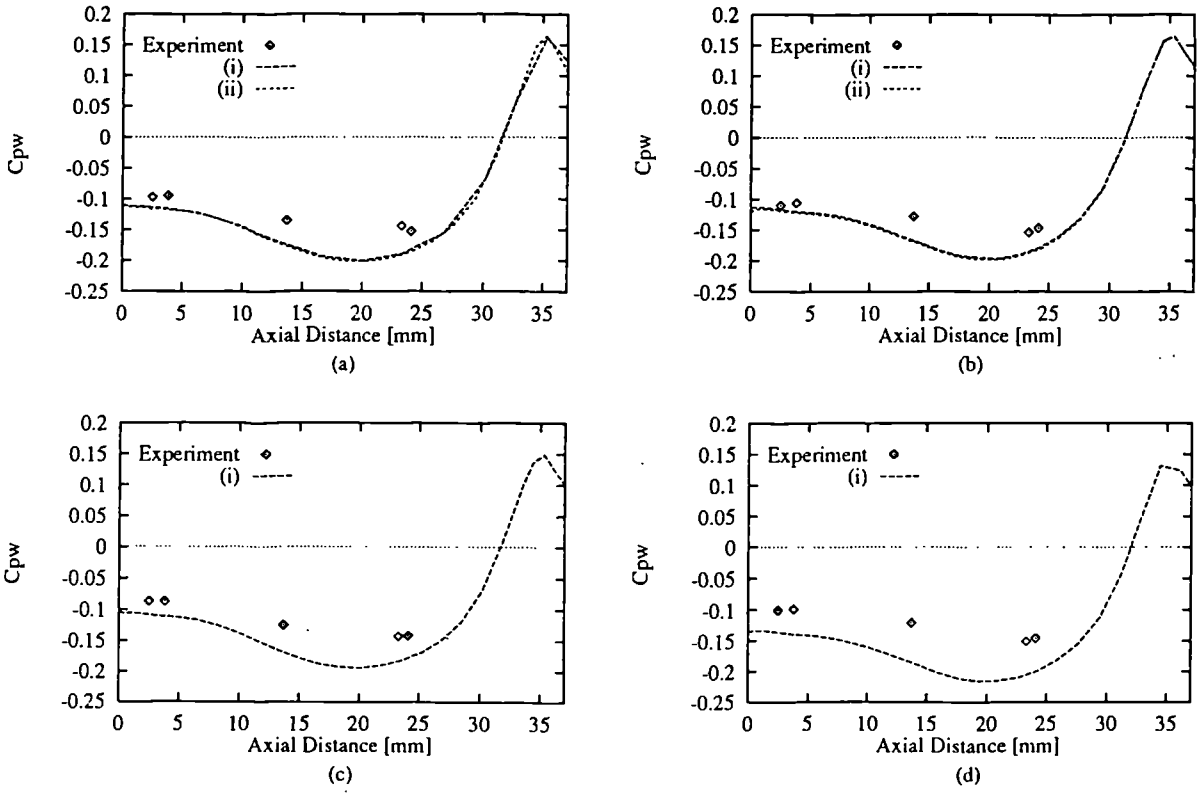

Figure 7.21 - Experimental and predicted wall static pressure coefficients for the 37 mm 180° expansion; (a) Case 37, (b) Case 42, (c) Case 57, (d) Case 62

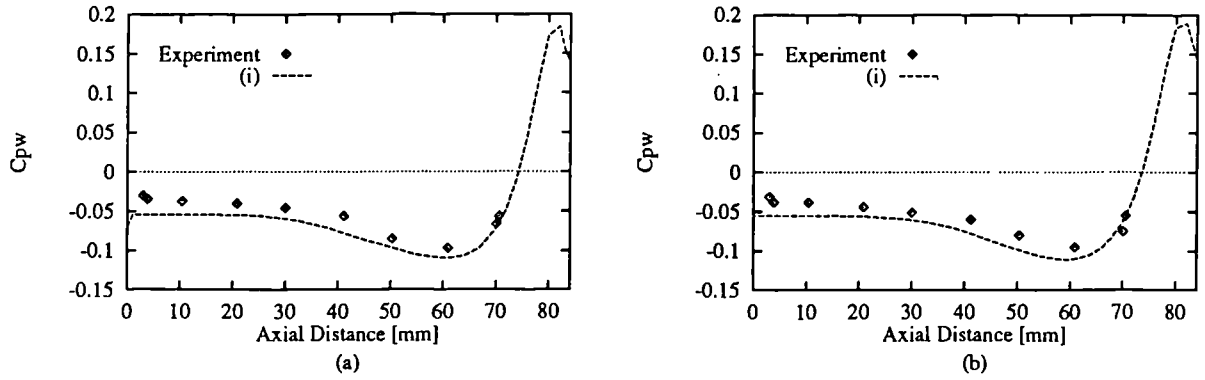

Figure 7.22 - Experimental and predicted wall static pressure coefficients for the 84 mm 180° expansion; (a) Case 39, (b) Case 44

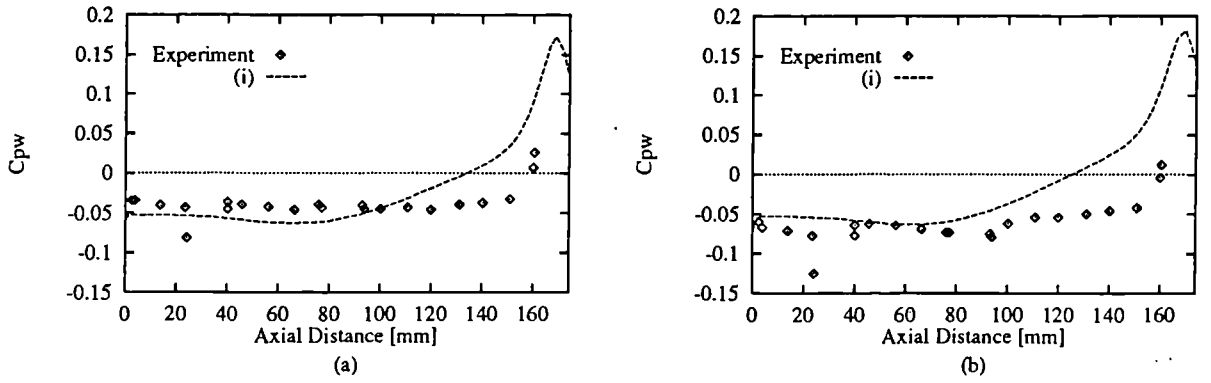

Figure 7.23 - Experimental and predicted wall static pressure coefficients for the 174 mm 180° expansion; (a) Case 41, (b) Case 46

8 REACTING CATALYST COMPUTATIONAL MODEL

Although it was demonstrated in Section 7 that the models presently being used to simulate the fluid dynamics in catalysts have several weaknesses, which lead to velocity profile predictions that are too flat, the development of a fully integrated catalyst model based on a commercial CFD code still represents a desirable aim. It is inevitable that weaknesses in the fluid dynamics model will be overcome such that accurate flow predictions can be attained. When this happens it would be advantageous to have a methodology that allows the immediate implementation of a full reacting catalyst model. It is also possible that sufficiently accurate flow predictions are already being obtained which enable a full reacting model to provide valuable data on important catalyst phenomena.

The catalyst model described in the following sections is an extension of the PHOENICS based isothermal fluid dynamics model, described in Section 4.4.1, to include the heat transfer, chemistry and mass transfer that occur in catalysts. The choice of PHOENICS as the platform for such a model was dictated by a number of specific options that the code offers which allow the implementation of an equivalent continuum approach. Although Will and Bennett [63] showed that PHOENICS can be used as part of a three-dimensional monolith model of the multiple channel type, the relative simplicity of an equivalent continuum model makes the approach more attractive. Although certain "bugs" associated with the PHOENICS flow predictions were identified in Section 7, their presence should not seriously affect the validity of the model.

8.1 Governing Equations

The equations that predict the thermodynamics and chemistry that occur in catalysts have been established for sometime [43]. If an equivalent continuum approach is being used the general transport and conservation equations need to be modified slightly. The equations given below, for such an approach, are essentially those described by Zygourakis [48]. They have been extended to include the behaviour of the exhaust gas outside the catalyst monolith and rearranged into forms in which they can be implemented within the PHOENICS code. (A full listing of the notation used can be found in the Nomenclature section.)

Like the momentum equations (c.f. Sections 4.1), the equations that govern the transport of scalar variables in turbulent flow need to be averaged in some way before they can be practicably solved. Once again time averaging produces additional transport terms, analogous to Reynolds stresses, that have to be modelled. In accordance with the practices adopted for the momentum equations (c.f. Section 4.2) a gradient transport hypothesis is taken such that a turbulent diffusivity can be introduced. The value of this turbulent diffusivity is obtained from the turbulent viscosity using

turbulent Prandtl (σ_p) and Schmidt (σ_s) numbers. It should be noted that the turbulent viscosity is zero within the monolith.

The temperature of the exhaust gas, T_g, is obtained from the conservation equation for the gas enthalpy, h_g,

$$\frac{\partial \rho_g h_g}{\partial t} + \nabla.\left(\rho_g U h_g\right) - \nabla.\left(\left(\frac{\mu_t}{\sigma_p} + \frac{k_g}{c_{pg}}\right)\nabla h_g\right) = S1 \qquad 8.1$$

the temperature being calculated from the expression,

$$h_g = T_g c_{pg} \qquad 8.2$$

In its full form there are a number of source terms in Equation 8.1. They include viscous dissipation, pressure gradient and mass transfer effects. Because these effects are considered small they will be neglected. One remaining source term has to be included however. It represents the transfer of heat between the monolith and exhaust gas, and as such is only active in the part of the calculation domain representing the catalyst. It is given by,

$$S1 = \frac{h a_v}{c_{pg}}\left(T_s c_{pg} - h_g\right) \qquad 8.3$$

where h is the heat transfer coefficient and a_v the monolith surface area per monolith unit volume.

The conservation equations for the chemical species in the exhaust gas are of the form,

$$\frac{\partial \rho_g C_{gi}}{\partial t} + \nabla.\left(\rho_g U C_{gi}\right) - \nabla.\left(\left(\frac{\mu_t}{\sigma_s} + \rho_g D_i\right)\nabla C_{gi}\right) = S2 \qquad 8.4$$

where C_{gi} is the mole fraction of the species i. It is assumed that the total number of moles remains constant. The source term S2 in Equation 8.4, like S1 in Equation 8.1, is only active in the catalyst. It is given by,

$$S2 = \rho_g K_{mi} a_v \left(C_{si} - C_{gi}\right) \qquad 8.5$$

where K_{mi} is the mass transfer coefficient for species i, and represents the transfer of chemical species between the monolith and exhaust gas. The concentration of the species on the monolith surface, C_{si}, are governed by equations of the form,

$$v_w \frac{\partial C_{si}}{\partial t} = K_{mi} a_v \left(C_{gi} - C_{si}\right) - \frac{M_{Rg}}{10^3 \rho_g} R_i \qquad 8.6$$

where M_{Rg} is the molecular mass of the exhaust gas and R_i the species reaction rate. Note that the transient term in Equation 8.6 is commonly assumed to be negligible, an assumption that is justified on the grounds that reaction rates occur so quickly they can be considered instantaneous. Thus species concentrations on the monolith at one time step have no influence on concentrations at the next time step. It is also usually the case that the volume available for storage of species, v_w, is so small the term approaches zero. If the transient term is neglected Equation 8.6 reduces to,

$$\frac{M_{Rg}}{10^3} R_i = \rho_g K_{mi} a_v \left(C_{gi} - C_{si}\right) \qquad 8.7$$

The variable that links all the others together is the temperature of the monolith, T_s. It is the only variable that can be transported between adjacent monolith channels. The equation governing its behaviour is essentially that of heat conduction in a solid. However, because an equivalent continuum approach is being used the orthotropic nature of the heat conduction in a monolith must be taken into consideration. Thus the governing equation becomes,

$$\rho_s \frac{\partial T_s}{\partial t} - \frac{k_s}{c_{ps}} \left\{ \frac{\partial^2 T_s}{\partial x^2} + \frac{G}{(1-\alpha)} \left(\frac{\partial^2 T_s}{\partial y^2} + \frac{\partial^2 T_s}{\partial z^2} \right) \right\} = S3 + S4 \qquad 8.8$$

Note that x is the flow direction of the gas, whereas y and z are the Cartesian directions perpendicular to the flow. G is defined as k_{eff}/k_s, where k_{eff} is the effective thermal conductivity of the composite of exhaust gas and substrate in the direction of y and z. The two source terms S3 and S4 are given by,

$$S3 = \frac{h a_v}{(1-\alpha) c_{ps}} \left(T_g - T_s\right) \qquad 8.9$$

$$S4 = \frac{\sum R_i \Delta H_i}{(1-\alpha)c_{ps}} \qquad 8.10$$

where ΔH_i is the enthalpy of reaction. S3 represents the transfer of heat between the monolith and gas. S4 represents the heat released through chemical reactions.

The reaction rate expressions that appear in Equations 8.6 and 8.10 are of general Arrhenius equation form. For the preliminary assessment of the model, the aim of which is to show that the technique works, the reaction rates derived by Volts et al. [66] have been used. These are of the intrinsic reaction rate type, being given as the number of moles reacted per second per unit surface area of noble metal. Thus the surface area of noble metal per unit monolith volume, a_c, is required. To keep the computational effort to a minimum only one emission species, CO, will be modelled, the concentrations of all the other species being taken as constant. The appropriate expressions are,

$$R_{CO}/a_c = r_{CO} = k_1 C_{sCO} C_{sO_2} / T_s J_1 J_2 J_3 \qquad 8.11$$

where,

$$J_1 = \left(1 + K_1 C_{sCO} + K_2 C_{sC_3H_6}\right)^2 \qquad 8.11a$$

$$J_2 = \left(1 + K_3 C_{sCO}^2 C_{sC_3H_6}^2\right) \qquad 8.11b$$

$$J_3 = \left(1 + K_4 C_{sNO}\right)^{0.7} \qquad 8.11c$$

$$k_1 = 6.699 \times 10^{13} \exp(-12556/T_s) \qquad 8.11d$$

$$K_1 = 65.5 \exp(961/T_s) \qquad 8.11e$$

$$K_2 = 2.08 \times 10^3 \exp(361/T_s) \qquad 8.11f$$

$$K_3 = 3.98 \exp(11611/T_s) \qquad 8.11g$$

$$K_4 = 4.79 \times 10^5 \exp(-3735/T_s) \qquad 8.11h$$

Several auxiliary relationships are used within the model. These included calculating the density of the gas from the ideal gas law,

$$\rho_g = \frac{P}{T_g R_g} \qquad 8.12$$

Where appropriate the auxiliary variables, such as the laminar viscosity of the gas, were calculated from algebraic expressions. The heat and mass transfer coefficients, h and K_{mi}, are calculated from Nusselt and Sherwood numbers respectively. During the initial stages of model testing both are assumed constant throughout the monolith, being taken as the asymptotic value for laminar flow in a circular pipe with constant wall temperature (i.e. 3.66).

The boundary conditions used for the above equations vary from case to case. Because a general purpose CFD code is being used a large number of options are available. The options used for the simulations carried out as part of the present project are discussed in Section 9.2.1.

The most obvious way of defining the species concentrations would be as mass fractions, however there are two considerations that led to the use of mole fractions. The reaction rate terms are expressed as functions of mole fractions, and although it is recognised that the mole fractions in these reaction rate terms can be converted to mass fractions, to do so requires the introduction of the mixture molecular mass for each concentration term. The mixture molecular mass is a variable and is not obtainable from the model equations; it has to be estimated. Although the M_{Rg} has to be used once in Equation 8.6, its repeated use in the R_i expressions could introduce greater errors than assuming the number of moles in the mixture remains constant. Ultimately, however, the decision to use mole fractions was made because the majority of existing catalyst models use them.

8.2 Equation Implementation

Although PHOENICS is ostensibly a CFD code it can provide solutions, using the finite volume method, to differential equations of the general form,

$$\frac{\partial f\rho\phi}{\partial t} + \nabla.(f\rho\mathbf{U}\phi) - \nabla.(f\rho\Gamma\nabla\phi) = fS \qquad 8.13$$

where ϕ stands for any conserved property, Γ the kinematic diffusivity, ρ the density of the phase, f the phase volume fraction and S any source terms. Any number of ϕ's can be solved at the same time, with 15 being especially set up to solve standard variables such as velocity, pressure and enthalpy. Because PHOENICS has the capabilities for solving two phase flow problems, any of the ϕ's not internally allocated can be associated with either of these two phases. By default the conservation equation for any variable will consist of a transient term, a convection term and a diffusion term. To allow flexibility a facility is provided for cancelling any of these terms. Source terms can be set by the user in a variety of ways.

Inspection of the conservation equations set out in the preceding section shows that they all consist of terms that are represented in Equation 8.13. In addition they are all linked with one of two phases; the exhaust gas or the solid monolith. Consequently an apparent way of implementing their solution would be to utilise the two phase flow option, with one phase being taken as the gas and the other the solid. Each dependent variable could then be assigned to the appropriate phase. In addition to fixing the solid phase velocity to zero, it would be necessary to fix its volume fraction to zero everywhere except in the region of the monolith. Unfortunately considerable difficulties were experienced when attempts were made to model the fluid dynamics of the catalyst system using such an approach. Even when a semi-converged solution could be achieved unrealistic answers resulted. It should also be noted that significantly more computational effort is required when solving for two phase flow. An alternative to using the two phase facilities is to assign all the dependent variables to a single phase, the exhaust gas, and introduce special procedures that convert the conservation equations of this phase into conservation equations for the solid phase. Many of these special procedures require the introduction of additional FORTRAN coding in the EARTH subroutine GROUND.

8.2.1 Gas Phase Variables

All the dependent variables associated with the gas are either standard variables (pressure, momentum and enthalpy) or their conservation equations are of the standard form set out in Equation 8.13 (species concentrations). Despite this they all still require special treatments within the monolith, the first of which is the prevention of their transfer perpendicular to the flow direction. Methods by which transfer of momentum can be prevented were discussed in Section 4.4.1. These methods are just as applicable to the other dependent variables. As mentioned in Section 4.4.1, the setting of cell face porosities in the radial and circumferential directions prevents transfer of all dependent variables in those directions. Unfortunately there is a dependent variable, T_s (see below), that can be transferred in these directions so this method is unsuitable. The preferred method is therefore the second one discussed in Section 4.4.1, where transport by diffusion and convection are cancelled separately. In addition to momentum, it is applied to h_g and the various C_{gi}'s.

The next special treatment is the setting up of the source terms S1 and S2. It can be seen that both terms are conveniently of the $TC(V - \phi_p)$ form, with the appropriate type being per unit volume. Because the V's in both terms are functions of other dependent variables additional FORTRAN coding has to be introduced into GROUND. If a constant Nu is being taken and k_g and c_{pg} are assumed to be constant, such that h is constant, the C value for S1 will also be a constant and can be set without using GROUND coding. The converse is true if h is not taken as constant. Even if K_{mi} can be taken as constant the density of the gas, which is not a constant, appears in the C of S2.

As mentioned in Section 4.4.1, there is a source type that automatically multiplies by the density of the phase in use. Unfortunately there is a "bug" within PHOENICS that can lead to erroneous results if this source type is used for transient simulations. Consequently the only safe way of setting the C of S2 is within GROUND, the gas density being calculated from the temperature and pressure when needed.

One further procedure that the gas phase variables require within the monolith is the suppression of the turbulent viscosity. If a variant of the k-ε turbulence model is being used the simplest way of achieving this goal is to fix the value of k within the monolith to be very small.

The actual form of the standard gas enthalpy equation included in PHEONICS includes pressure gradient and viscous dissipation source terms. It should be noted that while these source terms have little effect on the distribution of energy they are functions of velocity field variables. As a consequence they add considerably to the non-linear nature of the governing equations, such that divergence of the solution procedure becomes a problem. This in fact is the main motivation for their exclusion from Equation 8.1. It is therefore necessary to cancel these "built in" source terms. Note that the temperature of the gas is automatically calculated using Equation 8.2 when the appropriate PHOENICS option is selected.

8.2.2 Solid Phase Variables

The governing equations for the dependent variables associated with the solid phase differ from the gas phase governing equations in that they do not have convection terms. In addition, the equations for the species concentrations on the monolith surface do not have a diffusion term nor, if Equation 8.7 is being taken, a transient term, the resulting expressions being source-term-only equations. These equations can still be solved within PHOENICS using its finite volume approach. Their implementation is achieved by allocating each species concentration to one of the ϕ's, which then has its diffusion, convection and transient terms switched off. Both sides of Equation 8.7 are then introduced as sources associated with the appropriate ϕ variable. The right hand side of Equation 8.7 is set up in the same way that S2 is set up. It is less obvious how the left hand side of Equation 8.7 is implemented. Because most reaction rate terms include C_{si} as part of their numerator (c.f. Equation 8.11) the $TC(V - \phi_P)$ form of the source can be maintained if C_{si} is taken out of R_i, denoted as R_i', and C is made equal to $M_{Rg}R_i'/10^3$. Note that the reaction rates and C have to be calculated within GROUND and that V should be set to zero. The type for both sources is per volume.

Because the source terms in Equation 8.7 are only active in the monolith, and because there are no transport mechanisms, constant values are predicted for the C_{si}'s everywhere else in the calculation

domain. Although within PHOENICS the ϕ's used for the C_{si}'s are explicitly associated with the gas phase, the association has no effect on the calculation of the C_{si}'s. The influence of the gas phase is only felt in the transient, convection and diffusion terms.

The one remaining variable that needs to be solved is T_s. Inspection of Equation 8.8 reveals that it consists of a diffusion term, a transient term and two source terms. Thus, a similar approach to that adopted for the C_{si}'s can be used. One of the ϕ's is taken as T_s, which then has its convection term switched off. Unfortunately because of the way the code handles the solution of any variable a special treatment is required for the transient term and the diffusivity. In both cases the density of the phase to which the ϕ is associated, the exhaust gas density, forms an integral part of their discretized mathematical representation (c.f. Equation 8.14). Obviously the density that should appear in these terms is the density of the substrate. If the gas density could be taken as constant a simple cross multiplication could be implemented, however it varies with space and time. As a result the gas density cannot be taken outside the differential of the transient term and eliminated by cross multiplication. The most convenient way of overcoming its presence in the transient term was to cancel the term completely and introduce a hand built discretized transient term as an additional source term.

Discretization of the transient term, in accordance with the practise adopted within PHOENICS, was carried out using the fully implicit scheme. Its discretized representation thus becomes,

$$\frac{\partial \rho_s T_s}{\partial t} \approx \frac{\rho_s}{\Delta t}\left(T_s - T_s^o\right) \qquad 8.14$$

where T_s^o denotes the monolith temperature at the previous time step and Δt the length of the time step. The transient term needs to be integrated over the computational cell volume, ΔV, which introduces ΔV as a coefficient of the right hand side of Equation 8.14. Inspection of Equation 8.14 reveals that it is conveniently of the $TC(V - \phi_p)$ form, with $C = \rho_s \Delta V/\Delta t$ and $V = T_s^o$. If the integration over the cell volume is carried out externally, as above, the source is introduced on a per cell basis, however the integration can be carried out internally by making $C = \rho_s/\Delta t$ and the source type per volume. Both methods are comparatively easy to implement.

A more challenging obstacle is the storage of T_s^o. If the built in transient term of a variable is cancelled the values of that variable at the previous time step are automatically not saved, a procedure that cannot be overridden. Two approaches were developed for storing values from previous time steps. One uses two additional ϕ's as stores, one ϕ to be used on odd time steps, the other ϕ on even. The use of alternating stores is necessary because of the code's internal limitations

on when ϕ memory locations can be accessed. The second method, which was not used in this application (but was used for a later application, see Section 9.3.2), involves setting up a special user defined array within GROUND where old variable values can be stored. Neither method is straight forward, both having their pros and cons.

The presence of the gas density in the monolith thermal diffusivity can be cancelled, through the T_s Prandtl number, with some coding within GROUND. The orthotropic nature of the thermal conductivity of Equation 8.8 is implemented by adjusting, through PIL commands, the diffusivity of the cell faces in the appropriate directions. The source term S3 is set up in a similar way to S1. Although the reaction rates are a function of T_s their form means that the most practical way of introducing S4 is as a "fixed flux". By multiplying the C of the source by a very small number and dividing the V by the same very small number the source term effectively becomes equal to V, which can then be set equal to S4 (This procedure is carried out internally within PHOENICS if the correct PIL commands are used). Note that again the reaction rates have to be calculated within GROUND and that both S3 and S4 are only active in the monolith region.

Solutions to Equations 8.7 and 8.8 are only required in the part of the calculation domain representing the monolith. The method adopted means that by default solutions are provided for the whole calculation domain. The computational cells in the monolith can be isolated from the rest of the domain by setting an adiabatic boundary at its front and rear faces. (Note that for C_{si} the equivalent to an adiabatic boundary is used.) However computational effort is still expended on calculating values for T_s and C_{si} where they are not required; an unavoidable drawback of the method.

8.2.3 External Heat Loss

Although the boundary conditions used for the simulations carried out in the present work are discussed in Section 9.2.1, the modelling of external heat loss through the catalyst requires a more detailed description. Placed between the steel catalyst can and the monolith is a mat made from ceramic wool. Its purpose is to provide some thermal and vibrational insulation for the monolith. Calculation of the heat lost to atmosphere from the monolith must take into account the thermal inertia and low thermal conductivity of this mat. Inclusion of the thermal behaviour of the mat within the present model can be achieved relatively easily. Computational cells representing the mat should be provided at the monolith periphery. These cells are then isolated from all variables except the temperature of the solid, T_s, which is solved in the usual way. So that the matting density, specific heat and conductivity are used to calculate T_s, rather than the monolith properties, appropriate adjustments have to be made to the transient source term and diffusivity. Note that the

thermal resistance and inertia of the steel can is considered negligible compared to the mat. The loss of heat at the can surface is modelled using a heat sink of the form,

$$\text{Heat Loss}_{external} = h_{ext}(T_{\infty} - T_s) \qquad 8.15$$

where T_{∞} is the ambient air temperature and h_{ext} is the external heat transfer coefficient. h_{ext} is estimated from published empirical relationships for natural and forced convection, depending on the environment in which the catalyst is situated (see Appendix D).

9 REACTING MODEL APPRAISAL

As with the fluid dynamics model, before the catalyst model described in Section 8 can be used it is necessary to check the reliability of its predictions against experimental data. To allow a meaningful comparison to be made, suitable experimental data should include a full set of boundary conditions, catalyst dimensions and material properties. Unfortunately there is a limited amount of such data available. One source that has been identified as suitable is the work by Jasper et al. [90]. As part of their project they tested the light-off performance of a selection of ceramic and metallic catalysts under controlled conditions.

9.1 Experimental Data

A full description of the rig from which the Jasper et al. [90] experimental data was collect can be found in Jasper [91]. The exhaust gas supplied to the catalysts was taken from a fully warm 3.6 litre Jaguar AJ6 engine, with a closed loop control system, that was run at a steady load and speed. The reason for pre-warming the engine, with the catalysts isolated, was so that throughout a test the composition and temperature of the gas entering the catalyst section would remain virtually constant. As engines warm-up the temperature and composition of the exhaust gas changes significantly. Although pre-warming the engine meant that results from the study are not truly representative of real light-off conditions, the consistent composition of the gas provides a less demanding environment for the reaction rate expressions.

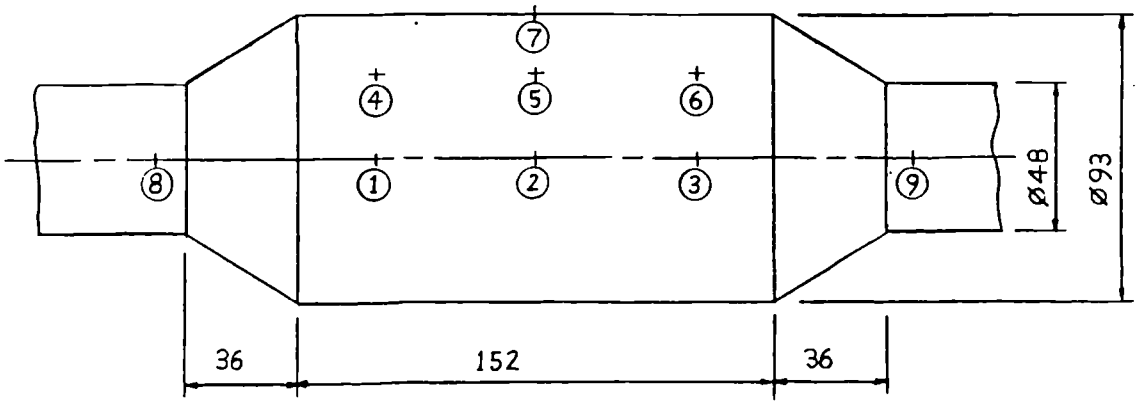

Figure 9.1 - Dimensions (mm) and thermocouple locations of the engine mounted catalyst

An added attraction of the Jasper et al. [90] study is that it includes warm-up characteristics of catalysts which have not been treated with noble metals; so-called washcoat only monoliths. Data

from washcoat only monoliths are particularly useful for establishing how reliable a model is at predicting the heat transfer and fluid flow, together, without the complication of chemical reactions. Because of uncertainties over heat transfer, mass transfer and reaction rate relationships there is great merit in being able to test the various components of a model separately. In view of these comments two cases from [90] were chosen for simulation, a catalyst treated with noble metals, referred to as active, and a washcoat only catalyst. Both consisted of 6 inch long, 3.66 inch diameter ceramic monoliths, with nominal cell densities of 400 cpsi, and both had the same assembly geometry, the dimensions of which are included in Figure 9.1. The active catalyst was described as "fresh", indicating that it had not previously been used.

The experimental data collected included nine temperature measurements, six at positions within the monolith, one on the external surface of the can, one in the inlet pipe and one in the outlet pipe. All temperatures were taken using type K thermocouples, their relative positions being indicated in Figure 9.1. Access to the measuring sites within the monolith was provided by radial holes, drilled into the monolith, down which the thermocouples were passed. As a result of being longer than the width of monolith channels, the measuring length of these thermocouples was partially in contact with the solid and partially in contact with the gas. However, the superior heat transfer between solids meant that the thermocouple temperatures were probably more representative of the solid than the gas. So that the conversion efficiency of the catalyst could be measured a CO meter was positioned downstream from the catalyst. The mass flow rate through the system was measured using a flow rate meter placed upstream of the engine throttle valve.

Although not measured, the catalyst inlet CO concentration throughout the tests was taken to be the initial outlet reading (when the catalyst was cold). Supporting evidence for this assumption was obtained from the washcoat only results, where the exhaust CO concentration remained essentially constant throughout the test. It is also not surprising to note that the inlet CO concentration was the same, at 0.5%, for both the active and washcoat only cases. The inlet O_2 concentration of 2% was estimated from O_2 measurements taken from a similar engine, run under similar conditions, by Jaguar Cars Ltd.

The engine was run at 1250 rpm with only a slight brake load (not specified) giving a constant mass flow rate of 13.89 g/s. Although the temperature of the gas entering the test section was held constant the thermal inertia of the pipework upstream from the catalyst meant that the measured inlet gas temperature rose exponentially from ambient. To reduce inconsistencies these experimental inlet temperatures were used as the gas inlet temperature for the simulations, linear interpolation being employed to obtain temperatures at times not resolved by the measuring frequency. Again it is worth noting that the variation in inlet gas temperature with time for both test cases was virtually identical. They are included as Figure 9.2. The ambient temperature was

assumed to be 300 K, and because the rig was stationary the external heat loss mechanism was taken to be natural convection (see Appendix D).

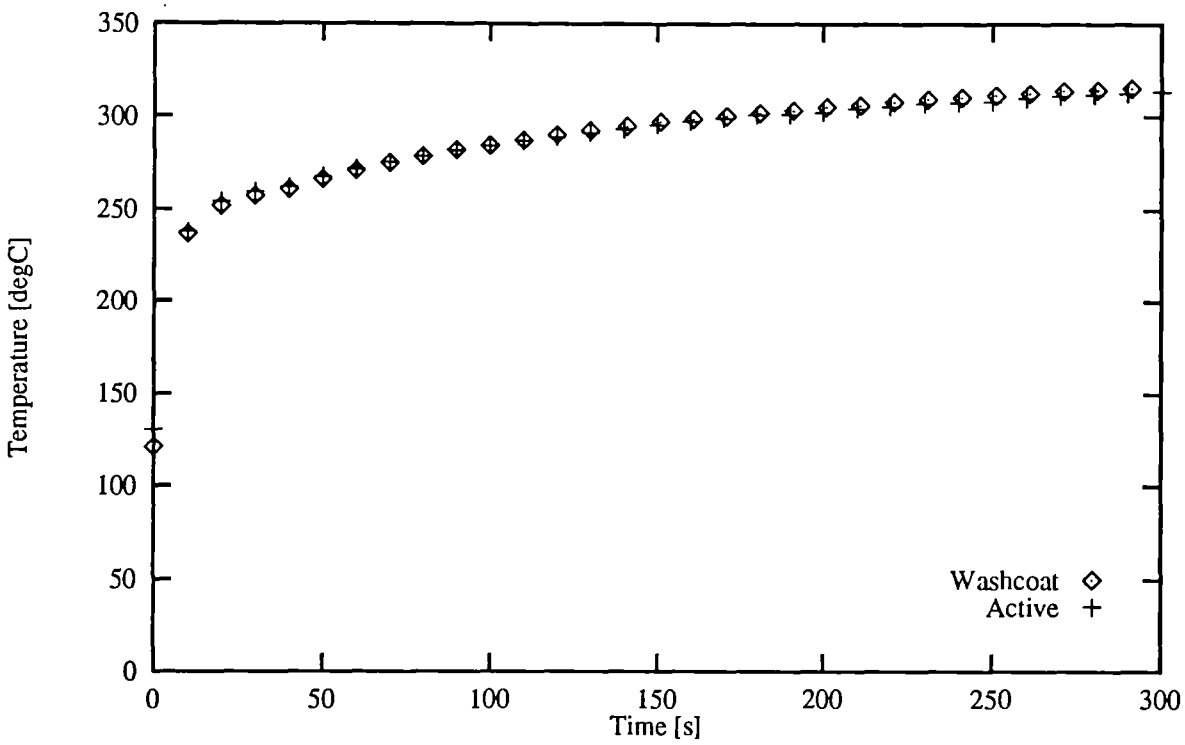

Figure 9.2 - Experimental inlet gas temperatures for the washcoat only and active catalysts

9.2 Simulation of Reacting Catalyst

To illustrate the capabilities of the model a full axisymmetric simulation of the reacting catalyst was carried out. Unfortunately these simulations require considerable computer run times (of the order of a week). To avoid lengthy run times during model development and refinement a simplified one-dimensional version was produced. Results from this version of the model have been included so that a comparison can be made between it and the full axisymmetric version. Note that for the one-dimensional simulation the mass flow was assumed to be uniformly distributed across the monolith.

9.2.1 Problem Specification

The dimensions of the calculation domain were those given in Figure 9.1, with a 0.1 m section of inlet pipe and a 0.05 m section of outlet pipe. The mat thickness was set at 5 mm. The computational mesh consisted of 25 cells across the flow field, 95 cells through the whole domain in the axial direction, including 30 within the monolith, and 5 cells covering the mat in the radial direction. For simplicity the distribution of the dependent variables at the inlet boundary where taken to be uniform. Likewise, the nature of the flow was approximated as being non-pulsating. As

stated above the gas inlet temperature was equated to the experimentally measured values. In the turbulent flow regions the standard k-ε turbulence model with wall functions was used, the inlet turbulence intensity being estimated at 2%. The outlet boundary condition was set to be a uniform pressure boundary. The boundary conditions for the monolith consisted of adiabatic front and rear faces, with radial heat loss through the mat. The turbulence intensity of the flow leaving the monolith was set at 2%. Again, for simplicity, radial heat loss through the steel inlet and outlet ducting was neglected, such that the gas entering the monolith would be at the same temperature as that entering the calculation domain.

The properties of the exhaust gas were taken to be those of dry air. The variation of the kinematic viscosity, ν, with temperature was calculated from,

$$\nu = \left(6.542\times10^{-11}T_g^2\right) + \left(6.108\times10^{-8}T_g\right) - 0.89\times10^{-5} \qquad 9.1$$

which was obtained by fitting a quadratic through tabulated data [92]. A listing of the remaining properties of the exhaust gas is included as Table 9.1. Note that all Prandtl and Schmidt numbers have been approximated as constants, and that all turbulent Prandtl and Schmidt numbers were set at unity. The material properties of the catalyst were assumed to be essentially the same as those used by Chen et al. [60]; they are presented in Table 9.1.

Table 9.1 - Constants used in reacting model

Gas Properties		Heat Transfer	
C_{pg}	1089 J/kgK	Nu	~ 3.6
R	287.1 J/kgK	h	170.0 W/m²K
M_{Rg}	29 kg/kmol	a_v	2000 m²/m³
Pr	0.736		
σ_p	1.0	Mass Transfer	
		Sh	~3.6
Monolith Properties		K_{mCO}	0.4793 m/s
C_{ps}	1050 J/kgK	K_{mO_2}	0.4956 m/s
k_s	0.8 W/mK	D_{CO}	1.332E-04 m²/s
ρ_s	1537 kg/m³	D_{O_2}	1.3541E-04 m²/s
G	0.1795	a_c	5.379E+04 m²NM/m³
α	0.65	ΔH_{CO}	283.2E+03 J/mol
		$Sc(CO \& O_2)$	0.98
Mat Properties		$\sigma_s(CO \& O_2)$	1.0
C_{pm}	600 J/kgK	$C_{gC_3H_6}$	4.5E-04 mol/mol
k_m	0.13 W/mK	C_{gNO}	5.0E-04 mol/mol
ρ_m	1000 kg/m³		

As mentioned in Section 8.1, only the conversion of CO has been modelled. To try and include the effect of the conversion of other emissions species a multiplication factor, Φ, has been used on the CO enthalpy of reaction. A reasonable value for Φ was found to be 1.2 [93]. To calculate the CO reaction rate it is necessary to estimate the concentration of NO and C_3H_6 on the surface of the washcoat. They will be taken as constants, their values, given in Table 9.1, being those used in [60] as inlet concentrations.

For any transient simulation the initial values of all the dependent variables must be known. Although a more realistic initial condition for the flow field would consist of zero velocities everywhere, to make obtaining a converged solution for the first time step easier the initial flow field was taken to be that produced by a steady state isothermal simulation. The initial temperature of the gas and solid where both taken to be 300 K, with the initial concentrations of the chemical species everywhere being set at the inlet values.

Although many of the simplifications and assumptions outlined above will introduce modelling inaccuracies, when considered in the context of the acknowledged weaknesses of the flow field predictions and other relationships, they should not represent serious handicaps. In addition several of the inaccuracies can be reduced relatively easily by introducing supplementary modelling procedures.

9.2.2 Results

Contour plots of the predicted change in T_s, T_g and pressure, with time, are presented in Figures 9.3 to 9.5. The axial distributions of T_s and gas CO concentration for a central channel, at various times, are given in Figures 9.6 and 9.7 respectively. These results show that from 0 seconds to 20 seconds the predominant process taking place in the monolith is the transfer of heat from the gas to the monolith. At about 20 seconds the temperature of the monolith at its front is sufficiently high for the conversion of CO to start (see Figure 9.7). The heat released from these reactions is only enough to cause a slight rise in the local monolith and gas temperatures. The heat in the gas is carried downstream where it is transferred back to the monolith. Consequently the sections just downstream from the monolith front become relatively hotter, creating an environment where a faster reaction rate can exist. Thus, at any given instant during the 20 to 60 second period, starting at the front and travelling in the axial direction, the monolith temperature rises gradually, reaches a maximum and then starts to decrease. As time progresses the maximum temperature gradually moves downstream. Figure 9.6 illustrates this processes.

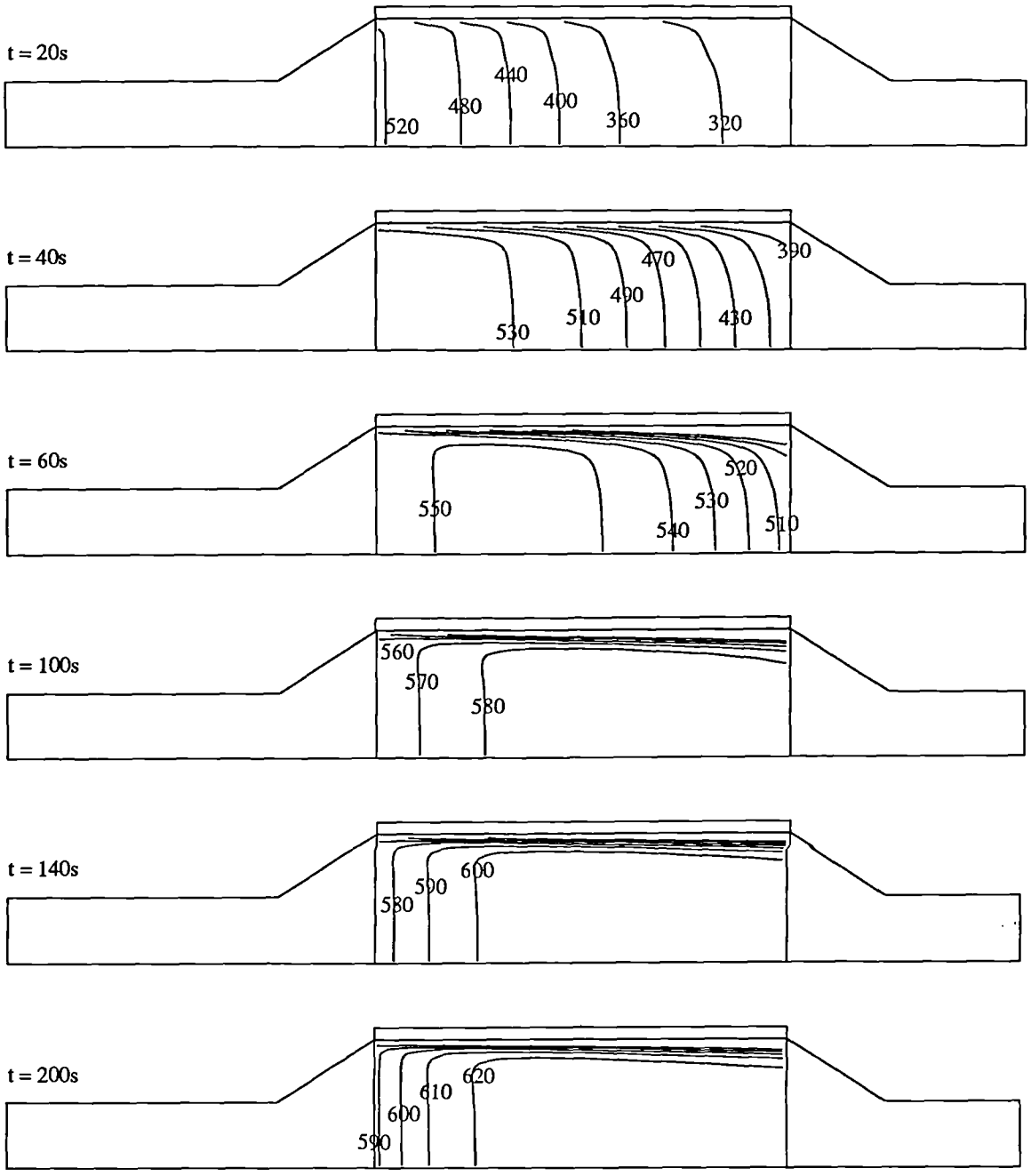

Figure 9.3 - Monolith temperature contours [K]
(flow direction - left to right)

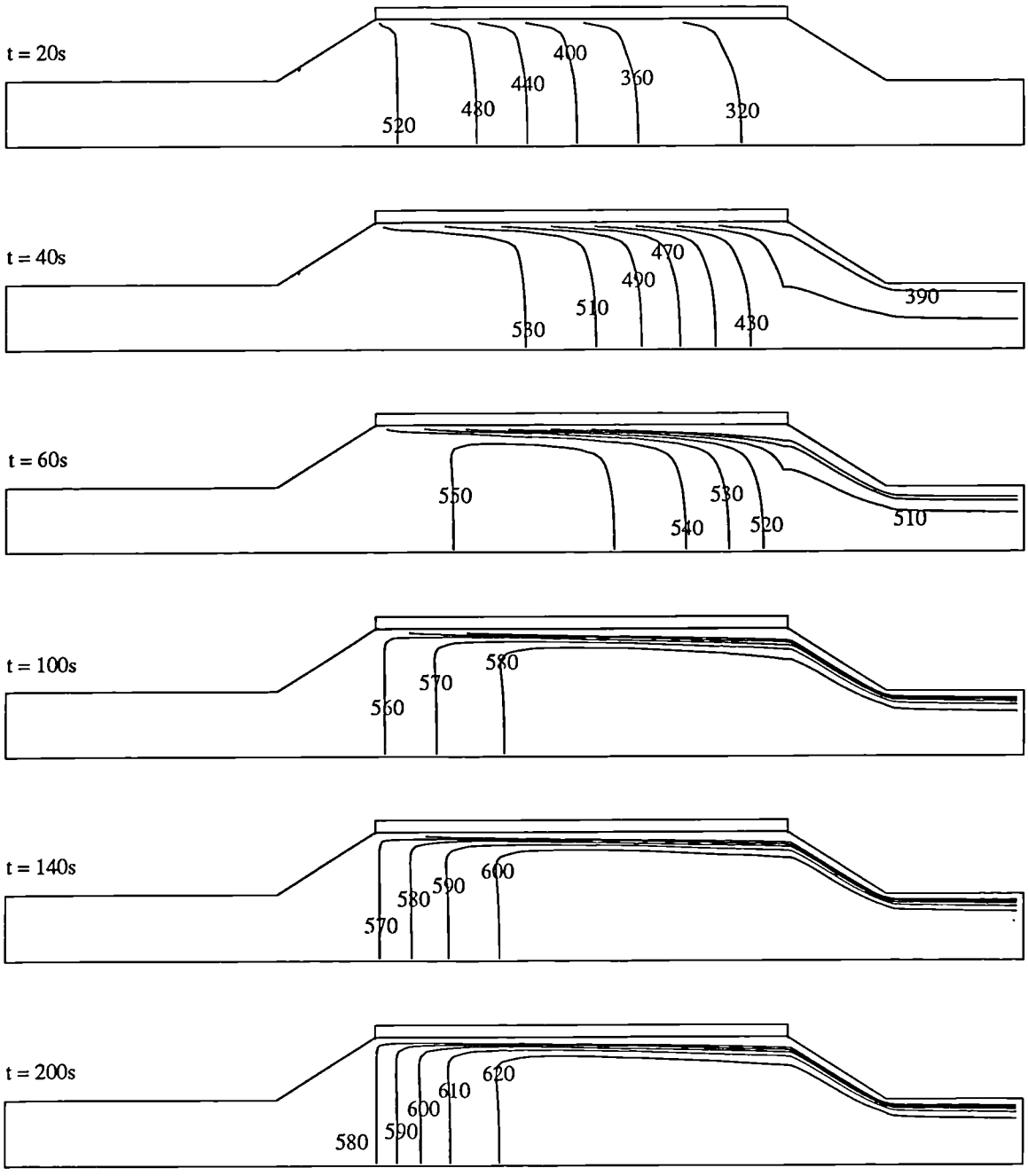

Figure 9.4 - Gas temperature contours [K]
(flow direction - left to right)

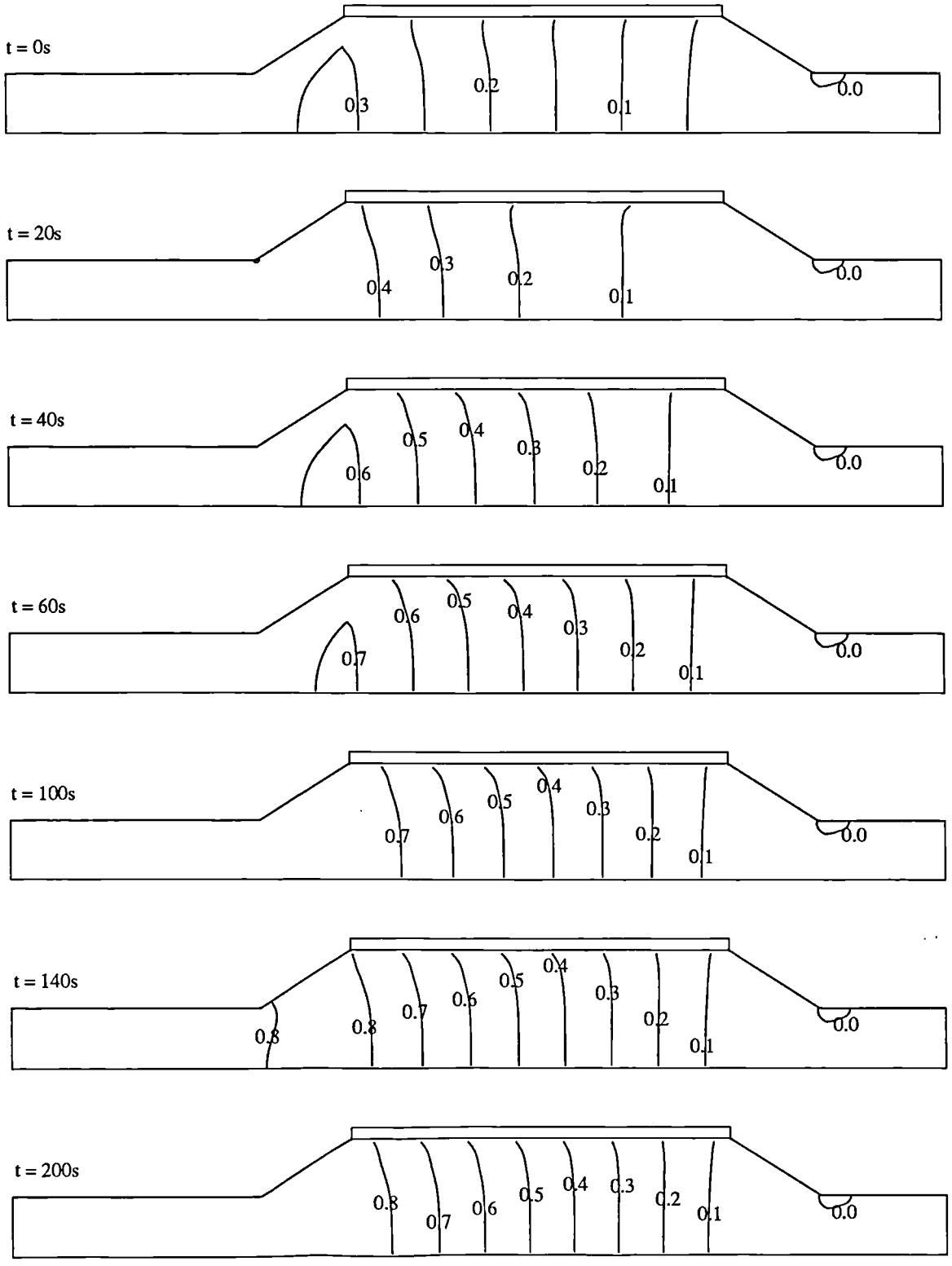

Figure 9.5 - Pressure contours [kPa]
(flow direction - left to right)

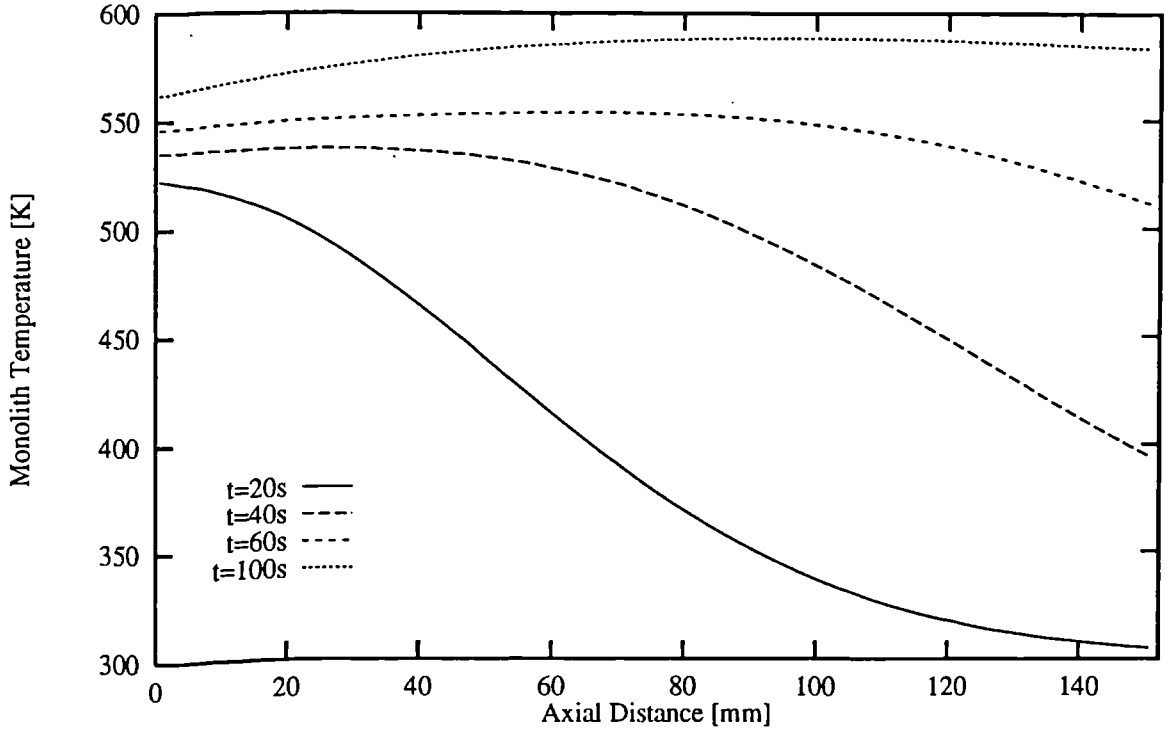

Figure 9.6 - Evolution of predicted distribution of T_s along monolith centreline

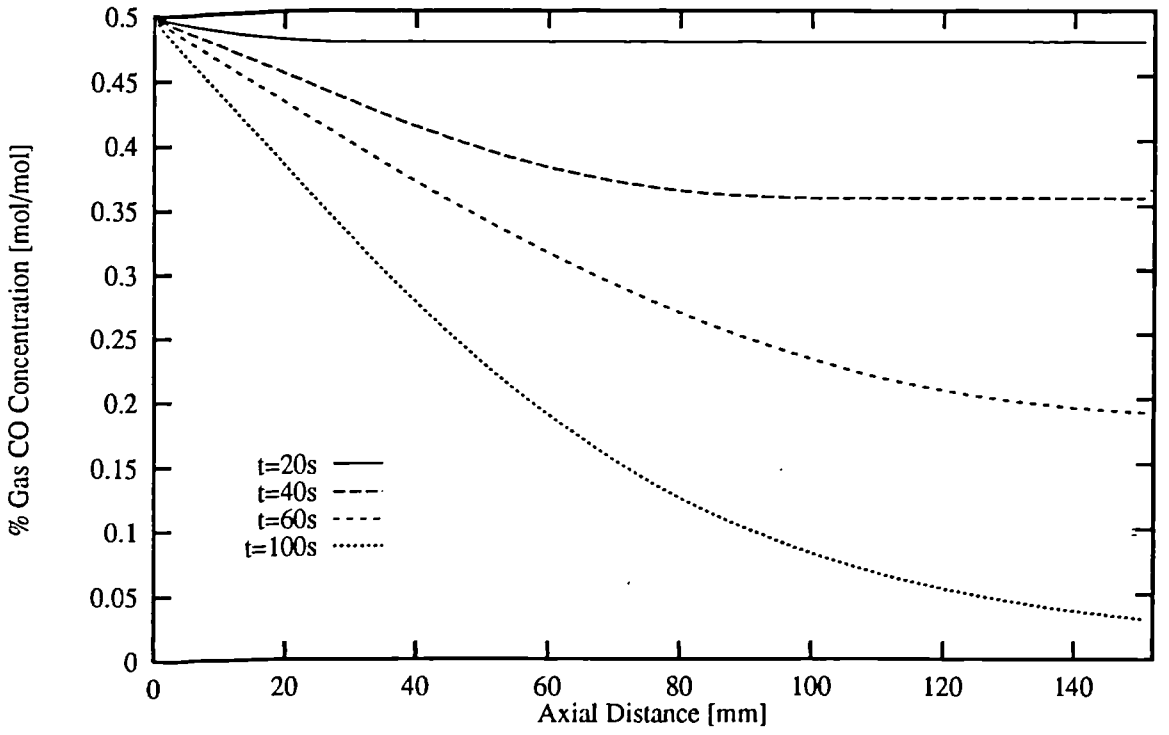

Figure 9.7 - Evolution of predicted CO concentrations along monolith centreline

Also during the 20 to 60 second period an increasing level of CO conversion takes place over the front portions of the monolith, while the rear portions are still absorbing considerable amounts of heat from the gas. By 100 seconds the catalyst is converting almost all the CO and the monolith rear section has effectively reached thermal equilibrium with the gas. Note that at 100 seconds 50% of the CO is converted over the front 25% - 30% of the catalyst. As time continues, and the front of the monolith becomes hotter, the area over which most of the reactions take place will reduce. However, the T_s contours in Figure 9.3 indicate that at 200 seconds the reactions are still occurring, almost uniformly, over the front third of the monolith. Such a pattern means that a well defined reaction front, where most of the reactions take place over a very short axial distance, is absent. Throughout the warm-up period the effects of external heat loss are only felt across the outer 15% of the radius, where large temperature gradients are experienced. Note that over the period 0 to 200 seconds the pressure drop across the system increases from less than 0.3 kPa to more than 0.8 kPa.

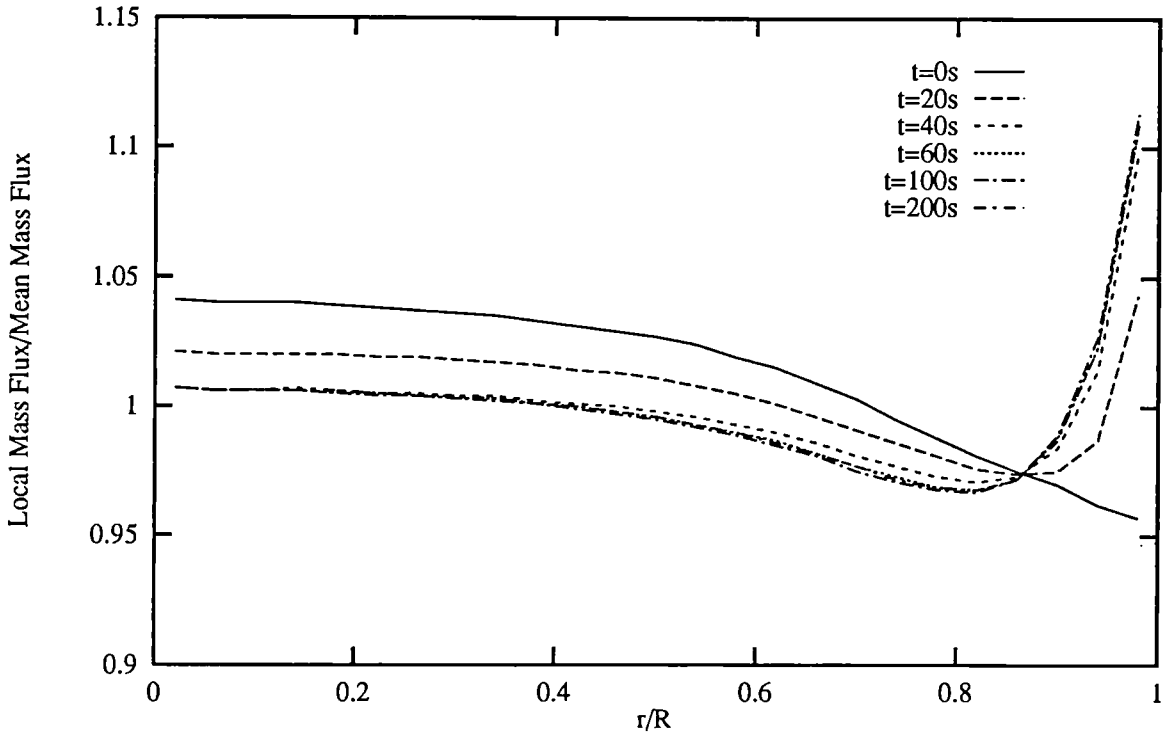

Figure 9.8 - Evolution of mass flux distributions across the monolith

The non-dimensional mass flux distributions across the monolith are shown, at various points in time, in Figure 9.8. Mass flux distributions give a better indication of the mass flow distribution under non-isothermal conditions than velocity distributions. Radial and axial variations in gas temperature create similar variations in gas density, which produce velocity distributions that are not representative of the mass flow distribution. It can be seen that the predicted profile at 0 seconds (isothermal) exhibits the usual features found in catalysts, a peak at the centre and a

minimum at the edge, although the virtually flat nature of the profile and the absence of local maxima at the periphery should be noted. As the monolith warms up the amount of mass flow passing through the central region decreases and a sharp maximum appears towards the edge. The decrease in flow rate through the middle results from the elevated gas temperatures within this region of the monolith. As exhaust gas temperature rises its viscosity increases at a faster rate that its density decreases, causing the flow resistance to increase. At the periphery, where external heat loss produces substantial cooling, the flow resistance becomes proportionately much lower, allowing a significant quantity of fluid to pass down the outer most monolith channels. After 100 seconds the shape of the flow distribution changes only very slightly, the sharp peak at the periphery being maintained.

As has been seen in Section 7, the validity of the 0 seconds flow prediction is doubtful. In reality the flow distribution will be more maldistributed, the turbulence model and course grid being used for these simulations making the prediction particularly poor. Therefore the quantitative details of the predicted flow profiles, as they evolve with time, should not be relied upon. However, the qualitative effect of an increased flow resistance in the central region, causing a flattening of the profile central region, and a reduced flow resistance at the periphery, causing a high local flow rate, is probably realistic. Whether the peripheral peak becomes greater than the central peak cannot be substantiated from the present predictions.

9.2.3 Comparison with Experimental Data

Figures 9.9 and 9.10 show the overall catalyst CO conversion efficiency and the gas outlet temperature, respectively, as they vary with time. In both figures the experimentally determined values are also shown, and in Figure 9.10 the inlet temperature is included for reference. The two-dimensional simulation predicted values were obtained by mass averaging the temperature and CO concentration across the monolith exit. It can be seen that were as the time scales and magnitude of the predicted rise in outlet temperature and conversion efficiency are similar to the experimental data, certain features of the time plots are different. The obvious difference between the conversion efficiencies is that while the predicted results show a relatively rapid rise, to almost full conversion, over the 20 to 150 second period, the measured efficiency, after an initial rapid rise to 65% in 70 seconds, tails off to a gradual rise, reaching 88% after 300 seconds. Also, at the start of the warm-up the model predicts the onset of light-off slightly later than the experimental results indicate. In essence the predicted conversion efficiency behaves in a similar way to the experimental results up to approximately 70 seconds. There after significant differences occur.

There are two notable differences between the conversion efficiency histories for the two-dimensional and one-dimensional simulations. The two-dimensional simulation starts to light-off

just before the one-dimensional simulation. Such an effect is consistent with the findings of a number of workers [2], that maldistributed velocity profiles produce faster light-off. The one-dimensional model assumes that the velocity profile is flat. It also assumes that there is no external heat loss, something the two-dimensional case includes. The slight flow maldistribution predicted by the two-dimensional simulation produces a higher flow rate in the centre of the monolith, which is insulated from the effects of external heat loss. A higher flow rate means that light-off temperatures are reached more rapidly.

The second difference occurs during the middle and latter stages of light-off, when the effects of external heat loss and velocity profile redistribution start to be felt in the two-dimensional simulation. Both these effects cause a slowing in the rate at which the conversion efficiency rises, relative to the one-dimensional case. The increased flow rate through the relatively cool peripheral area causes breakthrough of the CO.

The major differences between the predicted and experimental behaviour of the outlet temperatures occurs during the early part of the warm-up cycle. The experimental results show an initial rapid rise in temperature, to approximately 70 °C, where upon the temperature remains effectively static from 20 to 70 seconds. After 70 seconds the outlet temperature starts to rapidly rise again, eventually following an exponential type curve. In contrast, both predicted sets of results show an initial lag in outlet temperature which remains below 30 °C for almost 15 seconds, followed by an exponential rise that is similar in shape to the measured temperature, but which is advanced by 50 seconds. A similar pattern is found between the predicted and measured monolith temperatures (see Figure 9.15 - Note that only curve (i) is pertinent to the present discussion; curve (ii) is commented on below). A particularly revealing observation to be made from Figure 9.15 is the difference between predicted and measure temperatures once the rate of temperature rise has slowed. At thermocouple location 1 the temperature difference is approximately 50 °C, at location 2 the difference is approximately 25 °C and at location 3 the difference is approximately 20 °C. These trends indicate that in reality the axial temperature gradient right at the front of the monolith is steeper than the model predicts. In turn this suggests that a more pronounce reaction front exists than the model predicts.

The final gas outlet temperature predicted by the two-dimensional simulation is approximately 20 °C below the measured value, where as the one-dimensional simulation gives the same outlet temperature. Also, like the conversion efficiency predictions, and for the same reasons, after 30 seconds the two-dimensional simulation predicts an outlet temperature that is lower than the one-dimensional prediction. However, despite the discrepancies between the experimental and predicted results the model reproduces the general behaviour displayed by the test bed catalyst.

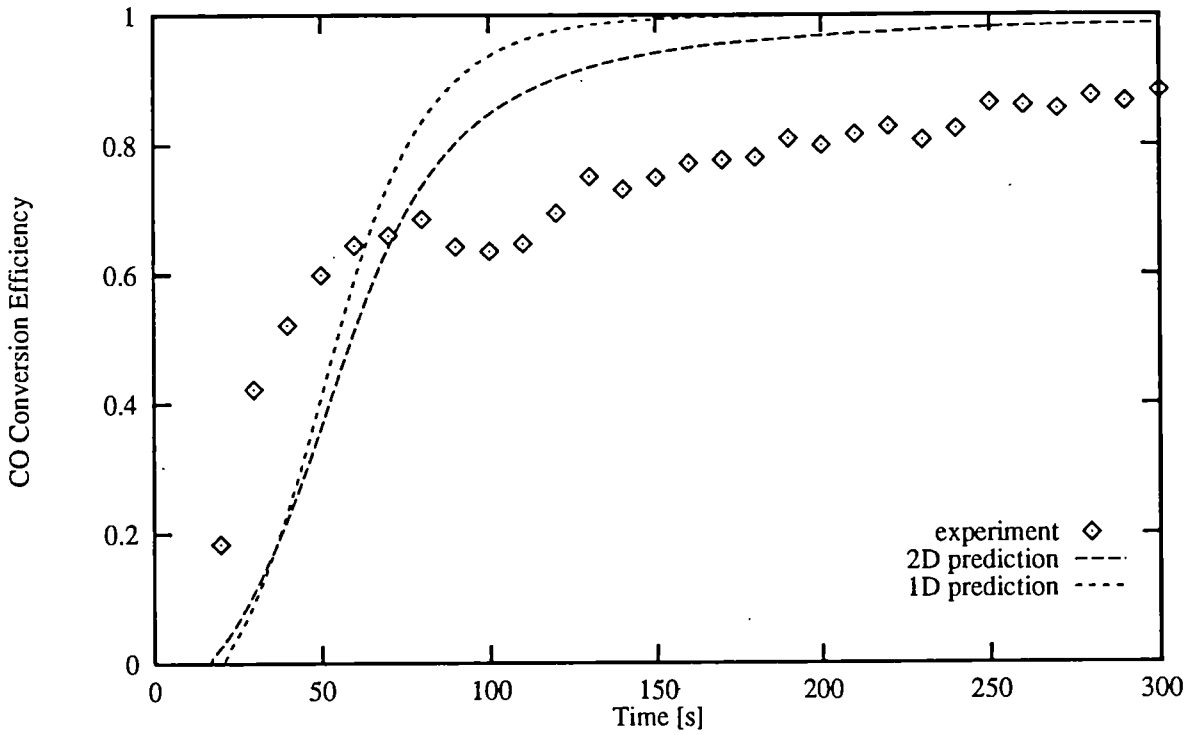

Figure 9.9 - Comparison between experimental and predicted CO conversion efficiency

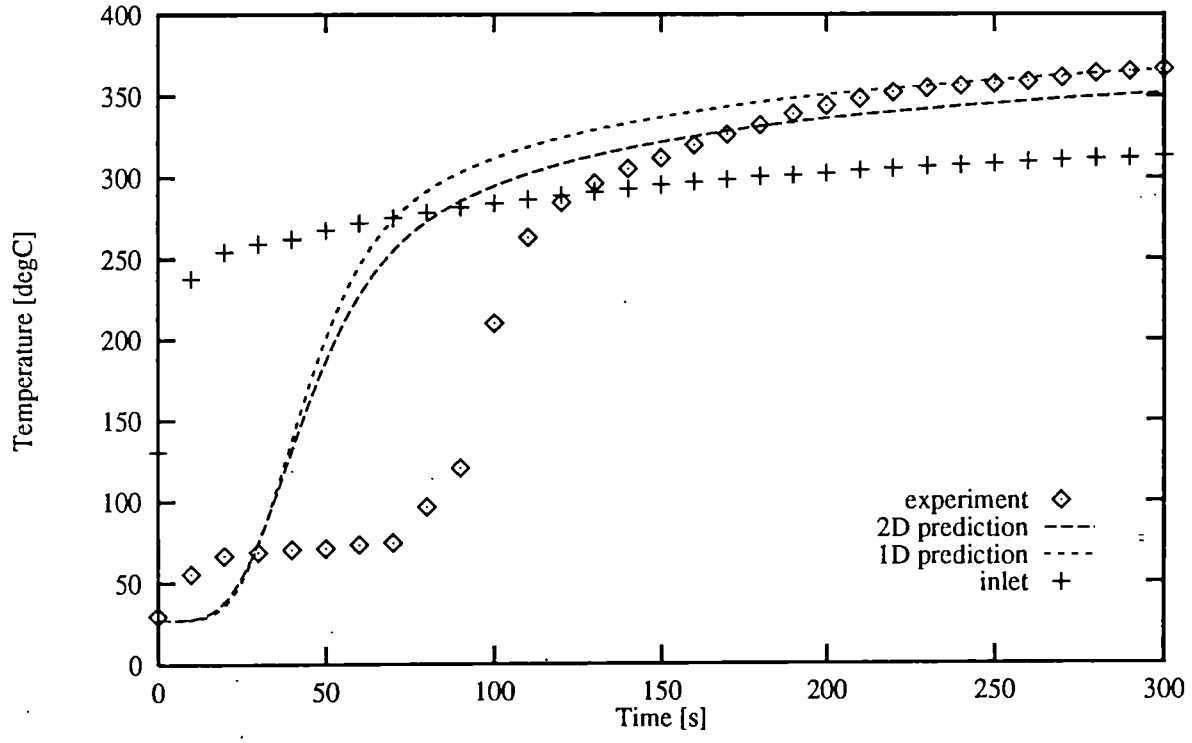

Figure 9.10 - Comparison between experimental and predicted outlet gas temperatures

9.2.4 Sources of Error

There are many possible, including a number of probable, reasons for the differences in the predicted and measured temperature and conversion efficiency histories. It is very likely that the predicted CO reaction rates are incorrect, which could account for the delayed onset of light-off and the high conversion efficiencies after 70 seconds. These incorrect reaction rates maybe caused by several factors. It is likely, for reasons discussed in Section 3.5, that the reaction rate expressions themselves, as well as the prescribed area of noble metal per unit reactor volume, a_c, are inaccurate. The use of a fresh catalyst, however, suggests that the assumption of a constant value for a_c is at least reasonable.

Even if the reaction rate expressions were correct, incorrect calculation of the solid temperature will lead to erroneous reaction rate predictions; the reaction rates are strongly influenced by the solid temperature. Incorrect calculation of solid temperatures can result from incorrect calculation of the heat transfer between the gas and solid, and/or prescription of inaccurate solid thermal properties. The same argument applies to the transfer of CO between the gas and solid. This is particularly true post-light-off, when the species conversion process is mass transfer controlled, such that an incorrect mass transfer rate can lead to an erroneous conversion efficiency. An experimental study by Ullah et al [94] suggests that the mass transfer coefficients encountered in catalysts are an order of magnitude lower than those encountered in conventional laminar flow environments.

Another possible reason for the discrepancies between the predicted and experimental results is the incorrect prediction of the monolith velocity distribution. The difference between assuming an adiabatic uniform flow field and allowing a changing non-uniform flow field, with external heat loss, has been seen above. A more maldistributed velocity profile should accentuate these differences. Errors in the external heat loss calculation may also be a contributory factor. If the external heat loss calculations are correct the prediction of low gas outlet temperatures and high conversion efficiencies, after 200 seconds, suggests that a value for Φ greater than 1.2 would be more appropriate, and that the solution of only one chemical species may be a significant handicap. It is also worth noting that the experimental CO and O_2 concentrations might be in error.

The failure of the model to predict the behaviour of the gas outlet and solid temperatures during the early stages of the warm-up would suggest that the heat transfer between the gas and solid is being incorrectly modelled. The most likely reason for the accelerated initial warm-up and subsequent plateau in the temperatures is moisture. Confirmation that these effects are not connected with the chemical conversion processes is provided by their existence in the results from the washcoat only catalyst (see Figures 9.11 to 9.13). It can be shown (Appendix E) that the

stoichiometric combustion of a typical fuel produces a mass fraction of moisture in the exhaust gas of approximately 7.6%. If the gas density during the early stages of the warm-up is approximately 1.2 kg/m^3, the specific volume of the moisture will be in the region of 11 m^3/kg, which equates to a saturation temperature of approximately 52 °C. Such a temperature is similar to the plateau temperature, indicating that the plateau may represent the evaporation of moisture from the washcoat. Condensation of moisture could also produce the accelerated warm-up occurring over the first 20 seconds. If these effects are real, a failure to simulate them may significantly affect the model's ability to predict the onset of light-off.

Simplifying the model flow field to be non-pulsating may also introduce errors. Pulsations in the exhaust gas are known to affect the heat transfer rates to the exhaust manifold and pipework (Wendland [95]), therefore it is conceivable that pulsations may affect the heat transfer within the monolith. Pulsating flow is also likely to alter the flow field in the inlet diffuser, which will have an effect on the monolith velocity profile. The influence of oscillations in the inlet CO concentration was discussed in Sections 2.4 and 3.6. From these comments it can be seen that introducing an oscillating inlet CO concentration, in the absence of accurate transient reaction rate expressions, will not necessarily improve the accuracy of the predictions.

The apparent failure of the model to predict a distinct reaction front at the front of the monolith may be due to the use of constant Nu and Sh values. In the same way that developing thermal and hydrodynamic boundary layers increase local Nu and Sh numbers, the existence of monolith entrance effects may lead to increased augmentation of heat and mass transfer rates at the monolith front. The absence of these increased heat and mass rates within the model means that the solid temperatures and reaction rates at the monolith entrance are lowered, causing a smearing out of the reaction front. Thus a possible model refinement would be the inclusion of one of the published Nu and Sh relationships that predict the effect of developing boundary layers. Most of the available relationships assume a uniform velocity and temperature field at the channel entrance. Although such an ideal inlet flow field is unlikely to apply to monolith channels, these relationships represent a closer approximation than constant Nu and Sh values.

9.3 Effect of Moisture

It was suggested above that one of the main reasons for the differences between the model predictions and the experimental results might arise from the influence moisture has on the initial stages of catalyst warm-up, an effect that the model does not include. To investigate this influence a simple mathematical representation of the likely condensation - evaporation processes taking place within monoliths, as they warm-up, was developed. The resulting moisture model is based on two moisture conservation equations, one for the concentration of moisture within the washcoat

and one for the concentration of moisture within the gas phase. So that these equations can be incorporated within the existing model they have been derived in a form consistent with the equivalent continuum approach.

9.3.1 Mathematical Representation

The mass fraction of moisture in the gas, c_{gw}, is obtained from a conservation equation of the usual form,

$$\frac{\partial \rho_g c_{gw}}{\partial t} + \nabla.\left(\rho_g U c_{gw}\right) - \nabla.\left(\left(\frac{\mu_t}{\sigma_s} + \rho_g D_w\right)\nabla c_{gw}\right) = S6 \qquad 9.2$$

Equation 9.2 can be solved in the same manor as Equation 8.4. The source term S6 represents the transfer of moisture between the gas and solid. It is only active in the monolith, and is given by,

$$S6 = \rho_g K_{mw} a_v \left(\frac{1}{\rho_g v'_{sw}} - c_{gw}\right) \qquad 9.3$$

where v'_{sw} is the specific volume of the saturated water vapour at the washcoat surface and K_{mw} is the mass transfer coefficient for the moisture. S6 can be introduced as a source term in a similar way to S2 in Equation 8.4. The formulation of S6 is based on the assumption that the moisture in the washcoat is predominantly in the liquid phase, with a thin layer of saturated vapour adjacent to it. The water and saturated vapour are taken to be in thermal equilibrium with the washcoat. Thus v'_{sw}, which will be a function of the monolith temperature, can be estimated from the thermodynamic properties of steam [92]. To facilitate its calculation within the computational model the algebraic function,

$$v'_{sw} = \exp\left(1.325\times10^{-4}\Theta_s^2 - 0.06\Theta_s + 5.175\right) \qquad 9.4$$

was derived. Note that Θ_s is the temperature of the monolith in °C, and that Equation 9.4 is only valid for $20 \le \Theta_s \le 120$. To obtain a representative value for D_w, the diffusivity of the water vapour, a Schmidt number of 0.6 and the kinematic viscosity of steam at 328 K were taken, giving D_w a value of $1.66\text{x}10^{-4}$ m²/s. The calculation of K_{mw} was based on the assumption that the Sh was constant at 3.66. Using the above value of D_w, makes K_{mw} = 0.5976.m/s.

The conservation equation for the moisture in the washcoat is,

$$\frac{\partial C'_{sw}}{\partial t} = K_{mw} a_v \left(\rho_g c_{gw} - \frac{1}{v'_{sw}} \right) \qquad 9.5$$

where C'_{sw} is the mass of water stored in the washcoat per unit monolith volume. The easiest way of solving such an equation is to discretize the transient term to obtain the algebraic expression,

$$0 = \left[C'^{o}_{sw} + K_{mw} a_v \Delta t \left(\rho_g c_{gw} - \frac{1}{v'_{sw}} \right) \right] - C'_{sw} \qquad 9.6$$

where Δt is the duration of the time step. Equation 9.6 is essentially a source term only equation and can be solved in the same manor as Equation 8.7.

The last part of the mathematical representation of moisture involves modelling the effect condensation and evaporation have on the temperature of the monolith. When moisture condenses on the washcoat the latent heat of vaporisation is given up to the monolith, which consequently increases in temperature. Conversely, for moisture to evaporate the latent heat of vaporisation mush be provided by the monolith, which, if not actually causing a fall in temperature, will prevent the monolith temperature from rising. Both these effects can be achieved with the addition of an extra source term in Equation 8.8. It takes the form,

$$S5 = \frac{C'_{sw} - C'^{o}_{sw}}{\Delta t} \frac{h_{fg}}{(1-\alpha) c_{ps}} \qquad 9.7$$

where h_{fg} is the latent heat of vaporisation. Like v'_{sw}, h_{fg} will vary with the monolith temperature and can be estimated from published data [92]. A very close approximation can be obtained from a linear relationship, however over the temperature range 20 °C to 100 °C acceptable accuracy is achieved by fixing h_{fg} at a constant value of 2370.1 kJ/kg. S5 is introduced as a "fixed flux" in a similar fashion to S4 in Equation 8.8. It should be noted that although Equation 9.6 can be directly substituted into Equation 9.7, there by eliminating the moisture concentration in the washcoat from the calculations, it is necessary to solve for C'_{sw} to ascertain when all the moisture has been evaporated from the washcoat. Note that coding has to be provided to prevent C'_{sw} from becoming negative. The storage of C'^{o}_{sw} is achieved by setting up a special GROUND array (c.f. solution of Equation 8.8, Section 8.2.2)

9.3.2 Washcoat Only Predictions

To avoid lengthy computer run times development of the moisture model was carried out using the one-dimensional version of the catalyst model. The loss of detail by adopting such an approach was not considered a handicap, particularly in view of the near uniform velocity distribution predicted by the full axisymmetric simulations. However, the absence of external heat loss should be borne in mind when comparisons are made between the gas outlet temperature.

To remove the uncertainty caused by reaction rate expressions and mass transfer coefficients, the initial assessment of the model's performance was restricted to the washcoat only case. For these simulations all parameters remained identical to the axisymmetric simulations, with the reactions switched off and the inlet gas moisture mass fraction being set at 0.076 kg/kg. Figure 9.11 compares the variation in experimental and predicted gas outlet temperature with time. For completeness a one-dimensional "dry" simulations has been included. Because the moisture mass transfer rate is so fast when a mass transfer coefficient of 0.5976.m/s is used, to resolve the condensation - evaporation process requires time steps of the order of 0.01 seconds. To investigate the influence of the mass transfer coefficient, a simulation was run using a value 10 times smaller. Use of this value allowed time steps of 0.1 second to be used, yet did not significantly affect the behaviour of the outlet temperature (Figure 9.11). These results show that the model quantitatively predicts the correct type of behaviour; an accelerated warm-up over the first 10 seconds, followed by a temperature plateau at approximately 55 °C. The length of the plateau, however, is only 20 seconds compared with the 50 seconds of the experimental data. (Note that the experimental results from this washcoat only catalyst show that the duration of the initial temperature rise and the plateau temperature differ from the active catalyst - see Figures 9.14 and 9.15).

Two factors that should influence the duration of the temperature plateau are the exhaust gas flow rate and the possibility that the washcoat may have absorbed atmospheric moisture prior to any exhaust gas entering the system. To test the flow rate relationship the mass flow was multiplied by a factor of 1.8 and 0.8, values that would also allow an assessment to made of the influence a maldistributed monolith velocity distribution has. Data supplied by Johnson Matthey indicates that monoliths do absorb moisture. The mass of a 1.675×10^{-3} m^3 400 cpsi ceramic monolith was measured at 0.979 kg immediately after being cured in an oven. 30 minutes later its mass had increased to 0.989 kg. If the mass increase is due purely to absorption of moisture the initial value of C'_{sw} will be 6 kg/m^3. It is possible that this figure may vary, depending on atmospheric humidity levels. To try and improve the model predictions further, without using an excessively high value, the initial washcoat moisture concentration was set at 10 kg/m^3. Figure 9.12 illustrates the effect of combining both the flow rate variations and an initial moisture concentration on the gas outlet temperature. These results confirm that an initial moisture concentration extends the duration of

the plateau and that a reduced flow rate delays both the initial rise in temperature and the termination of the plateau. An increase in the flow rate has the opposite effect. Included in Figure 9.12 is the effect of doubling the mass fraction of moisture within the gas, to 0.152 kg/kg, assuming the monolith to be initially dry. As might be expected the speed of the initial temperature rise and the temperature and length of the plateau are all increased.

Comparison between experimental and predicted monolith temperatures, including a "dry" simulation, is shown in Figure 9.13. The "wet" simulation used a moisture mass transfer coefficient of 0.05976 m/s, an initial washcoat moisture concentration of 10 kg/m^3 and a gas inlet moisture concentration of 0.076 kg/kg. With the moisture model very good agreement is achieved on initial temperature rise, the duration and temperature of the evaporation plateau and the final solid temperature, for all three thermocouple positions. The only difference is the rate at which the temperature rises, after the plateau, up to the final temperature.

From these results it can be seen that the moisture model correctly predicts the type of behaviour displayed by the experimental data. However, quantitatively there are still some discrepancies. Although close agreement on the duration of the evaporation plateau is achieved with the solid temperatures, it is lacking with the gas outlet temperature. This could be due to the position of thermocouple 9 (see Figure 9.1), which is different from the location where the predicted value is taken (at the monolith exit plane). It is possible that evaporation of moisture in the exit cone and pipe prolongs the duration of the plateau at position 9. The incorrect prediction of the rate of solid temperature rise after the evaporation plateau may be due to the use, within the model, of a monolith specific heat that is too low and/or too high a heat transfer rate. There are a number of other factors that may influence the accuracy of the model. No account is made of the effect moisture in the washcoat has on the specific heat and thermal conductivity of the solid and assumptions made about the moisture mass transfer coefficient and latent heat of vaporisation may be in error. Despite these weaknesses the model is sufficiently reliable to test whether the influence of moisture has a significant effect on catalyst light-off.

9.3.3 Active Catalyst Predictions

To test the influence of moisture on light-off the moisture model was coupled to the reacting model. Again all parameters were kept the same as previous simulations, including a moisture mass transfer coefficient of 0.5976 m/s, an initial washcoat moisture concentration of 10 kg/m^3 and an inlet gas moisture mass fraction of 0.076 kg/kg (for convenience referred to as the standard moisture simulation). To try and improve the accuracy of the prediction an additional simulation was carried out with the inlet gas moisture mass fraction set to 0.194 kg/kg and the moisture mass transfer coefficient multiplied by 0.01 (for convenience referred to as the increased moisture

simulation). The gas outlet temperature results from these cases are presented in Figure 9.14, where they are compared with the experimental data and a "dry" simulation using the same distribution of time steps. They show that the increased moisture simulation gives marginally more accurate results than the standard moisture simulation. Like the previous comparisons between the gas outlet temperature, the results displayed in Figure 9.14 show that the moisture model exhibits the correct type of behaviour, however the duration of the predicted evaporation plateau is too short.

Figures 9.15 shows a comparison between the T_s results from the increased moisture simulation, the dry simulation and the experimental data at thermocouple locations 1, 2 and 3 (Figure 9.1). Again close agreement is achieved between the moisture model and the experimental data, on the initial temperature rise and the plateau temperature and duration. Unlike the washcoat only simulations, however, good agreement is also achieved over the rate at which the solid temperature rises after the plateau. Comments made about the difference between the final solid temperatures in Sections 9.2.3 and 9.2.4 are again applicable.

Finally Figure 9.16 shows the CO conversion efficiency histories for the increased moisture and "dry" simulations. There is virtually no difference between the predictions from these simulations, indicating that for the particular catalyst conditions under examination the presence of moisture does not affect light-off times. This will be due to the concentration of the chemical reactions in the front third of the monolith, which will dry out and reach the light-off temperature at essentially the same time as a the dry simulation (see Figure 9.15(a)). It is possible that the presence of moisture will effect light-off times when the position of the light-off is towards the rear of the monolith or if the temperature at which the reaction rates become significant is reduced.

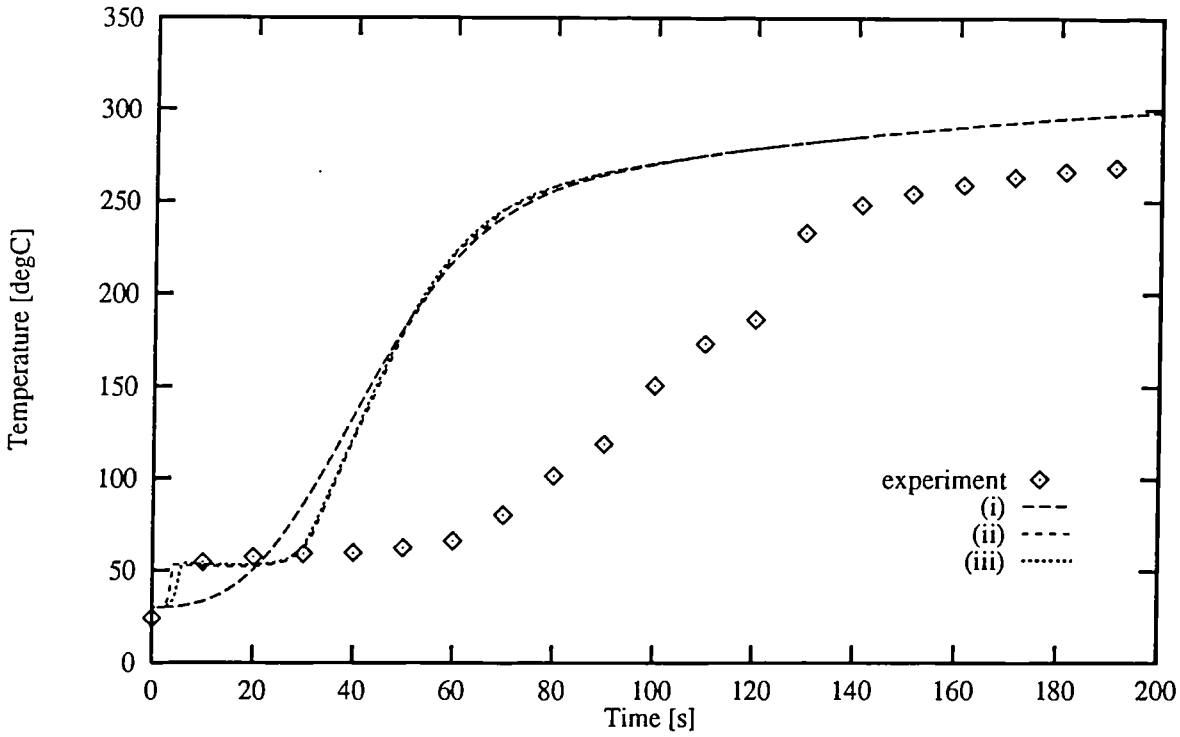

Figure 9.11 - Outlet gas temperature for washcoat only catalyst; (i) dry simulation, (ii) wet simulation with K_{mw} = 0.5976 m/s, (iii) wet simulation with K_{mw} = 0.05976 m/s

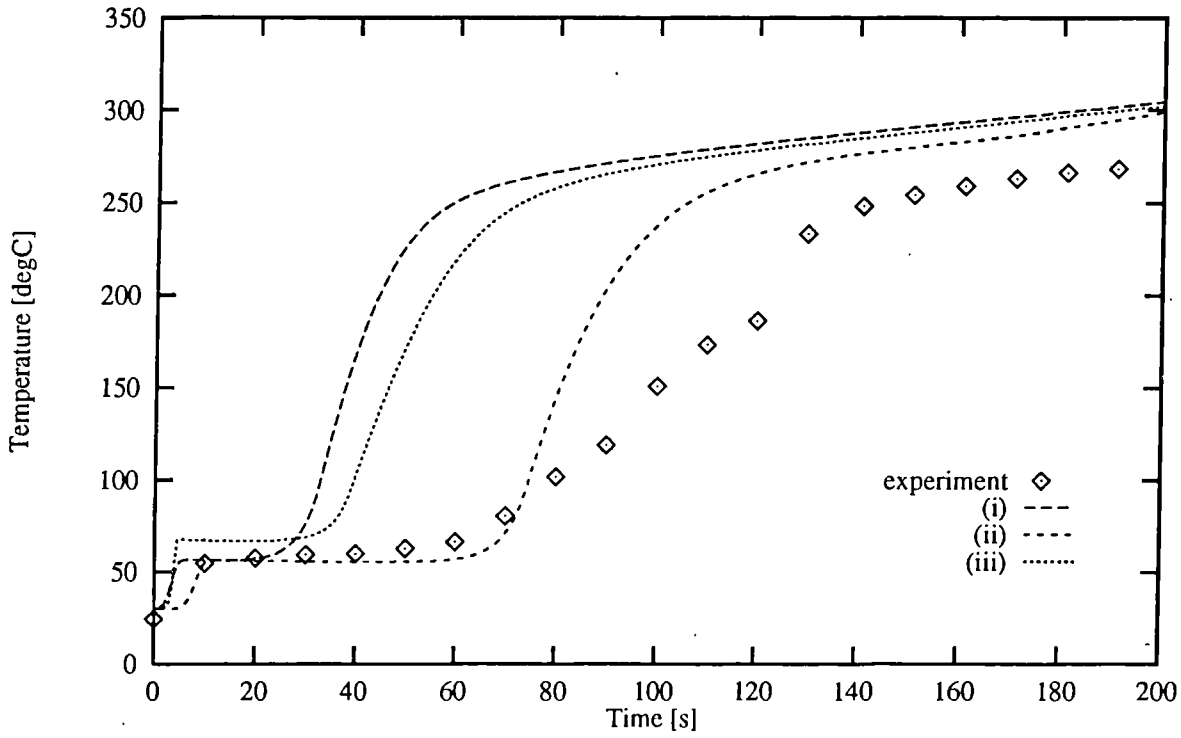

Figure 9.12 - Outlet gas temperature for washcoat only catalyst; (i) wet simulation with K_{mw} = 0.05976 m/s, mass flow rate multiplied by 1.8 and C'^{o}_{sw} = 10 kg/m^3 (ii) as (i) but mass flow rate multiplied by 0.8, (iii) as (i) but mass flow rate multiplied by 1.0, C'^{o}_{sw} = 0 and inlet c_{gw} = 0.152

In Figure 9.13 (results for the washcoat only catalyst) dry simulations are represented by (i) and the wet, with $K_{mw} = 0.05976$ m/s, $C'^{o}_{sw} = 10$ kg/m^3 and inlet $c_{gw} = 0.076$, by (ii).

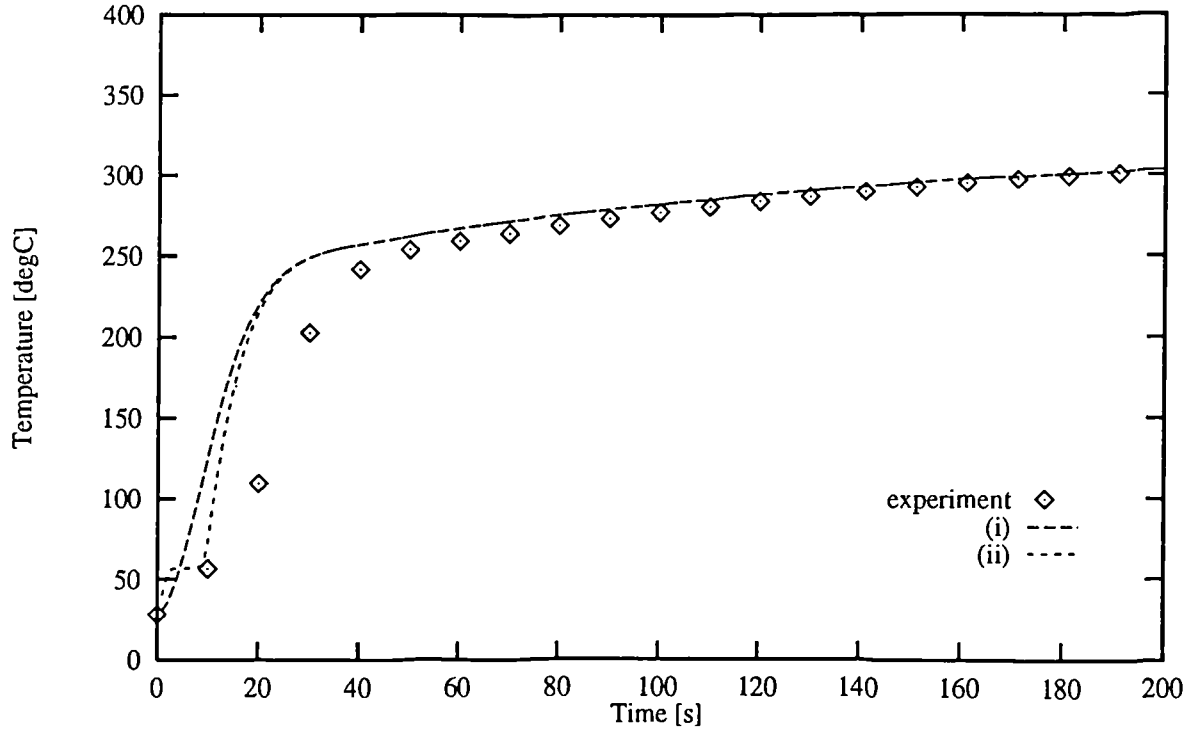

Figure 9.13(a) - T_s values at thermocouple location 1

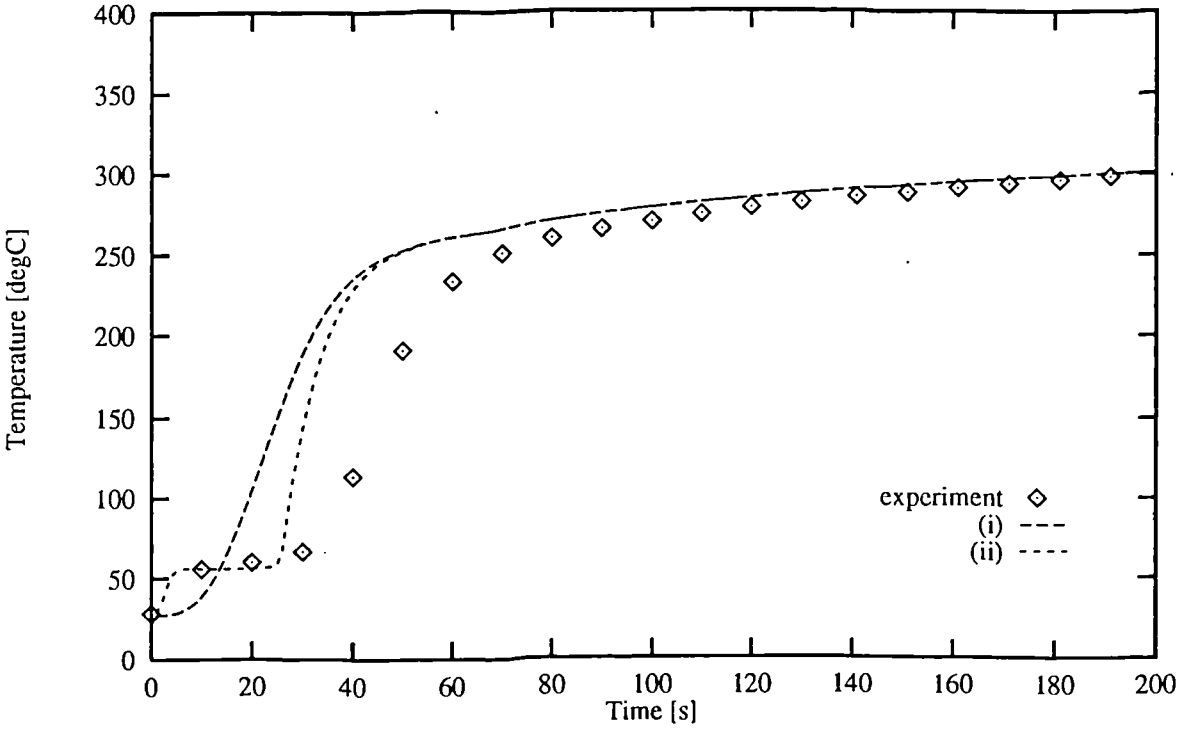

Figure 9.13(b) - T_s values at thermocouple location 2

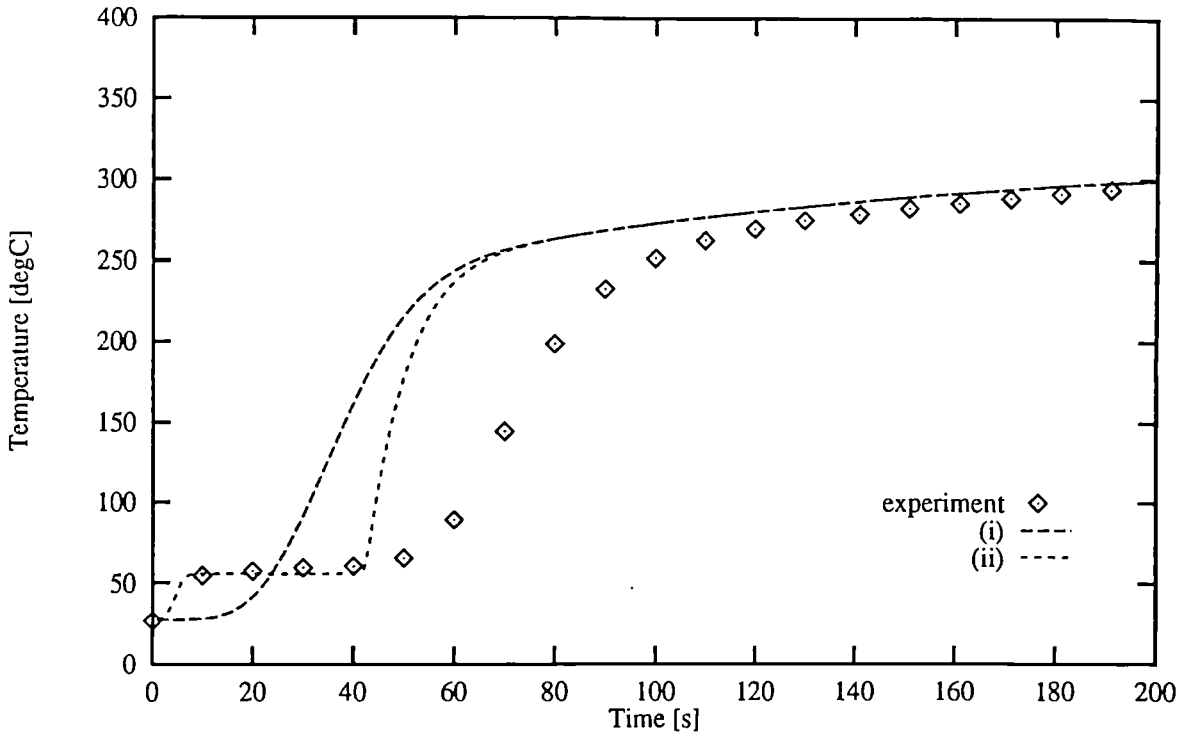

Figure 9.13(c) - T_s values at thermocouple location 3

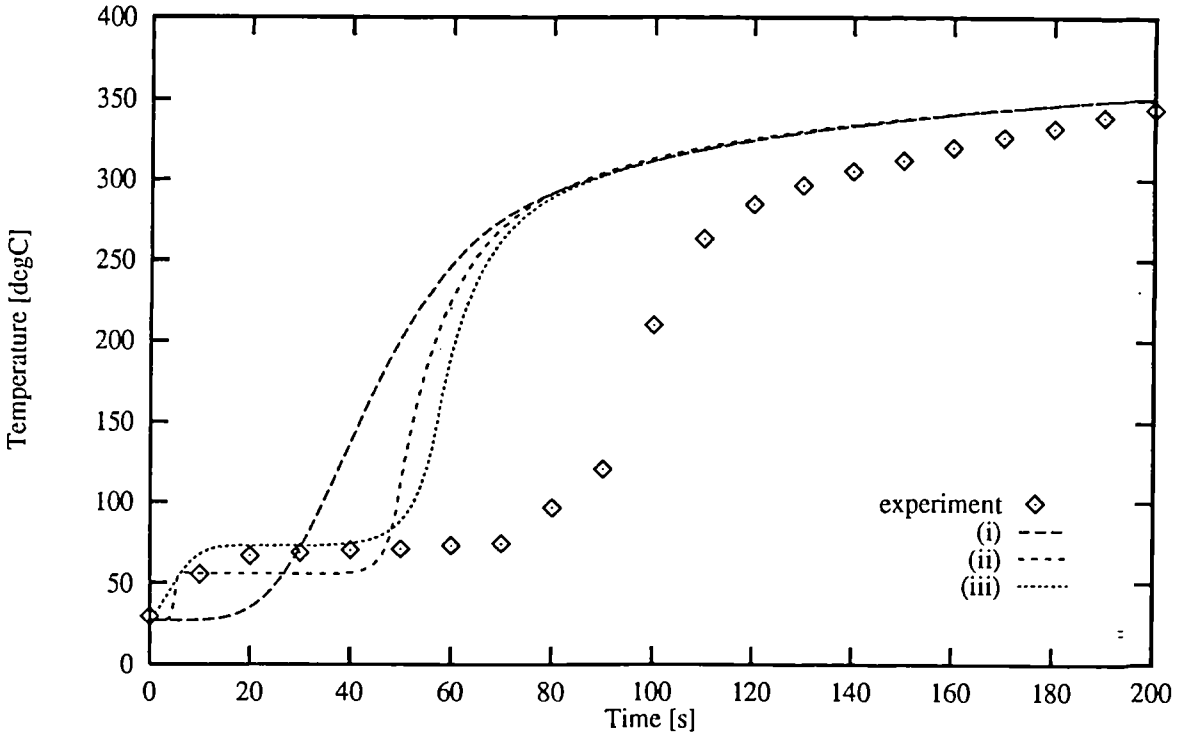

Figure 9.14 - Outlet gas temperature for active catalyst; (i) dry simulation, (ii) wet simulation with K_{mw} = 0.5976 m/s, inlet c_{gw} = 0.076 and C'^{o}_{sw} = 10 kg/m^3 (iii) as (ii) but K_{mw} = 0.005976 m/s and inlet c_{gw} = 0.194

In Figure 9.15 (results for the active catalyst) dry simulations are represented by (i) and the wet, with $K_{mw} = 0.005976$ m/s, $C'^{o}_{sw} = 10$ kg/m^3 and inlet $c_{gw} = 0.194$ (increased moisture), by (ii).

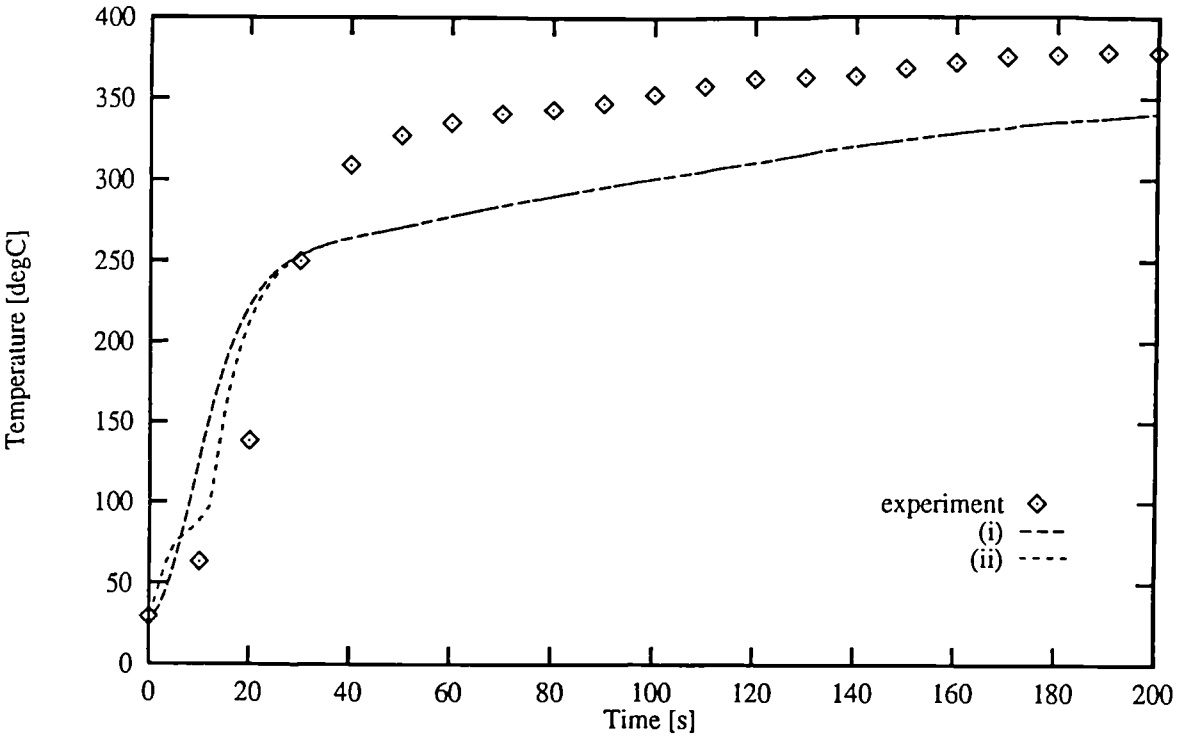

Figure 9.15(a) - T_s values at thermocouple location 1

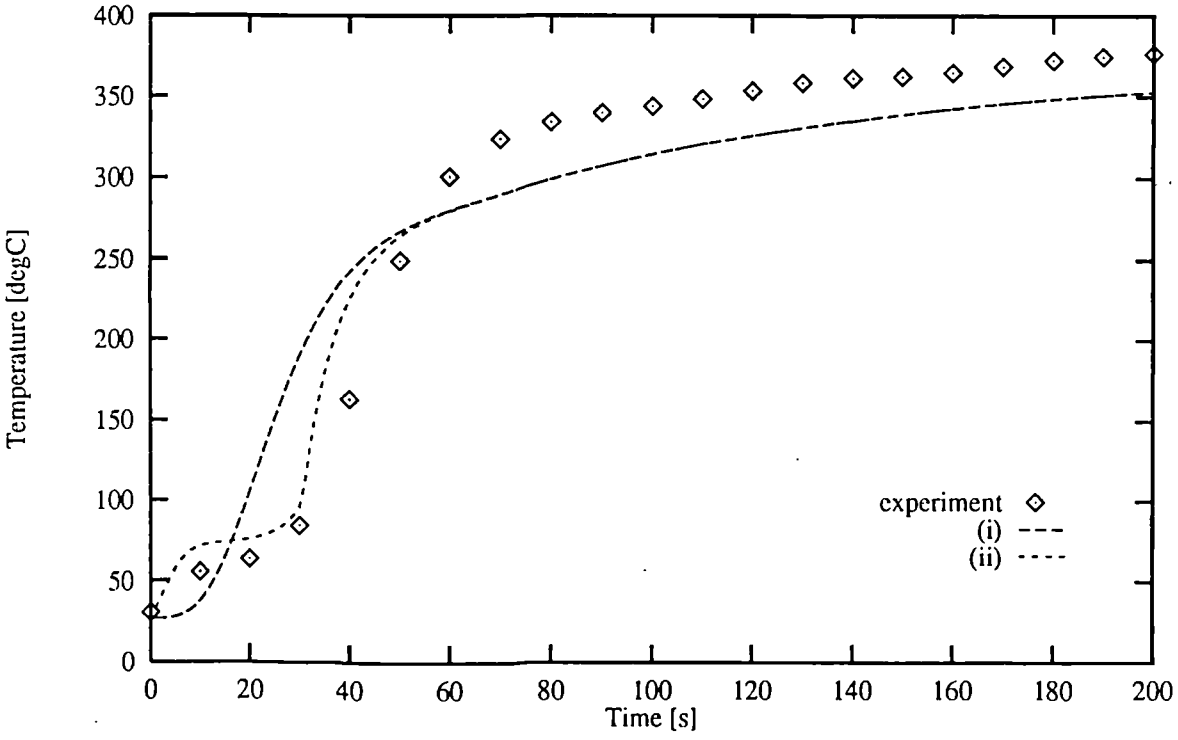

Figure 9.15(b) - T_s values at thermocouple location 2

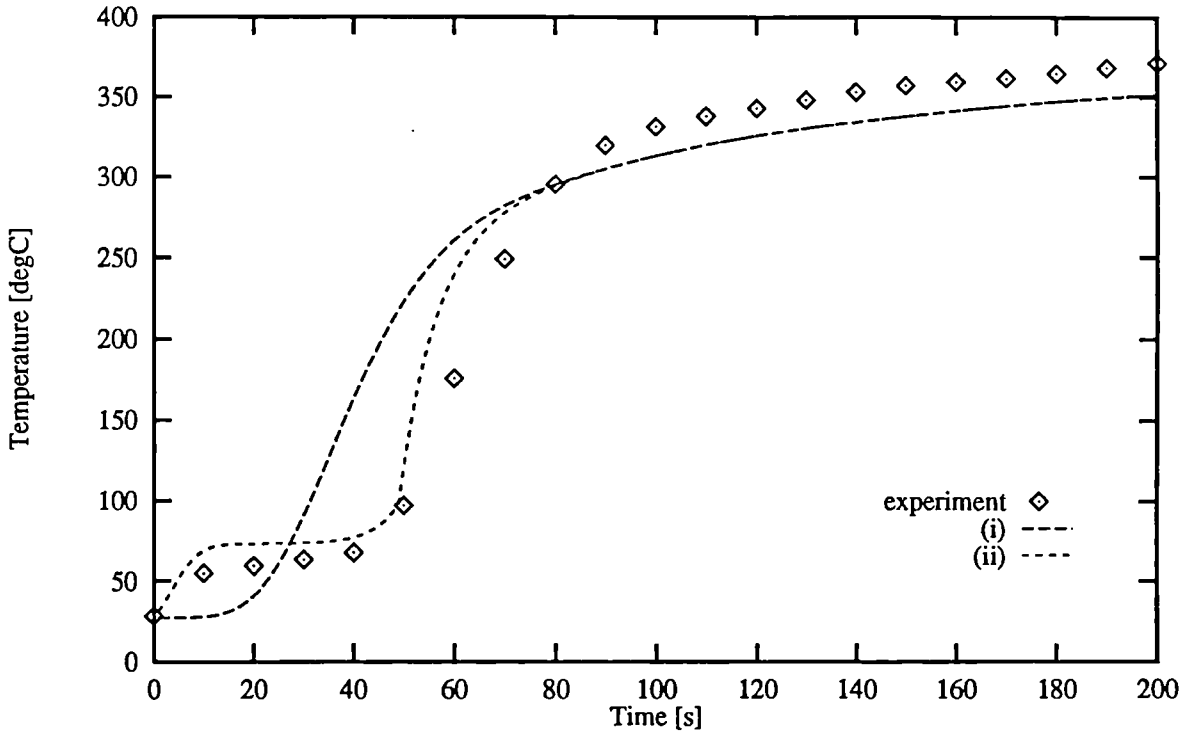

Figure 9.15(c) - T_s values at thermocouple location 3

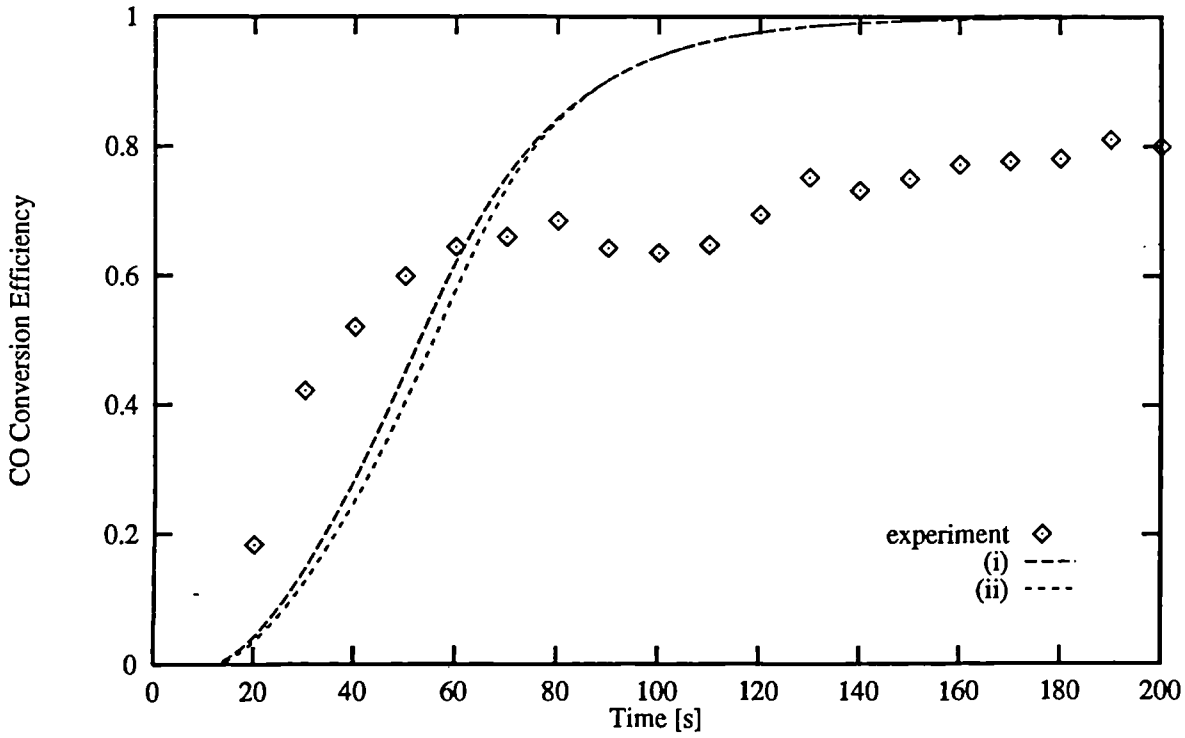

Figure 9.16 - Light-off comparison between dry (i) and increased moisture (ii) (K_{mw} = 0.005976 m/s, inlet c_{gw} = 0.194 and C_{sw}^{vo} = 10 kg/m^3) simulations

10 CONCLUSIONS

The following paragraphs highlight the conclusions and achievements of the work described in this thesis. After an initial review of the major contributions a brief listing is included of the most significant points that were raised and discussed within the main text.

As the preceding sections have shown the broad aims of the project have been achieved, namely, the development of a computational model, based on a commercial CFD code, that combines the prediction of catalyst assembly flow fields with the heat transfer, mass transfer and chemical reactions that occur in catalyst monoliths. As a result the model is a major contribution to catalyst technology because no other model is able to simulate the same range of catalyst phenomena. Of particular importance is its ability to model the feedback effects the heat transfer and chemical reactions, taking place in the monolith, have on the inlet flow field. Results from the model have shown that these effects are significant. The velocity distribution across the monolith does change during light-off, an effect that should be incorporated into catalyst models if accurate predictions are to be obtained.

In addition to implementing the model methodology, an extensive appraisal of its predictive performance has been carried out against experimentally derived data. The appraisal exercise was undertaken in two stages; investigation of the accuracy of the flow field predictions under isothermal conditions, followed by an assessment of the model's ability to predict light-off under reacting conditions. The results of the appraisal exercise highlighted a number of weaknesses in the model, however sufficiently accurate predictions where obtained to allow it to be used for studying catalyst phenomena and testing design options.

One of the model's main weaknesses is its failure to accurately predict the flow distribution across the monolith; predicted monolith velocity profiles are consistently too flat. The pressure drop predictions also tend to be too low. The part of the model that calculates the flow field was based on an established technique for modelling isothermal catalyst flows. No previous work has systematically studied the reliability of this modelling technique, nor highlighted its weaknesses. Possible reasons for these weaknesses have been investigated, and although inconclusive, some evidence does suggest that a major contributory factor is the neglecting of certain monolith channel entrance effects in the monolith pressure drop expression. Entrance effects caused by the acute angle at which the flow can enter a channel are thought to be particularly important.

During assessment of the model under transient warm-up conditions certain phenomena were identified as being caused by moisture in the exhaust gas and on the monolith. A set of relationships were subsequently derived that attempt to model the behaviour of the moisture. When

incorporated into the model they allowed the identified phenomena to be reproduced with a high degree of accuracy. The modelling of these moisture effects on catalyst warm-up is unique; no previous catalyst model has included them. Although affecting the temperature history of the catalyst, particularly during the early stages of warm-up, the model indicated that, for the particular set of circumstances being studied, moisture does not influence light-off times. It was postulated under what conditions moisture could play a significant part (light-off towards the rear of the monolith or if the temperature at which reaction rates become significant is reduced).

Data for the first stage of the model appraisal was obtained from a purpose built steady air flow rig. As part of the experimental programme 20 different axisymmetric catalyst assembly geometries were tested at two Reynolds numbers. Three data sets were collected; monolith velocity distributions, system pressure drops and inlet expansion wall static pressure distributions. In addition to providing information for comparison with model predictions, the results also represent a useful data base on the performance of conical diffusers and 180° expansions with large outlet resistances, which includes automotive catalysts.

10.1 Experimental Steady Flow Data

1. The distribution of the flow emerging from the rear of the monolith is a function of the inlet expansion dimensions, monolith length and Re. Specifically, for a fixed monolith cell density and inlet pipe to monolith expansion ratio, the distribution becomes flatter as;

(i) the monolith length increases,

(ii) the inlet expansion length increases,

(iii) the Re reduces.

The influence of the Re is the most significant of these effects. Although only confirming previous findings the quantitative nature of the data makes it unique.

2. For the same fixed monolith cell density and inlet pipe to monolith expansion ratio the pressure drop across the assemblies decreases as the,

(i) inlet expansion length increases

(ii) the monolith length decreases

(iii) the flow rate decreases.

3. A convenient and instructive way of presenting the trends highlighted by points 1 and 2 above is using a pressure drop versus maldistribution ratio diagram (Figure 6.30).

4. Although the effect of Re and monolith length on wall static pressure coefficient distributions is unclear, any influence will be small. The parameter that has the greatest effect on wall static

pressure coefficient distributions is the inlet expansion length, a series of distinct patterns being produced as the length increases. It is possible that these patterns could provide an insight into the state of the flow in the inlet expansion, with particular reference to separated flow regions.

5. Analysis of the drop in total pressure through the catalyst system suggests that the gas in the monolith channels does not behave as fully developed laminar flow, or laminar flow developing from a "plug" profile, and that additional flow effects are present which should be included in the monolith pressure drop expression. The detailed form of any additional pressure drop term cannot be easily inferred from the existing experimental data.

6. Slight variations in the inlet expansion geometry have a negligible effect on the monolith velocity distribution and system pressure drop.

10.2 Isothermal Flow Field Predictions

1. The choice of turbulence model, differencing scheme and level of mesh refinement can have a major effect on the accuracy of flow predictions. Specifically, a two-layer near wall turbulence model is superior to using wall functions in separated flow regions. A second order differencing scheme gives significantly better predictions than a first order scheme, and it is possible to increase the mesh density to obtain a mesh independent solution

2. Providing a two-layer near wall turbulence approach, a high order differencing scheme and sufficient mesh density are used the shape of the monolith velocity profiles and wall static pressure profiles are qualitatively the same as the experimental results. Close quantitative agreement is, however, lacking.

3. If the correct (i.e. measured) monolith internal dimensions are used, prediction of the assembly pressure drop should be at least within 10% of the experimental results The predicted peak monolith velocity, however, can be expected to be between 9% and 17.5% too low.

4. The catalyst inlet geometries that produced the best results were the 180° expansions. This may be due to greater certainty over the predicted inlet flow separation point, plus, possibly, the more orthogonal nature of their computational meshes.

5. The most likely sources of error in the predictions were identified as a too simplistic monolith pressure drop expression, errors resulting from the equation solving procedure (numerical errors) and remaining weaknesses in the turbulence models.

6. Despite the short comings of the flow field predictions, comparison of the experimental and predicted pressure drop versus maldistribution ratio diagrams shows that the model predicts the correct change in performance parameters as assembly dimensions and Re are altered.

10.3 Reacting Model Predictions

1. A two-dimensional axisymmetric simulation of an active catalyst, situated on an engine rig, and its associated assembly flow field was carried out. The predicted results displayed the correct type, and time scale, of behaviour as the experimental data, however there were several significant quantitative differences:

(i) The model over predicted the final CO conversion efficiency; after 300 seconds the model gave a conversion efficiency of 98%, compared with the 88% measured on the engine rig.

(ii) Comparison of the monolith temperature histories indicated that the model smeared out the reaction front thought to exist towards the front of the monolith.

(iii) The predicted exotherm was 20 °C below the experimental value.

When taken in the context of the assumptions incorporated into the model however, these inaccuracies do not invalidate the model methodology or its usefulness for studying catalyst phenomena.

2. Analysis of the errors in prediction indicates that a number of them can be attributed to over simplified modelling assumptions. Thus the accuracy of the predictions should be improved by incorporating greater complexity into the model (e.g. solving for more chemical species, using more sophisticated Nu and Sh number relationships, etcetera). Other sources of error were identified as arising from uncertainty over many of the material properties and empirical constants (e.g. constants in the reaction rate expressions, thermal properties of the monolith, etcetera).

3. In addition to the axisymmetric simulation a one-dimensional simulation was carried out. The axisymmetric simulation predicted the onset of light-off marginally before the one-dimensional simulation. However, once the effects of flow redistribution and external heat loss were felt by the axisymmetric simulation its light-off processes slowed, relative to the one-dimensional simulation, which reached full conversion efficiency after 150 seconds. These observations highlight some of the weaknesses of using a one-dimensional model.

4. Once the moisture model had been developed and implemented its results were compared with data from a washcoat only catalyst. Good agreement was achieved between temperatures taken along the centre of the monolith. The same level of agreement was achieved when a reacting catalyst was simulated.

5. Although reasonable predictive success has been achieved with the model it has only been tested against one active and one washcoat only catalyst, therefore further testing is still necessary. The ability of the model to simulate other, post-light-off, catalyst phenomena should also be investigated.

11 RECOMMENDATIONS FOR FURTHER WORK

In addition to reviewing the achievements of the work described in this thesis, the previous section also highlighted a number of shortcomings. The following section makes suggestions as to how these shortcomings might be addressed and resolved. The very complex interaction of fluid dynamics, heat transfer, mass transfer and chemical reactions within the model makes the identification of areas that are causing significant errors difficult. A logical approach is to test each part of the model separately, under controlled conditions, and gradually introduce greater complexity. This has already been done, in part, with the testing of the model under steady isothermal flow. The same kind of approach is possible with the heat transfer and chemical reactions.

11.1 Fluid Dynamics Model

To improve the accuracy of the flow field predictions it will be necessary to refine the monolith pressure drop expression to include entrance effects, the absence of which, in the present model, has been identified as a major source of error. Although a possible form for these additional relationships can be derived by intuitive reasoning, further experimental data is required to confirm and hone their details. One of the first details that requires confirmation is the form of the relationship when the monolith is presented with a uniform (one-dimensional) flow field, where the radial velocity component is zero. Two further, particularly valuable, sets of data would be the radial and axial velocity components just upstream of, and the static pressure distribution across, the monolith inlet face when it is presented with a non-uniform flow field. To make the measurement of the velocity components practical more sophisticated techniques than pitot tubes, such as hot wire anemometry (HWA) or laser doppler anemometry, will be needed. In lieu of such data, a trial and error approach might be used to try and fit predictions to the existing experimental results.

As commented on in Section 4.4, if accurate predictions of the flow field in the exit cone and outlet pipe are to be obtained the turbulence intensity of the flow as it emerges from the rear of the monolith should be known.

The present data base of catalyst flow field performance parameters could be greatly extended. The existing geometries could be tested at additional Re's such that regression curves relating pressure drop to maldistribution ratio, as a function of Re, monolith length and cone angle, might be derived using statistical techniques. Exit cones and various lengths of inlet pipe could also be fitted, to test their effect on monolith flow distribution and assembly pressure drop.

Once the modelling technique has been improved to an acceptable level of accuracy for axisymmetric geometries it should be tested against experimental data from non-axisymmetric geometries. Two variations that would be particularly pertinent to automotive catalyst would be bends in the inlet pipe and "race-track" type monoliths. A further complication that the model should be tested under is pulsed flow. A rotating disc with a hole in it would be a suitable means of generating such flow with the existing rig. Again, collecting velocity data from transient flow fields will require more sophisticated measuring techniques than pitot tubes. Another set of conditions under which the fluid dynamics model should be tested is transient warm-ups, however, meaningful appraisal of such predictions can only be carried out when the heat transfer and reaction part of the model has been suitably validated.

11.2 Modelling of Heat Transfer and Reactions

Removing some of the uncertainties in the model constants will require a simplified empirical approach. The first simplification that can be made to the heat transfer part of the model is the removal of chemical reactions. The simplest heat transfer situation that can exist is the steady state conduction of heat within the monolith with no flow passing through it. Although a somewhat false condition, it would provide valuable data on the anisotropic thermal conductivity of the monolith, and if extended to transient heat conduction could be used to obtain specific heat capacities. The most convenient way of setting up such a test would be to heat the centre of the monolith with a known heat load, from an electric element. Measurement of the thermal gradient, as it develops with time, will provide the necessary data.

A slightly more complicated heat transfer situation would be the transient warm-up of a monolith, with adiabatic external walls, under a one-dimensional (uniform velocity and temperature profiles) non-pulsating flow field. Additional complications could be introduced gradually, such as non-adiabatic external walls, a non-uniform flow field and pulsations, eventually leading to testing of washcoat only catalysts connected to engines. Once a data base of information on simple heat transfer cases has been compiled it can be used to refine the heat transfer part of the model. This process will include the testing, and possible alteration, of published channel Nu relationships and external heat loss expressions, plus an assessment of the effect of pulsations.

The predictions presented in Section 9 neglected the effect of radial temperature distributions in the gas as it enters the monolith. The accurate calculation of heat transfer in the inlet pipe and diffuser is required before more realistic temperature profiles can be used. There are known weaknesses (Launder [89]) in the model's present method of calculating heat transfer in turbulent flow, particularly across walls in recirculating flow; these must be assessed. If a non-pulsation flow field is to be retained some account also has to be made of the augmented surface heat transfer

rates pulsations cause. A possible approach would be to use empirically based heat sinks at the walls.

Once reliable predictions of the heat transfer processes are obtained assessment of the mass transfer and reaction rate expressions can begin. Assuming appropriate expressions, derived from specialised reactors, become available they can be tested against experimental results from rigs under simplified conditions. It may be necessary to start with a catalyst supplied with a non-pulsating synthetic exhaust gas, consisting of a limited number of species, and work up to an engine rig. The validity of the mass transfer coefficients proposed by Ullah et al. [94] could be tested, as well as the effect of pulsations on the chemical reactions.

In addition to the solution of more chemical species and incorporating more complex Nu and Sh relationships, a radiative heat transfer model could be included. An assessment of the importance of these refinements could then be undertaken. If the model is to be used to study catalyst behaviour, other than light-off, it will be necessary to investigate when, or if, erroneous multiple steady states occur. If they do occur methods by which they can be eliminated should be investigated. An aid to this exercise would be a multi-dimensional single channel model.

Even though the existing model could be greatly improved its ability to predict certain catalyst phenomena with acceptable accuracy means that it could be used to carry out a number of parametric studies. These include investigating:

(i) under what conditions condensation and evaporation of moisture affects light-off.

(ii) to what extent fixing the monolith velocity profile throughout the warm-up process affects light-off.

(iii) the effect of generating a greater degree of flow maldistribution by using, for example, a wider angled inlet diffuser.

REFERENCES

1. Comfort, E.H. - Monolithic catalytic converter performance as a function of flow distribution - ASME Winter Annual Meeting, Paper No. 74-WA/HT-30, 1974.

2. Howitt, J.S. and Sekella, T.C. - Flow effects in monolithic honeycomb automotive catalytic converters - SAE Paper 740244, 1974.

3. Lemme, S.J. and Givens, W.R. - Flow through catalytic converters - An analytical and experimental treatment - SAE Paper 740243, 1974.

4. Germidis, A., Castagna, F. and Banaigs J. - Thermal measurements inside a three-way catalytic converter on engine bench - SAE Paper 930624, 1993.

5. ESDU Item Number 76027 - Introduction to design and performance data for diffusers - 1976.

6. ESDU Item Number 87015 - Performance improvements of axial diffusers for incompressible flow - 1988.

7. Wendland, D.W. and Matthes, W.R. - Visualisation of automotive catalytic converter internal flows - SAE Paper 861554, 1986.

8. Wendland, D.W., Sorrell, P.L. and Kreucher, J.E. - Sources of monolith catalytic converter pressure loss - SAE Paper 912372, 1991.

9. Wendland, D.W., Matthes, W.R. and Sorrell, P.L. - Effect of header truncation on monolith converter emission-control performance - SAE Paper 922340, 1992.

10. Lai, M.-C., Kim, J.-Y., Cheng, C.-Y., Li, P., Chui, G. and Pakko, J.D. - Three-dimensional simulations of automotive catalytic converter internal flow - SAE Paper 910200, 1991.

11. Kim, J.Y., Lai, M.C., Li, P. and Chui, G. - Modeling diffuser-monolith flows and its implications to automotive catalyst converter design - SAE Paper 921093, 1992.

12. Bella, G., Rocco, V. and Maggiore, M. - A study of inlet flow distortion effects on automotive catalytic converters - ASME Journ. of Eng. for Gas Turbines and Power, Vol. 113, pp 419 - 426, 1991.

13. Dulieu, C.A., Evans, W.D.J., Larbey, R.J., Verrall, A.M., Wilkins, A.J.J. and Povey, J.H. - Metal supported catalysts for automotive applications - SAE Paper 770299, 1977.

14. Nonnenmann, M. - Metal supports for exhaust gas catalysts - SAE Paper 850131, 1985.

15. Oser, P. - Novel autocatalyst concepts and strategies for the future with emphasis on metal supports - SAE Paper 880319, 1988.

16. Kaiser, F-W. and Pelters, S. - Comparison of metal-supported catalysts with different cell geometries - SAE Paper 910837, 1991.

17. Nishizawa, K., Masuda, K., Horie, H. and Hirohashi, J. - Development of improved metal-supported catalyst - SAE Paper 890188, 1989.

18. Whittenberger, W.A. and Kubsh, J.E. - Recent developments in electrically heated metal monoliths - SAE Paper 900503, 1990.

19. Stroom, P.D., Merry, R.P. and Gulati, S.T. - Systems approach to packaging design for automotive catalytic converters - SAE Paper 900500, 1990.

20. Gulati, S.T., Reddy, K.P. and Thompson, D.F. - High temperature strength behavior of ceramic versus metal substrates - SAE Paper 902170, 1990.

21. Jasper, T.S., Robinson, K. and Cuttler, D.H. - Substrate effects on catalyst light-off: Their influence on catalyst design and performance - Worldwide Engine Emissions Standards and How To Meet Them, IMechE Seminar, 12-13 Feb., 1991.

22. Nonnenmann, M. - New high-performance gas flow equalizing metal supports for automotive exhaust gas catalysts - SAE Paper 900270, 1990.

23. Yamamoto, H., Kato, F., Kitagawa, J. and Machida, M. - Warm-up characyeristics of thin wall honeycomb catalysts - SAE Paper 9110611, 1991.

24. Day, J.P. and Socha, L.S. - Impact of catalyst support design parameters on automotive emissions - SAE Paper 881590, 1988.

25. Day, J.P. and Socha, L.S. - The design of automotive catalyst supports for improved pressure drop and conversion efficiency - SAE Paper 910371, 1991.

26. Day, J.P. - The design of a new ceramic catalyst support - SAE Paper 902167, 1990.

27. Church, M.L., Cooper, B.J. and Willson, P.J. - Catalyst formulations - 1960 to present day - SAE Paper 890815, 1989.

28. Monroe, D.R. and Krueger, M.H. - The effect of Pt and Rh loading on the performance of three-way automotive catalysts - SAE Paper 872130, 1987.

29. Lui, Y-K. and Dettling, J.C. - Evolution of Pd/Rh TWC catalyst technology - SAE Paper 930249, 1993.

30. Yamada, T., Kayano, K. and Funabiki, M. - The effectiveness of Pd for converting hydrocarbons in TWC catalysts - SAE Paper 930253, 1993.

31. Summers, J.C., Williamson, W.B. and Scaparo, J.A. - The role of durability and evaluation conditions on the performance of Pt/Rh and Pd/Rh automotive catalysts - SAE Paper 900495, 1990.

32. Tauster, S.J. - Base metal oxide promoters in TWC catalysts - SAE Paper 930250, 1993.

33. Cooper, B.J. and Truex, T.J. - Operational criteria affecting the design of thermally stable single-bed three-way catalysts - SAE Paper 850128, 1985.

34. Bartley, G.J.J., Shady, P.J., D'Aniello, M.J., Chandler, G.R., Brisley, R.J. and Webster, D.E. - Advanced three-way catalyst formulations for high temperature applications - SAE Paper 930076, 1993.

35. Ribbens, W.B. - Electronic engine control - Fuel Economy: Road Vehicles Powered by Spark Ignition Engines, Ch. 12, J.C.Hillard and G.S.Springer (Eds), Plenum Press, N.Y., 1985.

36. Kaneko, Y., Kobayashi, H., Komagome, R., Hirako, O. and Nakayama, O. - Effect of air-fuel ratio modulation on conversion efficiency of three-way catalysts - SAE Paper 780607, 1978.

37. Shulman, M.A., Hamburg, D.R. and Throop, M.J. - Comparison of measured and predicted three-way catalyst conversion efficiencies under dynamic air-fuel ratio conditions - SAE Paper 820276, 1982.

38. Herz, R.K. and Shinouskis, E.J. - Dynamic behaviour of automotive catalysts. 4. Impact of air/fuel ratio excursions during driving - Ind. Eng. Chem. Prod. Res. Dev., Vol 24, pp 385 - 390, 1985.

39. O'Sullivan, R.D. and Will, N.S. - The effect of intermittent engine misfire and air to fuel ratio excursions on exhaust catalyst temperature - SAE Paper 940927, 1994.

40. Taylor, K.C. - Automotive catalytic converters - Catalyst Science Technology, Vol. 5, pp 119-170, 1984.

41. Koberstein, E., Engler, B.H. and Volker, H. - Catalytic automotive exhaust purification - The European situation 1985 - SAE Paper 852094, 1985.

42. Moore, W.R. and Mondt, J.R. - Predicted cold start emission reductions resulting from exhaust thermal energy conservation to quicken catalytic converter light-off - SAE/IMechE Vehicle Thermal Management Systems Conference, Paper 931087, April 1993.

43. Kuo, J.C.W., Morgan, C.R. and Lassen, H.G. - Mathematical modelling of CO and HC catalytic convert systems - SAE Paper 710289, 1971.

44. Hawthorne, R.D. - Afterburner catalysts - effects of heat and mass transfer between gas and catalyst surface - 71st AIChE National Meeting, Dallas, Feb. 1973.

45. Schweich, D. and Leclerc, J.P. - Flow, heat and mass transfer in a monolithic catalytic converter - 2nd International Conference on Catalyst and Automotive Polution Control, Brussels, Nov. 1990.

46. Oh, S.H. and Cavendish, J.C. - Transients of monolithic catalytic converters: response to step changes in freestream temperature as related to controlling automobile emissions - Ind. Eng. Chem. Production, Research and Development, Vol. 21, pp 29 - 37, 1982.

47. Fueyo, N. - 1-D simulation of a catalytic converter for cars - PHOENICS Demonstration Report PDR/CFDU/IC/35, CHAM Ltd, 1987.

48. Lee, S-T. and Aris, R. - On the effect of radiative heat transfer in monoliths - Chem. Eng. Sci., Vol. 32, pp 827 - 837, 1977.

49. Psyllos, A. and Philippopoulos, C. - Modelling of monolith catalytic converters used in automotive pollution control - Appl. Math. Modelling, Vol. 16, pp 484 - 490, 1992.

50. Baruah, P.C., Benson, R.S. and Gupta, H.N. - Performance and emissions predictions for a multi-cylinder spark ignition engine with catalytic converter - SAE Paper 780672, 1978.

51. Sinha, N., Bruno, C. and Bracco, F.V. - Two dimensional, transient catalytic combustion of CO - air on platinum - PCH PhysicoChemical Hydrodynamics, Vol. 6, No. 4, pp 373 - 391, 1885.

52. Heck, R.H., Wei, J. and Katzer, J.R. - Mathematical modelling of monolith catalysts - AIChE Journal, Vol. 22, pp 477 - 484, 1976.

53. Young, L.C. and Finlayson, B.A. - Mathematical models of the monolith catalytic converters: Part I. Development of model and application of orthogonal collocation - AIChE Journal, Vol. 22, No. 2, pp 331 - 343, 1976.

54. Hegedus, L.L., Oh, S.H. and Baron, K. - Multiple steady states in an isothermal, integral reactor: the catalytic oxidation of carbon monoxide over platinum-alumina - AIChE Journal, Vol. 23, No. 5, pp 632 - 642, 1977.

55. Oh, S.H., Cavendish, J.C. and Hegedus, L.L. - Mathematical modeling of catalytic converter lightoff: single-pellet studies - AIChE Journal, Vol. 26, No. 6, pp 935 - 943, 1980.

56. Zygourakis, K. and Aris, R. - Multiple oxidation reactions and diffusion in the catalytic layer of monolith reactors - Chem. Eng. Sci., Vol. 38, No. 5, pp 733 - 744, 1983.

57. Ryan, M.J., Becker, E.R. and Zygourakis, K. - Light-off performance of catalytic converters: The effect of heat/mass transfer characteristics - SAE Paper 910610, 1991.

58. Jasper, T.S., Benjamin, S.F., Girgis, N.S. and Cuttler, D.H. - Computational fluid fynamics and its application to catalyst exhaust systems - 25th ISATA, Florence, Italy, June 1992.

59. Flytzani-Stephanopoulas, M., Voecks, G.E. and Charng, T. - Modelling of heat transfer in non-adiabatic monolith reactors and experimental comparisons of metal monoliths with packed beds - Chem. Eng. Sci., Vol. 41, pp 1203 - 1212, 1988.

60. Chen, D.K.S., Oh, S.H., Bissett, E.J. and Van Ostrom, D.L. - A three-dimensional model for the analysis of transient thermal and conversion characteristics of monolithic catalytic converters - SAE Paper 880282, 1988.

61. Zygourakis, K. - Transient operation of monolith catalytic converters: A two-dimensional reactor model and the effects of radially nonuniform flow distributions - Chem. Eng. Sci., Vol. 44, pp 2075 - 2086, 1989.

62. Chen, D.K.S. and Cole, E.C. - Numerical simulation and experimental verification of conversion and thermal responses for a Pt/Rh metal monolithic converter - SAE Paper 890798, 1989.

63. Will, N.S. and Bennett, C.J. - Flow maldistributions in automotive converter canisters and their effect on emission control - SAE Paper 922339, 1992.

64. Weltens, H., Bressler, H., Terres, F., Neumaier, H. and Rammoser, D. - Optimisation of catalytic converter gas flow distribution by CFD predictions - SAE Paper 930780, 1993.

65. Baxendale, A.J. - The role of computational fluid dynamics in exhaust system design and development - SAE/IMechE Vehicle Thermal Management Systems Conference, Paper 931072, April 1993.

66. Voltz, S.E., Morgan, C.R., Liederman, D. and Jacob, S.M. - Kinetic study of carbon monoxide and propylene oxidation on platinum catalysts - Ind. Eng. Chem. Prod. Res Develop., Vol. 12, No. 4, 1973.

67. Montreuil, C.N., Williams, S.C. and Adamczyk, A.A. - Modelling current generation catalytic converters: laboratory experiments and kinetic parameter optimization - steady state kinetics - SAE Paper 920096, 1992.

68. Boehman, A., Niksa, S. and Moffat, R.J. - Catalytic oxidation of carbon monoxide in a large scale planar isothermal passage - SAE Paper 922332, 1992.

69. Hinze, J.O. - Turbulence - Second Edition, McGraw-Hill, 1975

70. Benedict, R.P., Carlucci, N.A. and Swetz, S.D. - Flow losses in abrupt enlargements and contractions - ASME Journ. of Eng. for Power, Vol. 88, No. 1, pp 73 - 81, 1966.

71. Harlow, F.H. and Nakayama, P. - Transport of turbulence energy decay rate - Los Alamos Science Lab., University oof California Report LA-3854, 1968.

72. Yakhot, V. and Orszag, S.A. - Renormalization group analysis of turbulence. I. Basic theory - Journ. of Sci. Computing, Vol. 1, No.1, pp 3 - 51, 1986.

73. Launder, B.E. and Spalding, D.B. - The numerical computation of turbulent flows - Computer Methods in Applied Mechanics and Engineering, Vol. 3, pp 269 - 289, 1974.

74. Wilcox, D.C. - Comparison of two-equation turbulence models for boundary layers with pressure gradient - AIAA Journal, Vol. 31, No. 8, pp 1414 - 1421, 1993.

75. So, R.M., Lai, Y.G., Zhang, H.S. and Hwang, B.C. - Second-order near-wall turbulence closures: A review - AIAA Journal, Vol. 29, No. 11, pp 1819 - 1835, 1991.

76. Shaw, C.T. - Using computational fluid dynamics - Prentice Hall, 1992.

77. Patankar, S.V. - Numerical heat transfer and fluid flow - Hemisphere Publishing Corporation, 1980.

78. Spalding, D.B. - The PHOENICS Beginners Guide - CHAM Ltd, 1991.

79. Computational Dynamics - STAR-CD Users Guide - Version 2.2, 1994.

80. Schlichting, H. - Boundary-Layer Theory - 7th Edition, McGraw-Hill, 1979.

81. Heitor, M.V. and Rodrigues, J.M. - Intercomparison of flow measurements - Technical University of Lisbon, Department of Mechanical Engineering, May 1992.

82. Girgis, N.S. and Benjamin, S.F. - Prediction of the performance of engine exhaust systems with catalytic converters - Final SERC report, Grant GR/F/88797, Sept. 1993.

83. ESDU Item Number 73024 - Performance of conical diffusers in incompressible flow - 1973.

84. Pozzorini, R. - Das turdulente stromungsfeld in einem langen kreiskegel-diffusor - PhD Dissertation 5646, Eidgenossischen Technischen Hochschule Zurich, Ed. Truninger AG, Zurich, 1976.

85. ESDU Item Number 72011 - Flow through a sudden enlargement of area in a duct - 1972.

86. Habib, M.A. and Whitelaw, J.H. - The calculation of turbulent flow in wide-angled diffusers - Numerical Heat Transfer, Vol. 5, pp 145 - 164, 1982.

87. Norris, L.H. and Reynolds, W.C. - Turbulent channel flow with a moving wavy boundary - Report No. FM-10, Department of Mechanical Engineering, Stanford University, 1975.

88. Rodi, W. and Scheuerer, G. - Scrutinizing the k-e turbulence model under adverse pressure gradient conditions - Trans. of ASME, Journ. of Fluids Engineering, Vol. 108, pp 174 - 179, 1986.

89. Launder, B.E. - Current capabilities for modelling turbulence in industrial flows - Applied Science Research, Vol. 48, pp 247 - 269, 1991.

90. Jasper, T.S., Robinson, K. and Anderson, D. - Assessment of automotive catalyst light-off performance - Southampton University ISVR, Contract Report No. 89/10, 1989.

91. Jasper, T.S. - An investigation into parameters affecting catalyst light-off - MSc Thesis, Southampton University, 1988.

92. Rogers, G.F.C. and Mayhew, Y.R. - Thermodynamic and transport properties of fluids - Third Edition, Basil Blackwell, 1980.

93. Clarkson, R.J., Benjamin, S.F., Jasper, T.S. and Girgis, N.S - An integrated computational model for the optimisation of monolith catalytic converters - IMechE/SAE Vehicle Thermal Management Systems Conference, Paper 931071, April 1993.

94. Ullah, U., Waldram, S.P., Bennett, C.J. and Truex, T. - Monolithic reactors: Mass transfer measurements under reacting conditions - Chem. Eng. Sci., Vol. 47, pp 2413 - 2418, 1992.

95. Wendland, D.W. - Automotive exhaust-system steady-state heat transfer - IMechE/SAE Vehicle Thermal Management Systems Conference, Paper 931085, April 1993.

96. Rhie, C.M. and Chow, W.L. - Numerical study of the turbulent flow past an airfoil with trailing edge separation - AIAA Journal, Vol. 21, No. 11, pp 1525 - 1532, 1983.

97. Fletcher, C.A.J. - Computational Techniques for Fluid Dynamics; Volume 2 - Second Edition, Springer-Verlag, 1990.

98. Holman, J.P. - Heat Transfer - Seventh Edition, McGraw-Hill, 1990.

APPENDIX A - TURBULENCE MODELLING EQUATIONS

A.1 The Standard k-ε Model (from [73], in Cartesian tensor notation):

k equation

$$\frac{\partial \rho k}{\partial t}+\frac{\partial}{\partial x_j}(\rho U_j k)=\frac{\partial}{\partial x_j}\left[\frac{\mu_t}{\sigma_k}\frac{\partial k}{\partial x_j}\right]+\mu_t\frac{\partial U_i}{\partial x_j}\left(\frac{\partial U_i}{\partial x_j}+\frac{\partial U_j}{\partial x_i}\right)-\rho\varepsilon \qquad \text{A.1}$$

ε equation

$$\frac{\partial \rho \varepsilon}{\partial t}+\frac{\partial \rho U_j \varepsilon}{\partial x_j}=\frac{\partial}{\partial x_j}\left[\frac{\mu_t}{\sigma_\varepsilon}\frac{\partial \varepsilon}{\partial x_j}\right]+\frac{C_1\mu_t\varepsilon}{k}\frac{\partial U_i}{\partial x_j}\left(\frac{\partial U_i}{\partial x_j}+\frac{\partial U_j}{\partial x_i}\right)-C_2\rho\frac{\varepsilon^2}{k} \qquad \text{A.2}$$

where

$$\mu_t=C_\mu\rho\frac{k^2}{\varepsilon} \qquad \text{A.3}$$

The empirical constants that appear in the equations are set at,

$$\begin{aligned} C_\mu &= 0.09 \\ C_1 &= 1.44 \\ C_2 &= 1.92 \\ \sigma_k &= 1.0 \\ \sigma_\varepsilon &= 1.3 \end{aligned}$$

A.2 The RNG k-ε Model (from [79])

k equation - as A.1

ε equation:

$$\frac{\partial \rho \varepsilon}{\partial t}+\frac{\partial \rho U_j \varepsilon}{\partial x_j}=\frac{\partial}{\partial x_j}\left[\frac{\mu_t}{\sigma_\varepsilon}\frac{\partial \varepsilon}{\partial x_j}\right]+\frac{C_1\mu_t\varepsilon}{k}\frac{\partial U_i}{\partial x_j}\left(\frac{\partial U_i}{\partial x_j}+\frac{\partial U_j}{\partial x_i}\right)-C_2\rho\frac{\varepsilon^2}{k}$$

$$-\frac{C_\mu\eta^3(1-\eta/\eta_o)}{1+\beta\eta^3}\frac{\rho\varepsilon^2}{k} \qquad \text{A.4}$$

where μ_t is taken from A.3 and

$$\eta = \left[\frac{\partial U_i}{\partial x_j}\left(\frac{\partial U_i}{\partial x_j}+\frac{\partial U_j}{\partial x_i}\right)\right]^{1/2}\frac{k^2}{\varepsilon} \qquad \text{A.5}$$

The empirical constants are set at,

$C_\mu =$ 0.085
$C_1 =$ 1.42
$C_2 =$ 1.68
$\sigma_k =$ 0.719
$\sigma_\varepsilon =$ 0.719
$\eta_o =$ 4.38
$\beta =$ 0.012

A.3 The Norris-Reynolds One-Equation Model (from [79])

k equation - as A.1

ε equation

$$\varepsilon = \frac{k^{3/2}}{0.42C_\mu^{-0.75}y}\left(1+\frac{5.3\nu}{y\sqrt{k}}\right) \qquad \text{A.6}$$

with

$$\mu_t = f_\mu C_\mu \rho \frac{k^2}{\varepsilon} \qquad \text{A.7}$$

and

$$f_\mu = 1-\exp\left(-\frac{y\sqrt{k}}{50.5\nu}\right) \qquad \text{A.8}$$

APPENDIX B - THE FINITE VOLUME METHOD

The finite volume method is a general approach used for solving the partial differential equations (pde) that govern the transport and conservation of quantities such as momentum, mass, temperature, species concentrations and enthalpy, referred to as dependent variables. These pde's take the general form,

$$\frac{\partial \rho \phi}{\partial t} + \nabla.(\rho \mathbf{U}\, \phi) - \nabla.(\rho \Gamma \nabla \phi) = S \qquad \text{B.1}$$

where ϕ is any dependent variable. The terms in Equation B.1 are commonly referred to as, from left to right, the transient term, the convection term, the diffusion term and the source terms, where all remaining terms are grouped together. The essential feature of the method is the division of the physical domain, over which solutions are required, into small volumes or cells. The complete assembly of cells constitutes the computational mesh or grid. Associated with each cell is a node. The locations of these nodes are the points at which the dependent variables are calculated. Integration of the governing pde's over each cell produces an expression that relates the fluxes passing through each cell face, and the creation or destruction of the dependent variable within the cell, to the change in the dependent variable with time. Thus Equation B.1 becomes,

$$\iiint_V \frac{\partial \rho \phi}{\partial t} dV + \iint_A \rho \mathbf{U} \phi \, dA - \iint_A \rho \Gamma \nabla \phi \, dA = \iiint_V S \, dV \qquad \text{B.2}$$

The method is analogous to the control volume approach used for deriving the original pde's, and consequently has the feature of preserving the principle of variable conservation over each cell. Note that for transient problems Equation B.1 must also be integrated with respect to time, the duration of the physical processes under investigation being broken up into discrete time intervals.

Having obtained the integral version of the governing pde's it is necessary to make assumptions about how the dependent variables vary across each cell so that the various terms in Equation B.2 can be equated to nodal values, in addition to cell geometries. Note that these assumed variations do not have to apply to every term. For example, with the diffusion term it is common to assume that ϕ varies linearly between adjacent nodes, an approach referred to as central differencing, however for the source and transient terms it is normally assumed that ϕ has the same value throughout the cell.

When integrating the different terms with respect to time the variation of ϕ throughout the time intervals has to be specified. Various schemes have been developed, however they all fall between two extremes; the fully implicit and the explicit schemes. The explicit scheme assumes that the value of ϕ at the beginning of the time step, the old value, prevails throughout the time step, where as the fully implicit scheme assumes that the value of ϕ at the end of the time step, the new value, prevails throughout the time step. Although the explicit scheme would make obtaining the value of ϕ at the nodes straight forward, unless extremely small time steps are used its use can lead to physically unrealistic solutions. The fully implicit scheme, however, allows realistic solutions to be obtained with relatively large time steps.

B.1 Differencing Schemes

The term in Equation B.2 that causes the greatest problems is the convection term, for which it is necessary to specify the value of ϕ at the cell faces. The various ways in which this can be done are collectively referred to as differencing schemes (although it would be more appropriate to call them convection term differencing schemes). Included below are the mathematical representations of the differencing schemes used within the present project. Note that the definition of each scheme is only given for one cell face, the 'west' face. The notation used is in accordance with the normal conventions and is illustrated in Figure B.1.

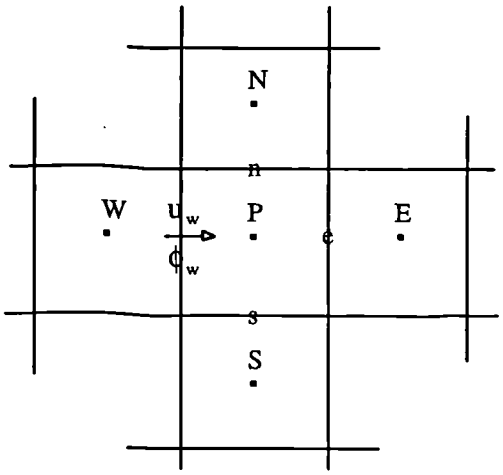

Figure B.1 - Notation used to describe nodes and cell faces surrounding point P.

(i) Central Differencing:

$$\phi_w = f\phi_P + (1-f)\phi_W \qquad \text{B.3}$$

(ii) Upwind Differencing:

$$\phi_w = \begin{cases} \phi_W \text{ for } u_w \geq 0 \\ \phi_P \text{ for } u_w < 0 \end{cases} \qquad \text{B.4}$$

(iii) Hybrid Differencing:

$$\phi_w = \begin{cases} \phi_W & \text{for } Pe > 2 \\ f\phi_P + (1-f)\phi_W & \text{for } -2 \le Pe \le 2 \\ \phi_P & \text{for } Pe < 2 \end{cases} \qquad \text{B.5}$$

(iv) Self Filtering Central Differencing (SFCD):

$$\phi_w = \begin{cases} \gamma[f\phi_P + (1-f)\phi_W] + (1-\gamma)\phi_W & \text{for } u_w \ge 0 \\ \gamma[f\phi_P + (1-f)\phi_W] + (1-\gamma)\phi_P & \text{for } u_w < 0 \end{cases} \qquad \text{B.6}$$

where f is an interpolation factor, Pe is the cell Peclet number and γ is a weighting factor evaluated from local gradients of ϕ, such that $0 \le \gamma \le 1$, and γ approaches 1 when the gradients are large. The cell Peclet number is a measure of the relative magnitudes of convection to diffusion and is defined as $u\delta x/\Gamma$, where δx is the width of the cell, u is the local velocity and Γ the kinematic diffusion coefficient.

The central differencing scheme is the immediately obvious way of specifying the value of ϕ at the cell faces and can be described as second order accurate (i.e. truncation error is of the order of $(\delta x)^2$). Unfortunately when the cell Peclet number is greater than 2 numerical instability and physically unrealistic solutions can result. The upwind scheme has greater numerical stability than the central differencing scheme, however, it is only first order accurate and can produce a phenomenon called numerical diffusion, particularly when the predominant fluid velocity is at an oblique angle to the cell axes. Numerical diffusion arises when the differencing scheme introduces additional, artificial, diffusion terms. These terms tend, incorrectly, to smooth out steep gradients.

The hybrid scheme, which is nominally first order accurate, attempts to reduce the numerical diffusion of the upwind scheme yet retain its stability. It achieves this by using the central differencing scheme when the Pe is less than two and the upwind scheme when the Pe is greater than two. In addition the hybrid scheme normally neglects the diffusion term when the Pe is greater than two. The central differencing scheme is usually only applied in directions perpendicular to the predominant fluid velocity, where its lack of numerical diffusion is more beneficially felt. The SFCD scheme is, as its name implies, essentially central differencing with a built-in facility for preventing physically unrealistic solutions. Consequently it is nominally second order accurate.

B.2 Momentum Equations

The procedures outlined above for solving the pde of the general variable ϕ can be used to solve the Navier-Stokes equations by making ϕ the velocity components. Although apparently straight forward a number of additional treatments are required. Amongst the source terms in the momentum equations is the pressure gradient. Unfortunately the pressure field, and thus its gradients, are normally unknown prior to any calculations and no specific pde is available from which it can be extracted. A way around this problem is to use the continuity equation to generate a pressure equation by replacing the velocity components with expressions containing some measure of the pressure field. A number of schemes based on this approach have been developed. Such schemes are collectively referred to as velocity-pressure coupling algorithms.

One of the earliest schemes developed was the SIMPLE algorithm. It works by first adopting a provisional, incorrect, pressure field which is subsequently used to calculate a provisional, incorrect, velocity field. These sets of data can then be used to define a pressure correction and a velocity correction, both being the difference between the correct pressures and velocities and the provisional pressures and velocities. From these correction parameters it is possible to construct expressions, based on the provisional velocities and pressure corrections, that estimate the correct velocity components. When substituted into the continuity equation these expressions produce a discretized pde of the pressure correction, which can then be solved. Once the pressure corrections are known they can be added to the provisional pressures to obtain an improved estimate of the correct pressure field, which in turn can be used as a new provisional pressure field. Iteration of the above process should result in a final pressure field that produces a continuity obeying velocity field.

Variations of the SIMPLE scheme arise from differences in the expressions substituted into the continuity equation and the addition of extra steps in the algorithm aimed at making further improvements in the provisional pressure field. Such variations can lead to greater numerical stability and speed of convergence. Other, substantially different, velocity-pressure coupling algorithms have been developed, for example the PISO algorithm, which is effectively non-iterative in nature. Such algorithms have not been used in the present work thus are not discussed.

The pressure gradients in the momentum equations, in conjunction with the velocity gradients in the continuity equation, represent a further obstacle to the solution of the flow field. When these terms are integrated over a cell volume, their natural discretized forms are only functions of surrounding nodal values; they are independent of that cell's nodal values. This characteristic can lead to pressures and velocities along any mesh direction that oscillate between high and low

values, producing a totally unrealistic "chequer board" type pattern. Two methods that have been developed for preventing such solutions are,

(i) the staggered grid, where the velocity components are discretized over a mesh whose nodes are displaced half a cell width in the direction of the velocity component, i.e. the velocity components are solved at locations on the faces of the normal mesh cells (Patankar [77]),

(ii) a method proposed by Rhie and Chow [96], which uses weighted linear interpolation to approximate the solution of the momentum equations at cell faces from surrounding nodal values (an approach referred to as a collocated variable mesh).

B.3 Boundary Conditions

To find a specific solution to the pde's it is necessary to know, and define, an appropriate set of boundary conditions. There are essentially three general types of boundary condition; points within the problem domain where the value of the dependent variables are known, points where the spatial gradients of the dependent variables are known and points where a dependent variable flux either leaves or enters the domain. The setting up of the first two types within finite volume codes is achieved by fixing the relevant nodes and gradients to their known values. Fluxes are usually introduced as additional source terms.

Four particular types of boundary condition have been used for the isothermal flow predictions presented in the present work; prescribed flow, fixed pressure, symmetry plane and wall boundaries. The prescribed flow boundary is normally used to specify an inlet plane where the velocities and properties of the fluid entering the domain are known. The fixed pressure boundary is used to specify a plane where the static pressure distribution is known, the most common application being outlet boundaries with uniform pressure profiles. Symmetry planes are used when it is assumed that the physical phenomena under investigation are symmetric, such that it is only necessary to model the domain on one side of that plane. They are generated by setting the spatial gradients normal to the plane to zero.

As discussed in Section 4.2.3, when modelling turbulent flows wall boundaries represent a specific type of problem. If the no slip condition is applied directly, in addition to using a special turbulence model, a very fine mesh is required to resolve the steep velocity and turbulence quantity gradients. The use of wall functions, which describe near wall velocity profiles as well as turbulence levels, removes the need for a fine mesh. However, it should be noted that when they are used it is necessary to ensure that the first node away from the wall is situated within the fully turbulent

region, yet close enough to the wall such that the wall function is still applicable. i.e. $30 \leq y^+ \leq 100$ where y^+ is the non-dimensional distance from the wall, defined as,

$$y^+ = \left(\frac{\tau_w}{\rho}\right)^{1/2} \frac{\rho y}{\mu} \; ; \; \tau_w = \mu \left.\frac{\partial U_x}{\partial y}\right|_{y=0} \qquad \text{B.7}$$

where τ_w is the shear stress at the wall, y is the distance from the wall, ρ the fluid density and μ its dynamic viscosity.

B.4 Closure

The various discretization practices outlined above generate an algebraic equation for each dependent variable at every node. These equations are functions of the surrounding nodal values and are typically non-linear. Hence, once a suitable discretized form of the pde's has been obtained an iterative procedure is used to progressively introduce the influence of boundary conditions. If numerical stability becomes a problem, such that the iterations start to diverge from the correct answer, under-relaxation factors may need to be used. These act in an analogous way to damping in dynamic systems. Finally, discretization of pde's expressed in rectangular Cartesian co-ordinates will lead to a mesh that is only suitable for simulating geometries that consist of co-alined, orthogonal shapes. To model the non-orthogonal geometries more widely found in nature it is necessary to transform the governing pde from Cartesian co-ordinates to a general curvilinear co-ordinate system. Details of these transformations can be found in Fletcher [97].

APPENDIX C - NUMERICAL INTEGRATIONS

```
      PROGRAM ENGEQ1
C     ==============
C
C       A program to calculate the volume flow rate of air through a circular
C       passage (eg monolith/pipe) given either the dynamic pressure (Pa)
C       or velocity (m/s) distribution across the passage. The distribution
C       must start from one side and proceed across the passage
C       (ie diametral distance[mm] vs velocity). It sorts the data into two
C       radial sets, giving a flow rate value for each radius using the
C       trapesium rule.
C
C       Note: i) the 1st and last diameter values MUST be given.
C            ii) last entries must be negative.
C           iii) diameters measured in mm.
C
C       by R J Clarkson, Sept 1993.
C
C       Annex: FRATE3 extended to calculate integrated dynamic pressure
C              across duct (ie V^3r vs r) and integrated monlith losses.
C              RJC, July 1994.
C
      COMMON /ONE/ RADIUS,ENUL,RK1,RK2,DELP
C
      DIMENSION D(100),R(100),V(100),R1(100),V1(100),
     *          R1IN(100),V1IN(100),R2(100),V2(100),VN(100),
     *          ANUL(4),ANUT(4)
C
      OPEN(UNIT=20,NAME='IN1.DAT',STATUS='OLD')
      OPEN(UNIT=21,NAME='FRATE.DAT',STATUS='OLD')
      OPEN(UNIT=22,NAME='VEL.DAT',STATUS='OLD')
C
      DATA (ANUL(I), I=1,4) /1.132E-5,1.343E-5,1.568E-5,1.807E-5/
      DATA (ANUT(I), I=1,4) /250.0,275.0,300.0,325.0/
C
      PARAMETER (TWOPI = 6.28318)
C
C       Reads input data from 'IN1.DAT' file. For file format see example.
C
      READ  (20,*) IOPTN
      READ  (20,*) MONO
      READ  (20,*) DELP
      READ  (20,*) TEMP
      TEMP = TEMP + 273.0
C
      IF (IOPTN.EQ.1) THEN
        WRITE (6,1010)
1010    FORMAT('ENGEQ - IN1.DAT is velocity data.')
        READ  (20,*) RHO
      ELSE
        WRITE (6,1011)
1011    FORMAT('ENGEQ - IN1.DAT is pressure data.')
        READ  (20,*) PRES
        RHO = (PRES * 1.0E+5) / (TEMP * 287.1)
C
C       RHO [kg/m3] from ideal gas equation
C
        WRITE (6,1012) RHO
1012    FORMAT(' Density of Air [kg/m3]     = ',F10.4)
      ENDIF
C
C       Calculates kinematic viscosity [m2/s] from f(TEMP in K)
C
      I = 1
      IF (TEMP.LT.ANUT(1)) STOP 'ERR=2'
2     CONTINUE
      IF (TEMP.GT.ANUT(I)) THEN
        I = I + 1
        IF (I.GT.4) STOP 'ERR=3'
```

```
        GOTO 2
      ELSE IF (TEMP.EQ.ANUT(I)) THEN
        ENUL = ANUL(I)
      ELSE
        ENUL = (ANUL(I+1)-ANUL(I))/(ANUT(I+1)-ANUT(I))
        ENUL = ENUL * (TEMP - ANUT(I))
        ENUL = ENUL + ANUL(I)
      END IF
      WRITE (6,1015) ENUL
1015  FORMAT(' Kinematic Viscosity [m2/s] = ',E12.5)
C
      IF (MONO.EQ.6) THEN
        BRIK = 0.152
        DHYD = 1.1E-3
        POR = 0.72540
        WRITE (6,1020)
1020    FORMAT(' Monolith Length = 6"')
      ELSE IF (MONO.EQ.5) THEN
        BRIK = 0.127
        DHYD = 1.1E-3
        POR = 0.72540
        WRITE (6,1021)
1021    FORMAT(' Monolith Length = 5"')
      ELSE
        BRIK = 0.1016
        DHYD = 1.09E-3
        POR = 0.70025
        WRITE (6,1022)
1022    FORMAT(' Monolith Length = 4"')
      ENDIF
      RK1 = (0.0445 * DHYD * DHYD)/(BRIK * ENUL)
      RK2 = TWOPI * BRIK * 28.455 * ENUL * RHO
      RK2 = RK2 / (DHYD * DHYD * POR)
C
C       Reads in input data
C
5     CONTINUE
      I = 1
10    READ  (20,*) D(I),V(I),DUMMY
        IF (D(I).LT.0.0) GOTO 12
C
C       Code to calc. velocity from dymamic pressure.
C
        IF (IOPTN.NE.1) THEN
          V(I) = SQRT( (2.0*V(I)) / RHO)
        END IF
C
        I = I + 1
        IF (I.GT.100) STOP 'ERR=1'
      GOTO 10
C
12    NTOT = I - 1
      RADIUS = D(NTOT) / 2.0
      DO 14 I = 1,NTOT
        R(I) = D(I) - RADIUS
14    CONTINUE
C
C       Splits data into two radial sets. Starts with 1st
C       which is inverted and consists of -ve values.
C
      I = 1
16    IF (R(I).LT.0.0) THEN
        R1IN(I) = R(I)
        V1IN(I) = V(I)
        I = I + 1
        GOTO 16
C
C       Sets zero radius values.
C
      ELSE IF (R(I).EQ.0.0) THEN
        R1IN(I) = R(I)
        V1IN(I) = V(I)
```

```
          N1 = I
          R2(1) = 0.0
          V2(1) = V(I)
          N2 = NTOT - N1 +1
          NCONT = I + 1
        ELSE
          R1IN(I) = 0.0
          V1IN(I) = 0.0
          N1 = I
          R2(1) = 0.0
          V2(1) = 0.0
          N2 = NTOT - N1 + 2
          NCONT = I
        END IF
C
C         Sets up 2nd radial set.
C
        J = 1
        DO 18 I = NCONT,NTOT
          J = J + 1
          R2(J) = R(I)
          V2(J) = V(I)
18      CONTINUE
C
C         Inverts 1st set to correct orientation (centre first).
C
        DO 20 I = 1,N1
          R1(I) = -R1IN(N1+1-I)
          V1(I) = V1IN(N1+1-I)
20      CONTINUE
C
        IF (N1.GT.N2) THEN
          M = N1
        ELSE
          M = N2
        END IF
C        DO 25 I = 1,M
C          WRITE (21,2100) R1(I),V1(I),R2(I),V2(I)
C2100      FORMAT(4F10.3)
C25      CONTINUE
C
30      WRITE (6,1000)
1000    FORMAT('Enter no. of trapezia : '$)
        READ  (5,*) ITRAP
        IF (ITRAP.GE.300) THEN
          WRITE (6,1004)
1004      FORMAT('  No. of Trapizia must be < 300')
          GOTO 30
        END IF
        ITRAP = ITRAP + 1
C
        WRITE (6,1002)
1002    FORMAT(' First Radius :')
        CALL TRAP_RULE (R1,V1,N1,ITRAP,RHO,VMN1,RE1,VM01
     *     ,PD21,ALP21,PD01,PLC1,PLD11,PLDC1,PLD21)
C
        WRITE (6,1003)
1003    FORMAT(' Second Radius :')
        CALL TRAP_RULE (R2,V2,N2,ITRAP,RHO,VMN2,RE2,VM02
     *     ,PD22,ALP22,PD02,PLC2,PLD12,PLDC2,PLD22)
C
        RE = (RE1 + RE2) / 2.0
        VM0 = (VM01 + VM02) / 2.0
        PD2 = (PD21 + PD22) / 2.0
        ALP2 = (ALP21 + ALP22) / 2.0
        PD0 = (PD01 + PD02) / 2.0
        PLC = (PLC1 + PLC2) / 2.0
        PLD1 = (PLD11 + PLD12) / 2.0
        PLDC = (PLDC1 + PLDC2) / 2.0
        PLD2 = (PLD21 + PLD22) / 2.0
        PTOT = PD0 + DELP
        DELPT = PTOT - PD2
```

```
      DPTNON = (2.0 * DELPT) / (VM0 * VM0 * RHO)
      WRITE (22,2000) RE,PD0,PTOT,PD2,ALP2,DELPT,DPTNON
      WRITE (6,2000) RE,PD0,PTOT,PD2,ALP2,DELPT,DPTNON
2000  FORMAT('# Averaged Values :-'/
     *       '# I/L: Re = ',1PE9.2,', Int.P-d = ',0PF8.3,
     *            ', P-t = ',F8.3/
     *       '# O/L: Int.P-d = ',F8.3,', Alpha    = ',F6.3/
     *       '#      DP-t    = ',F8.3,', DP-t/P-d = ',F6.3)
      WRITE (22,2001) PLC,PLD1,PLDC,PLD2
      WRITE (6,2001) PLC,PLD1,PLDC,PLD2
2001  FORMAT('#          Int.Pl-Cor      Pl-Diff'/
     *       '# Lam.   ',2F12.3/
     *       '# Lam*Dl ',2F12.3)
C
      WRITE (6,1005)
1005  FORMAT(' Mass Flow to be used to normalise velocities ?'/
     *       ' Enter 1(1st Rad), 2(2nd Rad), 3(Mean), 4(Other):'$)
      READ  (5,*) IOPTN
      IF (IOPTN.EQ.1) THEN
        VNORM = VMN1
      ELSE IF (IOPTN.EQ.2) THEN
        VNORM = VMN2
      ELSE IF (IOPTN.EQ.3) THEN
        VNORM = (VMN1 + VMN2) / 2.0
      ELSE
        WRITE (6,1006)
1006    FORMAT(' Enter Mass Flow in g/s: '$)
        READ  (5,*) MASSFL
        VNORM = (MASSFL*1E+03) / (3.14159*RADIUS*RADIUS*RHO)
      ENDIF
      WRITE (6,1007) VNORM
1007  FORMAT(' Normalizing Velocity [m/s] = ',F10.3)


C
      DO 35 I = 1,NTOT
        VN(I) = V(I) / VNORM
        WRITE (22,2002) D(I),V(I),VN(I)
2002    FORMAT(3F10.3)
35    CONTINUE
C
      END
C     ------------------------------------------------------------
      SUBROUTINE TRAP_RULE (R,V,N,ITRAP,RHO,VMEAN,REINL,VMINL
     *          ,PDYN,ALPHA,PDYNIN,PLCORE,PLDIF1,PLDCOR,PLDIF2)
C     ------------------------------------------------------------
C
C       Calculates area under V^3r vs r plot, to give integrated
C       dynamic pressure, and Vr vs r plot, to give mass
C
      DIMENSION R(100),V(100),VR(100),V3R(100),V2R(100),V2RDL(100)
     *         ,X(300),Y(300),Y1(300),Y2(300),Y3(300)
C
      COMMON /ONE/ RADIUS,ENUL,RK1,RK2,DELP
C
      PARAMETER (TWOPI = 6.28318)
      PARAMETER (PI = 3.1415926)
      PARAMETER (PDIA = 0.055)
C
C       Calculates V^3r and Vr products.
C
      DO 10 I = 1,N
        V3R(I) = R(I) * V(I) * V(I) * V(I)
        VR(I) = R(I) * V(I)
        V2R(I) = R(I) * V(I) * V(I)
        DL = SQRT(1 + (RK1*V(I)))
        V2RDL(I) = V2R(I) * DL
10    CONTINUE
C
C       Sets up trapezia abcissa.
C
      H = R(N) / REAL(ITRAP-1)
```

```
      X(1) = 0.0
      Y(1) = 0.0
      Y1(1) = 0.0
      Y2(1) = 0.0
      Y3(1) = 0.0
      DO  20 I = 2,ITRAP
        X(I) = (I-1) * H
20    CONTINUE
C
C       Calculates trapezia ordinates by linear interpolation.
C
      J = 2
      I = 2
30    CONTINUE
      IF (X(I).GT.R(J)) THEN
        J = J + 1
        IF (J.GT.N) GOTO 40
        GOTO 30
      ELSE
        FRAC = (X(I) - R(J-1))/(R(J) - R(J-1))
        Y(I) = FRAC * (V3R(J) - V3R(J-1)) + V3R(J-1)
        Y1(I) = FRAC * (VR(J) - VR(J-1)) + VR(J-1)
        Y2(I) = FRAC * (V2R(J) - V2R(J-1)) + V2R(J-1)
        Y3(I) = FRAC * (V2RDL(J) - V2RDL(J-1)) + V2RDL(J-1)
        I = I + 1
        IF (I.GT.ITRAP) GOTO 40
        GOTO 30
      END IF
C
40    CONTINUE
C      DO 300 I = 1,ITRAP
C        WRITE (21,301) X(I),Y(I),Y1(I),Y2(I)
C301     FORMAT (3F12.4)
C300   CONTINUE
      IF (N.GT.ITRAP) THEN
        M = N
      ELSE
        M = ITRAP
      END IF
C
C       Applies trapezium rule.
C
      VFLOW = (Y1(1) + Y1(ITRAP)) / 2.0
      DO  60 I = 2,(ITRAP-1)
        VFLOW = VFLOW + Y1(I)
60    CONTINUE
      VFLOW = H * VFLOW * TWOPI
      WRITE (6,1001) VFLOW/1.0E+6
1001  FORMAT(' Volume Flow Rate [m3/s] = ',E15.6)
C
      WRITE (6,1002) (VFLOW*RHO)/1.0E+3
1002  FORMAT(' Mass Flow Rate    [g/s] = ',2PE15.6)
C
      REINL = (4.0E-06 * VFLOW) / (PI * PDIA * ENUL)
      VMINL = (4.0E-06 * VFLOW) / (PI * PDIA * PDIA)
C
      WRITE (6,1003) REINL
1003  FORMAT(' Inlet Re                = ',1PE15.6)
C
C       Assigns appropriate alpha at inlet for Re (from e16 & e12)
C
      IF (REINL.LT.2.8E+4) THEN
        WRITE (6,1010)
1010    FORMAT(' Re<2.8E+4; Enter alpha-0 :'$)
        READ  (5,*) ALFINL
      ELSE IF (REINL.LT.4.5E+4) THEN
        ALFINL = 1.095
      ELSE IF (REINL.LT.6.6E+4) then
        ALFINL = 1.060
      ELSE
        WRITE (6,1011)
1011    FORMAT(' Re>6.6E+4; Enter alpha-0 :'$)
```

```
        READ  (5,*) ALFINL
      ENDIF
      PDYNIN = 0.5 * ALFINL * RHO * VMINL * VMINL
C
      VMEAN = VFLOW / (PI * RADIUS * RADIUS)
      CONST = RK2 / VFLOW
C
C        V^3r vs r integration.
C
      PDYN = (Y(1) + Y(ITRAP)) / 2.0
      DO  70 I = 2,(ITRAP-1)
        PDYN = PDYN + Y(I)
70    CONTINUE
      PDYN = H * PDYN * PI * RHO / VFLOW
      PDYNM = RHO * VMEAN * VMEAN / 2.0
      ALPHA = PDYN / PDYNM
C
C        V^2r vs r integration.
C
      PLCORE = (Y2(1) + Y2(ITRAP)) / 2.0
      DO  80 I = 2,(ITRAP-1)
        PLCORE = PLCORE + Y2(I)
80    CONTINUE
      PLCORE = H * PLCORE * CONST
C
C        V^2rDl vs r integration.
C
      PLDCOR = (Y3(1) + Y3(ITRAP)) / 2.0
      DO  90 I = 2,(ITRAP-1)
        PLDCOR = PLDCOR + Y3(I)
90    CONTINUE
      PLDCOR = H * PLDCOR * CONST
C
      PLDIF1 = DELP + PDYNIN - PDYN - PLCORE
C
      PLDIF2 = DELP + PDYNIN - PDYN - PLDCOR
C
      WRITE (21,1004)
1004  FORMAT(' ---------------------------------------------------'/,
     *       ' | Int. P-dyn | Mean P-dyn  | alpha    | Int. P-dyn |'/,
     *       ' |     [Pa]   |    [Pa]     |          | (I/L) [Pa] |'/,
     *       ' ---------------------------------------------------')
C
      WRITE (21,1005) PDYN,PDYNM,ALPHA,PDYNIN
1005  FORMAT(' |',F10.3,'  | ',F10.3,'  | ',F6.3,'  | ',F10.3,' |')
C
      WRITE (21,1006)
1006  FORMAT(' ---------------------------------------------------'/,
     *       ' |        | Int. Pl-Core [Pa] | Tot. Pl-Diff [Pa]  |'/,
     *       ' ---------------------------------------------------')
      WRITE (21,1007) PLCORE,PLDIF1
1007  FORMAT(' |  Lam   |  ',F13.4,'    |  ',F13.3,'     |'/,
     *       ' ---------------------------------------------------')
      WRITE (21,1008) PLDCOR,PLDIF2
1008  FORMAT(' | Lam*Dl |  ',F13.4,'    |  ',F13.3,'     |'/,
     *       ' ---------------------------------------------------')
C
      RETURN
      END
```

APPENDIX D - MONOLITH EXTERNAL HEAT LOSS

The following calculation estimates the surface heat transfer coefficient, h_{ext}, for a cylindrical catalyst can that is being cooled by natural convection.

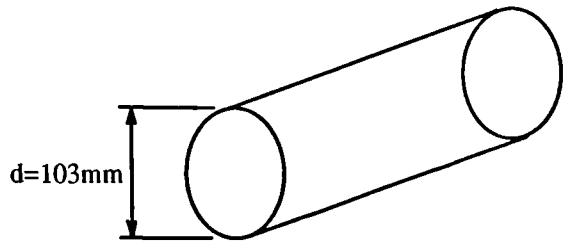

From Holman [98] the Nu is given by:

$$Nu = 0.53(Gr_d Pr)^{0.25} \qquad D.1$$

Estimates of the surface temperature, T_w, and the ambient temperature, T_∞, are taken to be 250 °C and 15 °C respectively. The properties of the fluid, air, are approximated to be those corresponding to the mean of these temperatures (T_f), i.e. 405.5 K. Therefore:

$k_g = 0.03406$ W/mK
$\beta = 1 / T_f = 1 / 405.5 = 2.47 \times 10^{-3}$ /K
$\nu_g = 2.654 \times 10^{-5}$ m^2/s
$Pr = 0.687$

$$Gr_d Pr = \frac{g\beta(T_w - T_\infty)d^3}{\nu^2} Pr \qquad D.2$$
$$= 6.0625 \times 10^6$$

Giving

$$Nu = \frac{hd}{k_g} = 26.3 \qquad D.3$$

Therefore

$$h_{ext} = 8.7 \text{ W/m}^2\text{K}$$

APPENDIX E - EXHAUST GAS MOISTURE CONTENT

A typical engine fuel will have a composition, by mass, of 86.7% carbon and 13.5% hydrogen. If the air-fuel ratio is 15:1 the mass flow rate of fuel entering the engine will be $\dot{m}/16$ kg/s, where $\dot{m}$ is the total mass flow rate through the engine. Therefore the mass flow rate of hydrogen entering the engine, $\dot{m}_H$, will be given by:

$$\dot{m}_H = \frac{0.135\dot{m}}{16} \qquad \text{E.1}$$

Assuming all the hydrogen atoms are oxidised to water vapour, for every kg of hydrogen 9 kg of water vapour will be produced. Thus the mass flow rate of water vapour passing out of the engine, $\dot{m}_w$, will be given by:

$$\dot{m}_w = \frac{0.135 \times 9 \times \dot{m}}{16} \qquad \text{E.2}$$

i.e. the mass fraction of water vapour in the exhaust gas will be:

$$\frac{\dot{m}_w}{\dot{m}} = 0.076 \qquad \text{E.3}$$

APPENDIX F - PUBLICATIONS RESULTING FROM THE PROJECT

Clarkson, R.J., Benjamin, S.F., Jasper, T.S. and Girgis, N.S - An integrated computational model for the optimisation of monolith catalytic converters - IMechE/SAE Vehicle Thermal Management Systems Conference, Paper 931071, April 1993.

Clarkson, R.J. and Benjamin, S.F. - Modelling catalytic converters as complete systems: fluid flow, chemistry, heat and mass transfer - 9th International Conference on Systems Engineering, Las Vegas, July 1993.

Clarkson, R.J., Benjamin, S.F., Girgis, N.S. and Richardson, S. - Theoretical and experimental investigation of the flow in catalytic converters - IMechE Seminar on the Validation of Computational Techniques in Vehicle Design, April 1994.